Evolution of Intermediate Redshift Galaxies

Physical Properties and Mass-Metallicity Relation

by

Lifang Xia

A Dissertation Presented in Partial Fulfillment
of the Requirements for the Degree
Doctor of Philosophy

Approved March 2012 by the
Graduate Supervisory Committee:

Sangeeta Malhotra, Chair
James Rhoads
Evan Scannapieco
Rolf Jansen
Patrick Young

ARIZONA STATE UNIVERSITY

May 2012

ABSTRACT

The first part of this dissertation presents the implementation of Bayesian statistics with galaxy surface luminosity (SL) prior probabilities to improve the accuracy of photometric redshifts. The addition of the SL prior probability helps break the degeneracy of spectro-photometric redshifts (SPZs) between low redshift 4000 Å break galaxies and high redshift Lyman break galaxies which are mostly catastrophic outliers. For a sample of 1138 galaxies with spectroscopic redshifts in the GOODS North and South fields at $z < 1.6$, the application of the surface luminosity prior reduces the fraction of galaxies with redshift deviation $\Delta(z) > 0.2$ from 15.0% to 10.4%.

The second part of this dissertation presents the study of the chemical evolution of the star-forming galaxies. The *Hubble Space Telescope* Probing Evolution and Reionization Spectroscopically (PEARS) grism Survey effectively selects emission line galaxies (ELGs) to $m_{AB} \sim 27$. Follow-up Magellan LDSS3+IMACS spectroscopy of the HST/ACS PEARS ELGs confirms an accuracy of σ_z = 0.006 for the HST/ACS PEARS grism redshifts. The luminosity-metallicity (L-Z) relation and the mass-metallicity ($M - Z$) relation of the PEARS ELGs at $z \sim 0.6$ are offset by $\sim$ – 0.8 dex in metallicity for a given rest-frame B absolute magnitude and stellar mass relative to the local relations from SDSS galaxies. The offsets in both relations are $\sim$ – 0.4 dex larger than that given by other samples at same redshifts, which are demonstrated to be due to the selection of different physical properties of the PEARS ELGs: low metallicities, very blue colors, small sizes, compact disturbed morphologies, high SSFR $> 10^{-9}$ yr^{-1}, and high gas fraction. The downsizing effect, the tidal interacting induced inflow of metal-poor gas, and the SNe driven galactic winds outflows, may account for the significant offset of the PEARS galaxies in the L-Z and the M-Z relations relative to the local relations. The detection of the emission lines of ELGs down to m $\sim$ 26 mag in the HST/ACS PEARS + HST/WCF3 ERS NIR composit grism spectra enables to extend the study of the evolution of the L-Z and M-Z relations to $0.6 < z < 2.4$.

I sincerely dedicate this thesis to the two prominent advisors in my study of astrophysics: Dr. Xu Zhou and Dr. Sangeeta Malhotra, for their hand-by-hand and step-by-step guidance in my exploration in this field.

ACKNOWLEDGEMENTS

I would first like to thank my advisor, Dr. Sangeeta Malhotra, with my sincere and deep gratitude. It is her tireless advice, great patience, and ongoing encouragement that support me to complete this dissertation. I would like to thank her for the great help and patience, which carries me through the years, in advising and encouraging me when I encountered different problems in language, data reduction, observation design and proposals and papers, especially when I was frustrated, inconfident and hesitated. I would like also to thank her for her efforts at encouraging me to present my research at meetings, talk to collegues, which have greatly helped me in communication and cooperation in research work. Finally, I would like to thank other committee members: Prof. James Rhoads, Prof. Sumner Starrfield, Prof. Evan Scannapieco, Prof. Rolf Jansen, and Prof. Patrick Young for their valuable suggestions and supervisions to this work.

I have been fortunate to study in ASU School of Earth and Space Exploration as a graduate student. The researchers around the department and across the country have been kind and helpful in providing comments, suggestions, and discussions and collaborations, which have accelerated and improved greatly my work. I would like to acknowledge them together here: Drs. Nor Pirzkal, Seth Cohen, Nimish Hathi, Norman Grogin, Amber Straughn, David Floyd, Lisa Kewley, Steven Finkelstein, Rogier Windhorst and Gerhardt Meurer. And the fellow graduate students: Tilvi Vithal Shet, Angel Fuentes, Emily McLinden, Michael Rutkowski, Nahks Tr'Ehnl, Natalie Hinkel, Mark Richardson, Zhenya Zheng, and Liubin Pan.

I have been supported over the years by a series of generous funding institutions. I am especially grateful for the several years of support as a teaching assisstant from the School of Earth and Space Exploration. The Graduate and Professional Student Association supported my trip to the meeting of the AAS in Austin, Texas. In particular, I would like to acknowledge the funding support for this work provided by NASA through a grant number HST-GO-10530 from the Space Telescope Science Institute, which is operated by the Association of Universities for Research in Astronomy, Inc., under NASA contract NASA5-26555.

TABLE OF CONTENTS

LIST OF TABLES

LIST OF FIGURES

Figure Page

Figure Page

Figure Page

Chapter 1

INTRODUCTION

1.1 Review

In the frame of cosmological cold dark matter (CDM) model, the hierarchical galaxy clustering scenario well depicts galaxy formation and evolution as a consequence of the growth of the primordial fluctuation. The overdense regions of dark matter collapse and gravitationally attract gas and become the seeds of the first stars and galaxies. The small size galaxies merge and form larger size galaxies and galaxy clusters, which is known as the "bottom-up" structure formation. From numerical simulation, this hierarchical scenario of forming ellipticals via major mergers of spiral galaxies is generally supported (Hernquist et al., 1995; Bender, 1996; di Matteo et al., 2005; Springel et al., 2005a,b; Hopkins et al., 2006, 2008). Observationally, galaxies in the nearby universe at $\sim z < 1$ are well classified to well-organized Hubble types: elliptical galaxies, spiral galaxies, and peculiar galaxies. While at high redshift universe, much larger fraction of irregular galaxies are observed (Driver et al., 1998; Glazebrook et al., 2004; Straughn et al., 2008).

The physical properties of galaxies in different evolutionary stages are quite different. For example, spiral galaxies are generally blue, gas rich, and actively star-forming; elliptical galaxies are of larger size, more massive, red, dust free and metal rich. In cosmic galaxy evolution, the redshift range $1 < z < 2$ is the era that hosts the emergence of the Hubble sequence of disk and elliptical galaxies and the buildup of most of the stellar mass in the universe (Dickinson et al., 2003). Hence, it is important to study the observational properties relationships within full redshift range to deepen our understanding of galaxy evolution.

The physical processes such as the inflow of pristine gas and the feedback processes play an important role in modulating galaxy star formation and hence galaxy observational properties such as metallicity. The “feedback” refers to the exchange of gas between star and interstellar medium (ISM) and between galaxy and intergalactic medium (IGM) due to the powerful stellar winds of massive stars and the supernovae (SNe) explosion. The winds are powerful enough to overcome the gravitational well of stars and galaxies and to eject the enriched metals into the ISM and IGM. Large-scale outflows of gas are ubiquitous among the most actively star-forming galaxies (Lehnert et al., 1996; Dahlem et al., 1998; Rupke et al., 2002; Shapley et al., 2001; Pettini et al., 2001, 2002; Frye et al., 2002; Weiner et al., 2009) and are complex, multiphase, hydrodynamical phenomenon (Strickland et al., 2002). Feedback modulates the star formation by removing the gas or by compressing and reheating the cold ISM (Larson, 1974; Larson et al., 1975; White et al., 1978). Despite the complexity of the galactic winds and the difficulty of accurate prescription in models, to quantify the impact of feedback in metal depletion, the simple closed-box chemical evolution model (Pagel et al., 1979) and modified chemical evolution model with inflows and outflows (Larson, 1974; Erb et al., 2006; Erb, 2008) are constructed to assess the predicted level of the galaxy chemical enrichment.

Stellar mass and metallicity are two of the most fundamental physical properties of galaxies. Galaxy stellar mass is the accumulated amount of gas converted into stars, reflecting the whole past star formation history of galaxy instead of the present star formation activity. Metallicity, which is defined as the mass ratio of metals (elements other than H and He) to hydrogen, reflecting the gas reprocessed by stellar nucleosynthesis, is sensitive to the evolutionary stage of galaxy, such as early-type elliptical galaxies, late-type spiral galaxies, or starburst, irregular galaxies. The study of the correlation of galaxy stellar mass versus metallicity and the evolution of this correlation with time provide insight into the details of the physical processes that govern the efficiency and timing of star formation and the gas enrichment or depletion.

The investigation of the relationship between mass and metallicity starts from late ’70s (Lequeux et al., 1979). The study of this correlation is firstly focused on the correlation between metallicity and blue luminosity ($L-Z$ relation) (Garnett & Shields, 1987; Skillman et al., 1989; Brodie & Huchra, 1991; Zaritsky et al., 1994; Garnett et al., 1997; Lamareille et al., 2004; Salzer et al., 2005) due to the difficulty of obtaining stellar mass. The $L-Z$ relation is studied in a range of Hubble types and spanning over 11 magnitudes in luminosity and 2 dex in chemical abundance. The later study of the relationship between mass and metallicity (Garnett, 2002; Pilyugin et al., 2004; Tremonti et al., 2004; Lee et al., 2006; Panter et al., 2008; Kewley & Ellison, 2008; Liu et al., 2008) show that galaxies with larger stellar masses have higher metallicities.

This relation is established from local universe $z \sim 0.07$ (Tremonti et al., 2004) to high redshift universe around z=0.7 (Savaglio et al., 2005; Rodrigues et al., 2008), z$\sim$1.5 (Cowie & Barger, 2008; Lamareille et al., 2009; Pérez et al., 2009), at z$\sim$2 (Erb et al., 2006; Halliday et al., 2008; Hayashi et al., 2009), and at z$\sim$3 (Kobulnicky & Koo, 2000; Pettini et al., 2001, 2002; Maier et al., 2006). The evolution of this relation with cosmic time show that metallicity decreases with increasing redshift for a given stellar mass.

The trend of the mass-metallicity relation is interpreted by several possible effects. The well-known “downsizing” effect is that the lower-mass galaxies form stars later and on longer time scales than more massive galaxies due to lower star-formation efficiency and therefore show lower metallicities (Gavazzi & Scodeggio, 1996; Cowie et al., 1996; Kobulnicky & Kewley, 2003; Ellison et al., 2008). Calura et al. (2009) have explained the evolution of the mass-metallicity up to z=3.5 as due to an increase of the efficiency of star formation with galaxy mass, without invoking differential galactic outflows. Another effect is the preferential metal loss, i.e. higher mass galaxies are expected to be more metal rich than lower mass galaxies because of the more important effect of outflows in less massive galaxies due to the lower gravitational potential (Larson, 1974; Edmunds et al., 1990; Garnett, 2002; Tremonti et al., 2004; Lamareille et al., 2004; Saviane et al., 2008). Tremonti et al. (2004) have shown that the mass loss is strongly anticorrelated with baryonic mass, with low-mass dwarf galaxies being 5 times more metal depleted than L_* galaxies at $z\sim0.1$. Many studies have also shown the evidence of both the ubiquity of galactic winds and the importance of the feedback in galaxy formation (Hernquist et al., 2003; Benson et al., 2003; Dekel & Woo, 2003; Nagamine et al., 2004; Murray et al., 2005). Other possibilities, such as galaxy mass dependent initial mass function (IMF), could also have effect on galaxy mass-metallicity relation (Koppen et al., 2007). All these effects have impacts on galaxy evolution, and the knowledge of their relative contributions is of crucial importance. Generally, the mass-metallicity relation at high redshifts is likely driven by the increase in metallicity as the gas fraction decreases through star formation and is modulated by metal loss from strong outflows in galaxies of all masses.

Different models have been built to reproduce the shape of the mass-metallicity relation in the local universe. The simple closed-box model (Pagel et al., 1979) is constructed to study galaxy chemical evolution with the assumptions that gas converted into a closed system (without inflows and outflows) and instantaneous recycling (Van den Bergh, 1962; Schmidt, 1963; Searle & Sargent, 1972). This model relates the metallicity to the yield from star formation and the gas fraction by a simple function. I use the empirical relation between SFR density and gas density to estimate the gas fractions of the galaxies, finding an increase in gas fraction with decreasing stellar mass. Combined with the observational properties that less massive galaxies tend to have larger gas fraction (McGaugh & de Blok, 1997; Bell & de Jong, 2000), and stellar masses, gas fraction, and evolutionary stages vary significantly among the galaxies, the simple closed-box model expect a relationship between galaxy mass and metallicity. While the G dwarf problem and the ubiquitous galactic winds, infall and mergers in galaxy formation and evolution (Pagel et al., 1975; Naab & Ostriker, 2006; Heckman et al., 1990; Lehnert et al., 1996; Martin, 1999; Strickland et al., 2004; Pettini et al., 2001; Shapley et al., 2003) suggests the limitation of the closed-box model. The modified model includes the effect of the inflow of less enriched gas and the outflow of to account for the mass-metallicity relation (Larson, 1974; Erb et al., 2006; Erb, 2008). Tremonti et al. (2004) use $\sim$53,000 star-forming SDSS galaxies at z$\sim$0.1 show that mass loss is strongly anticorrelated with baryonic mass, with low-mass dwarf galaxies being 5 times more metal depleted than L_* galaxies. Erb et al. (2006) study the gas fraction and the effective yields by a sample of LBGs at z$\sim$2 and find a slight increase of y_{eff} with decreasing baryonic mass, in constrast to a decrease in the local universe (Tremonti et al., 2004). The best fit of the variation of metallicity with gas fraction with model gives supersolar yield and an outflow rate $\sim$4 times higher than the SFR. The model fitting results show the evidence of both the ubiquity of galactic winds and their effectiveness in removing metals from galaxy potential wells.

There are different techniques utilized to derive galaxy stellar mass. Kauffmann et al. (2003) proposes a method, which rely on spectroscopic line indices $H\delta_A$ and 4000 Å Balmer break D_A to help circumvent the classical age-metallicity-reddening degeneracy issues and derive stellar mass-to-light (M/L) ratios. With the development of more sophisticated models for stellar populations synthesis code (Bruzual & Charlot , 2003), the ultraviolet, optical, near-IR photometry is combined together to measure stellar mass by SED fitting. The BC03 model is based on the evolutionary population synthesis technique with the main parameters of the stellar initial mass function (IMF), the star formation history (SFH) and the rate of chemical enrichment. Pirzkal et al. (2012) have shown that stellar mass can be estimated with small uncertainty and little dependence on detailed parameters.

Stellar metallicities can be measured based on the stellar absorption features via Lick indices (Worthey, 1994; Gallazzi et al., 2006; Panter et al., 2008; Halliday et al., 2008). The gas-phase oxygen abundance is a good proxy of the metallicity in the galaxy interstellar medium. In the assumption of instanteneous recycling mixing, the gas-phase abundance of ISM is a good measure of galaxy metallicity. The oxygen abundance is usually measured since oxygen makes up about half of the metal content of the ISM and exhibits strong emission lines from multiple ionization states in optical that are easy to measure. The electron temperature T_e measurement, which utilizes the ratio of the auroral to the nebular emission lines, is the direct method to measure gas-phase metallicity. However, the auroral lines (such as [OIII]λ4363) are extremely weak at high metallicity and hard to detect in low S/N spectra of distant faint galaxies. Hence, the strong nebular lines such as, [OII]λ3727,3729, [OIII]λ4959,5007, [SII]$\lambda\lambda$6717,6731 and [SIII]λ9069,9532 combined with hydrogen recombination lines such as Hα and Hβ, are widely explored and used. The most commonly used $R23$ diagnostic indicator was first proposed by Pagel et al. (1979), was later presented with the empirical relations (Edmunds & Pagel 1984, Zaritsky et al. 1994) and theoretically calibrated (McGaugh, 1991; Kewley & Dopita, 2002; Kobulnicky & Kewley, 2004) based on the stellar population synthesis and photoionization models. The strong emission-line diagnostic are widely applied to meatallicity measurements of HII regions and star-forming galaxies and extends greatly our ability to measure chemical abundances of high redshift and faint galaxies.

To better understand galaxy evolution by mass-metallicity relation, large sample of galaxies spanning wide orders of mass (luminosity) and metallicity are required. The imaging and spectroscopy of large survey, such as Sloan Digital Sky Survey (York, 2000; Stoughton et al., 2002), set a good benchmark in local universe. Tremonti et al. (2004) presents the mass-metallicity relation of ∼53,000 star-forming galaxies from SDSS at z∼0.1 and finds a tight (±0.1 dex) correlation between stellar mass and metallicity spanning over 3 index in stellar mass and 1 dex in metallicity. The NIR spectrographs in large diameter telescopes, such as the DEIMOS (Faber et al., 2003) on Keck II, LIRS-B on Keck I (Steidel et al., 2004), etc., enable to extend the sampling of galaxies to higher redshifts. Erb et al. (2006) use a sample of 87 rest-frame UV-selected star-forming galaxies from with $< z >$=2.26 to study the $M - Z$ correlation and find a monotonic increase in metallicity with increasing stellar mass. Mannucci et al. (2009) extend the investigation to high redshift at z∼3 by a sample of Lyman-Break Galaxies by deep NIR spectroscopic observations with adaptive optics and show strong evolution of the mass-metallicity relation from lower redshifts. The Space-based grism spectroscopy has the advantage of extending to fainter magnitudes and higher redshifts. The HST/ACS Probing Evolution And Reionization Spectrscopically project (PEARS; Malhotra et al. 2008, in preparation; Straughn et al. 2008) has effectively selected a large sample of strong emission line galaxies to fainter magnitudes, which provides a good starting points for studies of galaxy chemical evolution.

1.2 Outline

The outline of this dissertation is as follows. As one of the most basic physical variables, redshift denotes galaxies' distance and cosmological age. Chapter 2 presents the results of improved photometric redshift estimation with the implementation of Bayesian statistics of galaxy surface luminosity (SL) prior probabilities. Chapter 3 describes the follow-up spectroscopy HST/ACS PEARS grism emission-line galaxies. Chapter 4 presents the study of the chemical evolution of the HST/ACS PEARS grism emission-line selected star-forming galaxies at $< z >\sim 0.6$ and the relationship between galaxy physical properties such as color, size, SFR, mass and metallicity. Chapter 5 extends the study of the chemical evolution of the HST/ACS PEARS grism emission-line selected star-forming galaxies to $0.6 < z < 2.3$ by the low-resolution grism spectra. Chapter 6 summarizes the conclusions, drawing upon the results of each study. Chapter 2 and 3 are published in the Astronomical Journal (AJ), volume 138, page 95 and volume 141, page 64, respectively. At the time of this writing, Chapter 4 is resubmitted to Astronomical Journal (AJ) and Chapter 5 is to be submitted to Monthly Notices of the Royal Astronomical Society (MNRAS), and both will appear as Xia et al. 2012.

Chapter 2

IMPROVED PHOTOMETRIC REDSHIFTS WITH SURFACE LUMINOSITY PRIORS

2.1 Abstract

I apply Bayesian statistics with prior probabilities of galaxy surface luminosity to improve photometric redshifts. We apply the method to a sample of 1266 galaxies with spectroscopic redshifts in the GOODS North and South fields at $0.1 < z < 2.0$. We start with spectro-photometric redshifts (SPZs) based on PEARS grism spectra, which cover a wavelength range of 6000-9000Å, combined with $(U)BViz(JHK)$ broad-band photometry in the GOODS fields. The accuracy of SPZ redshifts is estimated to be $\sigma(\Delta(z)) = 0.035$ with an systematic offset of –0.026, where $\Delta(z) = \Delta z/(1+z)$, for galaxies in redshift range of $0.5 < z < 1.25$. The addition of the surface luminosity prior probability helps break the degeneracy of SPZ redshifts between low redshift 4000 Å break galaxies and high redshift Lyman break galaxies which are mostly catastrophic outliers. For the 1138 galaxies at $z < 1.6$, the fraction of galaxies with redshift deviation $\Delta(z) > 0.2$ is reduced from 15.0% to 10.4%, while the RMS scatter of the fractional redshift error does not change much.

2.2 Introduction

In recent years, the technique of photometric redshift has been widely used to determine redshifts of galaxies for large imaging sky surveys (Wolf et al., 2003; Mobasher et al., 2004, 2007). This technique is useful for redshift estimation of large numbers of faint galaxies at high redshift which are currently too faint for spectroscopy. There are typically two methods of redshift estimation by broad-band photometry. One approach is an empirical method, which calibrates an empirical training relation between photometric magnitudes or colors and galaxy spectroscopic redshifts, and applies it to the observed photometric sample (Connolly et al., 1995; Wang et al., 1999). Another approach is a template spectral energy distribution (SED) fitting method, which obtains best-fit redshifts by comparing the observed SEDs to that of a large empirical or model template library (Baum, 1962; Koo, 1985; Fernández-Soto et al., 1999; Bolzonella et al., 2000; Budavári et al., 1999, 2000, 2001; Csabai et al., 2000; Wolf et al., 2001; Blanton et al., 2003). The efficiency of SED fitting is based on fitting the overall shape of spectra, the detection of strong spectral properties, such as the 4000Å/Balmer break and Lyman break, and the amount of dust present in red galaxies.

The general accuracy of photometric redshift ranges from $\sigma_z = 0.02$ to 0.05, which strongly depends on the number of filters and other factors, such as the precision of the photometry, the zeropoints, the image FWHM, and of course the quality of the templates and the fitting code. Hickson et al. (1994) show that the redshift accuracy by SED fitting is comparable to slitless spectroscopy from a simulation of 40 band photometry. Practical multicolor sky surveys, such as the COMBO-17 (Classifying Objects by Medium-Band Observations) survey, using 17 intermediate-band filters (Wolf et al., 2003) and the BATC (Beijing-Arizona-Taipei-Connecticut) sky survey, using 15 intermediate-band filters, achieve a typical accuracy of $\sigma_z = 0.02$ for photometric redshift estimation (Zhou et al., 2001; Xia et al., 2002). The photometric redshift accuracy using by 5 broad-band filters is about 0.05 (Blanton et al., 2003). However, the depth of intermediate-band sky surveys are generally constrained to $z < 0.1$, and the observations of multiple bands can be quite time consuming. Broad-band photometry has the advantage of sensitivity which enables photometric redshifts of large samples of faint and high redshift galaxies. The photometric redshifts from broand-band fluxes tend to have large dispersion and strong degeneracy between low redshift Balmer break galaxies and high redshift Lyman break galaxies, which leads to the degeneracy of the photometric redshift estimation.

To break such degeneracies, Benítez (2000) developed a Bayesian method of photometric redshift estimation (BPZ) using galaxy magnitudes as Bayesian priors. This method produced an accuracy of $\sigma(\Delta(z)) \approx 0.06$, where $\Delta(z) = \frac{\Delta z}{1+z}$, for galaxies in HDF-N (Hubble Deep Field North) up to $z < 6$. Mobasher et al. (2007) estimate redshifts for galaxies at $z < 1.2$ with 16 bands photometry from 3500 to 23000 Å by different photometric redshift codes with and without luminosity function priors. The results give an accuracy of $\sigma(\Delta(z)) \approx 0.031$ and find slight improvement in the redshift estimation with LF priors.

Observed galaxy surface brightness is a promising observational parameter to break the redshift degeneracy (Koo, 1999). Tolman (1930) first showed that the surface brightness dims with redshift as $(1+z)^{-4}$ in an expanding universe independent of the cosmology. With this sensitive a dependence on (1+z), surface brightness should make a good prior for the redshift estimation. The only caveat is the evolution of intrinsic galaxy luminosity per area with redshift. Passive evolution of stellar populations leads to a significant brightening of intrinsic luminosities per unit area at higher redshifts (Pahre et al. 1996, Sandage & Lubin 2001) and therefore to a less steep surface brightness redshift relation.

Using surface brightness priors, Kurtz et al. (2007) provide a redshift estimator by taking the median redshift in small bins in galaxy surface brightness-color space. The estimator is applied to the 10-20% reddest galaxies from the SHELS survey (the Smithsonian Hectospec Lensing Survey), and achieves an accuracy of $\sigma(\Delta(z)) = 0.025$ for $z < 0.8$. Wray & Gunn (2008) use the five-band SDSS photometry, surface brightness and the Sérsic index to provide improved photometric redshifts in SDSS (Sloan Digital Sky Survey). They apply 7-dimensional probability arrays for spectroscopically confirmed galaxies at $z < 0.25$, which yields $\sigma(\Delta(z)) = 0.025$ for red galaxies and 0.03 for blue galaxies. Stabenau et al. (2008) apply surface brightness priors to ground based VVDS survey (VIMOS VLT Deep Survey) and the space-based GOODS (the Great Observatories Origins Deep Survey; Giavalisco et al. (2004)) field from HST, and improve the bias and scatter by a factor of two for galaxies in the range $0.4 < z < 1.3$ to get a scatter of $\sigma(\Delta(z)) \approx 0.08$. In this paper, we use spectro-photometric redshifts (SPZs) which use low resolution grism data and broad-band data in the GOODS fields as my starting point (Ryan et al., 2007; Cohen et al., 2009). The SPZs have a scatter in $\sigma(\Delta(z)) \approx 0.03$. We then use color and surface brightness priors, which we adopt the unit of luminosity per area (Hathi et al., 2008), $L_{\odot}/kpc^2$, and hereafter we call it surface luminosity (SL) priors, to break the redshift degeneracy to derive photometric redshifts for a sample of 1266 galaxies in the GOODS North and South fields with spectroscopic redshifts between $0.1 < z < 2.0$.

This paper is organized as follows. We briefly describe the observations, the data, and the result of the spectro-photometric redshift estimation in § 2 . The application of color and surface luminosity priors is given in § 3. The results of redshift estimation with hybrid of SPZ and surface luminosity priors are illustrated in § 4. Finally, we discuss the results and present the conclusions in § 5. Throughout this paper, we assume a ΛCDM cosmological model with matter density $\Omega_m = 0.28$, vacuum density $\Omega_\Lambda = 0.72$, and Hubble constant $H_0 = 100h$ km s^{-1} Mpc^{-1}, with $h = 0.7$ for the calculation of distances (Komatsu et al., 2009).

2.3 Observation and Data

I select a sample of 1266 galaxies in GOODS North and South fields which have both spectroscopic (Wirth et al., 2004; Grazian et al., 2006; Vanzella et al., 2008) and spectro-photometric redshifts (Cohen et al., 2009) to test the application of surface luminosity priors. Only spectroscopic redshifts with quality flag $Q = 0$, or 1 (0: very good quality, 1: good quality) are used. These galaxies have both grism spectra, from the HST/ACS PEARS (Probing Evolution and Reionization Spectroscopically, PI:Malhotra) survey, and optical broad-band *BViz* photometry from HST/ACS GOODS v2.0 images (Giavalisco et al., 2004). The ACS grism spectra cover a wavelength range from 6000 to 9000 Å (Pirzkal et al., 2004) for objects in parts of the GOODS North and South fields. The galaxies in our PEARS sample are located in 4 ACS pointings in GOODS North and 5 in GOODS South fields. The photometry in the GOODS-N field is supplemented with ground-based U-band data from Capak et al. (2004), and photometry in the GOODS-S field is supplemented with the JHK-band data from VLT ESO/GOODS project (Retzlaff et al., 2010). The photometry and the aperture correction between the broad-band data are described in detail by Ryan et al. (2007) and Cohen et al. (2009). Figure 1 shows the histogram of the distribution of galaxy spectroscopic redshifts. The redshifts of most galaxies are less than z∼2.0. The final sample of 1266 galaxies are selected with spectroscopic redshifts in the range of $0.1 < z < 2.0$.

The SPZs (Ryan et al., 2007; Cohen et al., 2009) are estimated based on the SED fitting of the combination of grism spectra and UV-optical-infrared broadband photometry by the photometric redshift code *HyperZ* (Bolzonella et al., 2000). The SPZ method achieves a redshift accuracy of $\sigma(\Delta(z)) = 0.035$ for the 465 galaxies in GOODS-N field at redshift range $0.5 < z < 1.25$ with a catastrophic outlier-fraction of 18.2%. The catastrophic outliers are defined as galaxies with fractional redshift errors, $\Delta(z)$, greater than 3σ of the RMS scatter in the sample. The best accuracy of the SPZ method is achieved for the redshift range $0.5 < z < 1.25$, where the 4000Å break falls in the peak sensitivity wavelength range of the ACS grism. The redshifts estimated by SPZ tend to show a strong redshift degeneracy. This is demonstrated in

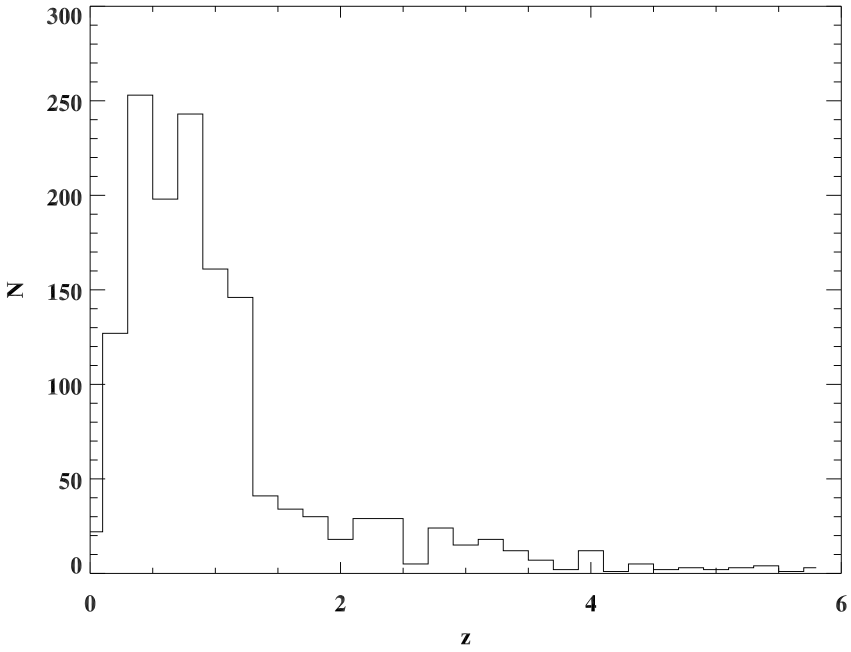

Figure 2.1: The histogram distribution of the spectroscopic redshifts of the total sample.

the upper panels of Figure 5, which compare SPZ redshifts with spectroscopic redshifts. A substantial fraction of galaxies at $z < 0.6$ scatter to SPZ $\simeq$2 - 3. To improve the redshift accuracy of the SPZ redshift estimation, we apply the prior probability of galaxy surface luminosity to constrain and break the degeneracy, since surface brightness is tightly related to redshift as approximately $(1+z)^{-4}$ for bolometric fluxes and $(1+z)^{-(4+\alpha)}$ for fluxes per unit frequency (Tolman, 1930).

2.4 Surface Luminosity Priors

If we were to observe a galaxy with a standard intrinsic luminosity per unit area (hereafter denoted at I) at different redshifts, its measured surface brightness would go down at $I \propto (1+z)^{-4}$. Due to the limitation of the available photometry in wavelength less than 10,000 Å, I choose the restfram surface luminosity in B band, I_B, as prior probability, with redshifts extending to z$\sim$2.0. The adoption of restframe B

band is more sensitive to galaxy types from starbursts, spirals to ellipticals than redder bands. The intrinsic evolution of galaxy type with redshift and the observation selection effect will make the relation deviate from power -4 and we will calibrate this relation first. A subsample of 283 elliptical galaxies (Ferreras et al., 2009) is used to examine the difference of the relation between the surface luminosity and redshift galaxy types. For galaxies with redshifts $z < 0.33$ we measure the surface luminosity I_B in the band closest to B: the V-band magnitude for galaxies at redshift $0.33 < z < 0.96$, the i-band for $0.96 < z < 1.35$, and the z-band for $1.35 < z < 2.0$.

The photometry of GOODS v1.9 catalog is measured in AB magnitudes (Oke & Gunn, 1983), which are defined as:

$$m = -2.5 \log f_\nu - 48.6, \tag{2.1}$$

where f_ν is the flux per unit frequency in unit of ergs s^{-1} cm^{-2} Hz^{-1}. The half light radii are measured by SExtractor and translated into angular radius, r_e (in arcsecond), by multiplying with the pixel scale $0.''03$ pix^{-1}. With the flux f_ν and half light radius r_e in the corresponding band for different redshift range galaxies, the restframe B-band surface luminosity is calculated as follows

$$I_B = \frac{\Delta\nu_B f_\nu 4\pi d_L^2}{(1+z)2\pi d_A^2 r_e^2} = \frac{2\Delta\nu_B f_\nu (1+z)^3}{r_e^2}, \tag{2.2}$$

where z is the redshift of galaxy, $\Delta\nu_B$ is the frequency interval corresponding to the wavelength range in the B band, f_ν is the flux in the observed filter band, d_L is luminosity distance and d_A is angular distance of galaxy, and I_B is surface luminosity in luminosity per unit area (in $L_\odot/kpc^2$). Figure 1 shows the distribution of the restframe B-band surface brightness with redshift for the spectroscopic galaxies. The range of I_B goes approximately from 10^6 to $10^{10} L_\odot/kpc^2$. The upper and lower limits of the observed surface brightness in magnitude per square arcsecond, 22.3 magnitude/arcsec^2 and 26.3 magnitude/arcsec^2 (corresponding to the magnitude range from 21 to 25 magnitude), are plotted as dotted lines in the figure. The relation between $logI_B$ and $log(1+z)$ is fitted linearly, which goes as $\log I_B = 2.61(\pm 0.06) \cdot \log(1+z) + 6.64(\pm 0.01)$. The triangular points in the figure represents the elliptical galaxies in the sample. The redshifts of ellipticals range from 0.3 to 1.4. The ellipticals show generally higher surface luminosities than blue galaxies while a much similar slope of 2.90($\pm$0.6). Compared with that found in Stabenau et al. (2008), for passively-evolving red galaxies, the observed surface brightness is close to $(1+z)^{-4}$, and the blue galaxies have a shallower slope, we don't find relatively flatter slope of the rest-frame surface lumimnosity for early type galaxies here, and it may be due to the relatively small number of the sample. The final results show that there is little difference of the improvement in redshift estimation accuracy for red galaxies and blue galaxies.

To apply the scaling of surface luminosity with redshift as prior probability, we use a color-shape (Koo, 1985) parameter $(B-V)-(i-z)$ to divide the sample into subsamples. Figure 2 plots the distribution of $(B-V)-(i-z)$ with redshift. We can see that this shape parameter declines linearly with redshift at $z < 1.3$ and it increases linearly with redshift at $z > 1.3$. This is because that the shape parameter traces the position of 4000 Å break. Three subsamples are obtained with $(B-V)-(i-z) > 0.65$, $0 < (B-V)-(i-z) < 0.65$, and $(B-V)-(i-z) < 0$, corresponding to galaxies in redshift bins of $z < 1.0$, $0.6 < z < 1.2$, and $z > 1.0$. The surface luminosity distribution is fitted by Gaussian functions for the three subsamples. The distribution of $logI_B$ with redshift and the Gaussian fits are plotted in Figure 3. The peak value of the Gaussian distribution slightly increases from $\log I_{B,0} = 7.02$, 7.03 to 7.30 with 1-σ width of 0.48, 0.49, and 0.44 for the three subsamples, respectively.

The SL prior probability is calculated with the formula as

$$p(z|I_B(z)) = \frac{\phi}{\sqrt{2\pi}\sigma} \exp(\frac{-(\log I_B(z) - \log I_{B,0})^2}{2\sigma^2}), \tag{2.3}$$

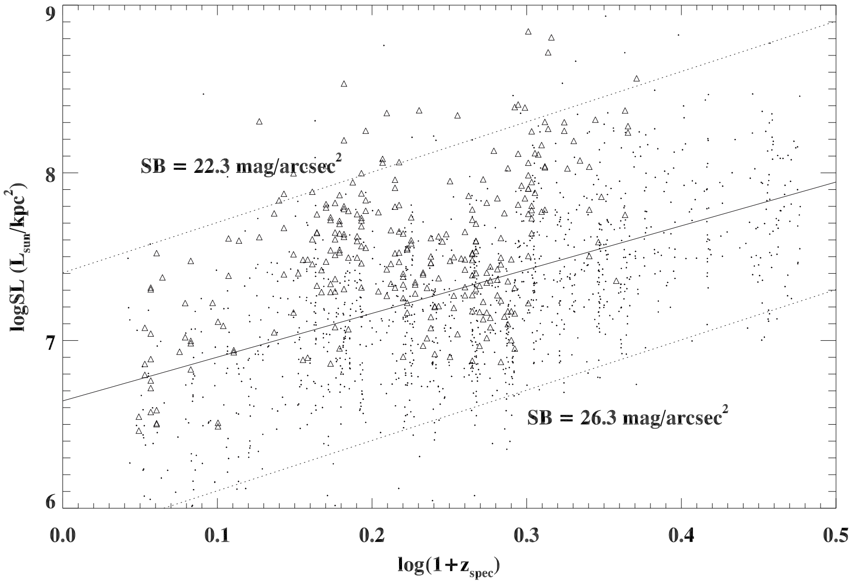

Figure 2.2: The distribution of rest-frame B band surface luminosity I_B as a function of redshift for the total sample. The triangular points represent elliptical galaxies in the sample. The upper and lower limits of the observed surface brightness, 22.3 and 26.3 magnitude per square arcsecond, are plotted in dotted lines. The points shows a good linear relation, $\log I_B \sim 2.61 \cdot \log(1+z)$, between surface luminosity and redshift. The ellipticals have a similar slope of 2.90.

where ϕ is the normalization constant so that the integration of the probability in the studied redshift range ($0 < z < 7$) is 7; σ is the width of the Gaussian profile; and $\log I_{B,0}$ is the Gaussian peak value. $I_B(z)$ is the surface brightness for one galaxy at different redshifts, calculated over a redshift range $0.10 < z < 7.0$ with a step of 0.005, the same as that of SPZs. The best redshift is estimated by the combination of SL prior probabilities and SPZ fitting probabilities, which are output from *HyperZ*. Using Bayes' theorem, the final probability of redshift can be computed as

$$p(z|I_B(z),C) = \frac{p(z|I_B(z)) \times p(C|z)}{p(C)}, \tag{2.4}$$

where $p(z|I_B(z))$ is the redshift probability given by surface luminosity priors, and $p(C|z)$, $P(C|z) = \exp(-\chi^2(z)/2)$, is the probability of the galaxy at redshift z with the observed color C given by the SPZs estimation.

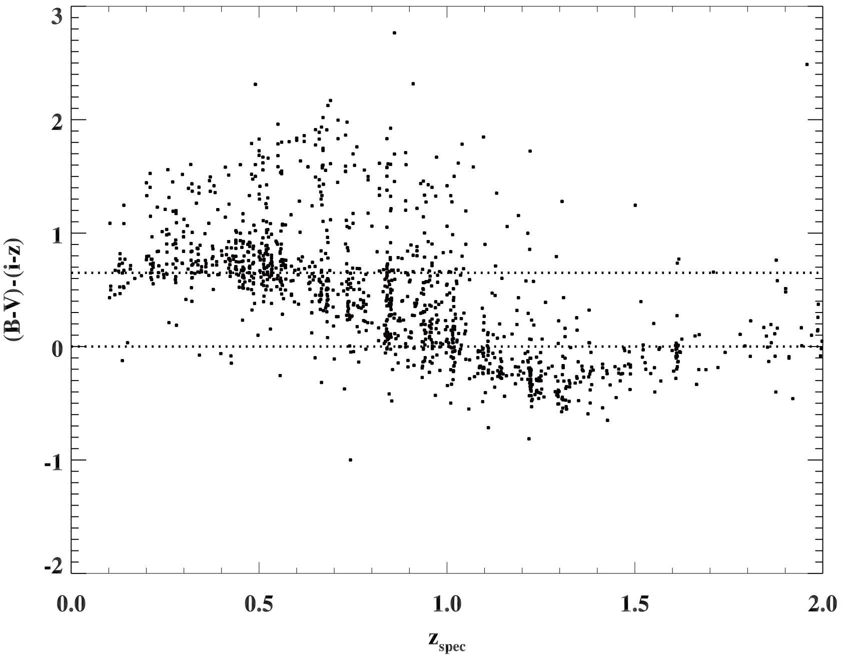

Figure 2.3: The distribution of color-shape parameter $(B-V)-(i-z)$ with redshift z for the spectroscopic galaxies. The dot lines represent the criteria of $(B-V)-(i-z) > 0.65$, $0 < (B-V)-(i-z) < 0.65$ and $(B-V)-(i-z) < 0$, which are implemented to divide sample into three redshift bin subsamples.

2.5 Implication and Results

For the 1266 galaxies, we first divide galaxies into subsamples by the color-shape parameter. Then we calculate the SL prior probability for galaxies by the corresponding Gaussian profiles in different subsamples. Combining the SL prior probability with the SPZ likelihood function, we obtain the best redshift as the maximum of the final probability distribution.

Figure 4 shows four examples of redshift probability distributions for galaxies in GOODS North field. The ID of the object is labeled at the right-bottom of the panel. The dashed line in the figure represents the likelihood function given by SPZ SED fitting. The dotted line represents the calculated probabilities by SL priors.

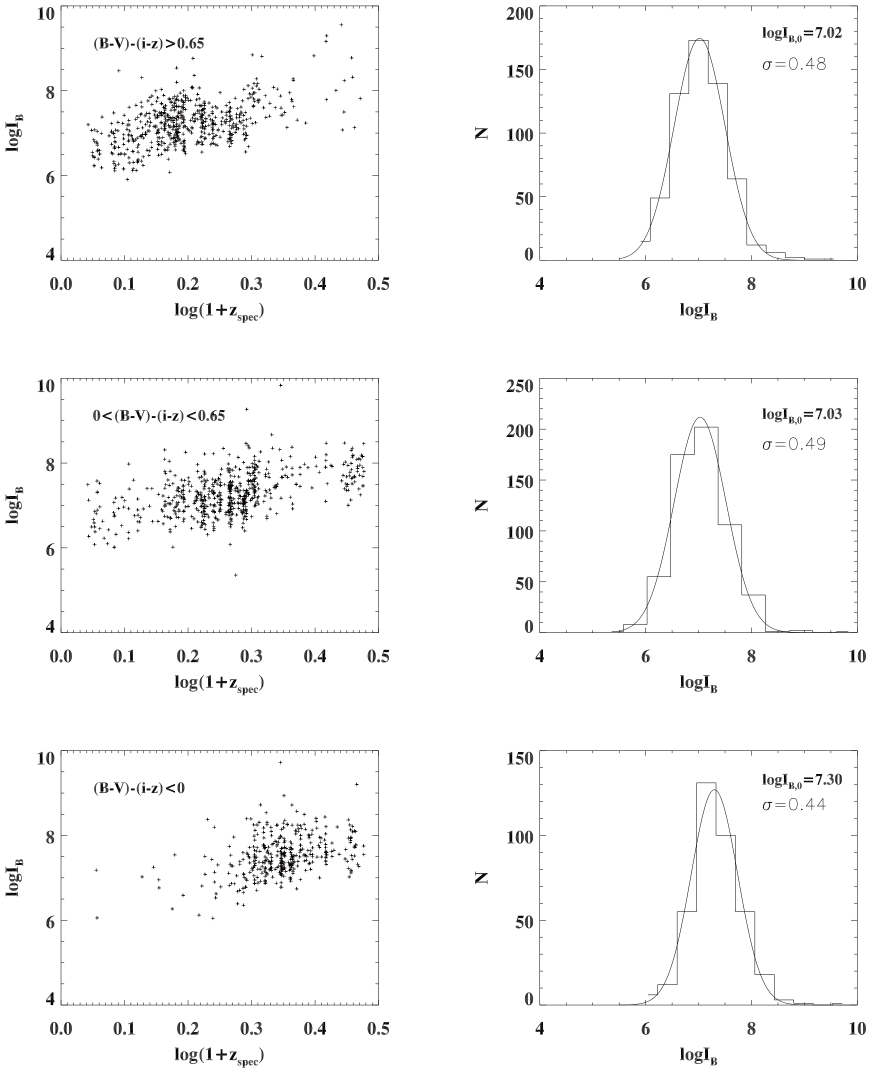

Figure 2.4: The distribution of logI_B with redshift and the Gaussian fitting for the three color-shape parameter divided subsamples. (left panel) From top to bottom, the three subsamples have $(B-V)-(i-z) < 0.65$, $0 < (B-V)-(i-z) < 0.65$ and $(B-V)-(i-z) < 0$, respectively. (right panel) The distribution of $\log I_B$ is fitted by a Gaussian function. The peak and the width of the Gaussian distributions are $\log I_{B,0} = 7.02$, 7.03, 7.30 and $\sigma = 0.48$, 0.49, 0.44 for the three subsamples, respectively.

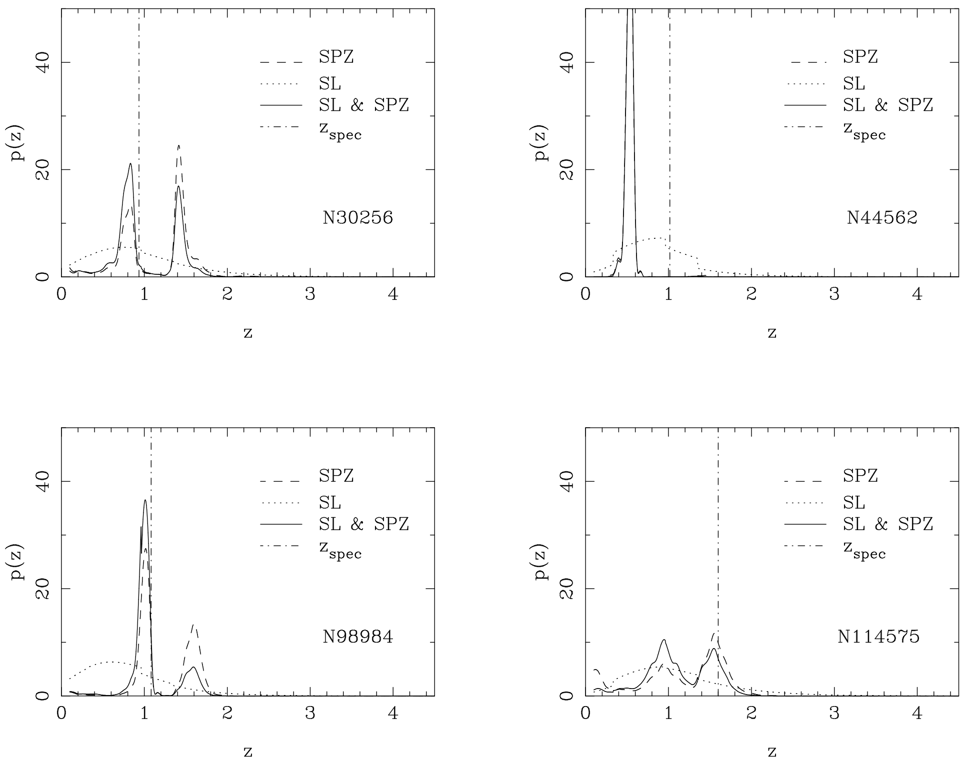

Figure 2.5: The probability distributions as a function of redshift obtained from the SPZ SED fitting, the SL priors, and the combination of SPZ SED fitting with SL priors. The dashed line represents the likelihood function given by SPZ SED fitting. The dotted line represents the calculated probabilities by SL priors. The solid line shows the combined probability distribution. The vertical dash-dotted line represents the position of the spectroscopic redshift. The object ID is labeled at the right-bottom in the panel.

The solid line shows the combined probability distribution from SPZ SED fitting and SL priors. The vertical dash-dotted line represents the position of the spectroscopic redshift. The upper-left panel shows a case where the SPZ redshift estimation gives two peaks in the redshift probability function. The addition of the SL priors probability gives the correct distribution around the spectroscopic redshift. With the combination of the two probabilities, the correct peak is chosen, and the probability of a catastrophic redshift estimation is reduced. The upper-right panel shows an example where the SPZ doesn't produce a reasonable likelihood distribution, though the SL priors give more reasonable estimation. The lower-left panel gives an example of the correct estimation of redshift by both methods. In the lower-right panel, the SL priors choose the wrong peak of the SPZ $p(z)$ distribution for a galaxy with redshift $z = 1.6$. This can be the reason of the larger deviation of redshift estimation with SL priors at redshift $z > 1.6$. The results of redshift estimation with SL priors are shown in Figure 5.

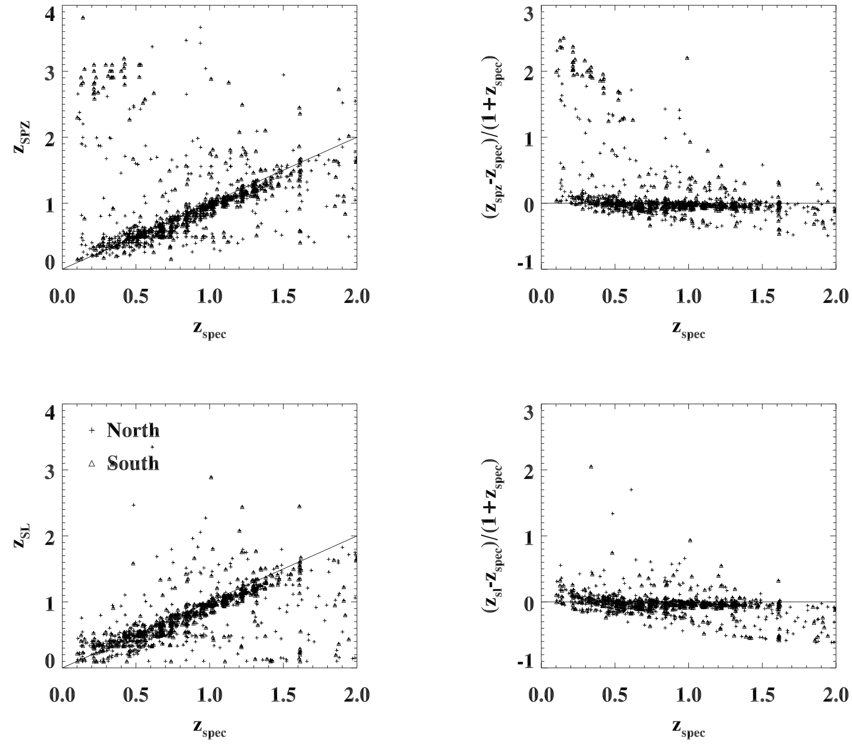

Figure 2.6: The left panels show the comparison between estimated redshifts and spectroscopic redshifts. The upper one is the comparison between SPZ redshifts and spectroscopic redshifts. The lower one is that of the improved SPZ redshifts by SL priors. The cross points illustrate the galaxies in GOODS-N field; the triangular points are galaxies in GOODS-S field. The right panels show the distribution of the fractional error $\Delta(z)$ with redshift for the redshift estimation with and without SL priors.

Figure 5 shows the comparison of SPZs with and without surface luminosity priors. The upper two panels in Figure 5 show the comparison between SPZ redshifts and spectroscopic redshifts, and the distribution of redshift fractional error

$\Delta(z) = \frac{\Delta z}{1+z}$ with spectroscopic redshifts. The triangular points in figure are galaxies in GOODS-S field which are supplemented with infrared JHK photometry, and the cross dots are galaxies in GOODS-N field, which have U-band data. From this comparison, we can see that many galaxies in the GOODS-S field with $z < 0.6$ are estimated to be around $z \simeq 2$–3 by the SPZ method. Because the 4000 Å break of $z < 0.6$ galaxies falls in the UV/B-band, it can be confused with galaxies of $z \sim 3.0$ with the Lyman break falling in B/V-band. From this comparison, we can see also that the scatter improves greatly for galaxies in GOODS-N field. The GOODS-N field has fewer catastrophic outliers because of U-band photometry for galaxies.

The bottom two panels show the results of the photometric redshifts with SL prior probabilities. From the comparison of the redshift estimation with and without SL priors, the effectiveness of SL priors is illustrated in breaking the redshift degeneracy, and in reducing the fraction of catastrophic outliers. For the total sample at $0.1 < z < 2.0$, the accuracy of the redshift estimation by SL priors (which is the width of the Gaussian error distribution) changes little from $\sigma(\Delta(z)) = 0.043$ with an systematic offset of –0.019 to $\sigma(\Delta(z)) = 0.044$ with an offset of –0.020. We can see from the figure that at redshifts $z < 0.3$ and $z > 1.6$, the SL priors do not work as well as in the intermediate redshift range. This is because the peak value of the surface luminosity sampled by the SL priors is slightly larger than the actual SL for galaxies with lower redshifts, and is slightly smaller than the actual SL for the galaxies with highest redshifts. For galaxies in the redshift range $0.5 < z < 1.25$, the RMS error remains the same at $\sigma_x = 0.035$ for both methods. For galaxies with redshift $z > 1.6$, the SPZ yields large scatter. We only use the 1183 galaxies at $z < 1.6$ to calculate the statistics of catastrophic outliers. For galaxies with $|\Delta(z)| > 0.2$, the fraction decreases from 15.0% to 10.4% by adding surface luminosity priors; and for galaxies with $|\Delta(z)| > 0.5$, the number reduces from 87 to 22. This effect is demonstrated clearly in Figure 6, which shows the histogram of the fractional redshift error. The solid line shows the histogram of galaxies with improved SPZ redshifts by SL priors. The dotted line represents that of galaxies with SPZ redshifts. We can see that the galaxies with fractional errors greater than 0.6 almost disappear with the SL priors method.

For the 283 elliptical galaxies, the redshift estimation shows same trend as that of the total sample, with little change in accuracy and improvement in catastrophic outliers. The redshift accuracy is $\sigma(\Delta(z)) \sim$0.01, much better than that of the blue galaxies, for both SPZs and SPZs with surface luminosity priors. The elliptical galaxies in the spectroscopic sample is not complete due to the selection effects and it can lead to small difference in the accuracy estimation. In the application to the photometric sample with this calibration, there is type selection bias in different redshifts. At higher redshifts, the photometric sample tends to have more luminous elliptical galaxies, which should be expected with better accuracy in redshift estimation.

The color and SL priors works well for lower redshift samples at $z < 1.6$. However, to apply this method to redshift estimation for the whole PEARS sample, we need to improve the method, since the whole sample will include such galaxies at $z > 1.6$ and the relation between the shape parameter $(B-V)-(i-z)$ and redshift will not be near linear. The value of $(B-V)-(i-z)$ will go up linearly with redshift at $z > 1.6$. The application of this method needs to be studied further, likely with additional near-IR filters. This can be done with the HST/WFC3 after 2008.

2.6 Summary and Conclusions

For an object with constant luminosity per unit area, the bolometric surface brightness scales as $(1+z)^{-4}$ in an expanding universe. That, combined with the fact that

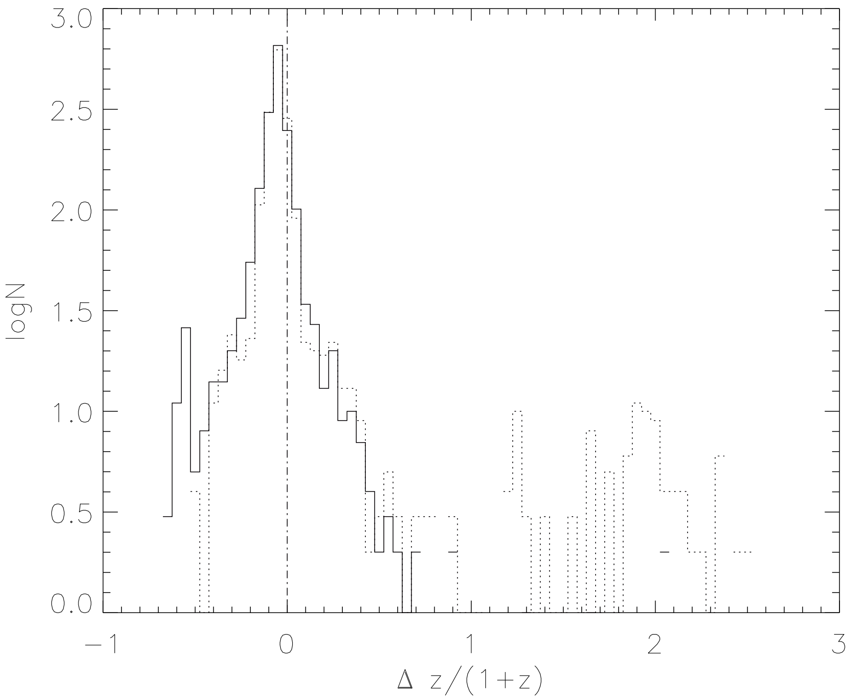

Figure 2.7: The histogram distribution of redshift fractional error *x*. The solid line shows the improved SPZ redshifts by SL priors. The dotted line represents the distribution of SPZ redshifts. The dash-dotted line shows the zero position of the histogram.

there is a definite upper limit to luminosity per unit area seen in starburst galaxies from $z = 0$–7 (Hathi et al., 2008; Meurer et al., 1997), would make for a very strong prior for photometric estimates. However, the mean luminosity per unit area is well below this upper limit and shows strong redshift evolution for blue late type galaxies. The early type galaxies show a generally higher surface luminosity and a similar slope of the redshift evolution.

To calibrate the evolution of luminosity per unit area, we divide the sample into three redshift bins using a color-based criterion; and then derive the distribution of luminosity per unit area in restframe *B*-band. The probability of the rest-frame surface luminosity is applied as a prior to the redshift probabilities given by SED fitting to broad-band + grism data.

The method is applied to 1266 galaxies observed with HST/ACS PEARS grism spectra and with GOODS *BViz* broad-band photometry and known ground-based redshifts in the range of $0.1 < z < 2.0$. The accuracy is assessed with the spectroscopic redshifts. By comparing the redshift estimation with and without SL priors, the new method improves the number of galaxies with $|\Delta(z)| > 0.2$ from 15.0% to 10.4%. The RMS scatter does not change much. The improvement seems same for the blue galaxies and the 283 red galaxies, while the red galaxies show higher accuracy in redshift estimation. The result shows the efficiency of the SL priors in breaking the degeneracy of SPZ redshifts for low-redshift Balmer break galaxies and high redshift Lyman break galaxies.

Chapter 3

SPECTROSCOPIC STUDY OF THE HST/ACS PEARS EMISSION LINE GALAXIES

3.1 Abstract

We present spectroscopy of 76 emission-line galaxies (ELGs) in CDF-S taken with the LDSS3 spectrograph on Magellan Telescope. These galaxies are selected to have emission lines with ACS grism data in the *Hubble Space Telescope* Probing Evolution and Reionization Spectroscopically (PEARS) grism Survey. The ACS grism spectra cover the wavelength range 6000-9700 Å and most PEARS grism redshifts are based on a single emission line + photometric redshifts from broad-band colors; the Magellan spectra cover a wavelength range from 4000 Å to 9000 Å, and provide a check on redshifts derived from PEARS data. We find an accuracy of σ_z = 0.006 for the ACS grism redshifts with only one catastrophic outlier. We probe for AGN in the sample via several different methods. In total we find 7 AGNs and AGN candidates out of 76 galaxies. Two AGNs are identified from the X-ray full-band luminosity, $L_{X-ray,FB} > 10^{43}$ erg s^{-1}, the line widths and the power-law continuum spectra. Two unobscured faint AGN candidates are identified from the X-ray full-band luminosity $L_{X-ray,FB} \sim 10^{41}$ erg s^{-1}, the hardness ratio and the column density, and the emission-line and X-ray derived SFRs. Two candidates are classified based on the line ratio of [NII]λ6584/Hα versus [OIII]λ5007/Hβ (BPT diagram), which are between the empirical and theoretical demarcation curves, i.e, the transition region from star-forming galaxies to AGNs. One AGN candidate is identified from the high-ionization emission line HeIIÅ4686.

3.2 Introduction

The HST/ACS/G800L grism survey Probing Evolution and Reionization Spectroscopically (PEARS, PI: S. Malhotra) produces low-resolution (R $\sim$ 100) slitless spectra in the wavelength range from 6000Å to 9700Å. The survey covers four ACS pointings in GOODS North (GOODS-N) and five ACS pointings Chandra Deep Field South (CDF-S) fields yielding spectra of all objects up to $z = 27$ magnitude up to $z = 28$ magnitude in the Hubble Ultra Deep Field (HUDF). We selected emission-line galaxies in CDF-S from the samples of Xu et al. (2007), and Straughn et al. (2008, 2009), regardless of the broad-band magnitude for followup with Magellan telescope for R $\sim$ 1900 spectroscopy. Thus we are able to get spectra for much fainter objects than have been selected traditionally (e.g. Vanzella et al. 2006, 2008). One of the aims of the followup spectroscopy is to confirm the redshifts obtained from the grism data.

The grism data, due to the limited wavelength coverage and low spectral resolution, often yields only a single unresolved line. For single-line spectra, the lines are identified as: [OII]λ3727Å, [OIII]$\lambda\lambda$4959,5007Å and $H\alpha$ based on photometric redshifts derived from the broad-band colors (Xu et al. 2007, Straughn et al. 2008, 2009).

In this paper, we present the confirmation of the ACS grism redshifts by the follow-up Magellan LDSS-3 multislit spectroscopic observation of a sample of 107 emission-line galaxies (ELGs) pre-selected by Straughn et al. (2009) in the GOODS-S field. We also compare the flux calibration in the two observations. The normal star-forming galaxies and AGNs are classified by the emission-line ratios of the BPT diagnostics diagram (Baldwin, Phillips, & Terlevich, 1981) and X-ray observations. The paper is organized as below. We briefly describe the observation and the data reduction in § 2. The result of redshift comparison with grism measurement, flux calibration comparison and AGNs classification are illustrated in § 3. Finally, we present the summary in § 4.

3.3 Data and Reduction

From the HST/ACS PEARS grism survey, Straughn et al. (2009) selected 203 emission-line galaxies by a 2-dimensional detection and extraction procedure in the GOODS-S field. The line luminosities of grism observations extend the studies of star-forming galaxies to $M \sim -18.5$ at $z \sim 1.5$. Starting from 107 pre-selected emission-line galaxies, we obtain 89 emission-line galaxies spectra from the follow-up Magellan LDSS-3 multislit spectroscopic observation after excluding the undetected spectra and bad spectra. With 13 galaxies observed twice, the final sample includes 76 different galaxies. Figure 1 shows the apparent magnitude distribution of the total pre-selected ELGs put on masks (dashed line) and the sample of 76 different galaxies with follow-up spectroscopic observation (solid line). The pre-selected emission-line galaxies cover magnitude range from 18.0 to 27.0 with a peak at 23.5. The subsample for follow-up observation follows the same distribution.

The spectroscopic follow-up was done in a total of four nights in November 2007 and December 2008 using the Magellan LDSS-3 spectrograph and using the VPH-Blue and VPH-Red grisms. The LDSS-3 instrument has a scale of $0''189$/pixel. The VPH-Blue grism covers the wavelength range from 4000Å to 6500Å with a resolution of $R = 1810$, dispersion of 0.682Å/pixel@5200Å. The VPH-Red grism covers the wavelength range from 6000Å to 9000Å with OG590 filter used to eliminate contamination from the second order. The red grism has a resolution of $R = 1900$ and dispersion of 1.175Å/pixel@8500Å. We used slit widths of $0''8$.

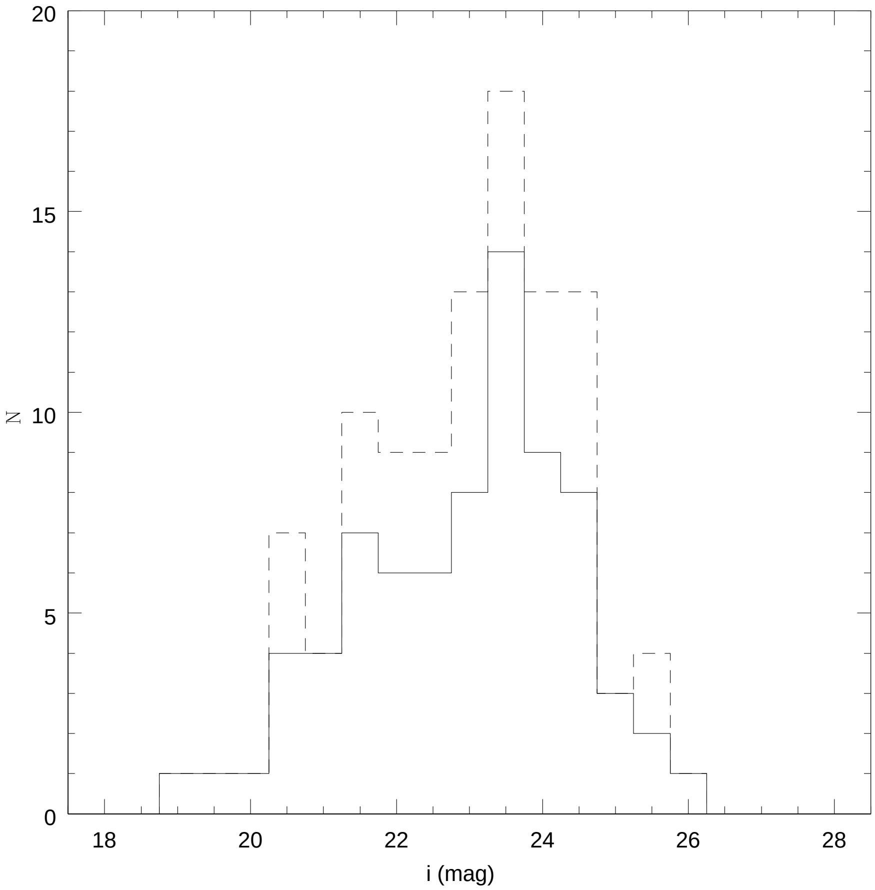

Figure 3.1: Histogram of the distribution of *i*-band (ACS F775W) apparent magnitudes. The dashed line is that of the total 107 emission-line galaxies put on masks. The solid line is that of the 76 emission-line galaxies with good quality redshift measurements from LDSS3. The magnitudes of the sample peak at $i = 23.5$.

Five masks were created to contain all of the science objects with 4-6 alignment stars located at different parts of each mask. The fields were observed with integration times of 5400s, 7200s, and 8100s. For masks observed in 2007, the spectroscopic standard star LTT1020 was observed for calibration; in 2008, the spectroscopic standard stars, LTT1020, LTT2415, EG21 and LTT3864 were observed for flux calibration.

We reduced the spectra using the *COSMOS* software package (Oemler et al., 2009, COSMOS Version 2.13), which is designed for multislit spectra obtained using the IMACS and LDSS3 spectrographs on Magellan. Following the reduction process of making alignment, subtracting bias, flattening, wavelength calibration, sky subtraction and 2-dimensional spectra extraction, the blue-end and red-end spectra were obtained for all objects. The 1-d spectra extraction and flux calibration were accomplished in *IRAF*.

To check the flux calibration from year to year we compared the calibrated spectra for objects observed in both years. Upon doing this, we realized that the flux calibration of 2007 data, which was based on a single calibration star was systematically higher. This, we conjectured, must be due to misplacement of the standard star in the slit. The sensitivity function of the CCD obtained from the spectroscopic standard stars observation in 2008 is applied to the flux calibration of the 2007 data. To check its robustness, we then used object 110494, which has strong continuum and is observed in both years. Figure 2 shows the two flux calibrated spectra for the object. The blue and red spectra are combined together to cover wavelength range from 4000Å to 9000Å. The spectra show consistency in the junction point at 6500Å of the blue and red ends. The dotted line shows the spectra obtained from 2007 data and the solid line represents that of 2008. The main strong emission lines emerging in the spectra are [OII]λ3727, Hβ, [OIII]$\lambda\lambda$4959,5007, and Hα. We fit the continuum of the two spectra and find a difference of 5% in the continuum flux from 5000 Å to 9000 Å. We measure the line fluxes and errors for Hβ and Hγ, and obtain the ratio of Hγ/Hβ = 0.45±0.05, and 0.48±0.07, separately. The ratios are in good agreement with each other and with the theoretical value, 0.469. The good agreement of the continuum and the line ratios of the two years spectra demonstrate that the calibration is sufficiently robust for the purpose.

From the 2-dimensional spectra, we finally obtained 89 sources which show clear detection of emission lines. The galaxy redshifts are first visually determined from the pattern of the emission lines. The accurate redshifts and uncertainties are determined by the average and variance of the redshifts obtained from the main emission lines in the spectra. In the 89 spectra, there are 13 objects which were observed in both years. We finally obtain 76 unique redshifts which are used to assess the accuracy of the grism redshifts at $0.1 < z < 1.3$.

Excluding objects only observed in blue or red end, objects with signal to noise ratio less than 3 in Hβ, and [OIII]$\lambda\lambda$4959,5007, and objects with one or more emission lines out of spectral coverage, we measure the line fluxes for 55 well extracted 1-d spectra with whole set of [OII]$\lambda\lambda$3727,3729, Hβ, and [OIII]$\lambda\lambda$4959,5007 lines. The emission-line fluxes are measured by Gaussian fitting (GAUSSFIT in IDL) expanding 40Å around the line peak. Most of the FWHM of the line profiles are in the range from 2 Å to 9 Å with line velocities $<$ 500 km s^{-1}, except two objects, 92839 and 102156, of 28 and 79 Å, corresponding to velocities $\sim$ 1000, 3800 km s^{-1} (discussed in § 3.3).

3.4 Results

Table 1 lists the general information and the measurement results of the galaxy sample, the PEARS ID (column 1), R.A. (column 2), Dec. (column 3), *i* magnitude (column 4), spectroscopic redshifts (column 5), grism redshifts (column 6), the FWHM of line Hβ (column 7), the flux and flux error of [OIII]λ4959,5007 in the Magellan spectroscopy (column 8) and the PEARS grism survey (column 9).

Redshift Comparison

We first compare the LDSS3 redshifts with the redshifts determined from ACS grism detections of 1 or 2 emission lines at ~80Å resolution. Among the 76 emission-line

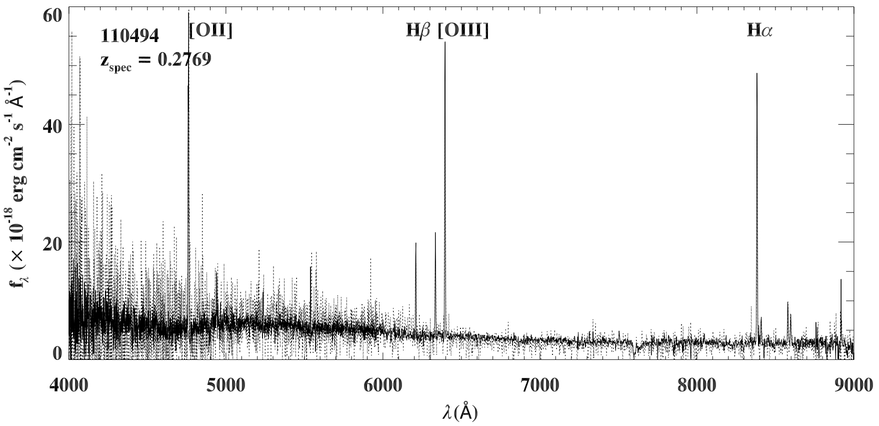

Figure 3.2: Flux calibrated spectra for object 10494 observed in both 2007 (dotted line) and 2008 (solid line). The flux uncertainties of the spectra in 2007 are much larger than that of 2008 due to the larger seeing. Due to the off-slit positioning of of the standard star in 2007 data, the spectra of 2007 is flux calibrated by the sensitivity function obtained from 2008 spectroscopic standard stars. The consistency of the continuum and the line ratio of Hγ/Hβ in the two years demonstrate the robustness and effectiveness of this application. The PEARS ID, the redshift and the main emission lines are labeled in the plot.

galaxies with LDSS3 redshifts, 62 have ACS grism redshifts from Straughn et al. (2009). For remaining 14 Straughn et al. (2009) find a line but cannot assign a line identification and redshift with confidence due to lack of secure photometric redshift for these sources. We plot the redshift differences between the LDSS3 and ACS redshifts in Figure 3. The ACS grism redshifts include only one catastrophic failure (object 89030, discussed below) and one object, 72509, with redshift difference of 0.05. Object 72509 has a redshift of 1.246 and only the [OII]3727 is observed in the red-end of the spectra. The ACS grism spectrum of this object is noisy and there are several peaks around 8400 Å which could be due to the contamination of sky line residuals. Among the remaining 60 objects, we measure a root mean square redshift difference of $\sigma_z = 0.006$ between the ACS and LDSS3 redshifts.

Object, 89030, with large deviation between the measured spectroscopic redshift, 0.6220, and the grism redshift, 1.449, has a well detected continuum, $f_\lambda \sim 10^{-18}$ erg s^{-1} cm^{-2} Å^{-1}, and a full set of lines, [OII] doublet, Hβ, and [OIII] doublet, in the Magellan spectrum. The ACS grism spectrum has the strongest line peaks around 9120Å, which is assigned to be [OII]λ3727, and a weak continuum $f_\lambda \sim 10^{-19}$ erg s^{-1} cm^{-2} Å^{-1}. From the *i*-band image of this object, it is found that object 89030 has two neighbors, an extended spiral and a bright compact object. Combined with the faint *i*-band magnitude, $i = 25.79$, We conclude that the spectrum obtained from Magellan could be the contamination of one of the adjacent two objects.

Flux Comparison

We compare emission-line fluxes as measured from the ground and the grism. Usually, [OIII]λ5007 is the strongest emission line in the spectra. Due to the low resolution of ACS grism spectra, the two lines [OIII]$\lambda\lambda$4959,5007 are blended into one wide peak. Figure 4 presents the comparison of the total emission-line fluxes of [OIII]$\lambda\lambda$4959,5007 for 33 common objects with both flux measurements. The *y*-axis is the flux ratio between the spectroscopic to the grism flux and the *x*-axis is the geometric mean of the grism and the spectroscopic line fluxes. From the figure, the ratio for most of the galaxies are in the range from 0.5 to 2 (dotted line), which agrees with the expectation. In the pre-selected ELGs sample about two-thirds have irregular and/or merging morphologies (Straughn et al., 2009). For irregular and extended morphologies the slit losses can lead to a factor of 2 underestimatation of the spectroscopic line fluxes. The ACS grism spectra are extracted for individual star forming knots based on the 2D detection (Straughn et al., 2009), which could introduce big differences for flux comparison also. Other factors, such as the uncertainty in the background continuum determination of the ACS spectra, the contamination

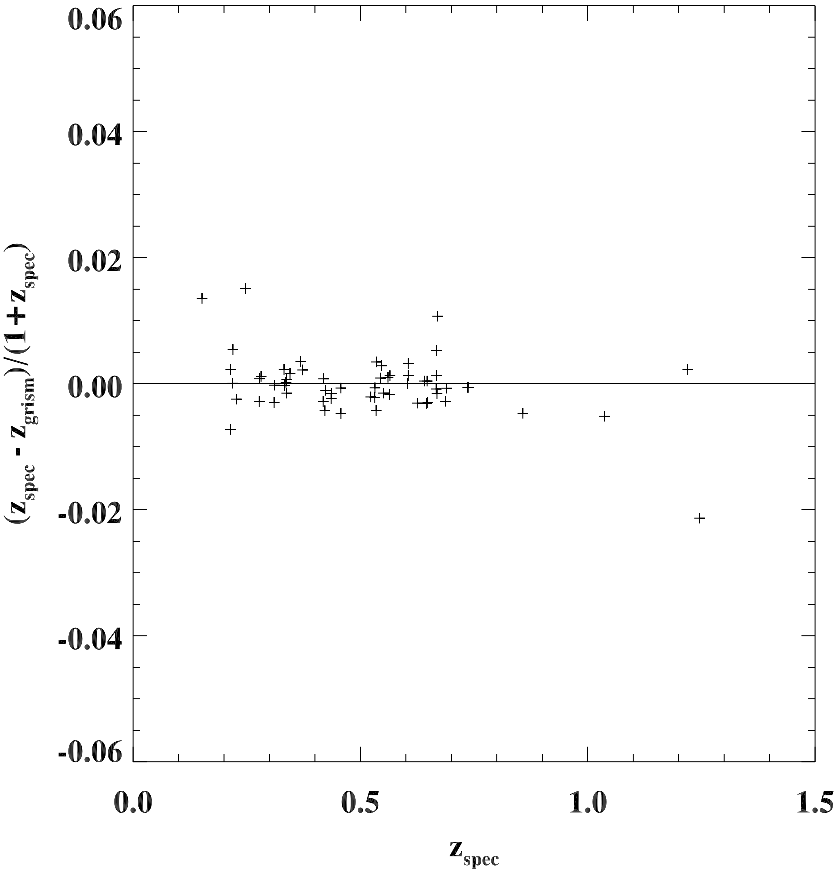

Figure 3.3: Redshift differences between the spectroscopic and the grism redshifts as a function of the spectroscopic redshifts. The accuracy of the grism redshift is measured to be $\sigma_z = 0.006$.

of the Hβ can introduce some factor to the line fluxes. Therefore, we assume that the factor from 0.5 to 2 in the flux ratio is in the reasonable range of the measurements.

AGN Identification

The contribution to the emission lines in spectra includes the ionized HII region by massive stars in normal star-forming galaxies and the narrow-line region (NLR) of AGNs. To classify the emission-line galaxies in the sample to be star-forming galaxies or AGNs, we use two methods: catalog matching to the CDF-S X-ray

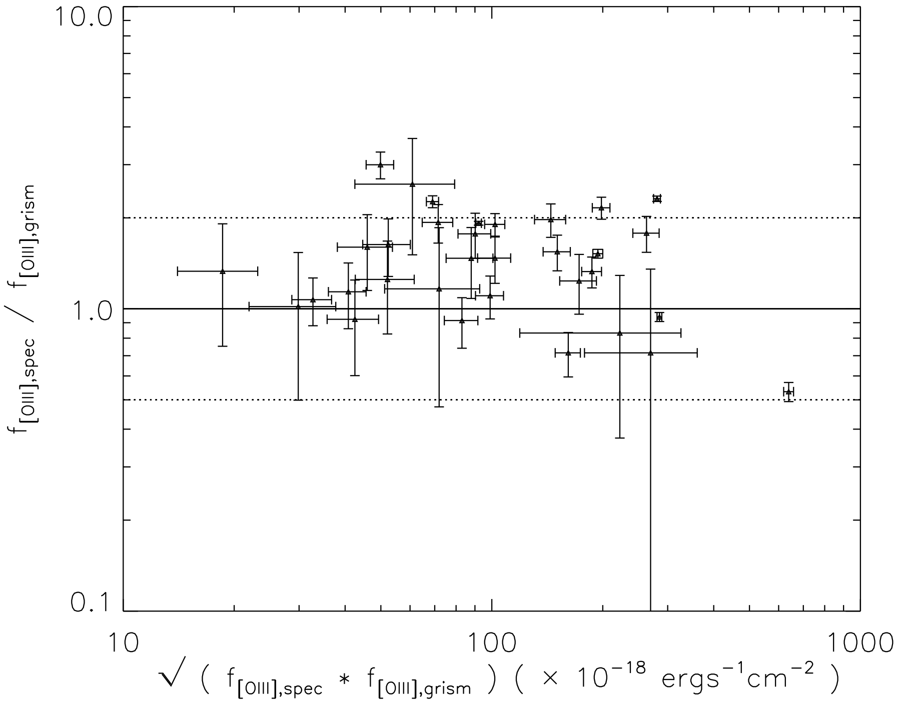

Figure 3.4: l

ine fluxes measured by ACS grism and LDSS-3.] Flux ratios of the spectroscopic to the grism as a function of the square root of the [OIII] line fluxes measured by ACS grism and LDSS-3, which is plotted in log scale. The ratios for most objects are in the range from 0.5 to 2.0 (the dotted lines, the solid line shows the ratio of 1), which is in the reasonable range due to the different sampling of galaxy light by the slit and grism, the uncertainty in the determination of the grism continuum.

sources catalog of Luo et al. (2008), and comparison of the [NII]λ6584/Hα versus [OIII]/Hβ line ratios (i.e. the well known BPT diagram; (Baldwin, Phillips, & Terlevich, 1981). The cross-check with the X-ray detections gives 5 X-ray counterparts with separation within $2''$, which are possible AGNs and are marked in Table 1. By checking the X-ray full-band flux, the two objects, 92839 and 102156, have a luminosity of $L_{FB} = 6.36\times10^{43}$ ergs s^{-1} and 3.36×10^{43} erg s^{-1}, respectively. From the spectra, these two objects show strong exponential-slope continuum. From the line widths, the lines of these two AGNs have velocities $\sim$ 3800 km s^{-1}, $\sim$ 1000 km s^{-1}. Thus, these two are determined to be broad-line AGNs.

The other three objects, 59018, 60143, and 79483, show $L_{FB} \sim 10^{41}$ ergs s^{-1} and are possible starburst galaxies and faint AGNs. We derive the hardness ratios, HR=(H-S)/(H+S), where S and H are counts in the soft-band (0.5-2 keV) and in the hard-band (2-7 keV), for the two galaxies, 59018 and 79483. The HRs are < -0.13 and < -0.29, respectively, which implies an intrinsic absorption of X-ray column density $N_H < 8.8$ and 2.4×10^{21} cm^{-2} (68% confidence level, for $\gamma = 2.0$ and solar metallicity). This suggests that the X-ray fluxes are dominated by star formation or unobscured faint AGN.

We use the extinction corrected (the extinction is obtained by the continuum SED fitting with the BC03 stellar population synthesis model, Bruzual & Charlot 2003) line fluxes of [OII] and $H\beta$ to derive the star formation rates (SFR) for the three possible starburst galaxies by the calibrations given by Kennicutt (1998), and use the soft-band (0.5-2 kev) and hard-band (2-10 kev) X-ray fluxes to get SFR by the relations given by Ranalli et al. (2003). The results are given in Table 2. The "$<$" in Table 2 denotes the upper limit X-ray detection. The X-ray flux of galaxy 60143 is only detected in the full band (0.5-7 keV). The SFRs of object 60143 agree very well between the [OII]-derived and soft-band derived results, ~ 10 $M_{\odot}$/yr, so galaxy 60143 are more likely a starburst galaxy. For object 59018 and 79483, the X-ray calibrations give the SFR ~ 10 $M_{\odot}$/yr, and the emission lines calibrations give the SFR ~ 1 $M_{\odot}$/yr. While the SFRs from X-ray are an order larger than the SFRs from the extinction-corrected emissions for galaxies 59018 and 79483, we treat these two galaxies as unobscured faint AGNs.

For the emission-line sources, the lines Hα and [NII]λ6584 can only be observed for galaxies at $z < 0.36$ due to the wavelength coverage of the spectra. The above 5 objects with X-ray detection all have redshift $z > 0.36$ and hence out of the analysis of the BPT diagonostic method. For 14 galaxies with good line flux measurements at $z < 0.36$, Figure 5 shows the plot of the [NII]λ6584/Hα and [OIII]/Hβ ratios for these objects. The theoretical maximum starburst limit (dashed line) from Kewley et al. (2001) and the empirical demarcation from Kauffmann et al. (2003) (dotted line) are also plotted. All of the 14 objects are below the theoretical upper limit (Kauffmann et al., 2003). Two object, 89923 and 111549, lie in the transition region between the empirical and theoretical demarcation curves. There are no X-ray detections for these two objects, no other distinct AGN high ionization indictator emission lines, e.g. [NeV] and HeII, and no broad lines. Hence, these objects could be star-forming galaxies, or low-luminosity AGNs, or some combination of the two.

For galaxies at $z > 0.36$ and without Hα and [NII] observation, we use the HeIIλ4686 as the indicator of the AGN activity. Only one object, 106761, has prominent HeII in the spectra and could be AGN.

The above analysis of the X-ray detection, line width, hardness ratio and column density, SFRs, BPT diagram and high ionization emission line, give 7 AGNs in the sample. We mark these objects in Table 1 with stars besides the object ID as the AGNs and AGN candidates identified in this paper.

3.5 Summary

We investigate the accuracy of the grism redshifts using the Magellan LDSS-3 follow-up spectroscopic observation of a sample of 76 emission-line galaxies. The galaxies are pre-selected to have emission lines (Straughn et al., 2009) in the GOODS-S field. The galaxies span the magnitude range $19.0 < i < 26.0$ and the redshift range $0.1 < z < 1.3$. In the spectral coverage from 6500Å to 9700Å, the most important emission line observed are [OII], Hβ, [OIII], and some Hα, and [NII] for low redshift galaxies. The spectroscopic redshifts are measured from the pattern of the emission lines. The spectroscopic redshifts of 76 galaxies are obtained. The

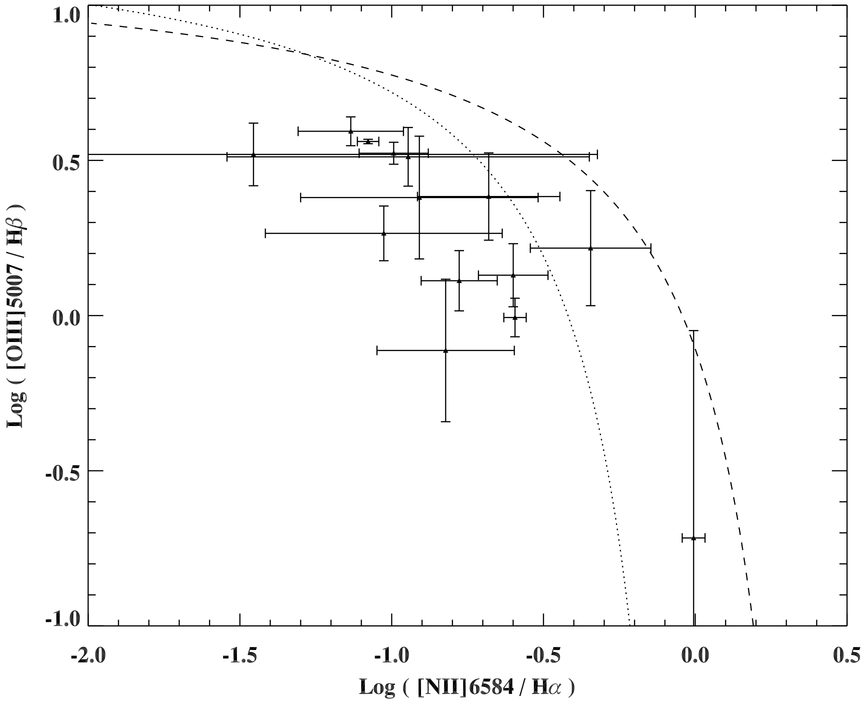

Figure 3.5: Emission-line ratios [NII]λ6584/Hα vs. [OIII]/Hβ for 14 objects at $z < 0.36$ with Hα and [NII]λ6584 observation and measurements. The dashed line is the theoretical maximum starburst limit from Kewley et al. (2001), and the dotted line represents the empirical demarcation from Kauffmann et al. (2003) (dotted line). Two objects in the locus between the two curves have large [NII]λ6584 line flux and have high probability to be AGNs.

accuracy of the grism redshifts is assessed using 62 galaxies with both redshift measurements. An accuracy of $\sigma_z = 0.006$ is found for the grism redshifts.

For 33 galaxies with both LDSS-3 flux measurements and grism fluxes, the emission-line fluxes of [OIII] are compared. A general agreement is found with the [OIII] flux ratio ranging from 0.5 to 2. The different sampling of light by the slit and the ACS grism, and the uncertainty in the continuum determination of the ACS grism spectra may result in this factor of 2.

By cross-checking with CDF-S X-ray catalog (Luo et al., 2008), two AGNs, 92839 and 102156, are identified with luminosities of $L_{FB} > 10^{43}$ erg s^{-1}. Another three X-ray detected galaxies show luminosity of $L_{FB} \sim 10^{41}$ ergs s^{-1} and are possible starburst galaxies or obscured faint AGNs. The SFRs for the three objects are derived from extinction corrected emission-line fluxes and X-ray soft-band and hard-band fluxes. One object, 60143, shows good agreement in the derived-SFRs, which is $\sim$ 10 $M_{\odot}$/yr, and is more likely a starburst galaxy. For another two galaxies, 59018 and 79483, the hardness ratio, HR $<$ – 0.13 and $<$ – 0.29, and the X-ray column density, $N_H < 8.8$ and 2.4×10^{21} cm^{-2}, suggests possible star formation or unobscured faint AGNs. Since the extinction corrected emission-line [OII] and Hβ derived SFRs are $\sim$ 1 $M_{\odot}$/yr, while the X-ray derived SFR is $\sim$ 10 $M_{\odot}$/yr, we treat these two galaxies as unobscured faint AGNs.

For 14 galaxies at $z < 0.36$ (without X-ray counterparts) and with Hα and [NII] emission lines observed in the spectra, we use the BPT diagram to identify star-forming galaxies and AGNs. All of the 14 objects locate below the theoretical upper limit (Kauffmann et al., 2003). Two objects, 89923 and 111549, locating in the transition region between star-forming galaxies and AGNs, could be possible AGNs. From the high ionization indictator emission lines, HeIIλ4686, one more object, 106761, is identified as possible AGN.

Table 3.1: Spectroscopic redshifts and emission line fluxes of the emission line galaxies obtained from the Magellan follow-up LDSS-3 observation. The corresponding grism redshifts and grism fluxes are listed in the table. The stars besides object ID represent AGNs and AGN candidates.

PEARS ID	RA	DEC	i_{mag}[a]	z_{spec}	z_{grism}	$FWHM$[b]	$f_{[OIII],spec}$[c]	$f_{[OIII],grism}$[c]
12250	3:32:37.61	-27:55:32.63	24.69	0.3391	–	6.1	100.5±10.7	–
13541	3:32:38.03	-27:55:08.07	21.41	0.3730	0.370	4.8	191.9±10.6	155.1±34.3
17587	3:32:38.60	-27:54:49.85	24.81	0.6447	0.650	1.2	58.3±8.5	46.6±15.5
17686	3:32:27.87	-27:54:51.56	29.73	0.6697	–	–	–	–
18862	3:32:32.72	-27:54:22.91	19.24	0.2018	–	3.3	82.6±35.8	–
19422	3:32:41.30	-27:54:34.74	24.51	0.5506	0.553	4.9	104.0±9.9	94.1±13.7
19639	3:32:34.92	-27:54:13.83	19.90	0.2802	0.280	3.0	178.9±17.2	125.0±83.3
22829	3:32:39.54	-27:54:00.67	21.52	0.5606	0.559	5.0	239.3±13.4	157.2±4.3
26009	3:32:33.10	-27:53:40.68	23.60	0.4356	0.439	–	–	–
31362	3:32:43.68	-27:53:05.90	24.17	0.6672	0.665	4.8	275.9±0.5	293.8±8.7
33294	3:32:38.08	-27:52:48.68	23.49	1.0354	1.047	–	–	–
37690	3:32:40.74	-27:52:16.92	23.57	0.3644	–	1.8	44.9±3.7	–
41078	3:32:43.39	-27:51:54.54	24.25	0.8573	0.866	–	–	–
43170	3:32:37.49	-27:51:38.84	24.02	0.6874	0.692	7.0	123.4±4.3	84.1±15.6
45454	3:32:43.63	-27:51:22.37	22.73	0.4233	0.425	4.1	43.6±0.1	38.2±9.0
46994	3:32:39.45	-27:51:13.16	24.29	0.6665	0.668	6.7	187.1±7.1	121.1±17.6
49766	3:32:42.00	-27:50:51.80	23.53	0.2184	0.213	1.9	30.1±10.9	–
52086	3:32:37.87	-27:50:39.52	23.47	0.5227	0.526	4.9	145.0±8.6	243.9±46.5
54022	3:32:41.93	-27:50:26.81	22.29	0.3360	0.336	5.6	120.0±3.0	67.7±13.7
55102	3:32:42.15	-27:50:18.71	21.83	0.4567	0.458	3.8	77.7±6.1	66.7±38.1
56801	3:32:34.82	-27:50:14.56	23.93	0.6491	0.653	4.3	45.6±7.1	–
56875	3:32:36.72	-27:50:15.70	24.48	0.5346	0.541	4.1	34.6±2.7	32.6±3.3
58985	3:32:47.98	-27:50:02.64	23.78	0.5650	0.563	–	–	–
59018 $\star$[d]	3:32:42.32	-27:49:50.33	20.59	0.4571	0.464	5.8	20.2±3.4	–
60143	3:32:35.61	-27:49:43.95	21.21	0.5464	0.542	–	–	–
65825	3:32:41.22	-27:49:18.45	23.51	0.9329	–	–	–	–
70651	3:32:36.75	-27:48:43.51	23.33	0.2143	0.212	3.1	179.1±27.5	102.9±15.4
72509	3:32:40.92	-27:48:23.73	24.46	1.2461	1.294	–	–	–
72557	3:32:32.19	-27:48:24.41	23.52	0.3378	–	–	–	–

Continued on Next Page…

Table 3.1 – Continued

PEARS ID	R.A.	DEC	$i_{mag}{}^{a}$	z_{spec}	z_{grism}	$FWHM^{b}$	$f_{[OIII],spec}{}^{c}$	$f_{[OIII],grism}{}^{c}$
73619	3:32:44.26	-27:48:18.58	24.77	0.6699	0.652	–	–	–
75506	3:32:35.34	-27:48:03.06	26.33	0.2794	0.277	–	33.9±6.9	31.6±4.4
75753	3:32:44.97	-27:47:39.22	21.57	0.3451	0.343	4.9	291.4±1.0	134.9±14.8
76154	3:32:36.29	-27:47:55.32	23.68	0.6049	0.600	5.2	34.1±11.3	66.4±0.7
79283	3:32:34.11	-27:47:12.10	20.75	0.2266	0.230	4.1	34.3±3.9	–
79483 $^{\star d}$	3:32:45.11	-27:47:24.00	20.81	0.4345	0.438	5.9	13.5±1.9	–
80500	3:32:35.32	-27:47:18.53	23.34	0.6677	0.658	4.5	66.9±12.0	41.0±9.6
81944	3:32:34.73	-27:47:07.62	22.48	0.2469	0.228	3.5	525.9±9.7	875.7±37.8
83381	3:32:42.37	-27:46:57.17	24.92	0.3318	0.329	–	–	–
85517	3:32:42.32	-27:46:51.06	24.79	0.5358	0.530	7.2	65.5±5.0	–
89030	3:32:38.50	-27:46:30.82	25.79	0.6220	1.449	5.0	15.8±6.8	–
89853	3:32:33.02	-27:46:08.76	21.63	0.3689	0.364	–	–	–
89923 $^{\star d}$	3:32:41.76	-27:46:19.39	21.25	0.3331	0.333	5.4	9.7±6.4	–
90116	3:32:46.76	-27:46:24.05	25.45	0.6250	0.630	–	–	–
91205	3:32:36.13	-27:46:16.37	23.18	0.2178	–	4.2	87.3±18.4	–
91789	3:32:35.29	-27:46:12.21	23.80	0.5313	0.533	4.2	21.0±5.2	–
92839 $^{\star\star e}$	3:32:39.08	-27:46:01.78	20.95	1.2222	1.215	79.^{f}	–	–
95471	3:32:42.56	-27:45:50.16	22.38	0.2191	0.219	–	–	–
96123	3:32:34.30	-27:45:49.21	23.12	0.5313	0.535	4.1	21.0±5.3	–
96627	3:32:40.91	-27:45:40.91	21.50	0.1516	0.136	4.1	288.0±40.1	–
97655	3:32:27.37	-27:45:40.61	23.71	0.5442	0.543	5.0	37.5±10.4	589.2±23.2
100188	3:32:24.31	-27:45:24.41	25.00	0.3107	0.311	–	–	–
102156 $^{\star\star e}$	3:32:30.22	-27:45:04.60	21.65	0.7368	0.738	28.	228.0±9.8	318.8±15.2
104408	3:32:27.85	-27:44:49.96	24.27	0.7371	0.737	5.0	97.9±8.6	37.9±22.6
105723	3:32:27.30	-27:44:28.68	20.03	0.2142	0.223	–	–	–
106491	3:32:27.28	-27:44:37.46	24.93	0.3372	0.337	5.7	110.4±13.5	72.5±20.7
106761 $^{\star d}$	3:32:29.12	-27:44:38.63	25.88	0.6673	–	2.2	54.9±12.7	52.4±3.2
109547	3:32:21.41	-27:44:09.59	23.64	0.3627	0.368	–	–	–
110494	3:32:25.91	-27:44:01.49	21.96	0.2775	0.281	3.8	332.8±18.1	197.0±31.9
111549 $^{\star d}$	3:32:24.60	-27:43:46.79	22.06	0.3096	0.314	4.6	58.1±7.8	36.3±11.3
114392	3:32:22.95	-27:43:33.09	23.63	0.5636	0.567	2.9	30.0±8.7	29.6±13.0
117138	3:32:17.36	-27:43:07.27	21.18	0.6480	–	2.9	92.4±6.1	51.5±9.2
117686	3:32:18.25	-27:43:10.95	24.44	0.6693	–	4.5	64.8±11.0	28.1±4.1

Continued on Next Page…

Table 3.1 – Continued

PEARS ID	R.A.	DEC	$i_{mag}{}^{a}$	z_{spec}	z_{grism}	$FWHM^{b}$	$f_{[OIII],spec}{}^{c}$	$f_{[OIII],grism}{}^{c}$
117929	3:32:29.52	-27:43:05.19	22.09	0.3378	0.340	3.2	86.4±6.4	28.8±4.4
118014	3:32:23.68	-27:43:08.72	23.60	0.9796	–	–	–	–
118100	3:32:16.87	-27:43:04.27	23.16	0.6467	0.646	7.2	140.8±10.6	74.0±7.4
118673	3:32:21.94	-27:43:03.41	24.62	0.7362	–	–	–	–
119341	3:32:16.81	-27:42:59.76	25.09	0.6909	0.691	6.2	56.3±10.9	–
121817	3:32:23.16	-27:42:39.98	24.48	0.6683	0.671	4.0	79.4±11.3	86.7±12.9
123008	3:32:16.65	-27:42:32.71	23.21	0.6410	0.640	5.0	215.4±5.9	162.1±19.4
123301	3:32:18.57	-27:42:29.50	22.50	0.6042	0.604	6.8	426.9±15.0	184.5±4.2
123859	3:32:15.45	-27:42:20.54	22.68	0.4190	0.418	3.9	103.9±5.5	45.9±2.6
127697	3:32:14.74	-27:41:53.29	22.56	0.4170	0.422	7.0	21.5±4.8	16.1±7.1
128538	3:32:12.76	-27:41:44.45	22.66	0.4214	0.457	4.6	40.9±4.8	44.2±13.1
129968	3:32:11.85	-27:41:39.52	23.50	0.6051	0.603	3.3	136.3±13.9	190.6±22.5
130264	3:32:11.26	-27:41:27.01	22.30	1.0574	–	–	–	–
134573	3:32:22.01	-27:40:59.21	22.99	0.3579	–	8.7	244.1±8.2	–

---

[1] a: The optical *i*-band magnitudes are obtained from HST/ACS GOODS version 2.0 images (Giavalisco et al. 2004).

[2] b: The line FWHMs are measured for $H\beta$ and in unit of $\AA$.

[3] c: The fluxes are in unit of $10^{-18} ergss^{-1}cm^{-2}$.

[4] d: One star marks AGN candidate identified by the CDF-S X-ray luminosity, hardness ratio and column density, SFRs, the BPT diagram, and the high ionization indictator emission lines.

[5] e: Two stars mark AGNs identified by the CDF-S X-ray luminosity, line widths, and spectral slope.

[6] f: The FWHM of object 92839 is measured from MgII since the H recombination lines are out of the spectral coverage.

[7] NOTE: No data indicates measurement was not possible. In case of z_{grism}, no data is because no suitable line ID was found for the given input guess redshift.

Table 3.2: Star formation rates ($M_\odot$/yr) derived from line luminosities (erg/s) of [OII] and $H\beta$, and X-ray soft-band (0.2-5 kev) and hard-band (2-10 kev) luminosities for the identified three starburst galaxies by X-ray cross-checking. The upper limit detection is denoted.

PEARS ID	z	$L_{[OII]}{}^a$	$SFR_{[OII]}{}^b$	$L_{H\beta}{}^a$	$SFR_{H\beta}{}^b$	$L_{SB}{}^a$	$SFR_{SB}{}^b$	$L_{HB}{}^a$	$SFR_{HB}{}^b$
59018	0.457	9.22e+40	1.29	2.92e+40	0.65	4.436e+40	9.76	$<$ 1.23e+41	$<$ 24.55
60143	0.546	8.54e+41	11.95	–	–	$<$ 4.411e+40	$<$ 9.70	$<$ 1.88e+41	$<$ 37.67
79483	0.435	1.26e+41	1.76	5.97e+40	1.33	6.632e+40	14.59	$<$ 1.31e+41	$<$ 26.17

[a]: The luminosities are in unit of $ergss^{-1}$.

[b]: The star formation rates are in unit of $M_\odot/yr$.

Chapter 4

MASS-METALLICITY RELATION OF STAR-FORMING GALAXIES FROM HST/ACS PEARS AT $0.2 < z < 0.9$

4.1 Abstract

We measure gas-phase oxygen abundances for 30 emission-line galaxies (ELGs) at $0.2 < z < 0.9$, which are pre-selected from the HST/ACS Probing Evolution and Reionization Spectroscopically (PEARS) grism Survey, with follow-up spectroscopy taken with the Magellan LDSS-3 and IMACS spectrographs. The gas-phase oxygen abundances, 12 + log(O/H), are estimated by the metallicity diagnostic indicator R_{23}, utilizing the [OII]λ3727, Hβ, and [OIII]$\lambda\lambda$4959,5007 emission lines. The oxygen abundances span the range $7.8 <$ 12 + log(O/H) < 8.9. The galaxy stellar masses are derived from SED fitting with the Bruzual & Charlot (2003) stellar population synthesis model. The masses span the range $7.5 < \log(M_*/\mathrm{M}_\odot) < 10.5$. The mass-metallicity ($M$-$Z$) relation of the PEARS sample with median redshift $\langle z\rangle \sim 0.5$ shows significant a offset by $\sim$ –0.5 dex in metallicity at given stellar mass relative to the local M-Z relation from SDSS galaxies. The luminosity-metallicity (L-Z) relation is also offset by $\sim$ –0.8 dex in metallicity relative to the local L-Z relation. The low metallicity galaxies in the PEARS sample show blue colors, small sizes, and compact disturbed morphologies, similar to the local green peas and LBG analogs. The SFRs span the range 0.1 – 10 $\mathrm{M}_\odot$/yr, and do not show significant correlation with galaxy metallicities. The specific star formation rates (SSFRs) are larger by $\sim$ 1 dex than the local SDSS galaxies. This is due to the higher SFRs and lower masses of the PEARS galaxies relative to the local ones. The projection of the PEARS galaxies on the fundamental metallicity relation (FMR) plane shows good agreement with that defined by local SDSS galaxies. The fit with the chemical evolutionary models with inflow and outflow shows that the

model of solar yield $y_{\odot}$ with inflow rate $f_i = 1\times\mathrm{SFR}$ and outflow rate $f_o = 0.1\times\mathrm{SFR}$ gives best fit to our data. The low-mass PEARS galaxies show high gas fractions. Hence, these galaxies may still at their intrinsic early evolutionary stages, i.e. the downsizing effect. The tidal interaction induced inflow of metal-poor gas, and the SNe driven galactic winds outflows, may also account for the significant offset of the PEARS galaxies in the L-Z and the M-Z relations relative to the local relations.

4.2 Introduction

The chemical enrichment of the universe is driven by stellar nucleosynthesis in galaxies (Tinsley, 1980). The metallicity is expected to be tightly related to the galaxy evolutionary state, which can be characterized by size, morphology, color, luminosity, stellar mass, and gas fraction, etc. In galaxy evolutionary scenario, the heavy elements can be diluted by a series of physical processes, such as stellar winds, supernovae explosions, galactic winds, and inflow of pristine gas (Larson, 1974; Garnett, 2002; Tremonti et al., 2004). Studying the relations between metallicity and stellar masses, luminosities, and star formation rates (SFRs) is crucial to understand the star formation history and the multiple physical processes interplaying in galaxy evolution (Tinsley & Larson, 1978; Larson & Tinsley, 1978).

At redshift $z \sim 0.1$, the relation between galaxy stellar masses and gas-phase oxygen abundances (M-Z relation) is well established by $\sim$ 53,000 SDSS star-forming galaxies (Tremonti et al., 2004). The results show that the gas-phase metallicity increases as stellar mass increases from $10^{8.5}$ to $10^{10.5}$ $\mathrm{M}_{\odot}$ and flattens above $10^{10.5}$ $\mathrm{M}_{\odot}$. The correlation is interpreted by the selective loss of metals from galaxies with shallow potential wells via galactic winds (Larson, 1974; Tremonti et al., 2004). At intermediate redshifts, Kobulnicky & Kewley (2004) presented the relation between the rest-frame blue luminosity and gas-phase metallicity (L-Z relation) by a sample of 204 emission-line galaxies at $0.3 < z < 1.0$ in the GOODS-

North field. A decrease of 0.14 ± 0.05 dex in average oxygen abundance from z = 0 to 1 is found within – 18.5 $< M_B <$ – 21.5. Zahid et al. (2011) studied the M-Z relation at 9.2 $< \log(M_*/\mathrm{M}_\odot) <$ 10.6 and the L-Z relation at – 19.5 $< M_B <$ – 22. using a large sample of $\sim$ 1350 emission-line galaxies from DEEP2 at z $\sim$ 0.8. They found a mean difference in metallicity of $\sim$ –0.15 dex in the M-Z relation and $\sim$ –0.2 dex in the L-Z relation comparing to the local ones. Redshift $1 < z < 2$ is a very important regime since the star formation rate (SFR) and metal production of galaxies peak in this range (Lilly et al., 1996; Madau et al., 1996; Chary & Elbaz, 2001; Somerville et al., 2001; Pérez et al., 2005; Tresse et al., 2007), and the Hubble type of disk and elliptical galaxies emerge in this period (Dickinson et al., 2003). The studies at these intermediate redshifts (Shapley et al., 2005; Maier et al., 2006; Liu et al., 2008) and at $z > 2$ (Erb et al., 2006; Maiolino et al., 2008; Hayashi et al., 2009; Mannucci et al., 2009) show strong evolution of the M-Z relation, with metallicity decreasing with increasing redshift for a given stellar mass. Based on the metallicity of 5 galaxies at $z \sim 1.4$, Maier et al. (2006) found that rapid chemical evolution is taking place in galaxies of lower luminosities as the universe ages. Liu et al. (2008) studied the mass-metallicity relation of 20 star forming galaxies at $1.0 < z < 1.5$ and demonstrated that the zero point of the M-Z relation evolves with redshift by $\sim$ 0.2 dex. Mannucci et al. (2009) presented a strong evolution of $\sim$ –0.8 dex toward low metallicity of the M-Z relation for a sample of 10 Lyman-Break Galaxies with 9 $< \log(M_*/\mathrm{M}_\odot) <$ 11 at $z \sim 3.1$.

There are two scenarios for the explanation of the origin of the mass-metallicity relation. One is “downsizing”, which means that low mass galaxies evolve later and on longer time scale than massive galaxies due to lower star-formation efficiency (Cowie et al. 1996; Kobulnicky et al. 2003). Another one is preferential metal loss in low-mass galaxies due to the shallower gravitational potential (Larson 1974, Tremonti et al. 2004, Lamareille et al. 2004, Saviane et al. 2008). We have presented observations, spectroscopic data reduction, and classification between star-forming galaxies and AGNs in an earlier paper for 76 emission-line galaxies at $0.2 < z < 0.9$ from Magellan LDSS-3 spectroscopic follow-up observation (Xia et al. 2011; Paper I hereafter). In this second paper, we study the gas-phase abundances, luminosities, stellar masses, sizes, morphologies and SFRs for 30 emission-line galaxies extending to low masses and low metallicities to study the relation and the evolution between these fundamental properties. The paper is organized as below. We briefly describe the observation and data in § 2. The methods of metallicity estimates, R_{23} method, and the results are presented in § 3. The galaxy stellar masses measurements by SED fitting with BC03 model are presented in § 4. In § 5, we show the results: including the luminosity-metallicity relation, the mass-metallicity relation, the color, morphology, and the SFR correlations with metallicity, and the evolution of the M-Z relation. The gas fraction and effective yield are studied to explain the M-Z relation by fitting with inflow/outflow-included galaxy chemical evolution model in § 6. Finally, we summarize our conclusions in § 7.

4.3 Observation and Data

From the HST/ACS PEARS (Probing Evolution and Reionization Spectroscopically, PI: Malhotra) grism survey, Straughn et al. (2008) selected 203 emission line galaxies (ELGs) with a 2-dimensional detection and extraction procedure from the one or two emission lines detected in the ACS grism spectra. These spectra cover the wavelength range from 5,500 Å to 9,500 Å with a resolution of $R = 100$. The line fluxes of the grism observation reach $\sim 5\times10^{-18}$ergs s^{-1} cm^{-2}, and extend the studies of star-forming galaxies to $M \sim -18.5$ at $z \sim 1.5$.

PEARS ELGs follow-up spectroscopy was carried out using Magellan LDSS-3 and IMACS spectrographs. The two observing runs using the Magellan LDSS-3 spectrograph with grisms of VPH-Blue (covering 4,000 Å to 6,500 Å) and VPH-Red (covering 6,000 Å to 9,000 Å) were done on 2007 November 28-29 and 2008 December 22-23. 105 ELGs were observed on 5 masks by LDSS-3 spectroscopy at magnitude range from 18.0 to 26.0 peaking at 23.5. The observation runs focused on the Lyman Alpha Emitters (LAEs) with ELGs were carried out on Magellan IMACS spectrograph (200l/mm) at 2009 September 10-11 with wavelength coverage from 4,000 Å to 10,500 Å.

With the follow-up spectroscopic observation, the accuracy of the grism redshift estimates is confirmed to be $\sigma_z = 0.006$ and the absolute flux calibration is assessed to be in good agreement with that of PEARS grism flux calibration by a factor of 2 (see Paper I). For the LDSS-3 spectrograph, since two separate grisms, VPH-Blue and VPH-Red, were used in the observation, the full set of emission lines, [OII]λ3727,3729, Hβ, and [OIII]λ4959,5007, could fall in the separate blue-end and red-end spectra depending on the redshifts of galaxies. For some galaxies with strong continua, the blue-end spectra and the red-end spectra show discrepancies in the absolute calibrated fluxes among the overlapping wavelength coverage from 6000 Å to 6500 Å. This discrepancy is partly due to the imperfect centering of object in the slit, which leads to the difference of the fraction of galaxy light sampled during two separate observations. The angle of the mask orientation, which is determined to maximize the object placement in slits on the mask, may also partly account for the difference between the blue-end and the red-end spectra because of the atmospheric refraction effects. We correct this discrepancy by taking the median of the flux ratios between the blue-end and red-end spectra in the overlapping wavelength coverage between 6,000 Å and 6,500 Å. The ratios of this correction range from 0.3 to 3. To investigate the effect of the correction of the emission line fluxes in the blue-end and red-end spectra in metallicity measurements, we use the difference between the metallicities measured from the emission lines before and after correction as the upper limit of the systematic errors of the metallicities.

The emission line fluxes are measured by the IDL codes $gaussfit$ and $mpfit$ (written by Craig B. Markwardt). For weak lines such as [OIII]λ4363 and [NII]λ6584, the lines are fitted with central wavelength set to the nominal redshifted value and the full width same as that of the stronger lines [OIII]λ5007 and Hα. The underlying Hβ absorptions are corrected using the best SED-fitting spectra from Bruzual & Charlot (2003) stellar population synthesis model. The equivalent widths of the Hβ absorption correction range from 2 – 6 Å, which agrees well with the correction applied in other studies, $\sim 3 \pm 2$ Å (Lilly et al., 2003). The extinction correction is done for the best fit $E(B-V)$ obtained from SED fitting using the IDL code $c$alz_unred (written by W. Landsman), which is based on the reddening curve from Calzetti et al. (2000). Studies show that the gas can suffer more extinction than the stellar content, hence we assume E(B-V)$_{stellar}$=0.44E(B-V)$_{gas}$ as has been found locally by Calzetti et al. (2000).

Finally we identify 90 galaxies at $0.2 < z < 0.9$ with full set of [OII], Hβ, and [OIII] emission lines in the spectra available for metallicity measurement by R_{23} method. Within the 90 galaxies, there are 28 galaxies with Hα and [NII]λ6584 in the coverage of the spectra wavelength. We use the $N2$ diagnostic indicator to measure metallicities for these galaxies. Table 1 lists the fluxes and errors of the emission lines [OII]λ3727,3729, [OIII]λ4363, Hβ, [OIII]λ4959,5007, Hα, and [NII]λ6584 for every galaxy in our sample, along with the PEARS ID, the redshift and the extinction value. The line fluxes are in unit of 10^{-18} ergs s^{-1} cm^{-2}.

4.4 Measurements

Metallicity

With the strong nebular lines, [OII]λ3727,3729, [OIII]λ4959,5007, and Balmer line Hβ, we measure the gas-phase oxygen abundance by the most commonly used R_{23} diagnostic indicator, which was first proposed by Pagel et al. (1979). The R_{23} ratio is defined as R_{23} = ([OII]+[OIII])/Hβ, which is related to both the metallicity and the ionization. The ionization is described by the ionization parameter q, which is the number of hydrogen ionizing photons passing through a unit area per second per unit hydrogen number density.

Given the relationship between log(q), log(O32), log(R32) and 12+log(O/H) from the theoretical photoionization models (Kewley & Dopita, 2002), we solve for q and metallicity by iteration.

$$log(q) = \frac{32.81 - 1.153y^2 + [12 + log(O/H)](-3.396 - 0.025y + 0.1444y^2)}{4.603 - 0.3199y - 0.163y^2 + [12 + log(O/H)](-0.48 + 0.0271y + 0.02037y^2)} \tag{4.1}$$

where $y = logO_{32} = log\frac{([OIII]\lambda 4959 + [OIII]\lambda 5007)}{[OII]\lambda 3727}$.

It is well known that the R_{23}-metallicity is a double valued relation, the high metallicity branch and the low metallicity branch. On the lower branch, the R_{23} increases with the increase of the gas-phase oxygen abundance. On the higher branch, the R_{23} decreases with the further increase of the metallicity due to the effective cooling of metals. In this paper we adopt the calibrations given by Kobulnicky & Kewley (2004), which are based on the stellar population synthesis models (PEGASE and STARBURST99) and photoionization models (using the MAPPINGS code Sutherland & Dopita (1993)), to measure the metallicities.

The parameterization of the two branches (Kobulnicky & Kewley, 2004) are, for the lower branch with 12+log(O/H)<8.5,

$$12+log(O/H)_{lower}=9.40+4.65x-3.17x^2-log(q)(0.272+0.547x-0.513x^3), \tag{4.2}$$

and for the upper branch with 12+log(O/H)>8.5,

$$\begin{aligned} 12+log(O/H)_{upper} &= 9.72-0.777x-0.951x^2-0.072x^3-0.811x^4 \\ &\quad -log(q)(0.0737-0.0713x-0.141x^2+0.0373x^3 \\ &\quad -0.058x^4), \end{aligned} \tag{4.3}$$

where $x=logR_{23}$.

For the degeneracy between R_{23} and metallicity, we use the presence of the auroral line [OIII]λ4363 in the spectra to break the degeneracy. The [OIII]λ4363 is strong in the hot temperature and low metallicity regime. For 90 galaxies with measurements of the full set of emission lines, 13 galaxies are selected with $S/N>2$ in the [O III]λ4363 auroral line. Galaxies with $S/N<2$ in [OIII]λ4363 line in the spectra could be galaxies of high metallicities or galaxies of low metallicities with the line fluxes of [OIII]λ4363 lower than the detection limit. Besides the method of using auroral line [OIII]λ4363, we apply another criteria given by (Kakazu et al., 2007; Hu et al., 2009) to break the degeneracy, EW(Hβ) $>$ 30 Å, which was used for the selection of ultra-strong emission line galaxies with a high fraction of low metallicity galaxies. Since we assume that the gas suffers more extinction than the stellar content, and the relation E(B-V)$_{stellar}$=0.44E(B-V)$_{gas}$ Calzetti et al. (2000), the EW of emission lines after extinction correction will be doubled. Hence we use EW(Hβ) $>$ 15 Å as our criteria to classify higher branch galaxies and lower branch galaxies. Figure 1 shows the estimation of the gas phase oxygen abundance versus the strong line ratio diagonostic logR_{23} and the criteria used to classify the branch are listed in the third column of Table 2. There are 44 galaxies with $R_{23} > 0.95$ are removed out of the sample which line fluxes may have significant contribution from the AGN activities, and 16 out of 44 have R_{23} within 1σ of 0.95. Since the metallicities are around the turning point $\sim$ 8.6 for galaxies with logR_{23} $\sim$0.95, which contribute little to the study of the M-Z relation, we do not include these galaxies in the sample.

Within the 90 galaxies, there are 28 galaxies with emission lines Hα and [NII]λ6584 present in the spectra. For these 28 galaxies, the diagnostic indicator $N2$, which is defined as $N2$ = log ([NII]λ6584/Hα) and was theoretically calibrated by Kewley & Dopita (2002); Kobulnicky & Kewley (2004), is used for metallicity measurements,

$$\begin{aligned} 12+log(O/H) &= 7.04+5.28X_{NII}+6.28X_{NII}^2+2.37X_{NII}^3 \\ &\quad -logq(-2.44--2.01X_{NII} \\ &\quad -0.325X_{NII}^2+0.128X_{NII}^3) \\ &\quad +10^{X_{NII}-0.2}log(q)(-3.16+4.65X_{NII}), \end{aligned} \tag{4.4}$$

where $X_{NII} = logN2$. The advantage of the $N2$ indicator is that it is insensitive to uncertainties arising from the flux calibration and the reddening extinction. Since the $N2$ indicator saturates and is not sensitive to oxygen abundance above roughly solar metallicity, we use it as branch identifier and estimate metallicities from R_{23} to avoid the difference arising from different metallicity indicators and calibrations. We compare the metallicities measured from R_{23} and $N2$ for the 8 galaxies (19 galaxies are removed out of 28 due to $R_{23} > 0.95$ which are beyond the model and are possible AGNs, and one has faint [NII]λ6584 line flux with negative value and we classify it directly at lower branch), which is shown in Figure 2. As shown in Figure 2, the metallicities computed by the $N2$ diagnostic indicator are generally consistent with that estimated by the R_{23} indicator.

Combining the galaxies obtained from these three criteria, requiring magnitude and mass measurements, and excluding galaxies with $R_{23} > 0.95$, the final sample consists of 22 lower branch galaxies and 8 higher branch galaxies. The metallicity and the ionization parameter q are finally computed by iteration from the R_{23}-q-O/H relations (Kobulnicky & Kewley, 2004). Figure 3 shows the relations of the ionization parameter log(q) versus [OII]λ3727/[OIII]λ5007 (left panel) and versus 12+log(O/H) (right panel). As can be seen clearly from the left panel, the ionization parameter decreases with the increase of [OII]λ3727/[OIII]λ5007. The value of [OII]λ3727/[OIII]λ5007 ranges from 0.3 to 10, which span one order larger range than previous work (Hu et al., 2009). In the right panel, the relationship between the ionization parameter q and the metallicity shows decreasing ionization with the increase of the metallicity with slightly larger scattering.

The ionization parameter and the oxygen abundances derived from the R_{23} indicator are listed in Table 2 in the fifth column and the sixth column. The errors on the oxygen abundances include systematic uncertainties, which arise due to the flux correction between the blue-end and the red-end spectra, and uncertainties due to the line flux uncertainties.

Stellar Mass

To derive the galaxy stellar mass, spectral age and the star formation history, we compare the observed photometry with the model spectral library produced by the Bruzual & Charlot (2003) stellar population synthesis code (BC03, hereafter). The BC03 model is based on the evolutionary population synthesis technique with the main parameters of the stellar initial mass function (IMF), the star formation rate (SFR) and the rate of chemical enrichment. With the stellar evolution prescription, Padova 1994 stellar evolutionary tracks, and the stellar spectral library, STELIB, the code computes the spectral evolution of stellar population at ages between 1×10^5

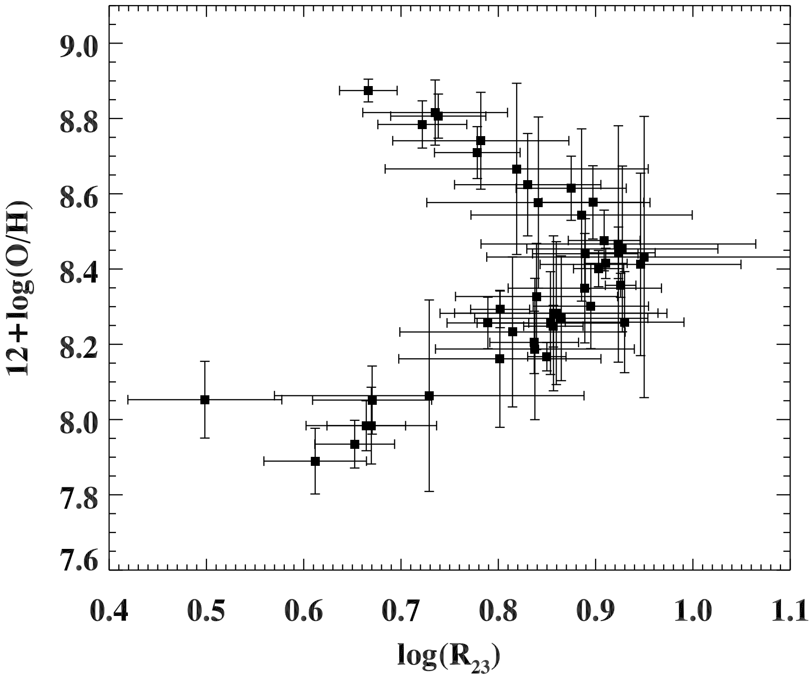

Figure 4.1: The log(R_{23}) versus oxygen abundance for the ELGs in our sample, the branch that galaxies belongs to is determined from the criteria of [OIII]λ4363, [NII]/Hα diagnostic and EW(Hβ), is given in the third column of Table 2. The error bars of the galaxies observed by Magellan LDSS3 spectrograph do not include errors due to the flux correction between the blue-end and the red-end spectra.

and 2×10^{10} yr. The output model spectra cover a wavelength range from 3200 to 9500 Å at a resolution of 3 Å for a wide range of metallicity from $Z = 0.0001$ to 0.05. In this paper, we adopt the Padova 1994 tracks, Salpeter IMF, and three types of star formation histories: instantaneous burst, exponentially declining star formation, and constant star formation, to produce the model spectra for ages 0.001, 0.005, 0.01, 0.035, 0.07, 0.1, 0.35, 0.7, 1, 2, 3, 4, 5, 6, 7, 8, 9, 10, 11, 12 Gyr and metallicity $Z =$ 0.0001, 0.0004, 0.004, 0.008, 0.02 ($Z_\odot$) and 0.05. The *e*-folding timescale τ of exponentially declining star formation is explored with values $\tau =$ 0.001, 0.005, 0.01, 0.035, 0.07, 0.1, 0.35, 0.7, 1, 2, 3, 4, 5, 6, 7, 8, 9, 10, 11, 12 Gyr. The final model library consists of 22 (SFHs) × 6 (metallicities) × 20 (ages)

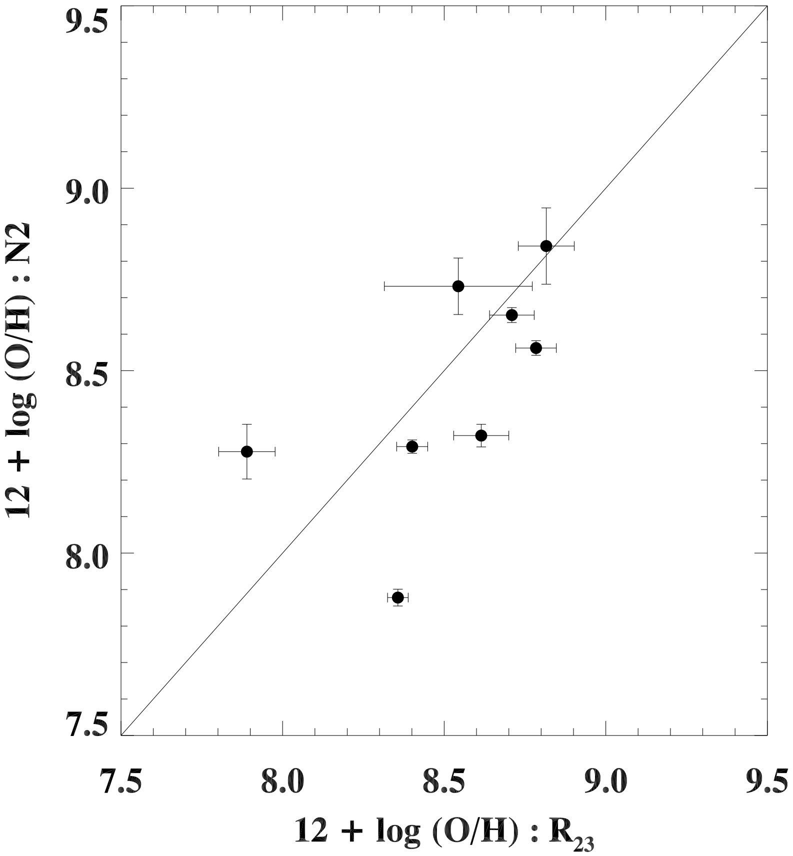

Figure 4.2: Comparison between the metallicities estimated by the $N2$ indicator vs. the metallicities estimated by the R_{23} indicator. The $N2$ indicator shows generally consistent estimates with that given by the R_{23} indicator. The error bars include the systematic uncertainties arising from the flux correction between the blue-end and the red-end spectra, and the uncertainties due to the line fluxes.

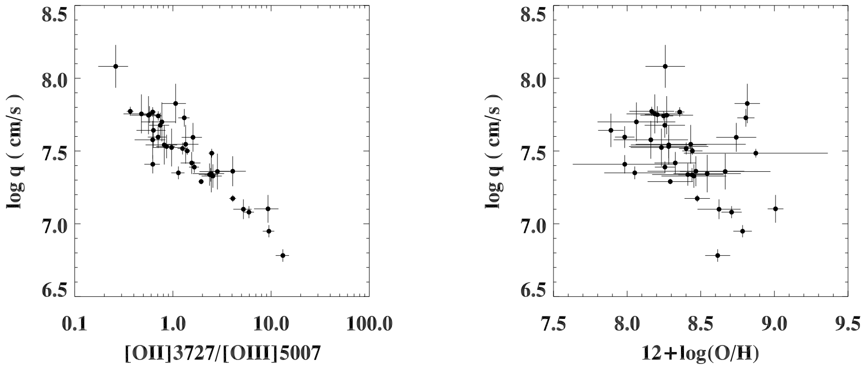

Figure 4.3: Left panel: the ionization parameter q vs. [OIII]λ3727/[OIII]λ5007. The ionization parameter decreases with the increase of [OII]λ3727/[OIII]λ5007. Right panel: the ionization parameter q vs. gas-phase oxygen abundance 12 + log (O/H). The ionization parameter shows a decreasing relationship with the metallicity.

spectra. The main parameter controling the attenuation by dust is the total effective V-band optical depth. We adopt 4 different values of extinction with $\tau_V = 0.2$, 0.5, 1.0, 1.5, which correspond to $E(B-V) = 0.07$, 0.14, 0.35 and 0.52.

The galaxies in our PEARS sample are located in the four ACS pointings in the GOODS-S field. The optical broadband *BViz* photometry is obtained from HST/ACS GOODS version 2.0 images (Giavalisco et al., 2004). The photometry is supplemented with the JHK-band data from ESO VLT/ISAAC observation (Retzlaff et al., 2010) and the U-band data from the MOSAIC camera (Capak et al., 2004). To fit with the BC03 model, we first subtract the contribution of the emission lines to the broad band photometry, and then fit with the model spectra at the exact redshift of the observed galaxy by minimum *chi*-square fitting. The ages of galaxies are constrained to be less than the age of the universe. To measure evolution in the relationship between mass and metallicity, we must demonstrate that there are no systematic differences in the stellar masses derived using different techniques. As a test, we compare our measurements with the stellar masses obtained using the

Markov Chain Monte Carlo (MCMC) technique by Pirzkal et al. (2012). We find very good agreement between the two methods measured stellar masses: the average fractional stellar mass difference is $\langle (M_{PEARS} - M_{Pirzkal})/M_{PEARS} \rangle = 0.04 \pm 0.06$. No systematic difference is found in the two techniques deriving stellar masses. Note that we derive stellar masses assuming a Salpeter stellar IMF, and divide by a factor of 1.8 to make it consistent with that derived from Chabrier (2003) IMF (Erb et al., 2006).

4.5 Results

In the previous sections we have measured metallicity, and stellar mass for our sample of PEARS emission-line galaxies. In this section, we study the luminosity-metallicity relation, mass-metallicity relation, morphology-metallicity relation and the SFR-metallicity relation and compare these relationships with those at different redshifts to provide important clues on the evolutionary state and the physical processes dominating the evolution of these galaxies.

The Luminosity-Metallicity Relation

Many previous studies (Lequeux et al., 1979; Garnett & Shields, 1987; Skillman et al., 1989; Vila-Costas & Edmunds, 1992; Zaritsky et al., 1994; Richer & McCall, 1995; Coziol et al., 1997; Kobulnicky & Zaritsky, 1999; Contini et al., 2002; Melbourne et al., 2002; Lilly et al., 2003; Kobulnicky & Kewley, 2004; Lamareille et al., 2004) focused on the luminosity-metallicity relation due to the difficulty of measuring the stellar mass. The L-Z relation spans 11 orders of magnitude in luminosity and 2 dex in metallicity. Important evolution with redshift in the slope and zero point of the relation is found from previous results, decreasing metallicity with increasing redshift at a given luminosity (Kobulnicky & Koo 2000; Shapley et al. 2004).

With our sample of 30 PEARS emission-line selected galaxies at $0.2 < z < 0.9$, we are trying to explore the evolution of the L-Z relation with redshift. Following the tradition we present the rest-frame absolute B-band magnitude as a measure of the luminosities. The restframe B-band absolute magnitudes are computed from the different bands photometries at different redshift bins, with the observed V-band which matches to the rest-frame B-band for redshift range $0.33 < z < 0.9$.

Figure 4 shows the relationship among the absolute rest-frame B magnitude versus the gas-phase oxygen abundance derived from R_{23} diagnostic indicator. We compare the relation we obtain for PEARS galaxies with the local L-Z relation obtained by Zahid et al. (2011) for SDSS galaxies at $z \sim 0.1$ (the solid line), with the L-Z relation obtained by Zahid et al. (2011) from 1350 DEEP2 emission line galaxies at z $\sim$ 0.8 (the dashed line), and with the L-Z relation obtained by Hu et al. (2009) from a sample of 31 Ultra-Strong Emission-Line (USELs) galaxies at $z = 0 - 1$ (the dotted line).

As we can see from Figure 4, the PEARS sample of 30 galaxies span a range in luminosity $–19 < M_B < –24$ and in metallicity $7.8 <$ 12+log(O/H) < 8.9. The red solid line shows the best linear fit of the mean of the PEARS galaxies in four magnitude bins, a relation of 12+log(O/H) $= (6.41 \pm 1.06) - (0.09 \pm 0.05) M_B$ with a correlation coefficient of –0.95. The objects show a prominent trend that metallicities increase with the brightening of the absolute B magnitudes. The SDSS galaxies with $\langle M_B \rangle$ = – 21 comparable to the average of the PEARS sample have $\langle$12+log(O/H)$\rangle$ = 9.0, $\sim$ 0.8 dex higher than that of the PEARS sample with $\langle$12+log(O/H)$\rangle$ = 8.2. We can see that the PEARS galaxies show a good match with the Hu et al. (2009) galaxies which are low metallicity galaxies selected by the ultra-strong emission lines and measured by the direct T_e method. We conclude that the big offset in the

L-*Z* relation with local and $z \sim 0.8$ samples is due to the selection of a sample of strong emission line galaxies.

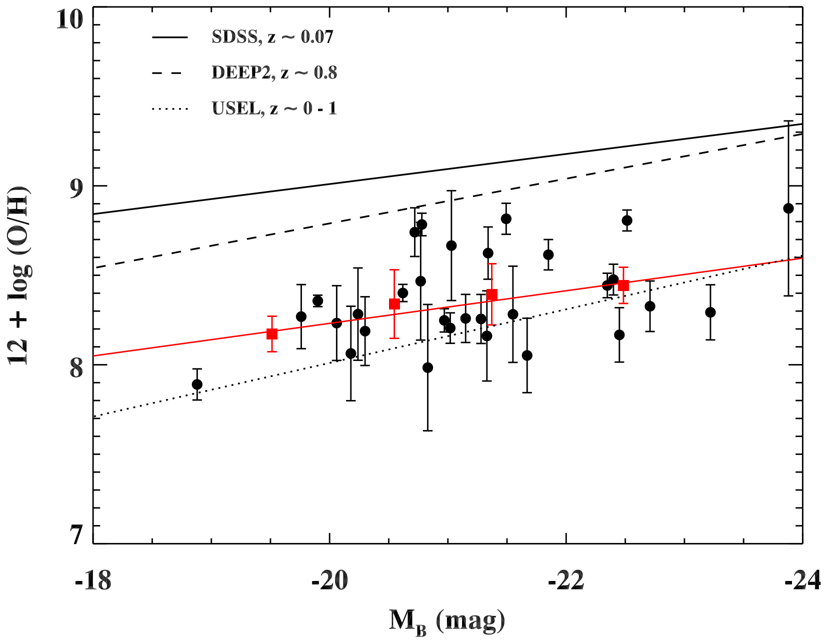

Figure 4.4: *L*-*Z* relation between the rest-frame *B*-band absolute magnitude versus the oxygen abundance for the 30 emission line galaxies at $0.2 < z < 0.9$. The metallicity is derived from the R_{23} indicator and the *x*-axis is the rest-frame *B*-band absolute magnitude. The solid line represents the relation obtained by Zahid et al. (2011) for SDSS star-forming galaxies at $z \sim 0.1$. The dashed line illustrates the relation obtained by Zahid et al. (2011) for DEEP2 galaxies at $z \sim 0.8$. The dotted line shows the relation obtained by Hu et al. (2009) for USEL galaxies at $z = 0 - 1$. The red solid line shows the best linear fit of the mean of the PEARS galaxies in four magnitude bins, a relation of $12+\log(\mathrm{O/H}) = (6.41 \pm 1.06) - (0.09 \pm 0.05)M_B$ with a correlation coefficient of –0.95. The PEARS sample shows an offset by ~ -0.8 dex in metallicity relative to the local relation at $z \sim 0.1$.

The Mass-Metallicity Relation

Figure 5 shows the relation between the stellar masses and the gas-phase oxygen abundances for the 30 star-forming galaxies in our sample at $0.2 < z < 0.9$. The solid line represents the *M*-*Z* relation obtained by Tremonti et al. (2004) for the local SDSS star-forming galaxies at $z \sim 0.1$. The uncertainties of the metallicities of the PEARS galaxies include the systematic errors, which arise from the blue-end over red-end flux ratio correction, and the errors due to the uncertainties in the line fluxes. All the presented data have been scaled to a Chabrier (2003) IMF and converted to the same metallicity calibration of Kobulnicky & Kewley (2004).

The PEARS sample spans the range 7.5 $<$log$M_*/\mathrm{M}_\odot < 10.5$ and $7.8 < 12 + \log(\mathrm{O/H}) < 8.9$, with the average values of $\langle \log(M_*/M_\odot) \rangle \sim 8.9$ and $\langle 12+\log(\mathrm{O/H}) \rangle = 8.3$. The sample shows a large scatter among metallicity and stellar mass. To understand the large scatter, the large offset to low metallicity relative to the local and similar redshift ones (Tremonti et al., 2004; Zahid et al., 2011), we study the relation between the metallicity and the physical properties of the galaxies such as broadband colors, morphologies, SFRs and SSFRs in the following subsections. Finally we will present the evolution of the *M*-*Z* relation by comparing the PEARS sample with other samples at different redshifts.

Metallicities and Broadband Colors

To study the different physical properties of galaxies in different regions on the mass-metallicity plot, we first plot out the $(B-V)$ vs. $(i-z)$ color-color diagram of these galaxies, which is shown in Figure 6. According to the positions of galaxies on the color-color plot and the mass-metallicity plot, we subdivide them into three different subsamples, bluest, low-metallicity and high-metallicity, which are shown as blue quadrangles, green triangles, and red dots in the figures.

The blue quadrangles represent 12 galaxies with lowest stellar masses, $7.5 < log(M_*/M_\odot) < 9.0$, and low metallicities, $8.0 < 12+\log(\mathrm{O/H}) < 8.5$ in Figure 5. These galaxies occupy the bluest region of color with $(B-V) < 0.7$ and $(i-z) < 0.2$ in Figure 6. For the remaining 18 galaxies, we divide them into two subsamples

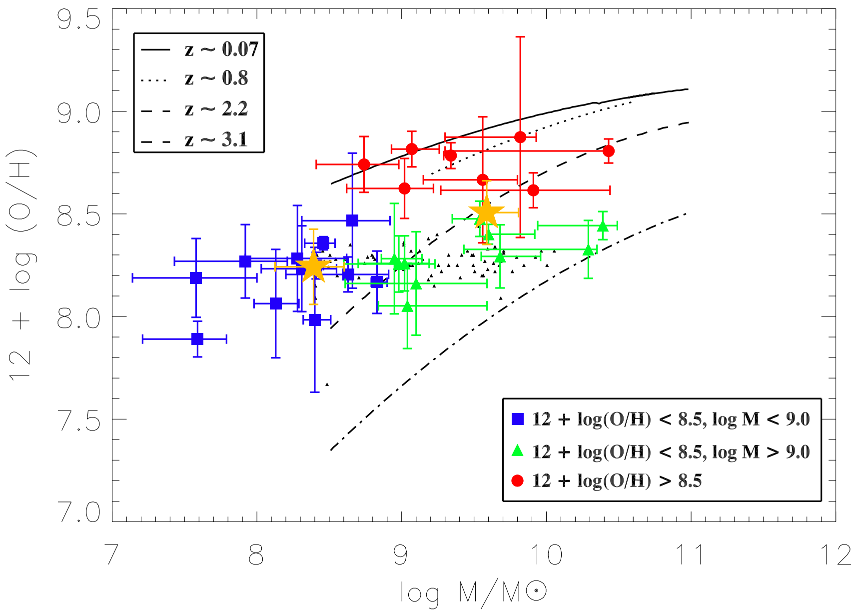

Figure 4.5: Relation between the stellar masses and the gas-phase oxygen abundances for PEARS galaxies at $0.2 < z < 0.9$. The metallicities are estimated from the R_{23} method and the stellar masses are estimated from the SED fitting with the $BC03$ model. The solid line represents the relation obtained for SDSS star forming galaxies at $z \sim 0.07$ (Zahid et al., 2011). The dotted line, dashed line and the dash-dotted line are the relations at $z \sim 0.8$ (Zahid et al., 2011), $z \sim 2.2$ (Erb et al., 2006) and $z \sim 3.1$ (Mannucci et al., 2009), respectively. The blue quadrangles represent galaxies with bluest colors, $(B-V) < 0.7$ and $(i-z) < 0.2$. The green triangles are the remaining galaxies with 12+log(O/H) < 8.5 and the red dots are the remaining galaxies with 12+log(O/H) > 8.5. The stars represent the mean of the galaxies in two mass bins: log $M_*/\mathrm{M}_\odot < 9.0$, log $M_*/\mathrm{M}_\odot > 9.0$.

according to the metallicities, 8 galaxies with 12+log(O/H) > 8.5 and 10 galaxies with 12+log(O/H) < 8.5.

The 8 galaxies with 12+log(O/H) > 8.5, show masses $> 10^9 M_{\cdot}$ spanning 2 dex. large range of galaxy stellar mass. This could be due to the different physical properties of these galaxies at their different evolutionary stages. As we can see from Figure 5 and Figure 6, the bluest galaxies are the less massive and metal-poor galaxies. With the colors getting redder, the masses and metallicities are getting higher. The subsample, low-metallicity galaxies with intermediate stellar masses, show much bluer color $(B-V)$ than the high-metallicity subsample. The subsample of galaxies with bluest colors have also the youngest ages. Figure 7 shows the stellar population age distribution as a function of the metallicity, i.e., mass. The ages of the bluest galaxies extend to 10 Myr. The galaxy, which shows blue color, low metallicity and an old age of 10 Gyr, may be due to the old stellar population and a recent starburst arising from the accretion of less enriched gas. The average age of the blue galaxies is $\sim$ 300 Myr, much younger than that of the more massive red galaxies with an average of $\sim$ 3 Gyr. It is shown that these blue and low metallicity galaxies are young dwarf galaxies. The separation in the color-color diagram and the M-Z relation demonstrates the different physical properties of the galaxies at different evolutionary stages. Next we will combine the information of the morphologies of galaxies and the SFRs of galaxies to continue the study of the mass-metallicity relation of our PEARS sample.

Metallicities and Morphologies

As shown in Figure 8, we put the HST/ACS GOODS *i*-band images of the sample of galaxies together in the similar order of their positions on the mass-metallicity plot. The masses of galaxies increase from left to right and the metallicities increase from bottom to top. The lower two rows are galaxies with metallicities on the lower branch and the upper one row is that of galaxies with higher metallicities. We can see clearly from the images that, the metal-poor galaxies all show compact morphologies, some with companions and some in irregular shapes (the lower two rows). The metal-rich galaxies in the top row and the massive galaxies at the most right column show spiral-like and disturbed morphologies. The compact core of the low mass and low metallicity galaxies can denote the AGN contribution. Trump et al. (2011) present a sample of ELGs at $z \sim 2$ and uses the [OIII] spatial profile and

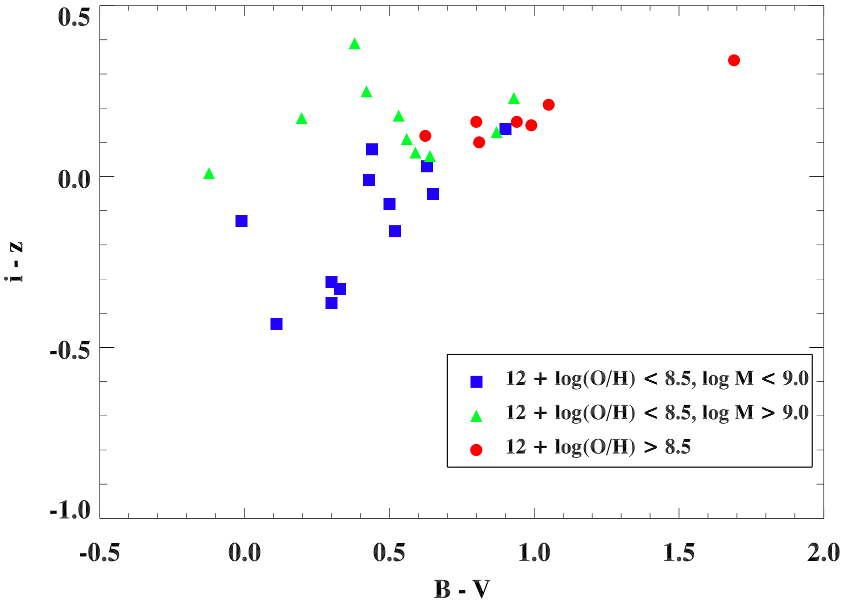

Figure 4.6: The color-color diagram, $(B-V)$ vs. $(i-z)$, for the 30 emission-line galaxies. The blue quadrangles represent galaxies with bluest colors. The green triangles are the remaining galaxies on the lower branch. The red dots are the remaining galaxies on the upper branch. The galaxies with different masses and metallicities have clearly different colors. With the increase of the galaxy stellar masses and metallicities, the galaxy colors get redder, which is consistent with galaxy evolution.

stacked X-ray data to show that some low mass low metallicity galaxies may harbor weak AGNs.

The morphologies of the galaxies in the sample are studied quantitatively with the Gini coefficient *G*, which quantifies the relative distribution of the galaxy's flux, and the second-order moment of the brightest 20% of the galaxy's flux (Abraham et al., 2003; Lotz et al., 2004), M_{20} from the galaxy images. Figure 9 shows the distribution of the galaxies in the G-M_{20} plane with the empirical line dividing normal galaxies with merger/interaction galaxies (Lotz et al., 2004). The blue stars represent that measured from GOODS *B*-band image and the red triangles show that measured from GOODS *i*-band image. We can see that from the *B*-band im-

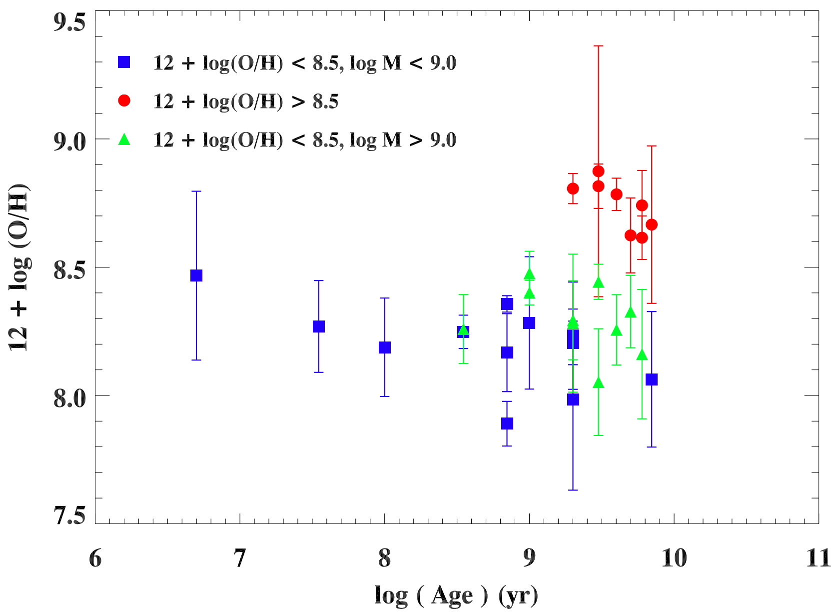

Figure 4.7: The metallicity as a function of the stellar population age obtained from SED fitting. The symbols are the same as that defined in Figure 6 and 7. The figure shows clear seperation between the bluest low metallicity galaxies and the redder galaxies. The galaxies with bluest colors have an average age of $\sim$ 300 Myr compared with the more massive red galaxies of $\sim$ 3 Gyr.

age, all of the galaxies lie above the dashed line, which is the region of the outlier galaxies showing merger/interaction and dwarf/irregular morphologies. From the *i*-band image, all of the galaxies are on, above and very close to the empirical discriminating line too. Since larger *G* coefficient corresponds to higher concentration, the systematically higher Gini coefficients *G* from the *B*-band images demonstrate more compact distribution of the star-forming regions. At the same time, the half light radii of the galaxies are shown in Table 3, with an average of 1.6 kpc, showing compact morphology. Hence, the PEARS ELGs show disturbed compact morphologies with interacting companions and tidal features, which demonstrate the ongoing active star-formation in these galaxies.

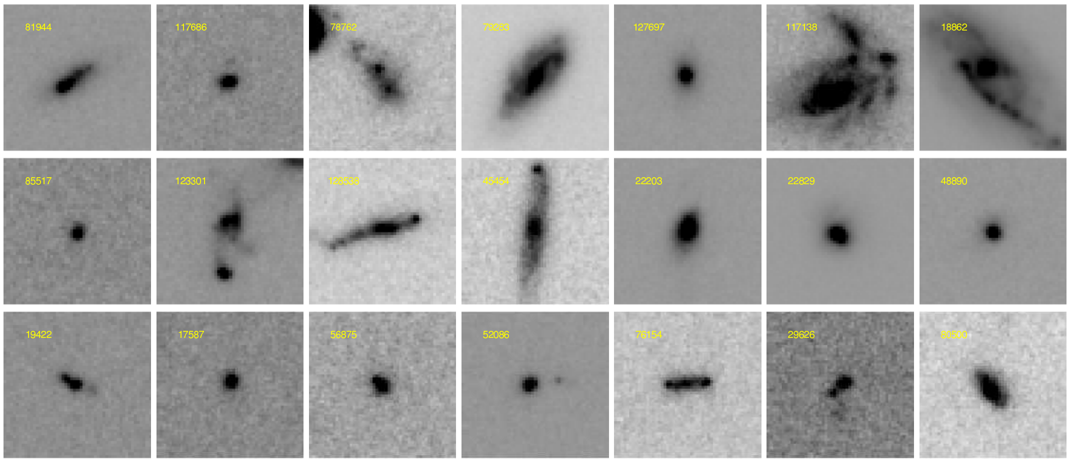

Figure 4.8: The HST/ACS GOODS *i*-band images with a size 1.″53×1.″53 of the PEARS star-forming galaxies. The images are put in the similar order of galaxies in the mass-metallicity plot. The masses of galaxies increase from left to right and the metallicities increase from bottom to top.

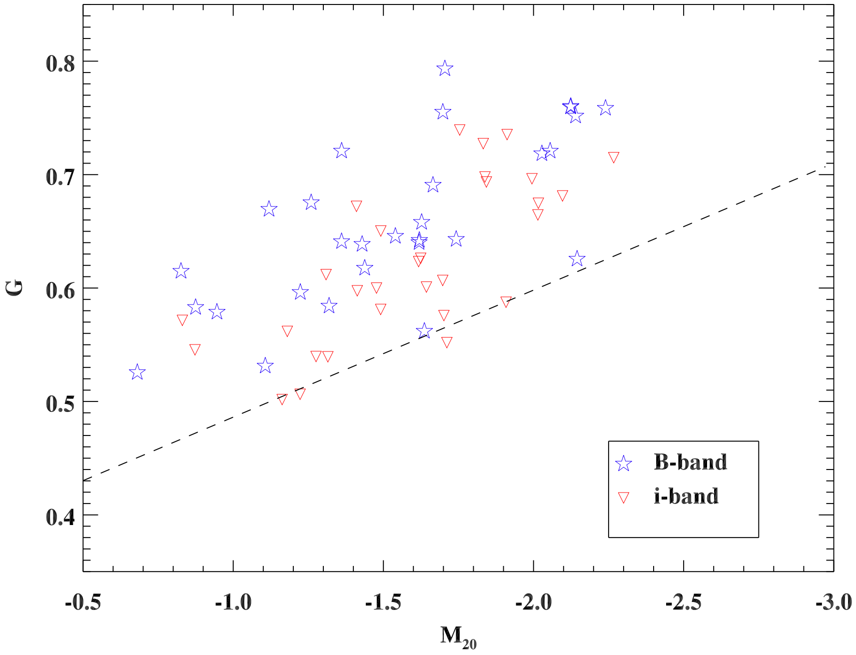

Figure 4.9: Gini coefficient *G* vs. M_{20} to demonstrate the morphology analysis of the 30 galaxies in the sample. The dashed line is the empirical line dividing interacting galaxies (upper region) with normal galaxies (lower region) from Lotz et al. (2004). The blue stars represent galaxies based on *B*-band image analysis. The red triangles are that based on *i*-band image analysis. Most galaxies lie above the line demonstrating interacting/disturbed morphologies.

Metallicity and Star Formation Rate

We compute the galaxy star formation rates by the dust extinction corrected Hβ emission line fluxes using the conversion given by Kennicutt (1998). Figure 10 shows the galaxy metallicity as a function of the SFR. The galaxy SFRs are tabulated in Table 3 and span a range 0.1 – 20 $M_\odot/yr$ and do not show a tight relation. This is likely due to the selection of our sample by strong emission line fluxes spanning a wide mass range. The galaxy specific star formation rates (SSFRs) are calculated by SFR/M_* (in unit of yr^{-1}). Figure 11 shows the galaxy gas-phase abundances as a function of the SSFRs. We compare this relationship with that obtained by Mannucci et al. (2010), which are plotted as the lines in Figure 11. The solid, dotted, dashed, and the dash-dotted lines are the fits for four values of $\log M_* =$ 9.4, 9.7, 10 and 10.9. For comparison, we split our sample into two mass bins, $\log M_* < 9.0$ and $9.0 < \log M_*$, which is approximately close to the bins used in Mannucci et al. (2010). The two subsamples are shown as blue quadrangles, and green triangles in Figure 11. As we can see from Figure 11, all of our PEARS galaxies have high SSFRs $10^{-10} <$ SSFR $< 10^{-7}/yr$, which extends to 2 order of magnitudes higher SSFRs than Mannucci et al. (2010) for SDSS galaxies with $10^{-12} <$ SSFR $< 10^{-9}/yr$. For specific mass bins, we do not see a prominent trend as that shown by Mannucci et al. (2010). Since the SFRs of the galaxies do not show significant relation with galaxy stellar masses or metallicities from Figure 11, the relation between the SSFRs with the metallicities is basically due to the change of the mass with metallicities.

Evolution of the Mass-Metallicity Relation

Figure 5 illustrates the M-Z relations obtained from other studies. To ensure the consistency of the comparison, the conversions given by Kewley & Ellison (2008)

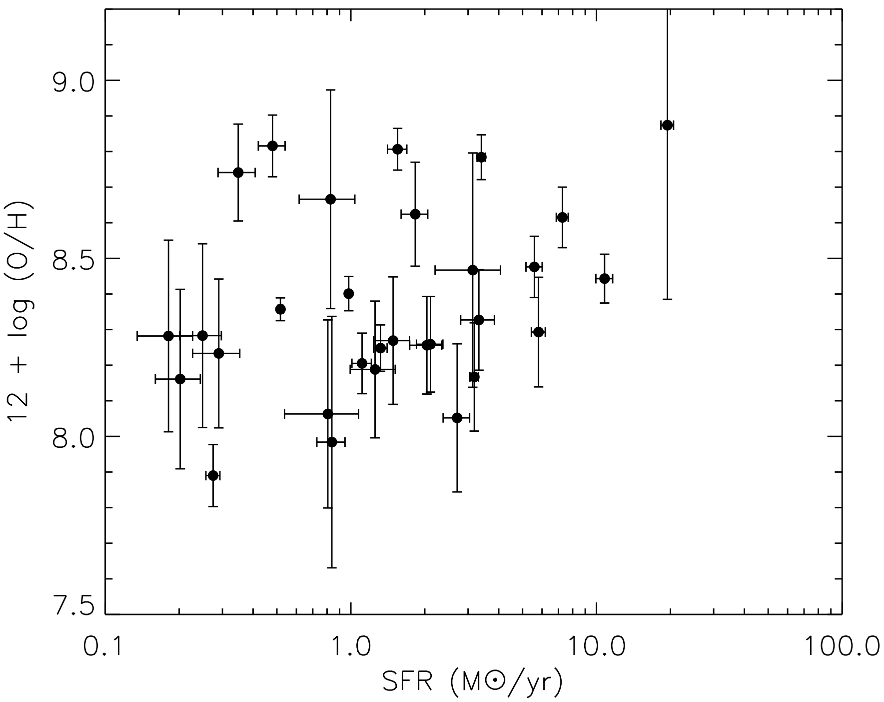

Figure 4.10: The galaxy oxygen-phase abundances as a function of the SFR. The galaxy SFRs span a range 0.1 – 10 $M_{\odot}/yr$ and do not show a tight relation with metallicity.

are used to correct the differences arising from different calibrations used (Zahid et al., 2011). In Figure 5, the solid line represents the M-Z relation at $z \sim 0.1$ from Zahid et al. (2011) for the local SDSS galaxies. The dashed line shows the M-Z relation at $z \sim 0.8$ for the 1350 DEEP2 galaxies from Zahid et al. (2011). The dotted line and the dash-dotted line are that at $z \sim 2.2$ from Erb et al. (2006) and at $z \sim 3.1$ from Mannucci et al. (2009), respectively. The black dots illustrate the sample of the "green peas" from Amorin et al. (2010). The metallicities of the green peas are recalculated by the R_{23} method.

As seen in Figure 5, the PEARS galaxies show a large scatter and offset as compared to the local M-Z relation. At the intermediate and low mass end, the SDSS galaxies with comparable mtallicity, $\langle$12+log(O/H)$\rangle$ = 8.2, have $\langle \log(M_*/M_{\odot}) \rangle \sim$

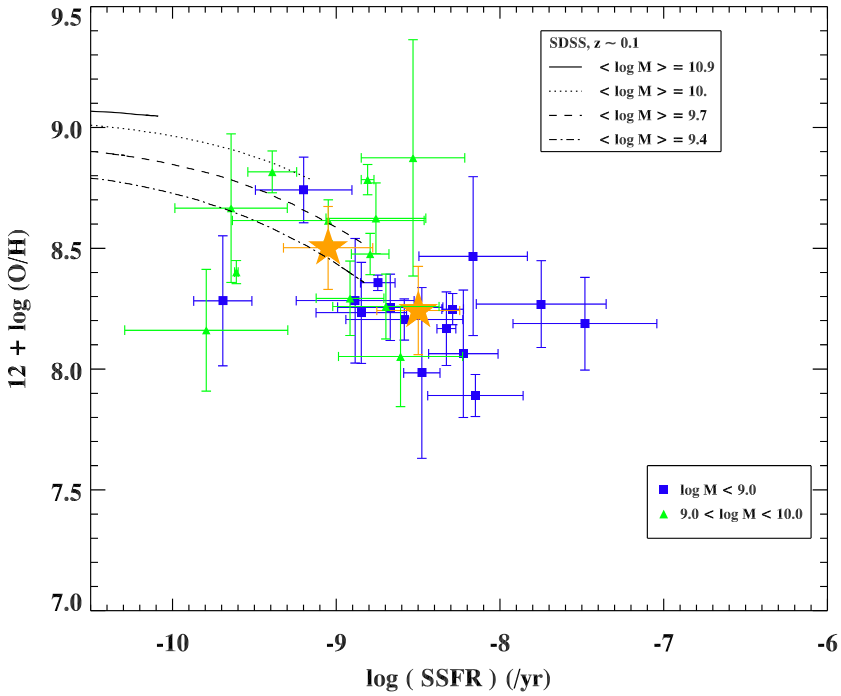

Figure 4.11: The galaxy gas-phase oxygen abundance versus the specific star formation rates. From top to bottom, the solid, dotted, dashed, and dash-dotted lines represent the fits for four values of $\log M_* = 9.4$, 9.7, 10 and 10.9 by Mannucci et al. (2010) from SDSS galaxies. The blue quadrangles, and the green triangles show the PEARS galaxies with $\log M_* < 9.0$, and $\log M_* > 9.0$. The PEARS galaxies extends to much higher SSFRs values, $10^{-10} < \mathrm{SSFR} < 10^{-7}/yr$, than that of the SDSS galaxies. The mean of the PEARS galaxies in the two mass bins show higher SSFRs of lower metallicities, same trend as that shown by SDSS galaxies.

7.5 which is around 2 order lower than the PEARS sample. In other words, the SDSS galaxies with comparable stellar mass to the average of the PEARS sample, $\log(M_*/M_\odot) \sim 9.1$, have $12+\log(O/H) \sim 8.8$, ~ 0.5 dex higher than the average of the PEARS galaxies. The low metallicity galaxies basically fall on the relation at $z \sim 2.2$ and $z \sim 3.1$. Combining with the physical properties of compact morphologies, small sizes, bluest colors, and high SSFRs of the PEARS galaxies, it is demonstrated that an emission-line selected sample such as ours is biased to select the young, compact, star-forming galaxies, and resembling the local green peas and

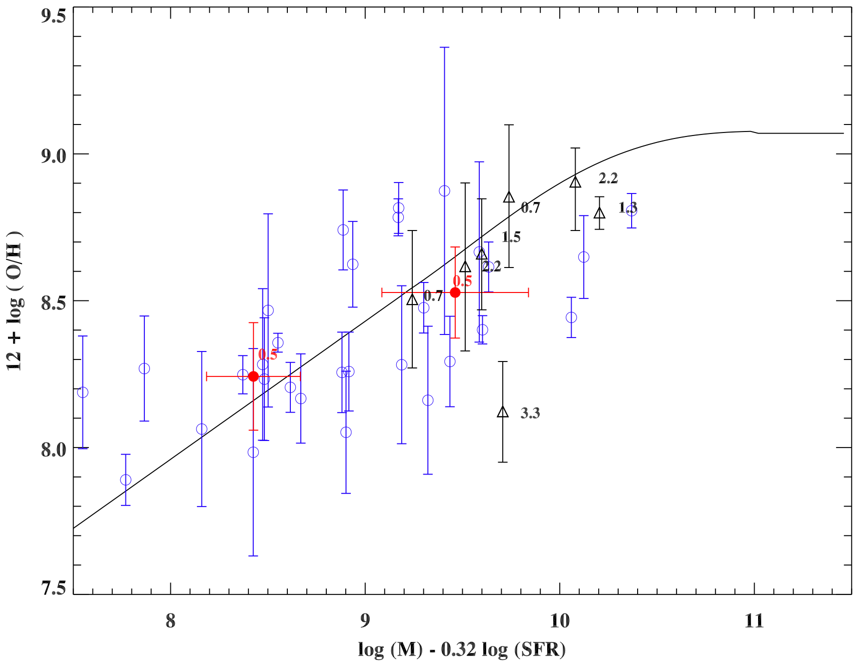

Figure 4.12: The projection of the PEARS ELGs on the FMR plane defined from local SDSS. The black empty triangles represent the projections of the galaxy samples at different redshifts upto z∼3.3. Mannucci et al. (2010) showed no evolution of galaxies on the FMR plane. Our PEARS galaxies follow well the FMR plane and shows no evolution of the FMR plane at z∼0.5 for low mass and metal poor galaxies.

LBG analogs with SSFR$> 10^{-9} yr^{-1}$ (Hoopes et al., 2007; Overzier et al., 2008; Amorin et al., 2010), which are found to be metal-poor by ~ 0.5 dex relative to other galaxies of similar stellar mass.

Mannucci et al. (2010) defined a fundamental metallicity relation (FMR) by including the SFR as a third parameter and showed that there is no evolution of the FMR for galaxies upto z∼2.5 (Cresci et al., 2011). The FMR investigates the relationship between the metallicity, 12+log (O/H), and $\mu_{0.32} = \log(M/M_{\odot}) - 0.32 \log(SFR)$, which minimizes the scattering due to the SFRs. We project the PEARS galaxies to the FMR plane in figure 12. The PEARS galaxies follow well the FMR defined by local SDSS galaxies though the trend of expected higher SFRs for lower metallicity galaxies is not obvious from figure 10. The red dots show the mean of the PEARS galaxies at the two mass bins.

4.6 Origin of the Mass-Metallicity Relation

The origin of the mass-metallicity relation is explained either by the "downsizing" scenario, which means that low mass galaxies evolve later and on longer time scales and thus are less enriched (Cowie et al. 1996; Kobulnicky et al. 2003), or by the preferential metal loss in low mass galaxies via galactic wind due to the shallower gravitational potential (Larson 1974, Tremonti et al. 2004, Lamareille et al. 2004, Saviane et al. 2008). To investigate the two effects, we study the gas mass fraction, effective yield, and the galaxy chemical evolution models.

Gas Fraction

By the extinction corrected Hβ line luminosity, we are able to estimate the SFR by the Schmidt star formation law (Kennicutt, 1998). Peeples et al. (2011) show that the gas masses estimated from the KS law roughly agrees with the total cold gas masses for the low gas fraction f_g ∼0.1, most massive logM$_\odot \sim$ 11 galaxies. The disagreement is over an order of magnitude for dwarf galaxies since the KS law traces star-forming molecular gas than atomic gas (Leroy et al., 2008). In spite of the absence of the calibration of gas density versus SFR for low mass galaxies at high redshift, we extend KS law assuming that the law holds for high redshift galaxies in the mass range that we are studying. The gas surface density is derived by the Schmidt-Kennicutt law (Kennicutt, 1998; Bouche et al., 2007) from the star formation rate surface density with the half-light radius adopted as the galaxy size. The derived SFR densities are between 0.1 and 10 M$_\odot$/yr/kpc^2, which is in general agreement with that at $z \sim 0$ (Kennicutt, 1998), $z = 2.2$ (Erb et al., 2006) and $z = 3.1$ (Mannucci et al., 2010). The gas densities are between 100 and 1000 M$_\odot$/pc^2, in the similar range from previous studies for LBGs and ULIRGs (Coppin et al., 2007; Tacconi et al., 2006; Mannucci et al., 2010). With the galaxy stellar mass derived from the SED fitting, we compute the gas mass fraction $\mu = M_{gas}/(M_{gas}+M_{star})$.

$$SFR(H\beta)(M_{\odot}yr^{-1}) = 2.8 \times 7.9 \times 10^{-42} L(H\beta)(ergs^{-1}) \tag{4.5}$$

$$\Sigma_{SFR} = 2.5 \times 10^{-4} (\frac{\Sigma_{gas}}{1M_{\odot}pc^{-2}})^{1.4} M_{\odot}yr^{-1}kpc^{-2} \tag{4.6}$$

Figure 13 shows the gas fraction as a function of the stellar mass. The solid blue circles represent the PEARS sample at $\langle z \rangle = 0.5$ and the open red circles demonstrate the LSD sample at $z \sim 3.1$ from Mannucci et al. (2010). The dashed line shows the gas fraction derived with a constant SFR = 1.5 M$_{\odot}$/yr of the median value of the PEARS sample and the median galaxy size of the sample $r_{hlr} = 1.5kpc$. The gas fraction of the PEARS sample ranges from 90% to 10%. The line shows a consistent fit to the sample with a small scatter, due to the limited range of the SFRs and the galaxy sizes. The PEARS galaxies show much smaller gas fraction compared to the $z \sim 3.1$ galaxies at a fixed stellar mass. This is because the gas mass is proportional to the SFR and the SFR of LBGs is higher by a factor of 10.

Effective Yield

In the frame of the instantaneous recycling closed-box chemical evolution model, i.e., no inflows or outflows, the metallicity is simply related to the stellar yield y and gas mass fraction μ as, (Tinsley 1980; Edmunds 1990)

$$Z = y_{\odot} ln(\frac{1}{\mu}) \tag{4.7}$$

Assume the stellar yield is constant (Garnett 2002; solar yield $y_{\odot} = 0.0126$, Asplund et al. 2004), we derive the effective yield, y_{eff}, from the measurements of the gas mass fraction μ and the gas-phase metallicity Z. The difference between the effective yield and the true yield is able to tell the effects of the inflows, such as through

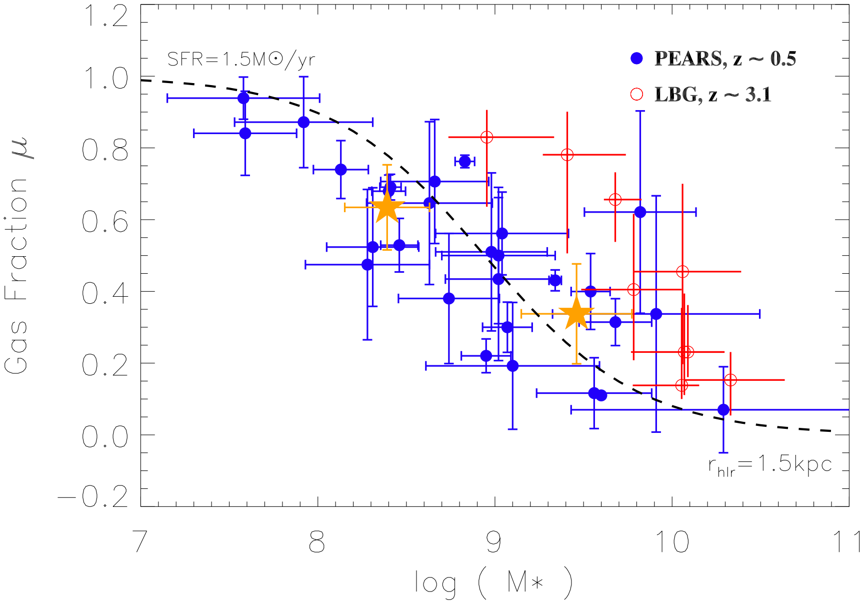

Figure 4.13: The relationship between the gas fraction and the stellar mass. The gas fractions are derived from the Schmidt law. The solid circles represent the PEARS galaxies. The open circles are the LSD galaxies at $z \sim 3.1$ from Mannucci et al. (2010). The dashed line shows the expected gas fraction with a constant SFR of 1.5 $M_{\odot}/yr$ and half-light radius of 1.5 kpc, which are the mean values for the PEARS sample. The magenta stars show the average of the galaxies in two mass bins: $\log M_{*} < 9.0$, and $\log M_{*} > 9.0$.

merging episodes and cold gas accretion, and outflows, such as the SN explosion and galactic wind. The effects of both inflows and outflows will decrease Z while inflows of pristine gas will increase the gas fraction μ and the outflows of enriched materials will decrease μ.

In Figure 14 we plot the effective yield as a function of the stellar mass. While the SDSS galaxies (Tremonti et al., 2004) (solid line) show that, lower mass galaxies have lower y_{eff}, which is explained as the consequence of the stronger depletion of metals by outflows in the shallower gravitational well of the lower mass galaxies, the PEARS galaxies at $\langle z \rangle \sim 0.5$ show an opposite trend, which is similar to that of samples at $z \sim 2.2$ (Erb et al., 2006) (cyan triangles), and $z \sim 3.1$ (Mannucci et al., 2010) (green up triangles). With the effective yield decreasing with the increased stellar mass, these samples demonstrates different physical processes of these samples compared to the $z \sim 0$ SDSS sample. The sample falls in the same region with the $z \sim 3.1$ LBG galaxies, extends to low mass galaxies with high effective yields, and shows offset with the samples at $z \sim 0.8$ and $z \sim 2.2$. Due to the effect of infalls and outflows, the effective yield at gas-rich systems may reveal the lower limit of the true yield. From Figure 14, we can derive the lower limit of the true yield $y \approx y_{\odot}$.

The study by Dalcanton (2007) shows that the metal-enriched outflows are the only mechanism that can significantly reduce y_{eff} for gas-rich systems while little effect to a gas-poor system, and subsequent star formation drives the effective yield back to the closed-box value. The results of that study is able to interpret the observed average relation between the effective yield and the gas fraction for the local SDSS galaxies. The high values of y_{eff} with large error bars for the two low mass galaxies are due to the high estimated gas fraction and then the high SSFRs. We will examine the effect of outflows in the next subsection.

Inflow and Outflow

The difference between the derived effective yield and the true yield suggests the deviation from the assumption of the closed-box model with no inflows or outflows. In the assumption of instant recycling and mixing, we follow the model introduced by Erb (2008) with infalls and outflows, and reproduce the y_{eff} on gas fraction μ by fitting the amount of inflow f_i and outflow f_o in unit of the SFR of the galaxy.

Figure 15 shows the metallicity as a function of the gas fraction in each mass bin. Three true yield $y = 0.6y_{\odot}, y_{\odot}, 1.5y_{\odot}$ are adopted in the fitting with the models. We fit the data both with the model in Erb et al. (2006) of purely outflows

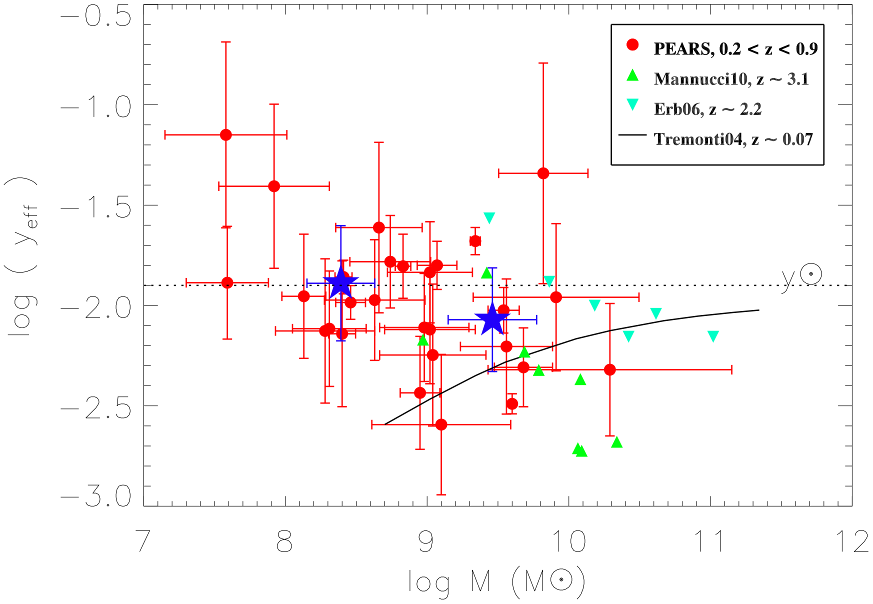

Figure 4.14: The effective yield as a function of the galaxy stellar mass. The red dots represents the PEARS galaxies at 0.2< z <0.9. The orange filled stars are the average of the effective yield in the mass bins of $logM < 9.0$, and $logM > 9.0$. The solid line, the dashed line, the cyan triangles, and the green triangles show the relations obtained from the samples at $z \sim 0.1$ (Tremonti et al., 2004), $z \sim 2.2$ (Erb et al., 2006), and $z \sim 3.1$ Mannucci et al. (2010), respectively.

(left panels) and with the model in Erb (2008) with both inflows and outflows (right panels). The lines in each panel correspond to different outflow rates: 0, 0.5, 1, 2, 4, 6×SFR from top to bottom. The model with outflow rate $\sim 0.8\times$SFR for massive galaxies and $\sim 0.2\times$SFR for low mass galaxies, and solar yield $y_\odot$ gives best fit to the data. The best fit values of f_i and f_o with the inflow and outflow model for the three yields are shown in the right panels. The model of $y = y_\odot$, $f_i = 1$ and $f_o = 0.1$ gives best fit to our data. From Figure 15 we can see that, for galaxies with lower gas fraction, i.e. more massive galaxies, the sample dots can be fit well either with both low true stellar yield $y = 0.8\, y_\odot$ without outflows, or with high true stellar yield $y = y_\odot$ and high inflow and outflow rates $f_i = 1$, and $f_o = 0.1$, these two effects are degenerate and are easily understandable. Models with an infall rate of $f_i = 1$

and different outflow rates with different true stellar yields are fitted also, which are shown as the dotted lines in the right panels and the corresponding best fit values marked on the left bottom corner. For true stellar yield $y = 1.5y_{\odot}$, the best fit gives an infall rate $f_i = 0.1$ and an outflow rate $f_o = 2.9$, which estimate a sharp increase of metallicity at low gas fraction, i.e. massive galaxies, which is not consistent with the M-Z relation. To determine the physical mechanisms in different mass galaxies in chemical evolution, the high mass galaxies with low gas fraction plays an important role in distinguishing them.

4.7 Summary

We have presented the relationship between the gas-phase oxygen abundances, stellar masses, rest-frame *B*-band absolute magnitudes, morphologies, and SSFRs for a unique sample of 30 emission-line selected galaxies from the HST/PEARS grism survey at $0.2 < z < 0.9$. The PEARS emission-line galaxies span the absolute magnitude range $-19 < M_B < -24$, galaxy stellar masses $7.5 < log(M_*/M_{\odot}) < 10.5$, and gas-phase oxygen abundances $7.8 <$ 12+log(O/H) < 8.9. The principle conclusions from this study are:

1. The *L-Z* and the *M-Z* relations of the PEARS ELGs at $\langle z \rangle \sim 0.5$ show that galaxies with brighter M_B and larger M_* have higher oxygen abundance. The *L-Z* relation of this sample is offset by ~ -0.8 dex in metallicity at given absolute magnitude relative to the local and the $z \sim 0.8$ *L-Z* relations. The *M-Z* relation shows a big offset by ~ -0.5 dex in metallicity at given stellar mass.

2. The scatter of the galaxies on the *M-Z* relation is basically due to the different evolutionary stages and the different physical properties of the galaxies. The high metallicity PEARS galaxies show spiral morphologies, red colors and

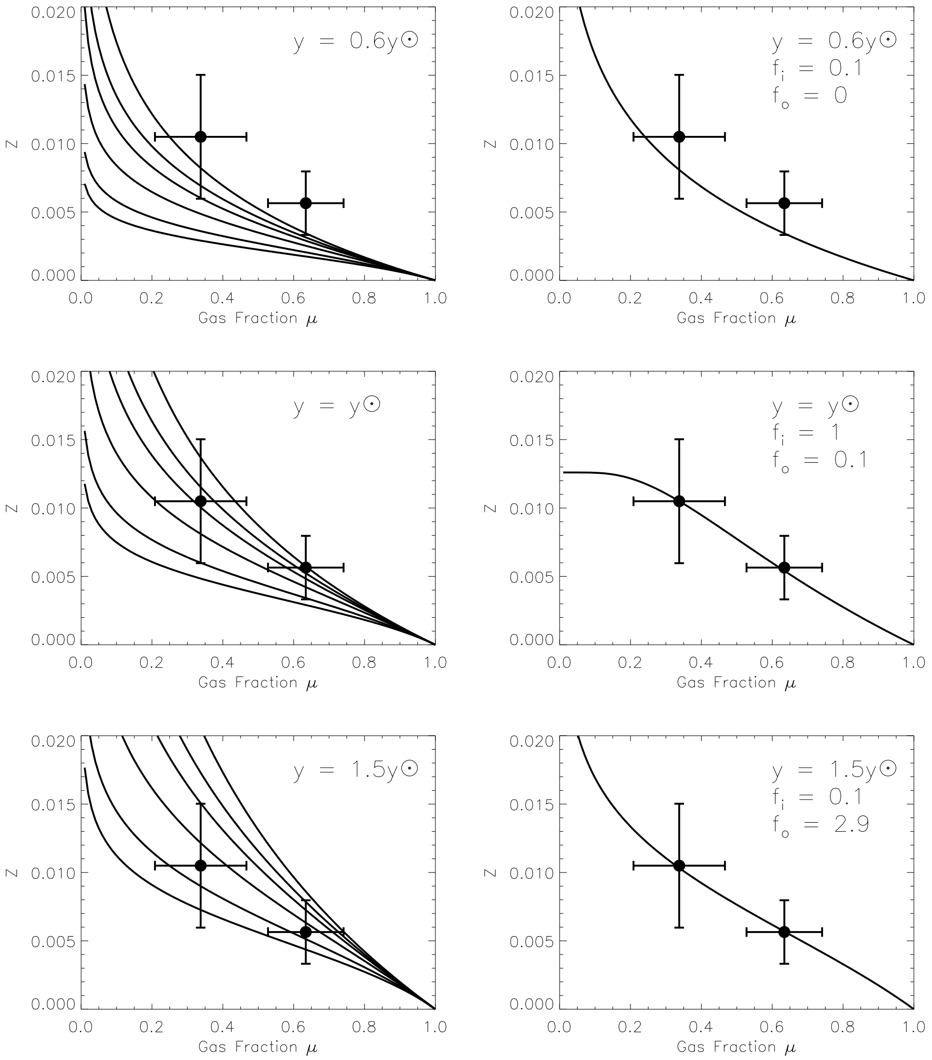

Figure 4.15: The metallicity as a function of the gas fraction. The dots are the means of the galaxies in the mass bins previously defined. We fit by the outflow model in Erb et al. (2006) (left panels) and the model in Erb (2008) with both inflows and outflows (right panels). The panels from top to bottom show the the fitting with different true yields adopted: y = 0.6y$_\odot$, y$_\odot$ and 1.5y$_\odot$. The lines in each panel are corresponding to different outflow rates: 0, 0.5, 1, 2, 4, 6×SFR from top to bottom. The model with outflow rate $\sim$ 0.8×SFR and yield y$_\odot$ gives best fit to the data. The best fit values of f_i and f_o with the inflow and outflow model for the three yields are shown in the right panels. The model of y = y$_\odot$, f_i = 1 and f_o = 0.1 gives best fit to our data. To determine the physical mechanisms in different mass galaxies in chemical evolution, the high mass galaxies with low gas fraction plays an important role in distinguishing them.

large masses. The low metallicity PEARS galaxies have low masses, blue colors, compact disturbed morphologies, and high SSFRs.

3. The big offsets in the *L*-*Z* and the *M*-*Z* relations of the PEARS ELGs demonstrate that the high EW emission line galaxies have low metallicities, low mass, blue, young, compact disturbed morphologies, and high SSFRs (SSFR $>$ $10^{-9} yr^{-1}$), which is similar the LBGs, the "green peas" (Hoopes et al., 2007; Cardamone et al., 2009; Amorin et al., 2010), and other emission-line selected galaxies at different redshifts.

4. One possible physical origin of the big offsets in the *L*-*Z* and the *M*-*Z* relations of the PEARS ELGs is the downsizing effect, i.e. the galaxies are at their early evolutionary stages with high gas fraction, which have not yet been converted into stars. The projection of the PEARS galaxies on the FMR plane, which removes the scatter due to SFRs, shows no evolution for the $\langle z \rangle \sim$0.5 PEARS low-mass metal-poor galaxies, which may denote similar chemical enrichment process as most galaxies.

5. Another possible physical mechanism resulting in the big offsets in the *L*-*Z* and the *M*-*Z* relations of the PEARS ELGs could be the effect of the interaction-induced metal-poor infalls and SNe driven metal-rich outflows. On fitting a chemical evolutionary model with inflows and outflows, we get a best fit model with solar yield y = $Z_\odot$ and a dominant inflow of 1×SFR and an outflow rate of 0.1×SFR. The gas fractions derived from the local K-S law may introduce uncertainties to the results of the true stellar yield and the estimation of the inflow and outflow rates from the model.

This paper includes data gathered with the 6.5 meter Magellan Telescopes located at Las Campanas Observatory, Chile. PEARS is an HST Treasury Program 10530 (PI: Malhotra). Support for program was provided by NASA through a grant

from the Space Telescope Science Institute, which is operated by the Association of Universities for Research in Astronomy, Inc., under NASA contract NASA5-26555 and is supported by HST grant 10530.

Table 4.1: The observed emission line fluxes (in 10^{-18}ergs s^{-1}cm^{-2}) for 55 galaxies observed with Magellan LDSS-3 and 35 galaxies observed with IMACS. Within the 90 galaxies, 13 galaxies have auroral line [OIII]λ4363 measurements with S/N $>$ 2, and 28 galaxies with $z < 0.35$ have line fluxes of Hα and [NII]λ6584 observed in the spectra.

PEARS ID	z	$E(B-V)$	[OII]3727	[OIII]λ4363	Hβ	EW([Hβ])	[OIII]λ4959	[OIII]λ5007	Hα	[NII]6584
12250	0.339	0.400	35.97 ± 11.99	–	16.74 ± 5.58	43	20.86 ± 5.37	75.42 ± 9.00	37.24 ± 15.01	2.41 ± 5.07
12665	0.128	0.300	9220.11 ± 3073.37	–	96.00 ± 3.82	32	164.57 ± 4.04	518.12 ± 7.17	221.98 ± 5.82	19.02 ± 5.44
13541	0.373	0.270	263.87 ± 12.84	–	83.14 ± 6.30	16	61.05 ± 5.85	129.91 ± 8.31	–	–
15116	0.335	0.400	178.65 ± 59.55	–	20.71 ± 2.24	143	44.51 ± 2.41	139.28 ± 3.87	33.44 ± 9.88	0.15 ± 2.80
17587	0.645	0.050	25.23 ± 8.41	–	15.54 ± 5.18	23	19.00 ± 4.94	36.71 ± 7.07	–	–
18862	0.203	0.400	293.71 ± 37.65	17.62 ± 5.28	115.33 ± 6.43	12	12.09 ± 4.03	66.76 ± 5.85	150.44 ± 12.55	16.18 ± 5.40
19422	0.551	0.130	30.82 ± 10.19	–	21.79 ± 4.54	51	23.37 ± 4.63	88.49 ± 8.22	–	–
19639	0.281	0.400	712.33 ± 27.82	10.85 ± 4.90	181.54 ± 6.10	11	31.23 ± 7.63	112.66 ± 8.74	287.06 ± 15.66	43.28 ± 5.68
20201	0.450	0.130	28.11 ± 9.37	10.68 ± 2.73	45.09 ± 2.34	512	96.19 ± 2.37	302.47 ± 4.39	–	–
22203	0.281	0.050	422.89 ± 46.40	–	122.15 ± 3.06	33	120.01 ± 3.12	384.72 ± 5.01	316.88 ± 6.36	14.73 ± 3.73
22829	0.561	0.130	270.89 ± 8.01	–	97.16 ± 6.32	24	70.76 ± 5.85	191.28 ± 9.95	–	–
26909	0.683	0.270	109.08 ± 9.74	–	62.18 ± 2.29	86	115.18 ± 4.50	330.78 ± 7.08	–	–
29057	0.365	0.270	90.79 ± 14.66	–	33.02 ± 2.53	46	43.72 ± 2.69	118.22 ± 4.95	–	–

Continued on Next Page…

Table 4.1 – Continued

PEARS ID	z	$E(B-V)$	[OII]3727	[OIII]λ4363	Hβ	EW([Hβ])	[OIII]λ4959	[OIII]λ5007	Hα	[NII]6584
29626	0.854	0.050	26.91 ± 8.97	–	21.25 ± 2.65	113	37.89 ± 3.23	114.53 ± 5.45	–	–
29968	0.605	0.300	32.06 ± 5.50	–	25.07 ± 3.06	24	50.80 ± 3.92	92.76 ± 4.79	–	–
31362	0.667	0.270	16.26 ± 3.59	6.86 ± 3.10	35.60 ± 2.76	168	87.88 ± 3.32	217.28 ± 7.60	–	–
37690	0.365	0.130	20.58 ± 6.86	–	10.04 ± 1.95	12	10.92 ± 2.00	35.29 ± 4.22	34.98 ± 11.46	-0.84 ± 4.01
43170	0.688	0.400	16.08 ± 5.36	–	11.58 ± 2.08	32	30.49 ± 2.75	90.35 ± 5.14	–	–
45223	0.666	0.400	53.98 ± 8.36	–	13.19 ± 2.50	47	25.87 ± 2.69	67.92 ± 7.20	–	–
45454	0.424	0.050	18.42 ± 6.14	–	10.12 ± 2.09	17	10.30 ± 1.90	33.62 ± 3.00	–	–
46994	0.667	0.270	130.05 ± 13.12	6.08 ± 2.75	35.64 ± 3.23	93	45.31 ± 3.02	146.28 ± 9.49	–	–
48890	0.903	0.130	60.51 ± 9.99	–	20.73 ± 3.27	19	16.07 ± 4.50	51.05 ± 8.02	–	–
49766	0.219	0.400	102.18 ± 34.06	–	8.43 ± 2.48	12	11.38 ± 2.86	17.42 ± 3.58	–	–
51976	0.858	0.050	49.26 ± 5.14	–	6.76 ± 1.75	2	25.26 ± 2.37	68.96 ± 5.37	–	–
52086	0.523	0.050	86.37 ± 6.95	6.68 ± 1.90	41.14 ± 2.61	73	63.33 ± 2.29	137.86 ± 3.60	–	–
54022	0.337	0.400	66.92 ± 9.83	–	24.62 ± 2.43	16	28.20 ± 2.24	88.68 ± 3.64	112.00 ± 11.99	4.44 ± 3.33
55102	0.457	0.130	24.92 ± 3.49	–	25.48 ± 1.98	22	26.86 ± 2.07	56.38 ± 3.54	–	–
56801	0.649	0.400	27.27 ± 9.09	–	Inf ± 5.02	5	16.69 ± 4.90	22.59 ± 5.82	–	–
56875	0.534	0.050	21.18 ± 7.06	–	8.62 ± 1.87	30	8.23 ± 1.71	24.69 ± 3.33	–	–
60827	0.759	0.050	50.65 ± 5.74	–	20.60 ± 1.91	12	13.69 ± 1.75	43.45 ± 2.89	–	–
70651	0.215	0.050	68.30 ± 22.24	–	61.81 ± 3.96	27	54.01 ± 3.77	123.60 ± 5.55	83.67 ± 11.82	2.88 ± 4.51

Continued on Next Page…

Table 4.1 – Continued

PEARS ID	z	$E(B-V)$	[OII]3727	[OIII]λ4363	Hβ	EW([Hβ])	[OIII]λ4959	[OIII]λ5007	Hα	[NII]6584
75506	0.280	0.050	33.45 ± 11.15	–	6.95 ± 1.92	31	8.02 ± 2.38	22.00 ± 3.39	7.03 ± 8.39	0.02 ± 3.58
75753	0.345	0.400	103.36 ± 6.89	4.79 ± 1.84	65.55 ± 2.46	37	75.24 ± 2.42	221.61 ± 4.73	290.20 ± 16.74	17.34 ± 3.04
76154	0.605	0.050	46.60 ± 6.82	–	24.81 ± 2.25	44	28.74 ± 2.62	90.94 ± 4.12	–	–
78762	0.458	0.050	43.94 ± 11.29	–	20.08 ± 2.36	14	13.80 ± 2.48	46.74 ± 4.39	50.72 ± 9.59	6.87 ± 3.20
79283	0.227	0.400	77.54 ± 8.59	–	45.00 ± 1.78	9	8.11 ± 1.24	24.24 ± 1.85	178.80 ± 6.66	35.58 ± 2.18
80500	0.667	0.130	52.59 ± 3.73	–	31.69 ± 3.91	24	18.66 ± 3.01	62.49 ± 8.57	–	–
81944	0.247	0.050	205.21 ± 16.73	6.15 ± 2.33	85.81 ± 2.06	61	119.70 ± 2.39	377.34 ± 4.20	136.68 ± 5.20	1.99 ± 2.13
85517	0.535	0.270	16.50 ± 5.50	–	12.00 ± 1.99	53	4.77 ± 1.49	56.61 ± 3.28	–	–
89030	0.621	0.400	50.41 ± 5.93	–	18.88 ± 4.54	7	5.40 ± 1.80	7.35 ± 2.45	–	–
91208	0.218	0.300	232.57 ± 19.90	–	56.04 ± 3.10	12	24.63 ± 2.62	61.93 ± 4.01	42.48 ± 7.55	4.61 ± 2.06
91789	0.533	0.050	30.64 ± 5.79	–	10.37 ± 1.79	14	7.21 ± 1.76	21.62 ± 2.97	–	–
94632	0.668	0.300	20.01 ± 6.67	–	4.71 ± 1.57	15	4.62 ± 1.54	21.77 ± 5.09	–	–
96123	0.532	0.270	44.00 ± 6.49	–	14.91 ± 1.85	13	5.58 ± 1.86	16.31 ± 2.46	–	–
96627	0.152	0.270	755.59 ± 45.98	–	149.03 ± 4.82	10	45.37 ± 3.96	179.04 ± 6.42	87.57 ± 4.68	5.03 ± 2.12
97655	0.545	0.050	33.59 ± 5.14	–	23.73 ± 3.13	20	13.30 ± 3.72	60.82 ± 5.83	–	–
101684	0.838	0.270	103.44 ± 6.38	–	41.19 ± 3.26	40	44.76 ± 3.12	132.57 ± 5.39	–	–
104408	0.736	0.130	37.11 ± 7.90	–	19.47 ± 2.90	27	25.30 ± 3.64	67.17 ± 5.95	–	–
106491	0.338	0.400	27.44 ± 7.34	–	21.28 ± 2.96	78	26.01 ± 2.55	78.28 ± 3.97	49.54 ± 8.31	0.54 ± 3.55

Continued on Next Page…

Table 4.1 – Continued

PEARS ID	z	$E(B-V)$	[OII]3727	[OIII]λ4363	Hβ	EW([Hβ])	[OIII]λ4959	[OIII]λ5007	Hα	[NII]6584
106761	0.667	0.400	19.74 ± 6.58	–	8.04 ± 2.68	7	13.83 ± 3.06	38.95 ± 8.95	–	–
110494	0.277	0.400	240.15 ± 38.31	17.31 ± 5.40	66.75 ± 2.46	19	57.36 ± 2.45	201.84 ± 3.85	227.02 ± 4.30	26.84 ± 2.86
110494	0.278	0.400	355.24 ± 19.08	24.91 ± 4.16	114.48 ± 3.93	21	80.57 ± 5.01	251.58 ± 7.89	141.20 ± 6.93	16.22 ± 5.05
114392	0.564	0.400	28.50 ± 4.16	–	5.34 ± 1.78	4	10.74 ± 3.58	25.29 ± 4.51	–	–
117138	0.648	0.400	73.53 ± 3.27	–	56.70 ± 3.35	14	22.81 ± 2.59	75.38 ± 4.23	–	–
117686	0.670	0.400	19.31 ± 2.94	–	8.75 ± 2.60	13	18.45 ± 6.15	11.99 ± 3.91	–	–
117929	0.338	0.400	154.92 ± 9.05	–	34.63 ± 3.42	14	30.33 ± 3.08	69.08 ± 4.49	98.30 ± 10.24	7.60 ± 3.00
118100	0.647	0.400	28.31 ± 4.13	–	24.16 ± 2.56	14	29.39 ± 2.65	105.12 ± 4.85	–	–
119341	0.690	0.050	28.11 ± 9.37	–	8.46 ± 2.33	165	11.76 ± 3.92	41.79 ± 7.09	–	–
121817	0.669	0.050	31.68 ± 10.21	–	11.50 ± 2.29	46	23.53 ± 3.70	60.21 ± 6.38	–	–
123008	0.641	0.400	60.09 ± 3.51	–	31.16 ± 3.14	34	58.11 ± 2.93	157.40 ± 4.32	–	–
123301	0.605	0.050	97.24 ± 7.46	–	71.06 ± 2.87	50	100.85 ± 3.09	297.74 ± 5.38	–	–
123859	0.419	0.130	64.10 ± 4.62	–	17.66 ± 2.15	7	24.32 ± 2.24	83.06 ± 4.28	–	–
127697	0.418	0.270	23.70 ± 5.95	–	10.14 ± 2.59	5	7.53 ± 2.51	16.59 ± 3.90	–	–
128538	0.422	0.050	22.93 ± 4.36	–	9.14 ± 2.30	34	10.25 ± 2.10	30.20 ± 3.14	–	–
134573	0.358	0.400	119.85 ± 12.99	–	44.09 ± 3.85	33	69.92 ± 3.66	169.65 ± 5.88	123.07 ± 16.45	35.34 ± 8.77
146104	0.330	0.270	127.85 ± 28.94	–	49.98 ± 2.31	28	61.93 ± 2.25	202.79 ± 3.71	122.27 ± 3.12	9.80 ± 3.46
146122	0.619	0.050	58.09 ± 9.82	–	12.93 ± 4.31	16	14.76 ± 4.36	39.71 ± 5.31	–	–

Continued on Next Page…

Table 4.1 – Continued

PEARS ID	z	$E(B-V)$	[OII]3727	[OIII]λ4363	Hβ	EW([Hβ])	[OIII]λ4959	[OIII]λ5007	Hα	[NII]6584
815lz_45	0.620	0.300	416.26 ± 9.92	9.59 ± 2.21	108.19 ± 4.94	21	61.09 ± 3.59	183.80 ± 5.45	–	–
815lz_52	0.620	0.300	54.73 ± 11.83	–	19.53 ± 3.48	18	20.98 ± 2.77	43.56 ± 3.75	–	–
815lz_64	0.620	0.300	62.65 ± 6.81	–	35.40 ± 2.63	23	27.37 ± 2.12	77.09 ± 3.24	–	–
823lz_65	0.649	0.300	96.16 ± 11.75	8.52 ± 2.20	85.44 ± 3.03	179	189.23 ± 2.47	599.46 ± 3.72	–	–
823lz_96	0.246	0.300	414.69 ± 138.23	–	21.92 ± 2.79	95	29.11 ± 2.95	77.20 ± 5.07	18.84 ± 3.68	2.31 ± 1.83
918lz_24	0.825	0.300	30.60 ± 6.77	–	9.48 ± 2.97	14	10.83 ± 3.61	31.01 ± 4.57	–	–
918lz_53	0.394	0.300	44.37 ± 14.79	–	9.54 ± 3.18	26	12.35 ± 3.80	31.87 ± 5.81	40.74 ± 4.86	8.20 ± 3.05
918lz_63	0.392	0.300	40.23 ± 13.41	–	16.39 ± 2.42	17	13.28 ± 2.58	35.31 ± 4.16	29.18 ± 3.85	4.81 ± 2.20
918lz_74	0.839	0.300	43.29 ± 7.30	–	7.95 ± 2.65	14	9.54 ± 2.10	33.92 ± 3.68	–	–
815lz_108	0.240	0.300	168.87 ± 56.29	–	48.84 ± 2.29	92	115.16 ± 2.34	371.30 ± 3.91	140.99 ± 3.21	0.97 ± 1.57
815lz_159	0.619	0.300	56.49 ± 10.33	–	12.57 ± 4.19	18	19.17 ± 4.14	31.32 ± 4.71	–	–
815lz_163	0.623	0.300	48.91 ± 9.88	–	17.12 ± 3.42	17	19.43 ± 3.19	42.07 ± 4.00	–	–
815lz_187	0.623	0.300	27.59 ± 8.30	–	12.32 ± 3.12	30	20.61 ± 2.53	90.13 ± 3.72	–	–
815lz_206	0.620	0.300	28.53 ± 9.10	–	25.32 ± 2.49	45	42.71 ± 2.24	145.38 ± 3.47	–	–
815lz_214	0.618	0.300	49.19 ± 11.06	–	10.68 ± 3.56	137	18.57 ± 4.01	53.98 ± 4.53	–	–
815lz_243	0.625	0.300	65.87 ± 5.98	–	22.78 ± 1.93	22	30.51 ± 2.36	79.80 ± 3.16	–	–
823lz_221	0.642	0.300	56.08 ± 7.01	–	22.06 ± 2.12	55	21.83 ± 1.83	46.65 ± 2.47	–	–
918lz_111	0.839	0.300	29.22 ± 9.74	–	12.36 ± 4.12	-9	18.93 ± 2.90	41.43 ± 4.50	–	–

Continued on Next Page…

Table 4.1 – Continued

PEARS ID	z	$E(B-V)$	[OII]3727	[OIII]λ4363	Hβ	EW([Hβ])	[OIII]λ4959	[OIII]λ5007	Hα	[NII]6584
918lz_136	0.834	0.300	46.29 ± 9.83	–	51.82 ± 2.73	20	38.41 ± 2.46	125.43 ± 3.89	–	–
etg_26792	0.732	0.300	54.19 ± 8.04	–	37.90 ± 4.87	25	7.29 ± 2.21	11.59 ± 2.74	–	–
elg_137	0.364	0.300	177.63 ± 23.61	–	57.76 ± 2.06	51	66.55 ± 2.07	209.27 ± 4.19	155.73 ± 4.41	12.27 ± 1.78
elg_2671	0.366	0.300	230.82 ± 25.87	–	94.64 ± 4.01	13	27.55 ± 2.89	84.18 ± 4.79	246.06 ± 6.69	52.84 ± 3.54
elg_522	0.841	0.300	77.04 ± 6.60	7.14 ± 2.06	29.77 ± 2.44	16	31.89 ± 1.68	159.56 ± 3.16	–	–

Table 4.2: The metallicity measurements of the PEARS emission-line galaxies: redshift z, the ionization parameter q, and oxygen abundances by R_{23} and N2 diagnostics.

ID	z	Criteria	$log(R23)$	$log(q)$	12+log(O/H) R23	12+log(O/H) N2
13541	0.373	Upper	0.91 ± 0.03	7.17 ± 0.02	8.48 ± 0.09	–
17587	0.645	EW($H\beta$)	0.73 ± 0.15	7.70 ± 0.13	8.06 ± 0.26	–
18862	0.203	N2	0.87 ± 0.05	6.78 ± 0.04	8.61 ± 0.09	8.32 ± 0.03
19422	0.551	EW($H\beta$)	0.84 ± 0.10	7.76 ± 0.13	8.19 ± 0.19	–
22203	0.281	N2	0.90 ± 0.02	7.52 ± 0.04	8.40 ± 0.05	8.29 ± 0.02
22829	0.561	EW($H\beta$)	0.80 ± 0.03	7.29 ± 0.02	8.29 ± 0.15	–
29626	0.854	EW($H\beta$)	0.93 ± 0.06	8.08 ± 0.15	8.26 ± 0.13	–
37690	0.365	N2	0.86 ± 0.10	7.54 ± 0.14	8.28 ± 0.26	–
45454	0.424	EW($H\beta$)	0.80 ± 0.10	7.58 ± 0.13	8.16 ± 0.25	–
48890	0.903	EW($H\beta$)	0.84 ± 0.08	7.55 ± 0.09	8.65 ± 0.14	–
52086	0.523	[OIII]4363	0.86 ± 0.03	7.74 ± 0.03	8.25 ± 0.06	–
56875	0.534	EW($H\beta$)	0.81 ± 0.11	7.52 ± 0.13	8.23 ± 0.21	–
60827	0.759	Upper	0.74 ± 0.04	7.73 ± 0.06	8.81 ± 0.06	–
70651	0.215	N2	0.61 ± 0.05	7.64 ± 0.12	7.89 ± 0.09	8.28 ± 0.08
76154	0.605	EW($H\beta$)	0.84 ± 0.04	7.75 ± 0.06	8.20 ± 0.09	–
78762	0.458	N2	0.74 ± 0.07	7.83 ± 0.14	8.82 ± 0.09	8.84 ± 0.10
79283	0.227	N2	0.72 ± 0.04	6.95 ± 0.04	8.78 ± 0.06	8.56 ± 0.02

Continued on Next Page…

Table 4.2 – Continued

ID	z	Criteria	$log(R23)$	$log(q)$	12+log(O/H) R23	12+log(O/H) N2
80500	0.667	EW($H\beta$)	0.67 ± 0.06	7.35 ± 0.04	8.05 ± 0.21	–
81944	0.247	N2	0.93 ± 0.01	7.77 ± 0.03	8.36 ± 0.03	7.88 ± 0.02
85517	0.535	EW($H\beta$)	0.86 ± 0.08	7.75 ± 0.13	8.27 ± 0.18	–
91789	0.533	Upper	0.78 ± 0.09	7.59 ± 0.10	8.74 ± 0.14	–
96123	0.532	Upper	0.83 ± 0.07	7.10 ± 0.07	8.62 ± 0.15	–
97655	0.545	EW($H\beta$)	0.67 ± 0.06	7.41 ± 0.06	7.98 ± 0.35	–
101684	0.838	EW($H\beta$)	0.92 ± 0.03	7.50 ± 0.03	8.44 ± 0.07	–
104408	0.736	EW($H\beta$)	0.85 ± 0.07	7.68 ± 0.09	8.26 ± 0.14	–
117138	0.648	Upper	0.67 ± 0.02	7.49 ± 0.03	8.87 ± 0.49	–
117686	0.670	Upper	0.92 ± 0.14	7.36 ± 0.10	8.47 ± 0.33	–
123301	0.605	EW($H\beta$)	0.85 ± 0.01	7.77 ± 0.03	8.17 ± 0.15	–
127697	0.418	Upper	0.82 ± 0.13	7.36 ± 0.12	8.67 ± 0.31	–
128538	0.422	EW($H\beta$)	0.86 ± 0.11	7.53 ± 0.08	8.28 ± 0.27	–
815lz_52	0.620	Upper	0.93 ± 0.09	7.33 ± 0.08	8.45 ± 0.22	–
815lz_64	0.620	EW($H\beta$)	0.79 ± 0.04	7.39 ± 0.04	8.26 ± 0.07	–
918lz_63	0.392	N2	0.89 ± 0.11	7.34 ± 0.13	8.54 ± 0.23	8.73 ± 0.08
815lz_163	0.623	Upper	0.94 ± 0.10	7.34 ± 0.08	8.41 ± 0.24	–
823lz_221	0.642	EW($H\beta$)	0.89 ± 0.05	7.34 ± 0.05	8.44 ± 0.09	–
918lz_111	0.839	Upper	0.94 ± 0.16	7.55 ± 0.13	8.43 ± 0.37	–

Continued on Next Page…

Table 4.2 – Continued

ID	z	Criteria	$log(R23)$	$log(q)$	12+log(O/H)	12+log(O/H)
					R23	N2
918lz_136	0.834	EW($H\beta$)	0.66 ± 0.04	7.60 ± 0.07	7.98 ± 0.07	–
etg_26792	0.732	EW($H\beta$)	0.49 ± 0.07	6.90 ± 0.06	8.05 ± 0.10	–
elg_2671	0.366	N2	0.78 ± 0.04	7.08 ± 0.04	8.71 ± 0.07	8.65 ± 0.0

Table 4.3: The physical properties of the PEARS emission-line galaxies: oxygen abundance, half-light radius, rest-frame *B* absolute magnitude, age, stellar mass, SFR, gas fraction and effective yield.

ID	z	12+log(O/H) R23	r_{hlr} (kpc)	M_B (mag)	log(Age) (yr)	$log(M_*)$ ($M_\odot$)	$log(M_{gas}/M_\odot)$ ($M_\odot$)	SFR ($M_\odot/yr$)	SSFR (/yr)	f_{gas}	$log(y_{eff})$
13541	0.373	8.48 ± 0.09	1.59	-22.40	9.00	$9.54^{+0.03}_{-0.19}$	9.36 ± 0.02	5.59 ± 0.42	1.61± 0.43	0.40 ± 0.06	-2.02 ± 0.11
17587	0.645	8.06 ± 0.26	0.77	-20.18	9.85	$8.13^{+0.16}_{-0.15}$	8.58 ± 0.10	0.81 ± 0.27	5.97± 2.92	0.74 ± 0.08	-1.95 ± 0.31
18862	0.203	8.61 ± 0.09	3.17	-21.85	9.78	$9.91^{+0.53}_{-0.64}$	9.62 ± 0.02	7.27 ± 0.41	0.89 ± 1.20	0.34 ± 0.30	-1.96 ± 0.37
19422	0.551	8.19 ± 0.19	0.92	-20.30	8.00	$7.58^{+0.42}_{-0.44}$	8.77 ± 0.06	1.25 ± 0.26	33.0 ± 33.4	0.94 ± 0.06	-1.15 ± 0.46
22203	0.281	8.40 ± 0.05	0.89	-20.62	9.00	$9.60^{+0.32}_{-0.00}$	8.68 ± 0.01	0.98 ± 0.02	0.25 ± 0.01	0.11 ± 0.00	-2.49 ± 0.05
22829	0.561	8.29 ± 0.15	1.38	-23.22	9.30	$9.68^{+0.28}_{-0.13}$	9.34 ± 0.02	5.81 ± 0.38	1.21 ± 0.58	0.31 ± 0.10	-2.31 ± 0.20
29626	0.854	8.26 ± 0.13	1.38	-21.15	8.54	$9.02^{+0.17}_{-0.32}$	9.03 ± 0.04	2.11 ± 0.26	2.01 ± 1.50	0.50 ± 0.19	-2.12 ± 0.27
37690	0.365	8.28 ± 0.26	0.83	-20.24	9.00	$8.28^{+0.34}_{-0.36}$	8.24 ± 0.06	0.25 ± 0.05	1.30 ± 1.08	0.47 ± 0.20	-2.13 ± 0.36
45454	0.424	8.16 ± 0.25	2.83	-21.33	9.78	$9.10^{+0.49}_{-0.49}$	8.48 ± 0.06	0.20 ± 0.04	0.16 ± 0.18	0.19 ± 0.18	-2.59 ± 0.35
48890	0.903	8.65 ± 0.14	1.24	-22.71	9.70	$10.29^{+0.06}_{-0.86}$	9.14 ± 0.05	3.32 ± 0.52	0.17 ± 0.34	0.07 ± 0.12	-2.32 ± 0.33
52086	0.523	8.25 ± 0.06	0.84	-20.97	8.54	$8.41^{+0.05}_{-0.07}$	8.76 ± 0.02	1.32 ± 0.08	5.14 ± 0.78	0.69 ± 0.03	-1.86 ± 0.08
56875	0.534	8.23 ± 0.21	1.08	-20.06	9.30	$8.31^{+0.24}_{-0.28}$	8.35 ± 0.07	0.29 ± 0.06	1.42 ± 0.91	0.52 ± 0.15	-2.12 ± 0.29
60827	0.759	8.81 ± 0.06	–	-22.51	9.30	$10.43^{+0.01}_{-1.13}$	–	1.15 ± 0.14	–	–	–
70651	0.215	7.89 ± 0.09	0.99	-18.88	8.85	$7.59^{+0.20}_{-0.38}$	8.31 ± 0.02	0.28 ± 0.02	7.08 ± 4.75	0.84 ± 0.09	-1.89 ± 0.28
76154	0.605	8.20 ± 0.09	1.79	-21.02	9.30	$8.63^{+0.28}_{-0.43}$	8.89 ± 0.03	1.11 ± 0.10	2.60 ± 2.14	0.65 ± 0.19	-1.97 ± 0.30
78762	0.458	8.82 ± 0.09	2.44	-21.49	9.48	$9.07^{+0.19}_{-0.14}$	8.71 ± 0.04	0.48 ± 0.06	0.41 ± 0.14	0.30 ± 0.07	-1.80 ± 0.12

Continued on Next Page…

Table 4.3 – Continued

ID	z	12+log(O/H)	r_{hlr}	M_B	log(Age)	$log(M_*)$	$log(M_{gas}/M_\odot)$	SFR	SSFR	f_{gas}	$log(y_{eff})$
		R23	(kpc)	(mag)	(yr)	($M_\odot$)	($M_\odot$)	($M_\odot/yr$)	(/yr)		
79283	0.227	8.78 ± 0.06	1.65	-20.78	9.60	$9.34^{+0.02}_{-0.05}$	9.22 ± 0.01	3.40 ± 0.13	1.55 ± 0.14	0.43 ± 0.02	-1.68 ± 0.07
80500	0.667	8.05 ± 0.21	1.64	-21.67	9.48	$9.04^{+0.55}_{-0.20}$	9.15 ± 0.04	2.71 ± 0.33	2.47 ± 2.15	0.56 ± 0.21	-2.25 ± 0.35
81944	0.247	8.36 ± 0.03	1.00	-19.90	8.85	$8.46^{+0.08}_{-0.13}$	8.51 ± 0.01	0.52 ± 0.01	1.79 ± 0.44	0.53 ± 0.06	-1.98 ± 0.08
85517	0.535	8.27 ± 0.18	0.71	-19.76	7.54	$7.92^{+0.29}_{-0.49}$	8.75 ± 0.05	1.49 ± 0.25	17.9 ± 16.3	0.87 ± 0.10	-1.41 ± 0.41
91789	0.533	8.74 ± 0.14	1.76	-20.72	9.78	$8.74^{+0.24}_{-0.33}$	8.53 ± 0.05	0.35 ± 0.06	0.63 ± 0.43	0.38 ± 0.16	-1.78 ± 0.23
96123	0.532	8.62 ± 0.15	1.01	-21.34	9.70	$9.02^{+0.20}_{-0.40}$	8.90 ± 0.04	1.83 ± 0.23	1.75 ± 1.23	0.43 ± 0.17	-1.83 ± 0.25
97655	0.545	7.98 ± 0.35	1.31	-20.83	9.30	$8.40^{+0.11}_{-0.08}$	8.73 ± 0.04	0.84 ± 0.11	3.33 ± 0.85	0.68 ± 0.05	-2.14 ± 0.36
101684	0.838	8.44 ± 0.07	–	-22.35	9.48	$10.39^{+0.10}_{-0.45}$	–	10.79 ± 0.85	–	–	–
104408	0.736	8.26 ± 0.14	1.28	-21.28	9.60	$8.98^{+0.25}_{-0.38}$	9.00 ± 0.05	2.04 ± 0.30	2.14 ± 1.58	0.51 ± 0.18	-2.11 ± 0.27
117138	0.648	8.87 ± 0.49	4.99	-23.88	9.48	$9.82^{+0.11}_{-0.52}$	10.03 ± 0.02	19.45 ± 1.15	2.94 ± 2.14	0.62 ± 0.17	-1.34 ± 0.55
117686	0.670	8.47 ± 0.33	0.89	-20.77	6.70	$8.66^{+0.26}_{-0.35}$	9.04 ± 0.09	3.13 ± 0.93	6.86 ± 5.23	0.71 ± 0.15	-1.61 ± 0.42
123301	0.605	8.17 ± 0.15	2.88	-22.45	8.85	$8.83^{+0.07}_{-0.04}$	9.34 ± 0.01	3.18 ± 0.13	4.71 ± 0.63	0.76 ± 0.02	-1.80 ± 0.16
127697	0.418	8.67 ± 0.31	1.10	-21.03	9.85	$9.56^{+0.24}_{-0.41}$	8.68 ± 0.08	0.83 ± 0.21	0.23 ± 0.18	0.12 ± 0.08	-2.20 ± 0.34
128538	0.422	8.28 ± 0.27	2.40	-21.55	9.30	$8.95^{+0.19}_{-0.09}$	8.40 ± 0.08	0.18 ± 0.05	0.21 ± 0.08	0.22 ± 0.06	-2.44 ± 0.28

Chapter 5

METALLICITIES OF EMISSION LINE GALAXIES FROM HST/ACS PEARS AND HST WFC3 ERS GRISM SPECTROSCOPY AT $0.6 < Z < 2.4$

5.1 Abstract

Galaxies selected on the basis of their emission line strength show low metallicities $-22 \lesssim M_B \lesssim -19$, regardless of their redshifts. We conclude this from a sample of faint galaxies at redshifts between $0.6 < z < 2.4$, selected by their prominent emission lines in low-resolution grism spectra in the optical with the Advanced Camera for Surveys (ACS) on the Hubble Space Telescope (HST) and in the near-infrared using Wide-Field Camera 3 (WFC3). Using a sample of 11 emission line galaxies (ELGs) at $0.6 < z < 2.4$ which have [OII], Hβ, and [OIII] line flux measurements from the combination of two grism spectral surveys, we use the $R23$ method to derive the gas-phase oxygen abundances: 7.5 <12+log(O/H)<8.5. The galaxy stellar masses are derived using Bayesian based Markov Chain Monte Carlo (πMC^2) fitting of their Spectral Energy Distribution (SED), and span the mass range $8.1 < \log(M_*/\mathrm{M}_\odot) < 10.1$. These galaxies show a mass-metallicity (M-L) and Luminosity-Metallicity (L-Z) relation, which is offset by –0.6 dex in metallicity at given absolute magnitude and stellar mass relative to the local SDSS galaxies, as well as continuum selected DEEP2 samples at similar redshifts. The emission-line selected galaxies most resemble the local “green peas” galaxies and Lyman-alpha galaxies at $z \simeq 0.3$ and $z \simeq 2.3$ in the M-Z and L-Z relations and their morphologies. The $G - M_{20}$ morphology analysis shows that 10 out of 11 show disturbed morphology, even as the star-forming regions are compact. These galaxies may be intrinsically metal poor, being at early stages of formation, or the low metallicities may be due to gas infall and accretion due to mergers.

5.2 Introduction

Nebular lines from HII regions are signposts for detection and measurement of current star-formation. They are also useful for measuring the metallicity of galaxies. From such studies (Lequeux et al., 1979; Garnett & Shields, 1987; Skillman et al., 1989; Zaritsky et al., 1994) we have learned the mass-metallicity and mass-luminosity relations (e.g. Tremonti et al. 2004), whereby galaxies with higher stellar mass and higher absolute luminosity show higher metallicities. It is expected, and observed, that going to higher redshifts should show a shift in the mass-metallicity relation (Erb et al., 2006; Mannucci et al., 2009). Higher redshift galaxies do show a lower metallicity for the same given stellar mass (e.g. Erb et al 2006, Maiolino et al. 2008) for galaxies in the early stages of star-formation. Effects of downsizing are also seen in mass metallicity effects. Since lower mass galaxies continue star-formation until later epochs, one would expect the slope of the mass-metallicity relation to also change the offset in the M-Z and L-Z relation. Zahid et al. (2010) show that at $z = 0.8$, the high mass ($M > 10^{10.6} M_{\odot}$) galaxies have attained the metallicities seen for the same mass galaxies at $z = 0$, but low mass galaxies ($M \approx 10^{9.2} M_{\odot}$) still show a metallicity deficit compared to the same mass galaxies at $z = 0$.

In order to go fainter (and lower stellar masses) at higher redshifts, We analyze nebular line emission of 11 galaxies in Chandra Deep Field- South, observed with HST-ACS grism in the optical (from the PEARS program; PI: Malhotra) and HST-WFC3 grism (from the ERS program; PI: O'Connell; e.g., Straughn et al. 2011) at near-infrared wavelengths. This sample is selected to show emission lines in the slitless spectra, reaching limits of 26.7 mag and redshifts at $z \lesssim 2.3$. Together, these grism data sets span a wavelength range from λ =0.6–1.6 μm. This allows us to measure metallicities using the R23 diagnostic indicator, $R23$ =

([OII]+[OIII])/Hβ, (Pagel et al., 1979; Kewley & Dopita, 2002) for a wide range of redshift, $0.5 \lesssim z \lesssim 2.4$, without interference by the Earth's atmosphere. Much of this redshift range is inaccessible to ground-based observations due to H_2O absorption bands, and even more is lost to OH airglow emission lines. Our work demonstrates the crucial value of slitless HST spectra in studying the physical properties of galaxies at an otherwise challenging redshift range.

The paper is organized as below. In § 2 we briefly introduce the surveys and the data sample. In § 3 we present the measurements of the metallicity and the stellar mass, and assess the metallicity accuracy by comparing with the metallicity measured from follow-up Magellan spectroscopy of two galaxies. We show the results of the mass-metallicity (M-Z) relation and the luminosity-metallicity (L-Z) relation in § 4. Finally, we discuss the results and give our conclusions in § 5. We use a "benchmark" cosmology with $\Omega_m = 0.27$, $\Omega_\Lambda = 0.73$, and $H_0 = 71 \mathrm{km\,s^{-1} Mpc^{-1}}$ (Komatsu et al., 2011), and we adopt AB magnitudes throughout this paper.

5.3 Data

The HST/ACS G800L Probing Evolution and Reionization Spectroscopically survey (PEARS, PI: S. Malhotra, program ID 10530) is the largest survey conducted to date with the slitless grism spectroscopy mode of the HST Advanced Camera for Surveys. PEARS provides low-resolution (R $\sim$ 100) slitless grism spectroscopy in the wavelength range from 6000Å to 9700Å. The survey covers four ACS pointings in the GOODS-N (Great Observatories Origins Deep Survey North) field and five ACS pointings in the CDF-S (Chandra Deep Field South) fields. Eight of these PEARS fields were observed in 20 orbits each (three roll angles per field), yielding spectra of all objects of $\mathrm{AB}_{F850LP} \lesssim 26.5$ mag. The ninth field was the Hubble Ultra Deep Field (HUDF), which was observed in 40 orbits. Combined with the earlier data from the GRAPES program (the GRism ACS Program for Extragalactic Science; PI: S. Malhotra, program ID 9793), the HUDF field reaches grism depths of $\mathrm{AB}_{F850LP} \lesssim 27.5$ mag.

The emission lines most commonly identified from the PEARS grism data are [OII]λ3727Å, the [OIII]$\lambda\lambda$4959,5007Å doublet, and Hα6563Å. Due to the low spectral resolution, the Hβ line is only marginally resolved from the [OIII] doublet. With the ACS G800L grism's wavelength coverage, galaxies at $0.6 < z < 0.9$ can be observed in both the [OII] and [OIII] lines, and galaxies at redshifts $0.9 < z < 1.5$ can be observed in only the single line of [OII]λ3727Å, and at $z < 0.5$ in the $H\alpha$ lines of typical line fluxs $\sim 1.5\text{–}2 \times 10^{-17}$erg cm^{-2} s^{-1} (Straughn et al., 2009).

The HST Wide Field Camera 3 (WFC3) Early Release Science (ERS) (PID GO-11359, PI: O'Connell) program consists of one field observed with both the G102 (0.8–1.14 microns; R$\sim$210) and G141 (1.1–1.6 microns; R$\sim$130) infrared grisms, with two orbits of observation per grism. This field overlaps with the ACS G800L PEARS grism survey, and hence faint galaxies can be observed with composite spectra in the wavelength range from $\lambda \simeq$0.6–1.6 μm with the detection of the emission lines, such as Hα at $z \lesssim 1.6$, [OIII] doublet at $0.2 \lesssim z \lesssim 2.4$, and [OII] doublet at $0.6 \lesssim z \lesssim 3.6$ with a S/N $\gtrsim 2$ line flux limit of $\sim 3.0 \times 10^{-17}$erg cm^{-2} s^{-1} (Straughn et al., 2011).

Straughn et al. (2009) selected 203 emission line galaxies (ELGs) from the PEARS southern fields, using a 2-dimensional line detection and extraction procedure. Straughn et al. (2011) presented a total catalog of 48 emission-line galaxies from the WFC3 ERS II program (Windhorst et al., 2011), demonstrating the unique capability of the WFC3 to detect star-forming galaxies in the infrared reaching to fluxes of $\mathrm{AB}_{(F098M)} \lesssim 25$ mag in a depth of 2 orbits. The combination of these two catalogs yields a sample of 11 ELGs with detection of the [OII], [OIII] and Hβ lines in the composite spectral range 0.6–1.6 μm, which enables us to utilize the

R23 method to measure metallicity, and to extend the study of the mass-metallicity relation of ELGs continuously from $z \simeq 0.6$ to 2.4. We compare the selection of the [OIII] line fluxes, the equivalent width (EW), redshifts, and the absolute B-band magnitude of the 11 ELGs from the combined catalog with respect to the Straughn et al. (2009) PEARS ELGs sample and the Straughn et al. (2011) WFC3 ERS ELGs sample. The comparison shows that the [OIII] emission line is representative of the two large samples at $> 5 \times 10^{-17}$erg cm^{-2} s^{-1}; the EW([OIII])s are in the similar range of the parent samples. The redshifts and the absolute B-band magnitudes are very representative of the ERS parent sample while offset to high redshift with respect to the PEARS sample, which is mainly at $z < 1$ and extends to $M_B \sim -15$..

The HST/ACS PEARS data reduction was similar to the GRAPES project's data analysis (Pirzkal et al., 2004), while further steps for identifying emission line sources are described in Meurer et al. (2007) and Straughn et al. (2009). The analysis of the WFC3 ERS data is discussed in Windhorst et al. (2011) and Straughn et al. (2011). The emission line fluxes are measured from 1D extracted spectra, using the *I*DL code *m*pfit to fit single or multiple Gaussian line profiles. Due to the marginal splitting of the Hβ and [OIII] doublet, the [OIII] line is fitted with a double Gaussian profile with the ratio of [OIII]λ4959 to [OIII]λ5007 constrained to be 1:3 with the same Gaussian widths.

The Hβ line wavelength is fixed at the redshifted wavelength of 4861 Å, given by the observed wavelength of the stronger [OIII]λ5007 line. The underlying Hβ absorption amounts are obtained by fitting galaxy SEDs (discussed in detail in the next section, Pirzkal et al. 2011) with the population synthesis model of Bruzual & Charlot (2003). The EW of the Hβ absorption features range from 4 – 7 Å, which agrees with the amount obtained in other studies, e.g. $\sim 3 \pm 2$ Å (Lilly et al., 2003). The absorption feature is smoothed to the same Gaussian profile as the [OIII] line, and then added to the grism spectra. The absorption-corrected Hβ line flux is finally measured by adding a Gaussian profile (same as that of the [OIII] Gaussian profile) with changing amplitude at the fixed wavelength, on the [OIII] already-fitted double Gaussian profiles. An Hβ line flux of S/N>3 is assumed as detection, and for line fluxes with S/N<3 ($1\sigma \sim 5 \times 10^{-18}$erg cm^{-2} s^{-1}), we use a 3σ upper limit to the Hβ line flux, which give in a lower limit to the galaxy oxygen abundance on the lower branch (see next section).

The amount of dust extinction is also obtained from the SED fitting, and ranges from $Av = 0$–1.2 mag. The extinction correction is done using the *I*DL code *c*alz_unred (written by W. Landsman), based on the reddening curve from Calzetti et al. (2000). Studies show that the gas can suffer more extinction than the stellar content, hence we assume E(B-V)$_{stellar}$=0.44E(B-V)$_{gas}$, as has been found locally (Calzetti et al., 2000). Due to the degeneracy of the extinction and the stellar population age, the extinction values have large uncertainties. The uncertainties of the extinction values are folded into the uncertainties in the metallicity. The results show that the uncertainty due to the extinction is in the order of 0.02–0.1 dex, and the dominant part of the uncertainties in the metallicities result from the faint line flux of Hβ compared to [OIII]λ5007.

Table 1 lists the extinction corrected emission line fluxes and restframe equivalent widths of the [OII]λ3727, Hβ, and the [OIII] doublet for the 11 galaxies in the sample, along with the WFC3 ERS ID and the redshift. Figure 1 shows the grism spectra with the Gaussian fit profiles of the [OII]λ3727, Hβ and [OIII] doublet lines of the 11 galaxies. Figure 12 shows the GOODS-S *i*-band postage stamps of the 11 galaxies.

To assess the morphologies of the galaxies in the sample, we measure the Gini coefficient *G*, which quantifies the relative distribution of the galaxy's flux, and the second-order moment of the brightest 20% of the galaxy's flux (Abraham et al., 2003; Lotz et al., 2004), M_{20} from the galaxy images. Figure 13 shows the distribution of the galaxies in the G-M_{20} plane with the empirical line dividing normal galaxies with merger/interacting galaxies (Lotz et al., 2004). The blue stars represent that measured from GOODS *B*-band image and the red triangles show that measured from GOODS *i*-band image. We can see that from the *B*-band image, all of the galaxies lie above the dashed line, which is the region of the outlier galaxies showing merger/interacting and dwarf/irregular morphologies. From the *i*-band image, 8 out of 11 galaxies are on and above the line and 3 are below the line. The visual check of the galaxies below the dashed line shows that two galaxies (246, 578) have obvious multiple knots and irregular shape, and the galaxy 258 is in the region of dwarf galaxies, which is in agreement with the low mass estimation $\log(M) = 8.74 M_{\odot}$. Therefore, we see that 10 out of 11 show disturbing morphologies, interacting companions and tidal features, which demonstrate the ongoing active star-formation in these galaxies. At the same time, the half light radii of the galaxies are shown in Table 2, which span the range from 1 – 8 kpc, with 8 out of 11, $r_{1/2} < 3$ kpc, showing compact morphology.

5.4 Measurements

Metallicity

Using the strong nebular lines [OII]λ3727, Hβ, and the [OIII] doublet measured from the combined grism spectra, We measure the gas-phase oxygen abundance by the most commonly used *R*23 (*R*23 = ([OII]+[OIII])/Hβ) diagnostic indicator (Pagel et al., 1979; Kewley & Dopita, 2002). We calculate the metallicities by iteration, using the parameterized calibrations between the oxygen abundance 12+log(O/H), the ionization parameter *q*, and *R*23 that are derived from theoretical photoionization models by Kewley & Dopita (2002) and Kobulnicky & Kewley (2004).

We select the R23 method, because it relies on measuring some of the brightest nebular emission lines, which allows it to be used for faint galaxies in the distant universe. However, it has one major drawback, which is that the relation between $R_{23} \equiv (f_{OII} + f_{OIII})/f_{H\beta}$ and the gas phase oxygen abundance $12 + log(O/H)$ is in general double-valued, with both a high- ($12 + log(O/H) > 8.5$) and a low- ($12 + log(O/H) < 8.5$), metallicity branch solution. For the present data set, we rely on a set of three secondary metallicity indicators to decide whether the galaxies lie on the upper or lower branch. First is the "O32" ratio, f_{OIII}/f_{OII}. While this is primarily sensitive to the ionization parameter q (Kewley & Dopita, 2002), it can also be used as a branch indicator (Maiolino et al., 2008), with ratios of $f_{OIII}/f_{OII} > 2$ indicating a lower branch solution, and $f_{OIII}/f_{OII} < 1$ indicating an upper branch solution. Second is the ratio $f_{OIII}/f_{H\beta}$, with $f_{OIII}/f_{H\beta} > 3$ indicating $7.4 \lesssim 12 + log(O/H) \lesssim 8.5$ (Maiolino et al., 2008). Third is the equivalent width of the $H\beta$ line. Hu et al. (2009) show that EW($H\beta$) correlates with metallicity, such that EW($H\beta$) $\gtrsim$ 30Å implies a lower branch solution, and EW($H\beta$) $\lesssim$ 10Å implies the upper branch solution.

Other popular branch indicators — notably the [OIII]λ4363 line strength and the $N2$ diagnostic indicator ($N2$ = log ([NII]λ6584/Hα) — are not practical for the data set, given the faintness of the [OIII]λ4363 line, and the blending of [NII]λ6584 with Hα in HST grism spectroscopy. Nevertheless, the combination of EW($H\beta$), f_{OIII}/f_{OII}, and $f_{OIII}/f_{H\beta}$ provides reasonable confidence in the branch identifications for most of the sample.

Figure 14 shows the log($R23$) versus 12+log(O/H) for the 11 ELGs on the lower branch. The lines represent the model relationships between log($R23$) and 12+log(O/H) at two ionizations with $q = 1.0 \times 10^7, 1.0 \times 10^8$. The use of the upper limit of Hβ line fluxes gives the lower limit of R23, and thereafter the lower limit of the metallicities on the lower branch, which are shown as right arrows and upward arrows. Since the galaxies are put on the lower branch, Table 2 shows $\log(R23)$, the ionization parameter $\log(q)$, and the oxygen abundances and their corresponding uncertainties. The large uncertainties on the oxygen abundances are mainly due to the large fractional flux uncertainties for Hβ in the data. All of the galaxies are on the lower branch, and some are near the peak in the $\log(R23)$ vs. metallicity curve, where the branch indicators become both ambiguous and largely irrelevant, and their metallicities are near 12+log(O/H)=8.5.

The galaxy oxygen abundances in the sample span the range from $7.5 <$ 12+log(O/H$) < 8.5$, i.e, ~ 0.1 Z$\odot$ – Z$\odot$. (A solar metallicity has Z$\odot$=0.015 and 12+log(O/H) = 8.72, see Allende Prieto et al. 2001). As we see from table 2, the low redshift galaxies at $0.6 < z < 1$ have an average metallicity of 12+log(O/H)$\simeq$7.95, and the galaxies at $z > 1$ have higher average metallicity of 12+log(O/H)$\simeq$8.26, brighter absolute mangitudes and larger stellar masses (see Table 2). This shows the selection effects at low redshift and high redshift of the sample. At same magnitude and line flux limits, the galaxies selected with larger redshifts tend to be more massive, brighter and higher metallicity galaxies. Hence, to evaluate the evolution of the metallicity for same mass galaxies at different redshifts, we need to enlarge the sample to include faint low-mass galaxies at high redshift.

Two galaxies out of the 11 ELGs (ERS ID numbers 339, 364) have followup Magellan spectroscopy, which covers the wavelength range from 4000 to 9000 Å, with a wavelength-resolution of ~ 3 Å (Xia et al., 2012). The metallicities measured from the Magellan spectra using the R23 method on the strong emission lines [OII], Hβ and [OIII] doublet give 12+log(O/H) = 8.07 ± 0.14 for ERS339 and 8.18 ± 0.15 for ERS364 (Xia et al., 2012). The metallicities obtained from the HST ACS/WFC3 grism spectra (12+log(O/H) = $8.10^{+0.20}_{-0.16}$ for ERS339 and $8.22^{+0.16}_{-0.13}$ for ERS364) and that obtained from the Magellan spectroscopic spectra agree to within 1 σ ($\sim$ 0.1 dex), underscoring the feasibility of emission-line galaxy metallicity measurements using the HST/WFC3 IR grism data.

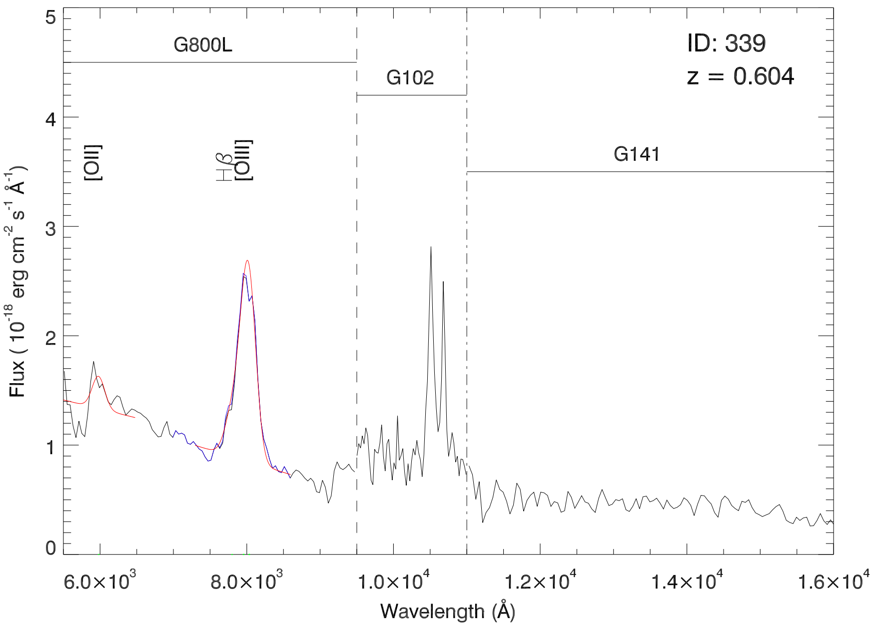

Figure 5.1: Example of composite grism spectra from the HST/ACS PEARS G800L grism spectroscopy and the HST/WFC3-IR ERS G102 and G141 grism spectroscopy. The emission lines, [OII]λ3727, Hβ, and [OIII]λ5007, Hα and [SII] are detected. The Hβ, and [OIII] doublet are detected in both G800L and G102 grisms, and the G102 grism resolves the [OIII]$\lambda\lambda$4959,5007. The fitting of the [OIII] doublet is constrained to make the ratio of the [OIII]λ4959 to [OIII]λ5007 fluxes 1:3, and to use the same line width for both. The detection of both [OII] and [OIII] in the composite spectra enables the meatallicity measurement using the R23 method.

Stellar Mass

The galaxy stellar masses are derived by comparing the observed photometry with the model spectra library produced by the Bruzual & Charlot (2003) stellar population synthesis code (BC03, hearafter). The galaxies in the sample are located in the ACS pointings of the GOODS-South field. The optical broadband *BViz* photometry is obtained from HST/ACS GOODS version 2.0 images (Giavalisco et al., 2004).

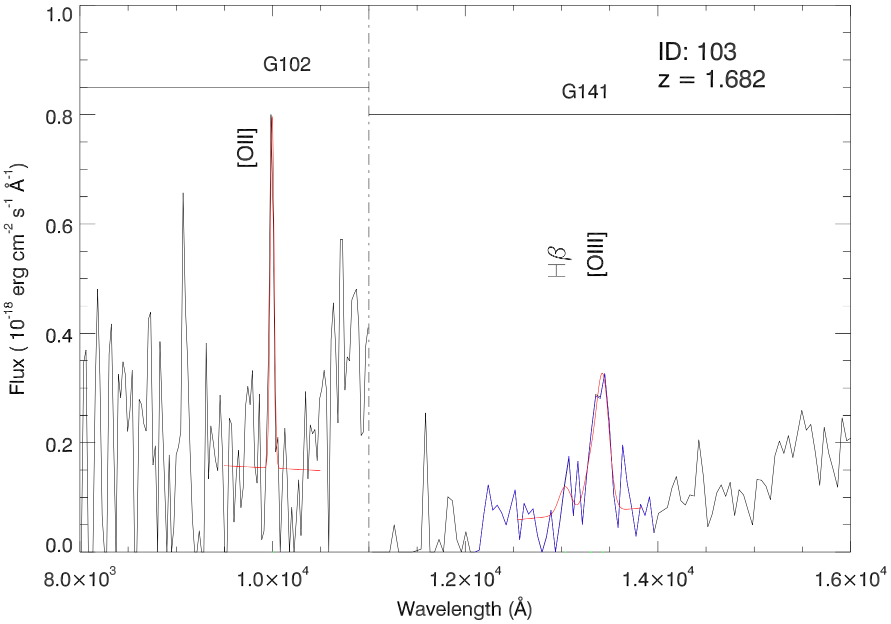

Figure 5.2: Continued. Spectra of PEARS+ERS galaxies and the Gaussian fitting of the emission lines.

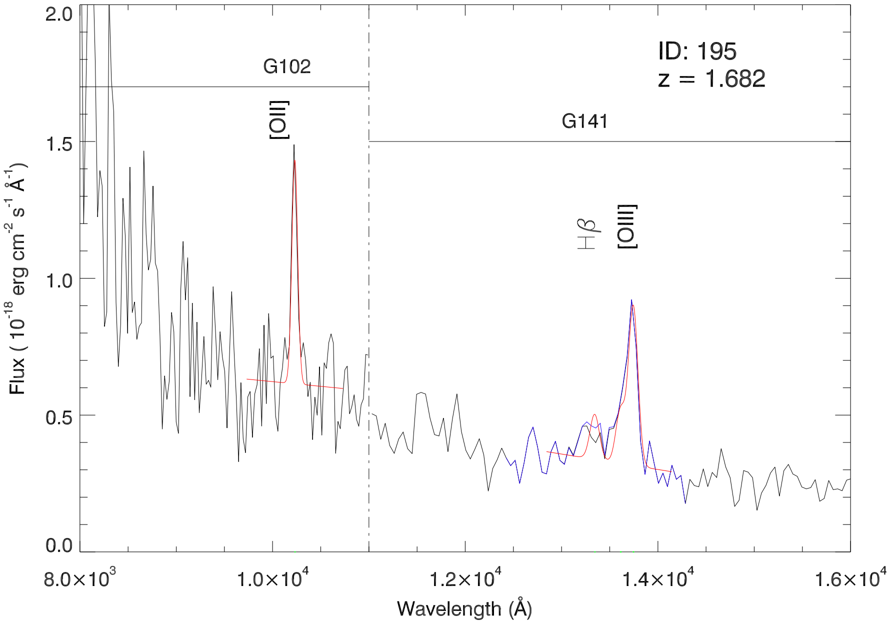

Figure 5.3: Continued. Spectra of PEARS+ERS galaxies and the Gaussian fitting of the emission lines.

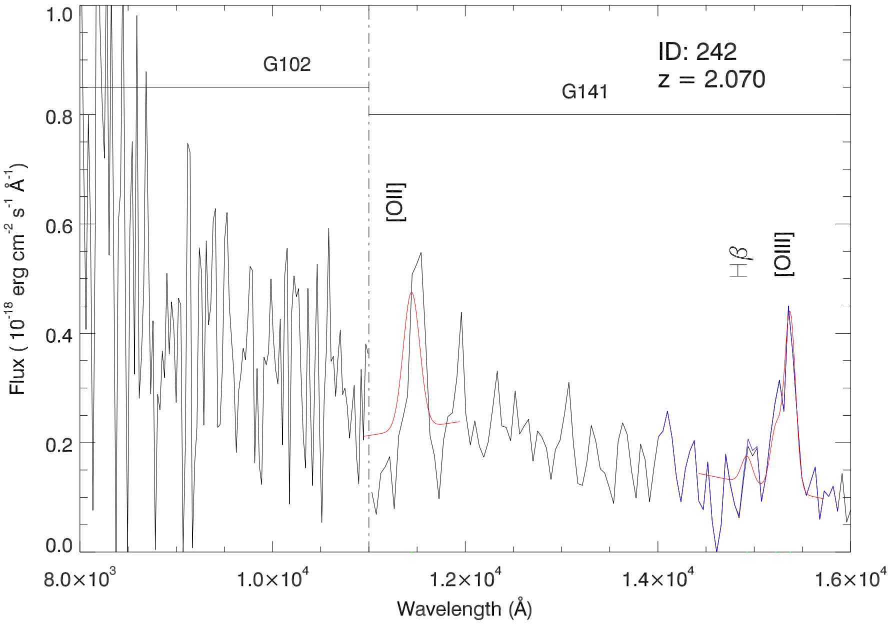

Figure 5.4: Continued. Spectra of PEARS+ERS galaxies and the Gaussian fitting of the emission lines.

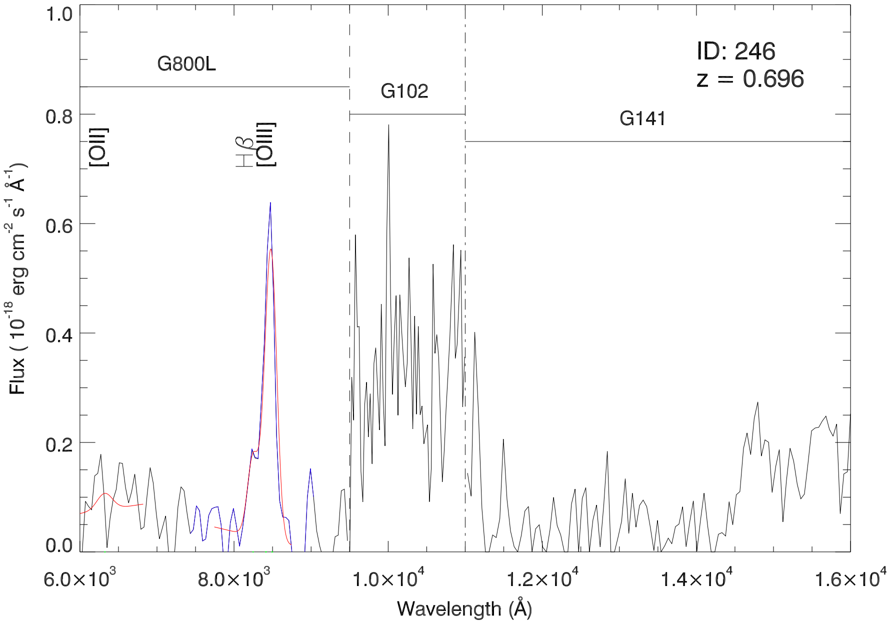

Figure 5.5: Continued. Spectra of PEARS+ERS galaxies and the Gaussian fitting of the emission lines.

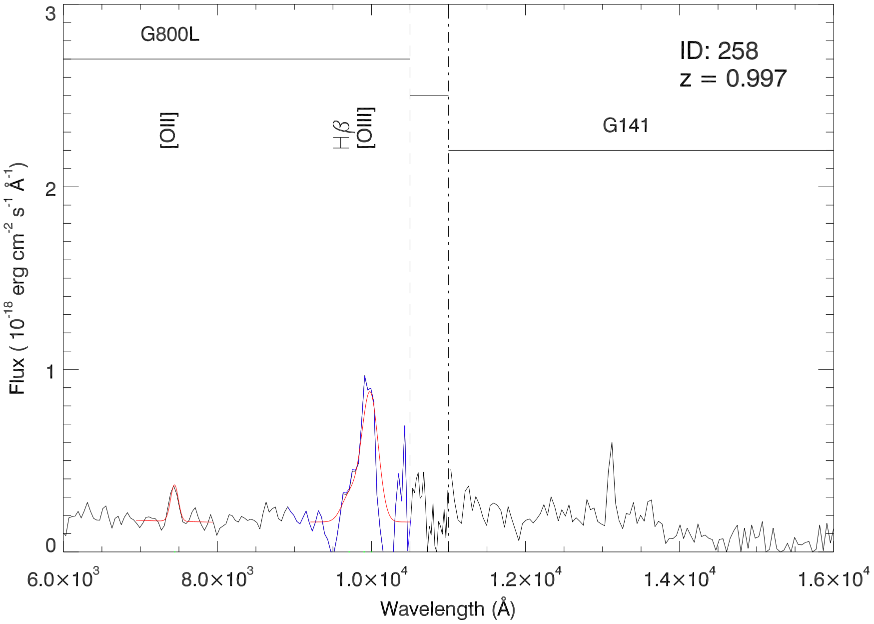

Figure 5.6: Continued. Spectra of PEARS+ERS galaxies and the Gaussian fitting of the emission lines.

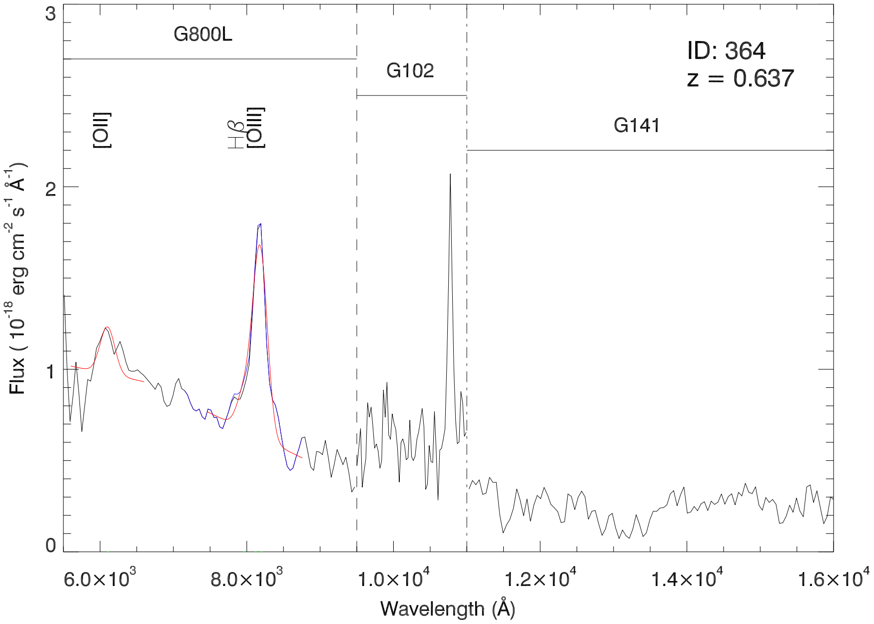

Figure 5.7: Continued. Spectra of PEARS+ERS galaxies and the Gaussian fitting of the emission lines.

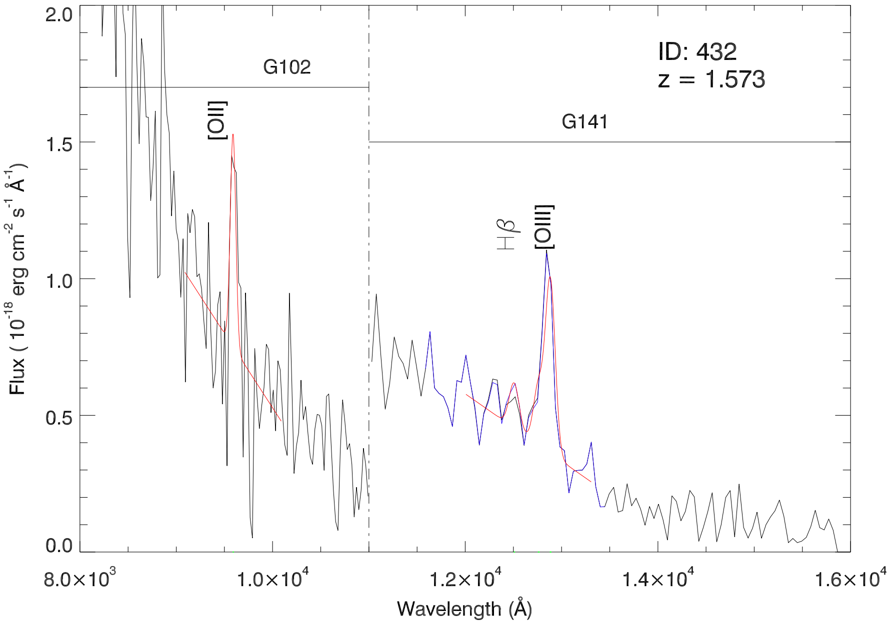

Figure 5.8: Continued. Spectra of PEARS+ERS galaxies and the Gaussian fitting of the emission lines.

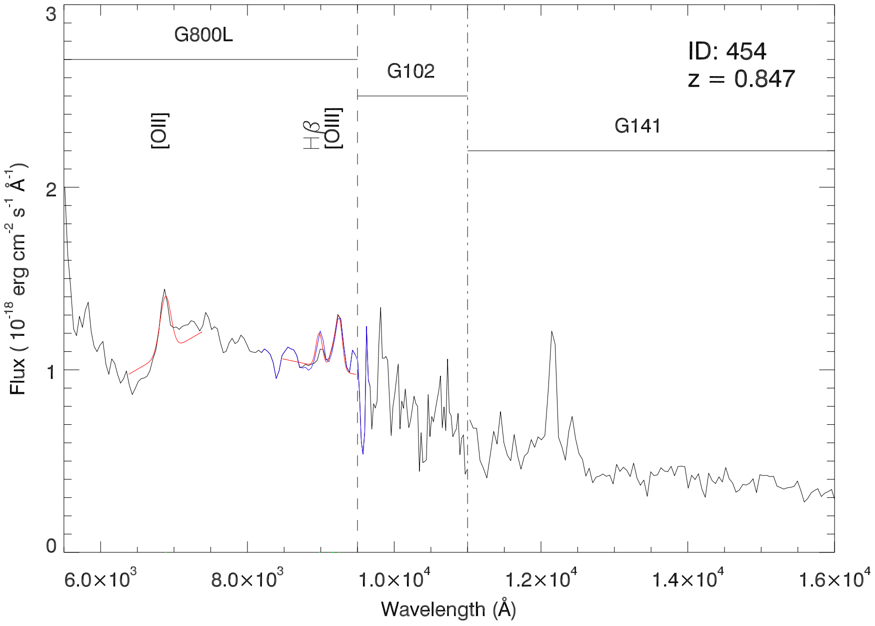

Figure 5.9: Continued. Spectra of PEARS+ERS galaxies and the Gaussian fitting of the emission lines.

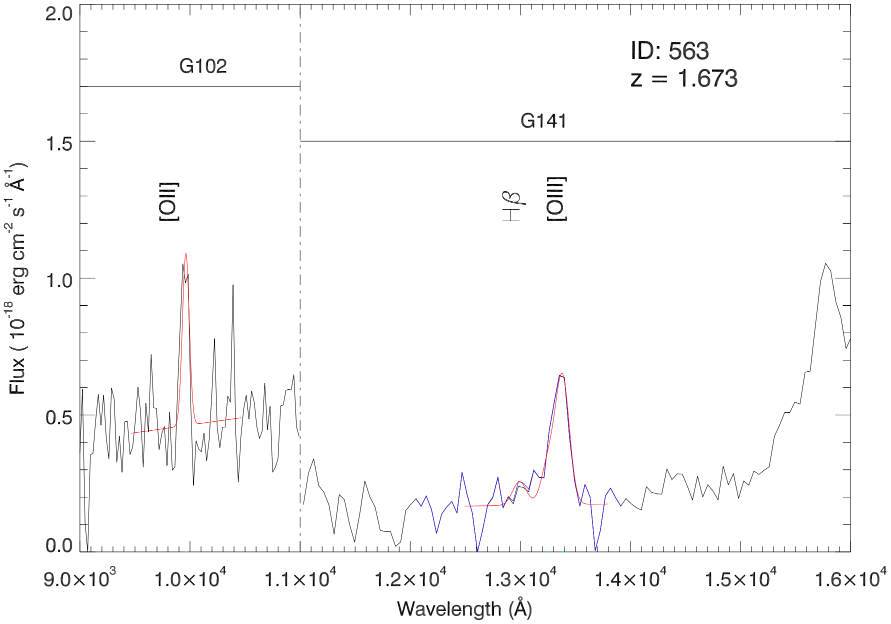

Figure 5.10: Continued. Spectra of PEARS+ERS galaxies and the Gaussian fitting of the emission lines.

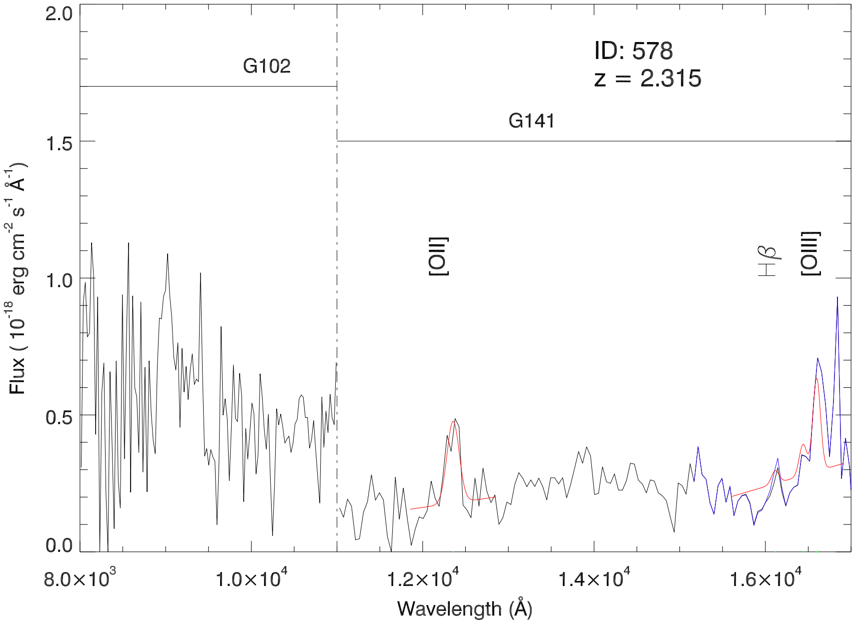

Figure 5.11: Continued. Spectra of PEARS+ERS galaxies and the Gaussian fitting of the emission lines.

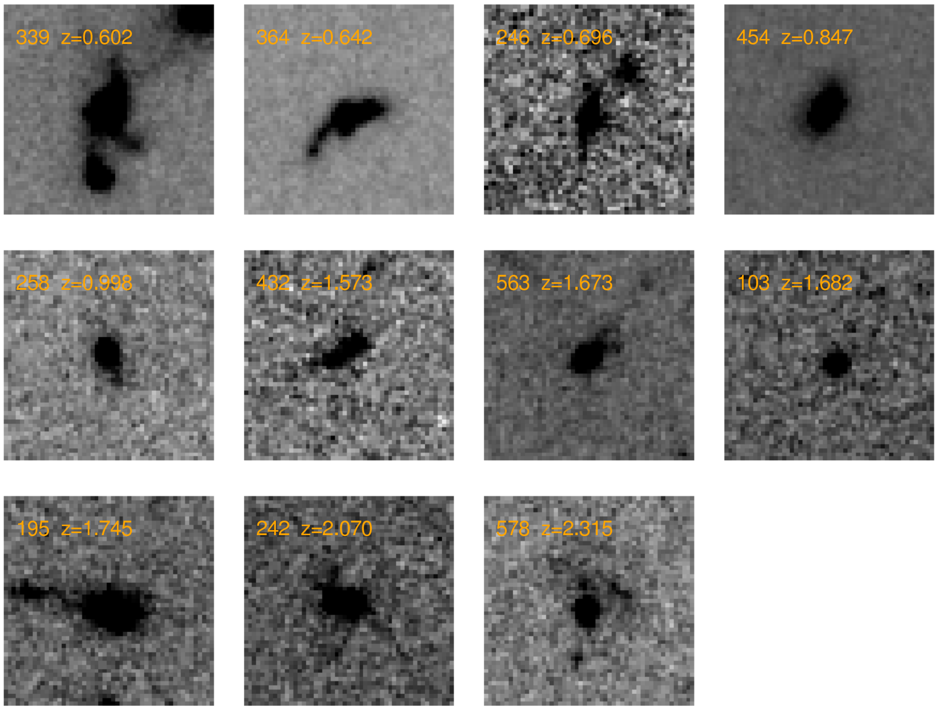

Figure 5.12: The GOODS-S *i*-band postage stamps of the 11 ERS galaxies in the sample. The irregular morphologies, interacting companions, and tidal features demonstrate ongoing star formation of these galaxies.

The UV photometry in F225W, F275W, and F336W, as well as the near-IR photometry in F098M (Ys), F125W (J), and F160W (H) are from the new WFC3 ERS mosaics (Windhorst et al., 2011). In this paper, we adopt the galaxy stellar masses measured by the method of Bayesian based Markov Chain Monte Carlo (πMC^2), which allows us to compare the observations to arbitrarily complex models, and to compute 95% credible intervals that provide robust constraints for the model parameter (see Pirzkal et al. 2011 for details). The models are generated using the single (SSP), two (SSP2) stellar instantaneous populations, or an exponentially decaying star formation history model (EXP). The parameters assumed in the models are Salpeter initial mass function (IMF), metallicities ranging from $Z = 0.004$ to 0.02 ($Z_\odot$), the stellar population ages, the relative ratio between the old and young stellar populations, the Calzetti et al. (2000) extinction law, and the half-life τ value

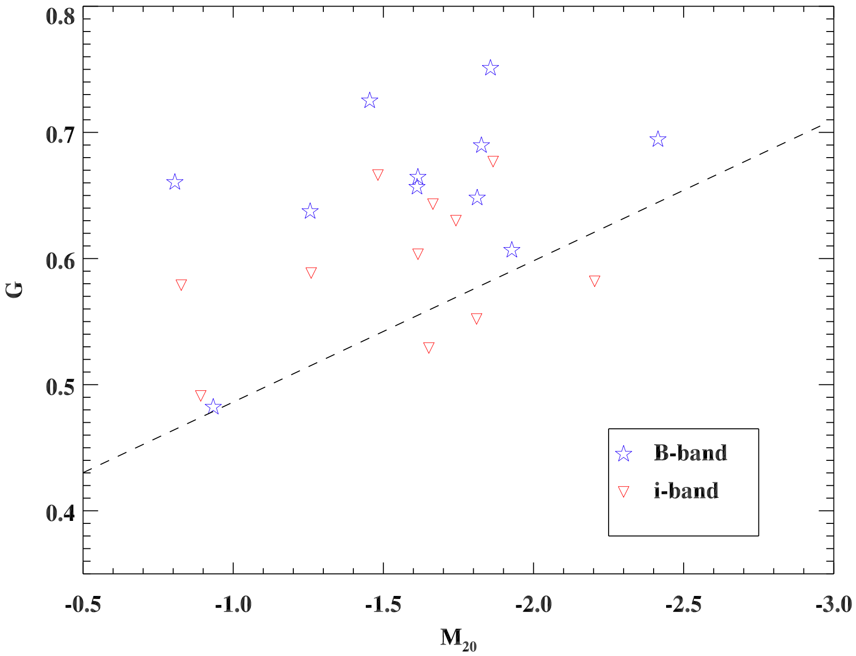

Figure 5.13: Gini coefficient *G* vs. M_{20} to demonstrate the morphology analysis of the 11 galaxies in the sample. The dashed line is the empirical line dividing interacting galaxies (upper region) with normal galaxies (lower region) from Lotz et al. (2004). The blue stars represent galaxies based on *B*-band image analysis. The red triangles are that based on *i*-band image analysis. Most galaxies lie above the line demonstrating disturbed morphologies.

in the case of EXP models. The results of the galaxy stellar masses and stellar population ages are shown in the sixth column of Table 2. The galaxies show young ages of 20–90 Myr and low masses $\sim 10^8 - 10^{10} M_\odot$.

5.5 Results

The wide spectral coverage of the HST/ACS PEARS and WFC3 ERS composite grism spectra provide galaxies at $0.6 < z < 2.4$ with full set of emission lines [OII], Hβ and [OIII], which extend the study of the evolution of the L-Z relation and the M-Z relation to redshift $z \simeq 2.5$. In this section, we will show the results of the luminosity-metallicity relation and the mass-metallicity relation, which provide im-

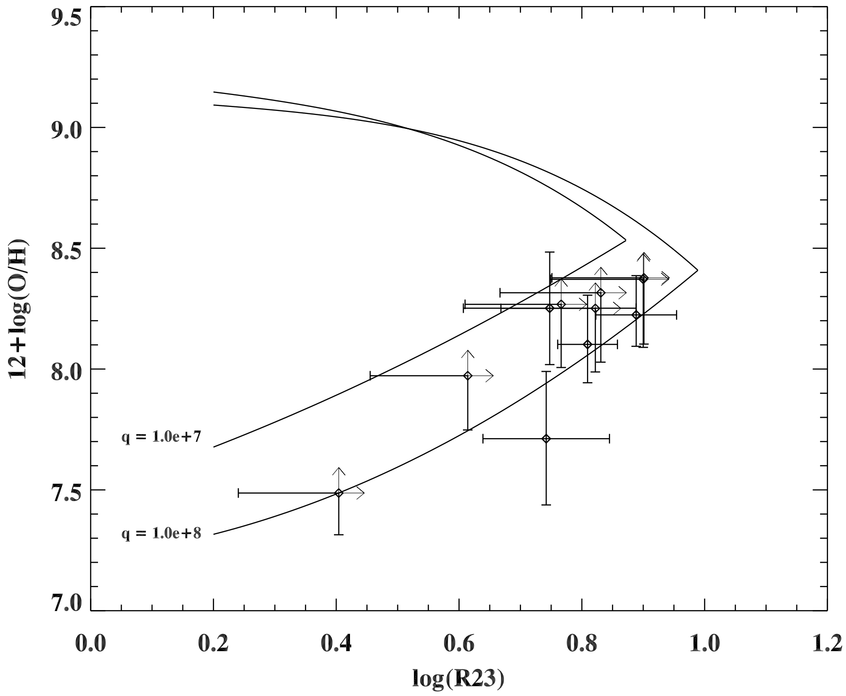

Figure 5.14: The log(R23) versus oxygen abundance for the 11 ELGs in the sample. The overplotted lines represent the theoretical lines at $q = 1.0 \times 10^7, 1.0 \times 10^8$ (Kobulnicky & Kewley, 2004). All of the galaxies are put on the lower branch according to the branch criteria. The 3σ upper limit of the Hβ line fluxes give the lower limit of log(R23) and hence the lower limit of 12+log(O/H) at the lower branch, which are shown as arrows.

portant clues to the evolution of galaxies by comparing with the relations at different redshifts.

L-Z relation

Previous results show important evolution of the slope and the zero point of the L-Z relation with respect to redshift, decreasing metallicity with increasing redshift at a given luminosity. With the sample of 11 grism ELGs at $0.6 < z < 2.4$, we investigate the evolution of the L-Z relation with redshift. Following traditions, we present the rest-frame absolute *B*-band magnitude as a measure of the luminosities.

The restframe B-band absolute magnitudes are computed from the best-fit SED with the BC03 stellar population synthesis model.

Figure 15 shows the relationship between the absolute rest-frame B magnitude versus the gas-phase oxygen abundance derived from $R23$ diagnostic indicator. The lines plotted in Figure 15 are the local L-Z relation obtained by Tremonti et al. (2004) for ∼53,000 SDSS galaxies at $z \sim 0.1$ (solid line), the L-Z relation obtained by Zahid et al. (2011) from 940 DEEP2 emission line galaxies at z $\sim$ 0.8 (dashed line), that obtained by Hu et al. (2009) from a sample of Ultra-Strong Emission-Line (USELs) galaxies at $z \simeq 0$–1 (dotted line and empty stars), and that of Salzer et al. (2009) for 15 star-forming galaxies at $z \sim 0.3$ (open upside down triangles). Our sample of 11 galaxies span a range in luminosity $–17 < M_B < –23$ and in metallicity $7.5 < 12+\log(\mathrm{O/H}) < 8.5$. The red solid dots represent the galaxies with $z > 1$, and the green triangles represent the galaxies with $z < 1$. The blue solid line shows the best linear fit of the 11 galaxies, a relation of $12+\log(\mathrm{O/H}) = (4.75 \pm 0.86) - (0.17 \pm 0.04) M_B$ with a correlation coefficience of –0.77.

Compared to the other relationships shown in Figure 15, ACS+WFC3 grism galaxies are about 7 magnitudes brighter in luminosities than the local SDSS galaxies and the $z \sim 0.8$ DEEP2 galaxies at fixed metallicity. The DEEP2 sample (Zahid et al., 2011) shows little evolution compared to the SDSS sample, about ~ 0.1 dex relative to the local L-Z relation, while the ERS grism galaxies show ~ 0.6 dex lower metallicities than the SDSS galaxies at given luminosity. The grism galaxies show a good match with metal-poor galaxies of Hu et al. (2009); Salzer et al. (2009) along the fitted L-Z relation.

The Hu et al. (2009) USELS galaxies have high equivalent width with EW(H$\beta >$ 30Å), extend to fainter galaxies to M$_B \sim$ –16 and show low metallicities of $7.1 < 12+\log(\mathrm{O/H}) < 8.4$. The Salzer et al. (2009) are [OIII]-selected galaxies ([OIII]/Hβ >3) at z ~0.3 and show brighter luminosity and higher metallicities. The difference of the galaxies on the L-Z figure shows the different physical properties of the three samples: the USELS are basically selected to be fainter dwarf galaxies, the low redshift Salzer et al. (2009) are [OIII]-selected lower redshift more evolved brighter galaxies. Since the three samples follow well of the L-Z relationship of the metal-poor galaxies, and the L-Z relations of the SDSS galaxies and the DEEP2 galaxies are obtained by averaging large samples, we conclude that the big offset in the L-Z relation between the local and the three metal-poor galaxies samples is due to the selection of a sample of young strong emission-line star-forming galaxies, which will be further illustrated in the next subsection.

M-Z relation

Figure 16 shows the relation between the stellar masses and the gas-phase oxygen abundances for the 11 star-forming galaxies in the sample at $0.6 < z < 2.4$. The solid line represents the *M-Z* relation at $z \sim 0.1$ from Tremonti et al. (2004) for the local SDSS galaxies, which are selected to be star-forming galaxies based on lines Hα, Hβ, and [NII]. The dashed line shows the *M-Z* relation at $z \sim 0.8$ for the 940 Hβ selected blue DEEP2 galaxies from Zahid et al. (2011). The dotted line and the dash-dotted line are UV-color selected galaxies at $z \sim 2.3$ from Erb et al. (2006) and the UV-selected Lyman Break Galaxies (LBGs) at $z \sim 3.1$ from Mannucci et al. (2009), respectively. The red line shows the best fit to the M-Z relation for the ELGs in the sample.

The green triangles illustrate the sample of the "green peas" from Cardamone et al. (2009) and Amorin et al. (2010), which are extremely compact (r$<$ 3 kpc) star-forming galaxies at $0.11 < z < 0.35$ selected by color from the SDSS spectroscopic observation, with an unsual large equivalent width of up to $\sim$ 1000 Å. We recalculate the gas-phase oxygen metallicity by the R23 method for the "green peas"

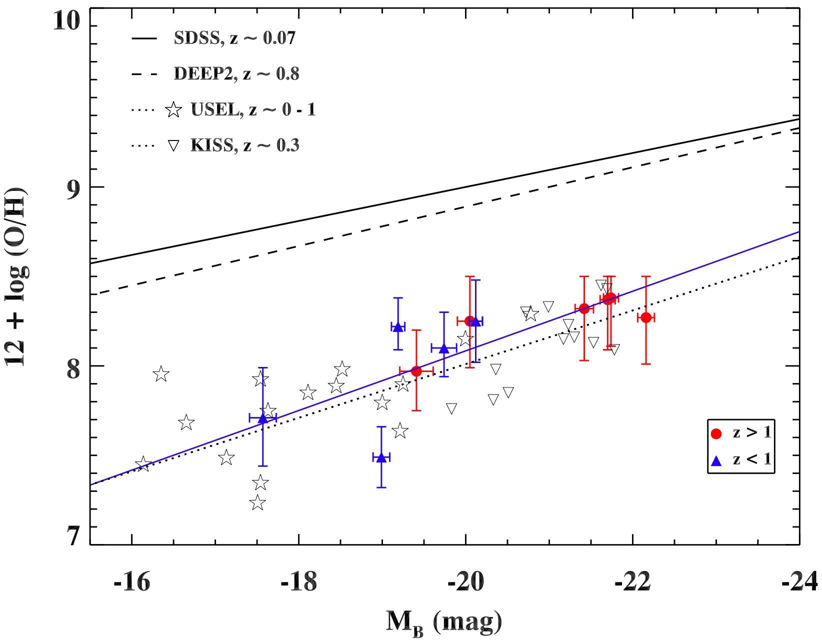

Figure 5.15: *L*-*Z* relation between the rest-frame *B*-band absolute magnitude versus the oxygen abundance for the 10 emission line galaxies at $0.6 < z < 2.4$. The metallicity is derived from the *R*23 indicator and the *x*-axis is the rest-frame *B*-band absolute magnitude. The red solid dots represent the galaxies with $z > 1$, and the blue triangles represent the galaxies with $z < 1$. The solid line represents the relation obtained by Tremonti et al. (2004) for SDSS star-forming galaxies at $z \sim 0.1$. The dashed line illustrates the relation obtained by Zahid et al. (2011) for DEEP2 galaxies at $z \sim 0.8$. The dotted line and the empty stars show the relation obtained by Hu et al. (2009) for USEL galaxies at $z = 0 - 1$. The empty upside down triangles are that of Salzer et al. (2009) for [OIII]-selected $z \sim 0.3$ galaxies. The blue solid line shows the best linear fit of the sample, which gives a relationship of $12 + log(O/H) = (4.75 \pm 0.86) - (0.17 \pm 0.04)M_B$. The PEARS sample shows an offset by about –0.6 dex in metallicity relative to the local relation at $z \sim 0.1$.

sample. Also plotted are the Lyα emitters at $z \sim 0.3$, and $\sim$2.3 from Finkelstein et al. (2011a,b), shown in empty red circles and black asterisks with 2 σ and 3 σ upper limits, and one extremely metal poor galaxies XMPG WISP5-230 (Atek et al., 2011). All data presented have been scaled to a Chabrier (2003) IMF. To ensure the consistency of the comparison, the conversion given by Kewley & Ellison (2008) is used to convert to the same metallicity calibration of Kobulnicky & Kewley (2004) to avoid the differences arising from different metallicity indicators (Zahid et al., 2011). The metallicity of the XMPG galaxy from Atek et al. (2011) is measured by the direct *Te* method, and is not converted to the same metallicity diagnostic due to the absence of the [OII] flux and the conversion relationship between the direct *Te* method and the R23 method in Kobulnicky & Kewley (2004).

From Figure 16, the grism galaxies span the range 8.1 $<$log$(M_*/\mathrm{M}_\odot) < 10.1$ and 7.5 $<$ 12+log(O/H) $<$ 8.5, with the average values of $<$log($\mathrm{M}_*/M_\odot$) $>=$ 9.3 and $<$12+log(O/H)$>=$ 8.1. Although this is a small sample, it shows a similar correlation between metallicity and stellar mass, increasing oxygen abundance with the increase of the stellar masses. The red dots in Figure 16 show the 6 galaxies with redshift $z > 1$ and with emission lines observed in WFC3 ERS. The blue triangles represent the galaxies with $0.6 < z < 1$. We fit the mass-metallicity relation with a second-order polynomial (Maiolino et al., 2008):

$$12 + log(O/H) = A[log(M) - log(M_0)]^2 + K_0, \tag{5.1}$$

the best fit parameters to the 11 ELGs in the sample give A=-0.07, log(M_0)=11.87, K_0=8.63. From Table 2, we see that these high redshift galaxies have higher stellar masses with a mean of $< logM_*/\mathrm{M}_\odot > \simeq$ 9.6 and higher metallicities with a mean of $<$12+log(O/H)$>\simeq$ 8.3. The low redshift subsample have lower galaxy stellar masses with a mean of $<$log$M_*/\mathrm{M}_\odot$$>\simeq$ 8.8 and lower metallicities with a mean of $<$12+log(O/H)$>\simeq$ 8.0. The offset shown between the high redshift subsample and the low redshfit subsample includes the evolution of the M-Z relation with redshift, and the selection effect, that for the same emission line detection the high redshift galaxies tend to be more luminous, more massive and more metal-enriched than the low redshift galaxies.

We examine the M-Z relation by comparing our sample with that at different redshift ranges. Compared with the local relation at $z \sim 0.1$, the SDSS galaxies with comparable stellar mass to the average of the grism sample, $M_* \sim 10^{9.3}$ $\mathrm{M}_\odot$, have $12+\log(O/H) \simeq 8.8$, which is about ~ 0.6 dex higher than the average of the grism galaxies. For the low redshift subsample with a mean of $z \simeq 0.8$, the M-Z relation show a large offset of ~ 0.6 dex with that of Zahid et al. (2011) at $z \simeq 0.8$ too. This big difference between our sample and that of Tremonti et al. (2004) and Zahid et al. (2011) is mainly due to the different selection criteria of the galaxies. The local SDSS galaxies (Tremonti et al., 2004) and the DEEP2 galaxies (Zahid et al., 2011) are obtained from large spectroscopy survey, and the M-Z relations show the average relationships of the dominant galaxy populations at that redshift. Table 3 lists the physical properties including redshift range, selection, absolute magnitude, emission line EW, half light radius and SFR of the different comparing samples. We can see that the SDSS and DEEP2 samples are not selecting high EW star-forming galaxies compared with the "green peas" (Amorin et al., 2010), USELS (Hu et al., 2009), LBGs (Mannucci et al., 2009) and our PEARS/ERS ELGs, which are biased to high EW emission-line (up to ~ 1000 Å) and compact ($r_{1/2} < 3$ kpc) galaxies.

For the high-redshift subsample with a mean of $z \simeq 2$, the M-Z relation shows an offset of ~ 0.2 dex with respect to that of the LBGs at $z \simeq 2.3$ (Erb et al., 2006). The low metallicity galaxies basically fall between the relation at $z \simeq 2.3$ and $z \simeq 3.1$ and have low metallicities down to 12+log(O/H)$\sim$7.5, 7.7. The "green peas" (Hoopes et al., 2007; Overzier et al., 2008; Amorin et al., 2010) at $z \simeq 0.3$ are found to be metal-poor by ~ 0.5 dex relative to other galaxies of similar stellar mass, and show compact and distrubed morphology. From Figure 16, we find that 7 out of 11 of the HST/ACS+WFC3 grism emission line galaxies are in the similar metallicity range 12+log(O/H)$\sim$8.3 and four galaxies are more metal-poor by up to 0.6 dex, compared with the green peas at the same galaxy stellar masses, which shows significant chemical enrichment from $z \simeq 0.8$ to $z \simeq 0.3$ at the low stellar mass range. To confirm this evolution with higher statistical significance, we will need larger sample of galaxies extending to low mass faint galaxies at high redshifts. The strong emission line selected Lyα galaxies at $z \simeq 0.3$, at $z \simeq 2.3$ and XMPG WISP5_230 at $z \simeq 0.7$ show similar lower metallicities at $7.2 < 12 + log(O/H) < 8.2$ with respect to the average M-Z relations obtained from large survey samples.

The detailed analysis of the morphologies, sizes, colors, SSFRs based on the M-Z relation (Pirzkal et al., 2006; Xia et al., 2012) show that the strong emission-line selected grism galaxies are biased towards young compact interacting dwarf star-forming galaxies. Pirzkal et al. (2006) shows small physical sizes of $\sim$ 1–2 kpc for the emission line galaxies observed from the GRAPES survey, and Xia et al. (2012) presents high SSFRs $10^{-9} - 10^{-7}/yr$ for the ELGs from the PEARS survey. Since the galaxies in our sample are partly the subsample of the PEARS ELGs, the results of the sizes and the SSFRs are consistent with the previous results, with $r_{1/2} < 3kpc$ and $SSFR \sim 10^{-9}/yr$. This confirms the selection effects of the young compact disturbed emission line galaxies in the sample. The early stage of galaxy evolution (downsizing effect) or interaction-induced pristine gas inflow picture may account for the offset of the grism galaxies in metallicity relative to the local sample.

5.6 Discussion and Summary

We use a sample of 11 emission line galaxies at $0.6 < z < 2.4$ observed by HST/ACS PEARS and HST WFC3 ERS programs at 0.6–1.6 μm to demonstrate the effective-

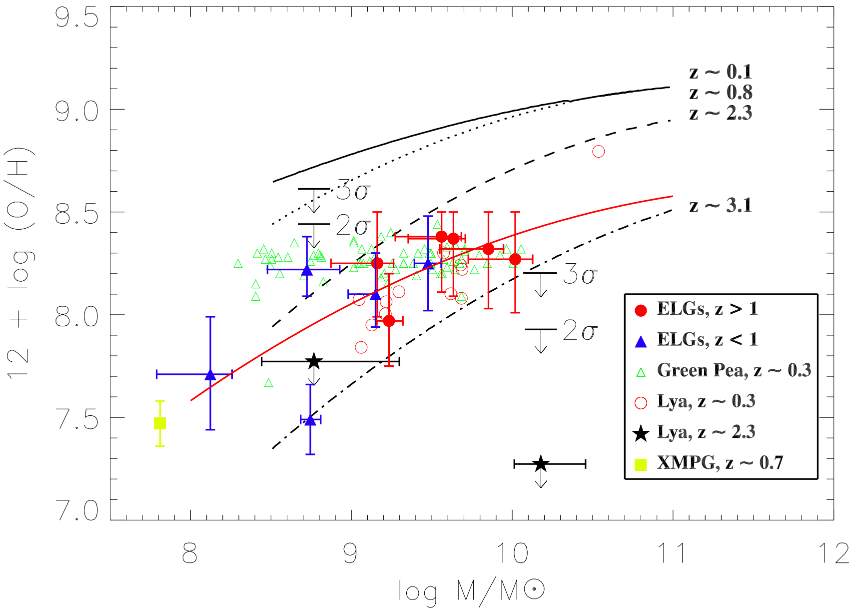

Figure 5.16: Relation between the stellar masses and the gas-phase oxygen abundances for our sample of 11 ELGs from PEARS and ERS grism data at $0.6 < z < 2.4$. The metallicities are estimated from the $R23$ method and the stellar masses are estimated from the SED fitting with $BC03$ model. The definition of the points of our sample are the same as Figure 14. Also plotted for comparison are the green peas (empty green triangulars) at z≃0.3 (Amorin et al., 2010), Lyα galaxies at $z \simeq 0.3$ and $z \simeq 2.3$ (Finkelstein et al., 2011a,b), and the WISP XMPG galaxy at $z \simeq 0.7$ (Atek et al., 2011). The solid red line is the best fit of the M-Z relation to the 11 ELGs in our sample. The solid line represents the M-Z relation at $z \simeq 0.1$ from Tremonti et al. (2004) for the local SDSS galaxies. The dashed line shows the M-Z relation at $z \simeq 0.8$ for the 940 DEEP2 galaxies from Zahid et al. (2011). The dotted line and the dash-dotted line are that at $z \simeq 2.3$ from Erb et al. (2006) and at $z \simeq 3.1$ from Mannucci et al. (2009), respectively. The M-Z relations at different redshifts are calibrated to the same metallicity indicator of Kobulnicky & Kewley (2004) from Zahid et al. (2011). The large offset of ~ 0.5 dex of this sample relative to the other relations at similar redshift demonstrates that these galaxies may be at the early-stages of galaxy evolution. Infall of gas due to mergers is another popular explanation, e.g. Peeples et al. (2009).

ness of the grism spectra (R $\sim$ 100–300) used for the metallicity measurement. With the [OII], Hβ, and [OIII] lines in the composite spectra of the two grism spectra surveys, we use the $R23$ method to derive the gas-phase oxygen abundances, 12+log(O/H). For two galaxies which have the follow-up Magellan spectroscopy, the metallicities obtained from the grism spectra and from the Magellan spectroscopic spectra are consistent to within 1 σ (0.1 dex), which demonstrates the feasibility of the HST/WFC3 IR grism spectra used here for the study of galaxy metallicities.

The measured gas-phase abundances are in the low metallicity range 7.5 $<$ 12+log(O/H) $<$ 8.5. The galaxy stellar masses are derived from MCMC SED fitting and span the range 8.1 $<$ log($M_*/\mathrm{M}_\odot$) $<$ 10.1. Both the L-Z relation and the M-Z relation show that with the increase of the galaxy stellar mass or the luminosity, the metallicity increases, which agrees with the enrichment history of galaxy evolution. The M-Z relation of this sample show significant offset by about –0.6 dex in metallicity at given stellar mass relative to the local M-Z relation from SDSS galaxies and the galaxies from the DEEP2 survey at similar redshifts $z \simeq 0.8$. The L-Z relation is fitted by a straight line of 12+log(O/H) $= (4.75 \pm 0.86) - (0.17 \pm 0.04) M_B$ with a correlation coefficience of –0.77, which is also offset by about –0.6 dex in metallicity relative to the local and $z \simeq 0.8$ L-Z relations.

Our sample of galaxies at $z \simeq 0.8$ show similarity to the local green peas in morphology and low metallicity. Two galaxies show significant poorer metallicity by $\sim$0.5 dex compared with the "green peas" at the same galaxy stellar masses, which signifies different physical processes in the galaxy evolution and chemical enrichment from $z \simeq 0.8$ to $z \simeq 0.2$ at the low stellar mass range. The different contribution by downsizing and gas inflow/outflow need to be examined in detail by larger samples further.

By comparing the PEARS/ERS sample with other emission-line selected samples, We find that the physical properties of the ELGs galaxies at different redshifts show great similarities: e.g. (1) ultra-strong emission lines of about 10^{-17}erg cm^{-2} s^{-1}, high emission-line EWs up to ~ 1000 Å, and hence very high SSFRs to $10^{-9}/yr$; (2) compact morphology ($r_{1/2} < 3kpc$); (3) evidence for mergers/interactions from the asymmetries of the morphology, such as companions and wispy tidal tails around a compact star-forming region, three "green peas" shown in Cardomone et al. (2009), and 10 out of 11 galaxies in our sample (see Figure 12). Hence, we conclude that the offsets shown in the M-Z and L-Z relations with respect to that obtained from average of large sample are mainly due to the selection effects based on prominent emission lines. van der Wel et al. (2011) shows an abundant population of extreme emission line galaxies (EELGs) from the HST/WFC3 CANDELS Survey (Cosmic Assembly Near-IR Deep Extragalactic Legacy Survey) and confirms the physical properties of low stellar masses $\sim 10^8 M_{\odot}$, and strong outflows due to enormous starbursts in the EELGs by the HST/WFC3 grism spectra.

Taken together, the properties of the ELGs: compact starbursts, low metallicities, disturbed morphologies, and low masses, indicate that these are dwarf galaxies undergoing their early stages of galaxy evolution with prominent signs of strong activities of interaction (gas accretion and outflow) with companion galaxies. Both the downsizing effect and the inflow/outflow play important roles in these low metallicity galaxies' evolution. To examine the mode of the star-formation of these low-mass, low-metallicity galaxies in the whole scenario of galaxy evolution requires a larger sample of this kind of ELGs from optical to NIR spectroscopy with morphologies to give us a more comprehensive picture of these galaxies. Trump et al. (2011) presents a sample of 28 emission line galaxies at $z \sim 2$ with prominent [OIII] and Hβ in the GOODS-S region of the Cosmic Assembly Near-infrared Deep Extra-galactic

Legacy Survey(CANDELS). Combined with the PEARS spectra, this sample will greatly enhance the sample at redshift z 2 at the low-mass low-metallicity region of the M-Z relation, which is important to study and understand the physical processes effecting galaxy evolution.

This paper is based on Early Release Science observations made by the WFC3 Scientific Oversight Committee. PEARS is an HST Treasury Program 10530 (PI: Malhotra). Support for program was provided by NASA through a grant from the Space Telescope Science Institute, which is operated by the Association of Universities for Research in Astronomy, Inc., under NASA contract NASA5-26555 and is supported by HST grant 10530.

Table 5.1: The extinction corrected emission line fluxes and equivalent widths of the PEARS/ERS grism galaxies. The Hβ line fluxes are absorption corrected by the SED fitting. The detections of the Hβ line are set with S/N>3. The 3σ upper limit of the Hβ line is used for galaxies with S/N<3. These galaxies are marked with stars.

ID	z	R.A. (deg)	DEC. (deg)	E(B-V) (mag)	[OII]3727 (10^{-18}erg s^{-1} cm^{-2})	EW([OII]) (Å)	Hβ (10^{-18}erg s^{-1} cm^{-2})	EW(Hβ) (Å)	[OIII] (10^{-18}erg s^{-1} cm^{-2})	EW([OIII]) (Å)
339	0.602	53.0773392	-27.7081985	$0.30^{+0.30}_{-0.30}$	645.51 ± 162.65	29	468.41 ± 45.19	61	2373.95 ± 56.24	334
364	0.642	53.0693359	-27.7090893	$0.03^{+0.18}_{-0.03}$	80.90 ± 15.93	40	50.35 ± 7.24	38	308.61 ± 9.59	248
246	0.696	53.0700035	-27.7165890	$0.03^{+0.16}_{-0.03}$	4.50 ± 4.50	26	22.90 ± 5.22	352	121.91 ± 6.92	1605
454	0.847	53.0761719	-27.7011452	$0.16^{+0.09}_{-0.10}$	166.57 ± 17.80	28	45.22 ± 13.92	11	86.35 ± 18.02	22
258	0.998	53.0857124	-27.7113400	$0.03^{+0.06}_{-0.03}$	29.98 ± 4.25	74	73.63 ± 35.74 $\star$	525	241.91 ± 47.48	729
432	1.573	53.0484200	-27.7095337	$0.08^{+0.16}_{-0.08}$	101.97 ± 23.19	44	24.21 ± 11.76 $\star$	16	132.11 ± 15.56	108
563	1.673	53.0705452	-27.6956444	$0.14^{+0.20}_{-0.14}$	93.91 ± 17.34	46	13.95 ± 9.06 $\star$	19	122.04 ± 11.86	165
103	1.682	53.0633392	-27.7272835	$0.06^{+0.13}_{-0.06}$	43.55 ± 10.23	93	9.84 ± 7.81 $\star$	45	52.83 ± 10.33	193
195	1.745	53.0656700	-27.7203941	$0.09^{+0.09}_{-0.09}$	87.84 ± 13.89	37	21.25 ± 8.28 $\star$	17	109.87 ± 10.91	94
242	2.070	53.0821304	-27.7137547	$0.19^{+0.17}_{-0.17}$	94.79 ± 29.03	72	13.39 ± 8.57 $\star$	25	79.46 ± 11.19	143
578	2.315	53.0589218	-27.6978111	$0.26^{+0.11}_{-0.19}$	116.58 ± 21.06	98	12.29 ± 10.42 $\star$	10	65.98 ± 13.53	35

Table 5.2: The ionization parameter, metallicity, half-light radius, absolute magnitude, galaxy stellar mass and SFR, SSFR of the PEARS/ERS grism galaxies. The missing upper errors in log$R$23 and 12+log(O/H) denote the lower limits due to the use of the upper limits of Hβ line fluxes.

ID (1)	z (2)	log(R23) (3)	log q (4)	12+log(O/H) (5)	$r_{1/2}$ (kpc)	M_B (mag)	log M_* ($M_\odot$)	Age (Myr)	SFR ($M_\odot$/yr)	SSFR ($\times10^{-9}$/yr)
339	0.604	$0.81^{+0.05}_{-0.05}$	8.12 ± 1.28	$8.10^{+0.20}_{-0.16}$	8.10	–19.74	$9.19^{+0.02}_{-0.34}$	—	15.20 ± 1.72	10.64 ± 4.16
364	0.637	$0.89^{+0.07}_{-0.07}$	7.97 ± 0.10	$8.22^{+0.16}_{-0.13}$	1.72	–19.19	$8.72^{+0.21}_{-0.25}$	$56.9^{+27.7}_{-53.7}$	1.70 ± 0.39	1.90 ± 0.84
246	0.691	$0.74^{+0.10}_{-0.10}$	8.58 ± 0.51	$7.71^{+0.28}_{-0.27}$	1.97	–17.57	$8.12^{+0.14}_{-0.33}$	$50.4^{+0.04}_{-47.1}$	1.06 ± 0.21	3.31 ± 0.81
454	0.847	$0.75^{+0.14}_{-0.14}$	7.29 ± 0.17	$8.25^{+0.23}_{-0.23}$	1.37	–20.12	$9.48^{+0.08}_{-0.08}$	$60.8^{+71.5}_{-32.1}$	2.41 ± 1.40	0.60 ± 0.37
258	0.997	$0.40^{+}_{-0.16}$	8.02 ± 0.11	$7.49^{+}_{-0.17}$	2.20	–18.99	$8.74^{+0.06}_{-0.06}$	$90.1^{+35.8}_{-35.3}$	5.78 ± 3.66	7.83 ± 5.61
432	1.573	$0.82^{+}_{-0.15}$	7.58 ± 0.13	$8.25^{+}_{-0.26}$	4.14	–20.05	$9.16^{+0.10}_{-0.29}$	$51.0^{+44.5}_{-47.8}$	2.71 ± 2.44	1.73 ± 1.56
563	1.673	$0.90^{+}_{-0.15}$	7.64 ± 0.13	$8.37^{+}_{-0.28}$	1.58	–21.70	$9.63^{+0.07}_{-0.28}$	$46.5^{+52.2}_{-43.3}$	3.66 ± 2.24	0.51 ± 0.37
103	1.682	$0.61^{+}_{-0.16}$	7.46 ± 0.12	$7.97^{+}_{-0.22}$	1.07	–19.41	$9.23^{+0.08}_{-0.07}$	$93.1^{+72.8}_{-68.8}$	1.59 ± 1.35	0.88 ± 0.83
195	1.745	$0.90^{+}_{-0.15}$	7.61 ± 0.10	$8.38^{+}_{-0.27}$	1.89	–21.74	$9.56^{+0.13}_{-0.29}$	$23.9^{+29.2}_{-20.8}$	3.80 ± 2.02	2.30 ± 1.22
242	2.070	$0.83^{+}_{-0.16}$	7.46 ± 0.21	$8.32^{+}_{-0.29}$	2.09	–21.42	$9.85^{+0.09}_{-0.30}$	$39.7^{+55.1}_{-36.5}$	14.51 ± 9.60	1.91 ± 1.37
578	2.315	$0.77^{+}_{-0.16}$	7.32 ± 0.16	$8.27^{+}_{-0.26}$	5.82	–22.16	$10.02^{+0.11}_{-0.29}$	$19.0^{+40.2}_{-15.8}$	19.17 ± 12.81	0.50 ± 0.53

Table 5.3: The selection criteria and physical properties of the comparison samples in the paper.

Sample (1)	Survey (2)	z (3)	Selection (4)	f_{line} (10^{-17}erg cm^{-2} s^{-1})	M_B (mag)	EW (Å)	r$_{1/2}$ (kpc)	SFR (M$_{\odot}$/yr)
Tremonti et al. (2004);	SDSS	$0.005 < z < 0.25$	Hα, Hβ, [NII]	—	(-16, -22)	EW(Hα) $\sim$3-200	–	–
Salzer et al.(2009);	KISS	$z \sim 0.3$	[OIII]	—	(-19.5, -22.5)	—	–	–
Amorin et al. (2010); green pea	SDSS	$0.11 < z < 0.35$	color	—	—	EW([OIII]) < 1000	< 3	< 30
Zahid et al. (2011)	DEEP2	$0.75 < z < 0.82$	Hβ, color	—	(-19.5, -22)	$<$EW(Hβ)$>\sim$8.9	–	–
Hu et al. (2009); USELS	DEMOS	$0 < z < 1$	[OIII], Hα	> 1.5	(-16, -21)	EW(Hβ) < 500	–	–
Erb et al. (2011);	LRIS-B	$z \sim 2.3$	UV-colors	> 15	(-20.5, -23.5)	—	–	20 – 60
Mannucci et al. (2009); LBGs	AMAZE, LSD	$2.6 < z < 3.4$	—	> 1.1	—	—	0.7 – 2.4	5 – 40
This paper	PEARS, ERS	$0.6 < z < 2.3$	Emission lines	> 5	(-17.5, -22.5)	EW([OIII]) < 1600	1 – 8.1	1 – 20

Chapter 6

CONCLUSIONS

This dissertation presents the results of the study of galaxy chemical evolution by HST/ACS PEARS emission-line selected galaxies. The primary goal of this study is to extend the galaxy mass-metallicity relation to faint low mass end and to high redshift, to explore the orgin of the mass-metallicity relation and hence to understand the physical processes effecting galaxy formation and evolution.

In Chapter 2, I apply the surface luminosity priors to 1266 galaxies observed with HST/ACS PEARS grism spectra, with GOODS *BViz* broad-band photometry, and with known ground-based redshifts in the range of $0.1 < z < 2.0$. By comparing the redshift estimation with and without SL priors, the new method improves the number of galaxies with $|\Delta(z)| > 0.2$ from 15.0% to 10.4%. The RMS scatter does not change much. The improvement seems same for the blue galaxies and the 283 red galaxies, while the red galaxies show higher accuracy in redshift estimation. The result shows the efficiency of the SL priors in breaking the degeneracy of SPZ redshifts for low-redshift Balmer break galaxies and high redshift Lyman break galaxies.

In Chapter 3, I present the Magellan LDSS-3 follow-up spectroscopy of a sample of HST/ACS PEARS emission-line pre-selected galaxies. The first part of this Chapter assess the accuracy of the grism redshifts which are measured from the pattern of the emission lines and find an accuracy of $\sigma_z = 0.006$ for the grism redshifts. The emission-line galaxies are classified to star-forming galaxies and AGNs by methods of cross-checking with CDF-S X-ray detection, BPT diagram, and high ionization indictator emission lines.

In Chapter 4, I use the catalog of the star-forming galaxies produced from the work of Chapter 3 to study the relationship between the gas-phase oxygen abundances, stellar masses, rest-frame B-band absolute magnitudes, half-light radii and morphologies. The PEARS star-forming galaxies span the rest-frame B-band absolute magnitude range – 19 $< M_B <$ – 24, extend to low mass 7.5 $< log(M_*/M_\odot) <$ 10.5 and span the low metallicity range 7.8 $<$ 12+log(O/H) $<$ 8.9. Both the $M-Z$ relation and the L-Z relation of the PEARS galaxies show that galaxies with brighter M_B and larger M_* also have higher oxygen abundance, and the PEARS galaxies are offset by $\sim$ – 0.5 dex in metallicity for a given luminosity and stellar mass relative to the local relations. By examining the physical properties of the PEARS ELGs, it is shown that the scatter of the galaxies on the M-Z relation is basically due to the different evolutionary stages and the physical properties of the galaxies. The high metallicity PEARS galaxies show spiral morphologies, red colors and large masses. The low metallicity PEARS galaxies have low masses, blue colors, compact disturbed morphologies, and high SSFRs.

The study of the evolution of the M-Z relation at different redshifts show that the PEARS ELGs lie on the relationships of $z \sim$ 2.2 and 3.1 Erb et al. (2006); Mannucci et al. (2009), which is characterized by $<$ 12+log(O/H) $>$ = 8.2 and $< log(M_*/M_\odot) >=$ 9.12 , and overlap with the region of the “green peas” of Amorin et al. (2010). The big offset of PEARS ELGs relative to the local galaxies and other similar redshift galaxies in the $M-Z$ relation can be interpreted basically by the different evolutionary stages of the galaxies and the interacting-induced pristine inflow gases or outflows. By fitting with the models with inflows and outflows, the best fit gives the model with solar true yield $y = Z_\odot$ and a dominant inflow of 1$\times$SFR and an outflow rate of 0.1$\times$SFR. Due to the different calibrations of the gas fraction for massive galaxies and dwarf galaxies, and due to the absence of the calibration for high redshift galaxies, the gas fractions derived from the local K-S law may introduce uncertainties to the results of the true stellar yield and the estimation of the inflow and outflow rates from the model.

In Chapter 5, I extend the study of the chemical evolution of PEARS galaxies to high redshift $0.6 < z < 2.4$ by a sample of 11 galaxies with the composite grism spectra (R $\sim$ 100–300) at 0.6–1.6 μm observed by HST/ACS PEARS and HST WFC3 ERS programs. The first goal of this study is to demonstrate the effectiveness of the grism spectra used for metallicity measurement extending to faint galaxies at high redshift and to study the chemical evolution of early stages galaxies at high redshift. The results show that the PEARS ELGs have low gas-phase abundances with $7.5 <$ 12+log(O/H) < 8.5 and low galaxy stellar masses $8.1 < \log(M_*/\mathrm{M}_\odot) < 10.1$. Both the L-Z relation and the M-Z relation show that with the increase of the galaxy stellar mass or the luminosity, the metallicity increases, which agrees with the enrichment history of galaxy evolution. The large offsets in the both relations relative to the local galaxies combined with the physical properties of distrubing compact morphologies, high specific SFR of these galaxies, the downsizing and the interaction trigered star formation with inflows or outflows may account for the large offset in the $L-Z$ and $M-Z$ relations. While the more accurate explanation of the origin of the evolution require larger sample of emission-line galaxies at high redshift and spanning wide range of physical properties.

REFERENCES

Abraham, R., van den Bergh, S., & Nair, P. 2003, ApJ, 588, 218

Allende Prieto, C. A., Lambert, D. L., & Asplund, M. 2001, ApJ, 556, L63

Amorin, R. O., Enrique, P. M., & Vilchez, J. M. 2010, ApJ, 715, 128

Asplund, M., Grevesse, N., Sauval, A. J., Allende Prieto, C., & Kiselman, D. 2004, A&A, 417, 751

Atek, H., et al. 2011, Arxiv:1109.0639

Baldwin, J. A., Phillips, M. M., & Terlevich, R. 1981, PASP, 93, 5

Baum, W. A. 1962, IAU Symp. 15: 15, 390

Bell, E. F., & de Jong, R. S. 2000, MNRAS, 312, 497

Bender, R. 1996, New Light on Galaxy Evolution (Dordrecht: Kluwer)

Benítez, N. 2000, ApJ, 536, 571

Benson, A. J., Bower, R. G., Frenk, C. S., Lacey, C. G., Baugh, C. M., & Cole, S. 2003, ApJ, 599, 38

Blanton, M. R. et al. 2003, AJ, 125, 2348

Bolzonella, M., Miralles, J.-M., & Pelló, R. 2000, A&A, 363, 476

Bouche, N., Cresci, G., Davies, R. et al. 2007, ApJ, 671, 303

Brodie, J. P., & Huchra, J. P. 1991, ApJ, 379, 157

Bruzual, G., & Charlot, S. 2003, ApJ, 405, 538

Budavári, T., Szalay, A. S., Connolly, A. J., Csabai, I., Dickinson, M. E., & the HDF/Nicmos Team 1999, ASPC, 191, 19

Budavári, T., Szalay, A. S., Connolly, A. J., Csabai, I., & Dickinson, M. E. 2000, AJ, 120, 1588

Budavári, T., et al. 2001, AJ, 121, 1163

Calura, F., Jimenez, R., Panter, B., Matteucci, F., & Heavens, A. F. 2008, ApJ, 682, 252

Calura, F., Pipino, A., Chiappini, C., et al. 2009, A&A, 504, 373

Calzetti, D., et al. 2000, ApJ, 533, 682

Capak et al. 2004, AJ, 127, 180

Cardamone, C., et al. 2009, MNRAS, 399, 1191

Chary, R., & Elbaz, D. 2001, ApJ, 556, 562

Cohen, S. et al. 2009, AAS, 21342426

Connolly, A. J., Csabai, I., Szalay, A. S., Koo, D. C., Kron, R. G., & Munn, J. A. 1995, AJ, 110, 2655

Contini, T., Treyer, M. A., Sullivan, M., & Ellis, R. S. 2002, MNRAS, 330, 75

Coppin, K. E. K., Swinbank, A. M., Neri, R., et al. 2007, ApJ, 665, 936

Cowie, L. L., Songaila, A., Hu, E. M., & Cohen, J. G. 1996, AJ, 112, 839

Cowie, L. L. & Barger, A. J. 2008, ApJ, 686, 72

Coziol, R., Contini, T., Davoust, E., & Considere, S. 1997, ApJ, 481, 67

Cresci, G., Mannucci, F., Sommariva, V., Maiolino, R., Marconi, A., & Brusa, M. 2011, ArXiv:1110.4408

Csabai, I., Connolly, A. J., Szalay, A. S., & Budavari, T. 2000, AJ, 119, 69

Dahlem, M., Weaver, K. A., & Heckman, T. M. 1998, ApJS, 118, 401

Dalcanton, J. J. 2007, ApJ, 658, 941

Dekel, A., & Woo, J. 2003, MNRAS, 344, 1131

Di Matteo, T., Springel, V., & Hernquist, L. 2005, Nature, 433, 604

Dickinson, M., Papovich, C., Ferguson, H. C., & Budavari, T. 2003, ApJ, 587, 25

Driver, S., Windhorst, R., Griffiths, R. 1998 ApJ 453, 48

Edmunds, M. G. & Pagel, B. E. J. 1984, ApJ, 211, 507

Edmunds, M. G. 1990, MNRAS, 246, 678

Ellison, S. L., Patton, D. R., Simard, L., & McConnachie, A. W. 2008, ApJ, 672, 107

Erb, D. K., Shapley, A. E., Pettini, M., et al. 2006, ApJ, 644, 813

Erb, D. K., Shapley, A. E., Pettini, M., et al. 2006, ApJ, 644, 813

Faber, S. M., et al. 2003, Proc. SPIE, 4841, 1657

Fernández-Soto, A., Lanzetta, K. M., Yahil, A. 1999, ApJ, 513, 34

Ferreras, I. et al. 2009, 396, 1573

Finkelstein, S. L., et al. 2011, ApJ, 729, 140

Finkelstein, S. L., et al. 2011, ApJ, 733, 117

Frye, B., Broadhurst, T., & Benitez, N. 2002, ApJ, 568, 558

Gallazzi, A., Charlot, S., Brinchmann, J., & White, S. D. M. 2006, MNRAS, 370, 1106

Garnett, D. R., & Shields, G. A. 1987, ApJ, 317, 82

Garnett, D. R., Shields, G. A., Skillman, E. D., Sagan, S. P., & Dufour, R. J. 1997, ApJ, 489, 63

Garnett, D. R. 2002, ApJ, 581, 1019

Gavazzi, G. & Scodeggio, M. 1996, A&A, 312, L29

Giavalisco, M., et al. 2004, ApJ, 600, 93

Glazebrook, K. et al. 2004, Nature, 430, 181

Grazian, A., et al. 2006, A&A, 449, 951

Halliday, C., Daddi, E., Cimatti, A., et al. 2008, A&A, 479, 417

Hathi, N. P., Malhotra, S., & Rhoads, J. E. 2008, ApJ, 673, 686

Hayashi, M., Motohara, K., Shimasaku, K., et al. 2009, ApJ, 691, 140

Heckman, T. M., Armus, L., & Miley, G. K. 1990, ApJS, 74, 833

Hernquist, L. & Mihos, J.C. 1995, ApJ, 448, 41

Hernquist, L., & Springel, V. 2003, MNRAS, 341, 1253

Hickson, P., Gibson, B. K., & Callaghan, K. A. S. 1994, MNRAS, 267, 911

Hoopes, C. G., et al. 2007, ApJS, 173, 441

Hopkins, P., Hernquist, L., Cox, T., Di Matteo, T., Robertson, B., k Springel, V. 2006, ApJS, 163, 1

Hopkins, P., Hernquist, L., Cox, T., k Dusan, K. 2008, ApJS, 175, 365

Hu, E. M., Cowie, L. L., Kakazu, Y., & Barger, A. J. 2009, 698, 2014

Kakazu, Y., Hu, E. M., & Cowie, L. L. 2007 ApJ, 668, 853

Kauffmann, G. et al. 2003, MNRAS, 346, 1055

Kennicutt, R. C. 1998, ARAA, 36, 189

Kewley, L. J., Dopita, M. A., Sutherland, R. S., Heisler, C. A. & Trevena, J. 2001, ApJ, 556, 121

Kewley, L. J., & Dopita, M. A. 2002, ApJS, 142, 35

Kewley, L. J., & Ellison, S. L. 2008, ApJ, 681, 1183

Kobulnicky, H. A., & Zaritsky, D. 1999, ApJ, 511, 118

Kobulnicky, H. A., & Koo, D. C. 2000, ApJ, 545, 712

Kobulnicky, H. A. et al. 2003, ApJ, 599, 1006

Kobulnicky, H. A., & Kewley L. J. 2004, ApJ, 617, 240

Komatsu et al. 2009, ApJS, 180, 330

Komatsu, G., et al. 2011, ApJS, 192, 18

Koo, D. C. 1985, AJ, 90, 418

Koo, D. C. 1999, ASPC, 191, 3

Koppen, J., Weidner, C., & Kroupa, P. 2007, MNRAS, 375, 673

Kurtz, M. J., Geller, M. J., Fabricant, D. G., Wyatt, W. F., & Dell Antonio, I. P. 2007, AJ, 134, 1360

Larson, R. B. 1974, MNRAS, 169, 229

Larson, R. B., & Tinsley, B. M. 1978, ApJ, 219, 46

Larson, R. B., & Dinerstein, H. L. 1975, PASP, 87, 911

Lamareille, F., Mouhcine, M., Contini, T., Lewis, I., & Maddox, S. 2004, MNRAS, 350, 396

Lamareille, F., Brinchmann, J., Contini, T., et al. 2009, A&A, 495, 53

Lee, H., Skillman, E. D., Cannon, J. M., et al. 2006, ApJ, 647, 970

Lehnert, M. D., & Heckman, T. M. 1996, ApJ, 472, 546

Lequeux, J., Rayo, J. F., Serrano, A., Peimbert, M., & Torres-Peimbert, S. 1979, A&A, 80, 155

Leroy, A. K., et al. 2008 AJ, 136, 2782

Lilly, S. J., Le Fevre, O., Hammer, F., & Crampton, D. 1996, ApJ, 460, L1

Lilly, S. J., Carollo, C. M., & Stockton, A. N. 2003, ApJ, 597, 730

Liu, X. et al. 2008, ApJ, 678, 758

Lotz, J. M., Parimack, J., & Madau, P. 2004, AJ, 128, 163

Luo, B., et al. 2008, ApJS, 179, 19

Madau, P., et al. 1996, MNRAS, 283, 1388

Maier, C. et al. 2006, ApJ, 643, 584

Maiolino, R., Nagao, T., Grazian, A., et al. 2008, A&A, 488, 463

Malhotra, S. 2005, HST, prop10530

Mannucci, F., Cresci, G., Maiolino, R. et al. 2009, MNRAS, 398, 1915

Mannucci, F., Cresci, G., Maiolino, R., & Gnerucci, A. 2010, MNRAS, 408, 2115

Martin, C. L. 1999, ApJ, 513, 156

McGaugh, S. S. 1991, ApJ, 380, 140

McGaugh, S. S., & de Blok, W. J. G. 1997, ApJ, 481, 689

Melbourne, J., & Salzer, J. J. 2002, AJ, 123, 2302

Meurer, G. R., Heckman, T. M., Lehnert, M. D., Leitherer, C., & Lowenthal, J. 1997, AJ, 114, 54

Meurer, G. R., et al. 2007, AJ, 134, 77

Mobasher, B., et al. 2004, ApJ, 600, 167

Mobasher, B., et al. 2007, ApJ, 172, 117

Murray, N., Quataert, E., & Thompson, T. A. 2005, ApJ, 618, 569

Naab, T., & Ostriker, J. P. 2006, MNRAS, 366, 899

Nagamine, K., Springel, V., Hernquist, L., & Machacek, M. 2004, MNRAS, 350, 385

Noeske, K. G., et al. 2007, ApJ, 660, L43

Oemler, A., Clardy, K., Kelson, D., Walth, G., Villanueva, E. 2009, COSMOS Version 2.13

Oke, J. B., & Gunn, J. E. 1983, ApJ, 266, 713

Overzier, R. A., et al. 2008, ApJ, 677, 37

Pagel, B. E. J., & Patchett, B. E. 1975, MNRAS, 172, 13

Pagel, B. E. J. et al. 1979, MNRAS, 189, 95

Pahre, M. A., Djorgovski, S. G., & de Carvalho, R. R. 1996, ApJ, 456, 79

Panter, B., Jimenez, R., Heavens, A. F., & Charlot, S. 2008, MNRAS, 391, 1117

Peeples, M. S., Pogge, R. W., & Stanek, K. Z. 2009, ApJ, 695, 259

Peeples, M. S., & Shanker, F. 2011, MNRAS, 417, 2962

Perez-Gonzalez, P. G., et al. 2005, ApJ, 630, 82

Perez-Montero, E., Contini, T., Lamareille, F., et al. 2009, A&A, 495, 73

Pettini, M., Shapley, A. E., Steidel, C. C., Cuby, J., Dickinson, M., Moorwood, A. F. M., Adelberger, K. L., & Giavalisco, M. 2001, ApJ, 554, 981

Pettini, M., Rix, S. A., Steidel, C. C., Adelberger, K. L., Hunt, M. P., & Shapley, A. E. 2002, ApJ, 569, 742

Pilyugin, L. S., Vilchez, J. M., & Contini, T. 2004, A&A, 425, 849

Pirzkal et al. 2004, APJS, 154, 501

Pirzkal, N., et al. 2004, ApJ, 636, 582

Pirzkal, N., Rothberg, B., Nilsson, Kim K., Finkelstein, S., Koekemoer, A., Malhotra, S., & Rhoads, J. 2012, ApJ, 748, 122

Ranalli, P., Comastri, A., Setti, G. 2003, A&A, 339, 39

Retzlaff, J. et al. 2010, A&A, 511, 50

Richer, M. G., & McCall, M. L. 1995, ApJ, 445, 642

Rodrigues, M., Hammer, F., Flores, H., et al. 2008, A&A, 492, 371

Rupke, D. S., Veilleux, S., & Sanders, D. B. 2002, ApJ, 570, 588

Ryan, R. et al. 2007, ApJ, 668, 839

Salzer, J. J., Lee, J. C., Melbourne, J., Hinz, J. L., Alonso-Herrero, A., & Jangren, A. 2005, ApJ, 624, 661

Salzer, J. J., Willams, A. L., & Gronwall, C., 2009, ApJ, 695, L67

Sandage, A., & Lubin, L. M. 2001, AJ, 121, 2271

Savaglio, S., Glazebrook, K., Le Borgne, D., et al. 2005, ApJ, 635, 260

Saviane, I. et al. 2008, A&A, 487, 901

Schmidt, M. 1963, ApJ, 137, 758

Searle, L., & Sargent, W. L. W. 1972, ApJ, 173, 25

Shapley, A. E., Steidel, C. C., Adelberger, K. L., Dickinson, M., Giavalisco, M., & Pettini, M. 2001, ApJ, 562, 95

Shapley, A. E., Steidel, C. C., Pettini, M., & Adelberger, K. L. 2003, ApJ, 588, 65

Shapley, A. E. et al. 2004, ApJ, 612, 108

Shapley, A. E. et al. 2005, ApJ, 635, 1006

Shen, S., Mo, H. J., White, S. D. M., et al. 2003, MNRAS, 343, 978

Skillman, E. D., Kennicutt, R. C., Jr., & Hodge, P. W. 1989, ApJ, 347, 875

Somerville, R. S., Primack, J. R., & Faber, S. M. 2001, MNRAS, 320, 504

Springel, V., di Matteo, T., & k Hernquist, L. 2005a, ApJ, 620, 79

Springel, V., di Matteo, T., & Hernquist, L. 2005b, MNRAS 361, 776

Stabenau H. F., Connolly, A., Jain, B. 2008, MNRAS, 387, 1215

Steidel, C. C., Shapley, A. E., Pettini, M., Adelberger, K. L., Erb, D. K., Reddy, N. A., & Hunt, M. P. 2004, ApJ, 604, 534

Stoughton, C., et al. 2002, AJ, 123, 485

Straughn, A. N. et al. 2008, AJ, 135, 1624

Straughn, A. N. et al. 2009, AJ, 138, 1022

Straughn, A. N., et al. 2011, AJ, 141, 14

Strickland, D. K., Heckman, T. M., Weaver, K. A., Hoopes, C. G., & Dahlem, M. 2002, ApJ, 568, 689

Strickland, D. K., Heckman, T. M., Colbert, E. J. M., Hoopes, C. G., & Weaver, K. A. 2004, ApJ, 606, 829

Sutherland, R. S., & Dopita, M. A. 1993, ApJS, 88, 253

Tacconi, L. J., Neri, R., Chapman, S. C. et al. 2006, ApJ, 640, 228

Tinsley, B. M., & Larson, R. B. 1978, ApJ, 221, 554

Tinsley, B. M. 1980, ApJ, 89, 246

Tinsley, B. M. 1980, Fundam. Cosm. Phys., 5, 287

Tolman, R. C. 1930, Proceedings of the National Academy of Science, 16, 511

Tremonti, C. A. et al. 2004, ApJ, 613, 898

Tresse, L., Ilbert, O., Zucca, E., et al. 2007, A&A, 472, 403

Trump, J. R. et al. 2011, ApJ, 743, 144

van den Bergh, S. 1962, AJ, 67, 486

van der Wel, A. et al. 2011, arXiv:1107.5256v2

Vanzella, E. et al. 2006, A&A, 454, 423

Vanzella, E., et al. 2008, A&A, 478, 83

Vila-Costas, M. B. & Edmunds, M. G. 1992, MNRAS, 259, 121

Wang, Y., Bahcall, N., & Turner, E. L. 1999, AJ, 116, 2081

Weiner, B. J., Coil, A. L., Prochaska, J. X., et al. 2009, ApJ, 692, 187

White, S. D. M., & Rees, M. J. 1978, MNRAS, 183, 341

Windhorst, R. A., et al. 2011, ApJS, 193, 27

Wirth, G. D., et al. 2004, AJ, 127, 3121

Wray, J. J., Gunn, J. E. 2008, ApJ, 678, 144

Worthey, G. 1994, ApJS, 94, 687

Wolf, C. et al. 2001, A&A, 365, 681

Wolf, C. et al. 2003, A&A, 401, 73

Xia, L., et al. 2002, PASP, 114, 1349

Xia, L. et al., 2012, AJ, 141, 64

Xu, C. et al. 2007, AJ, 134, 169

York, D. G., et al. 2000, AJ, 120, 1579

Zahid, H. J., Kewley, L. J., & Bresolin, F. 2011, ApJ, 730, 137

Zaritsky, D., Kennicutt, R. C. & Huchra, J. P. 1994, ApJ, 420, 87

Zhou, X., Jiang, Z. J., Xue, S. J., Wu, H., Ma, J., & Chen, J. S. 2001, ChJAA, 1, 372

Appendix A

Spectra of Emission Line Galaxies

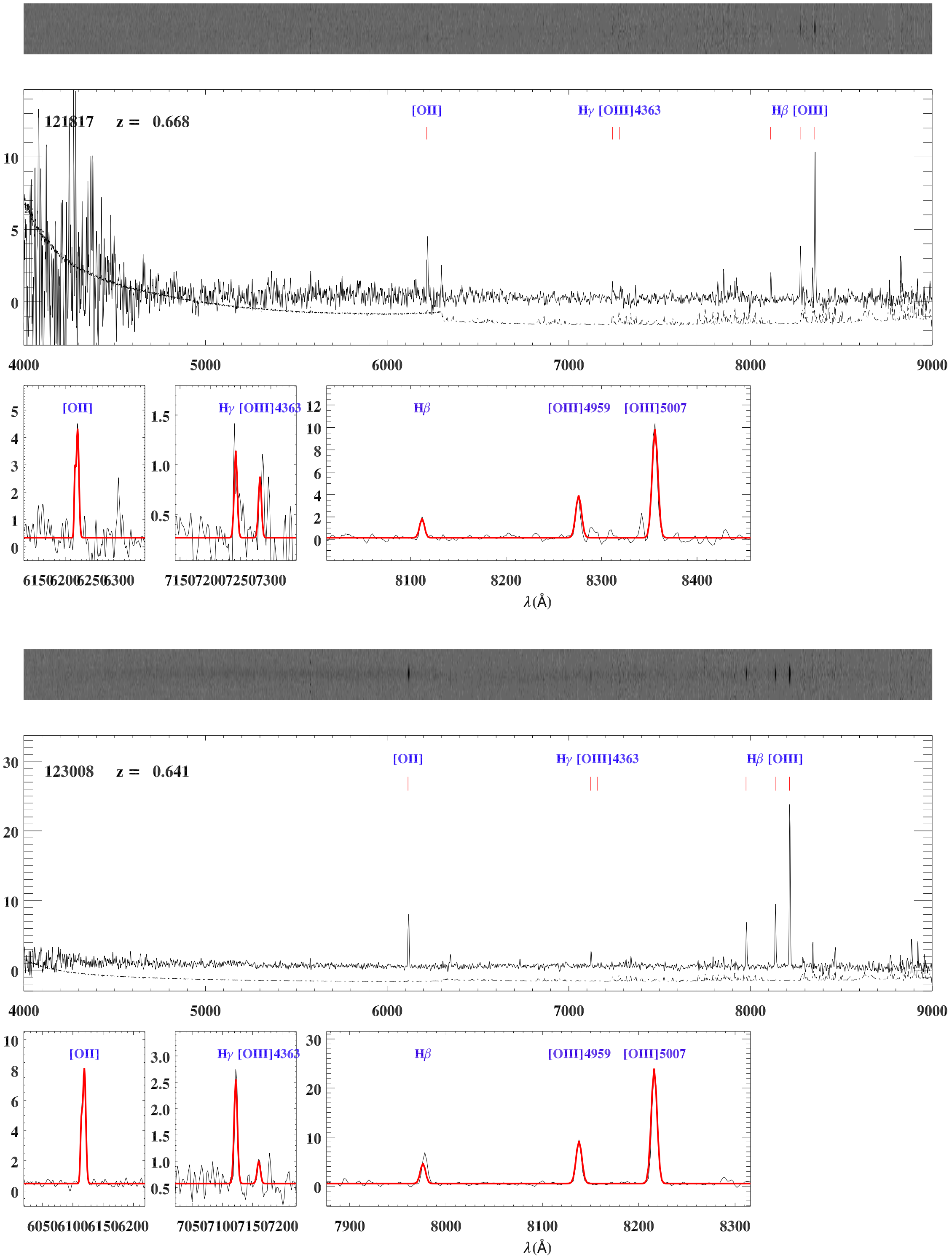

Figure A.1: Spectra of emission line galaxies. The upper panel shows the 2-d spectra, the central panel shows the extracted 1-d spectra, and the lower panels show the gaussian fit of the emission lines.

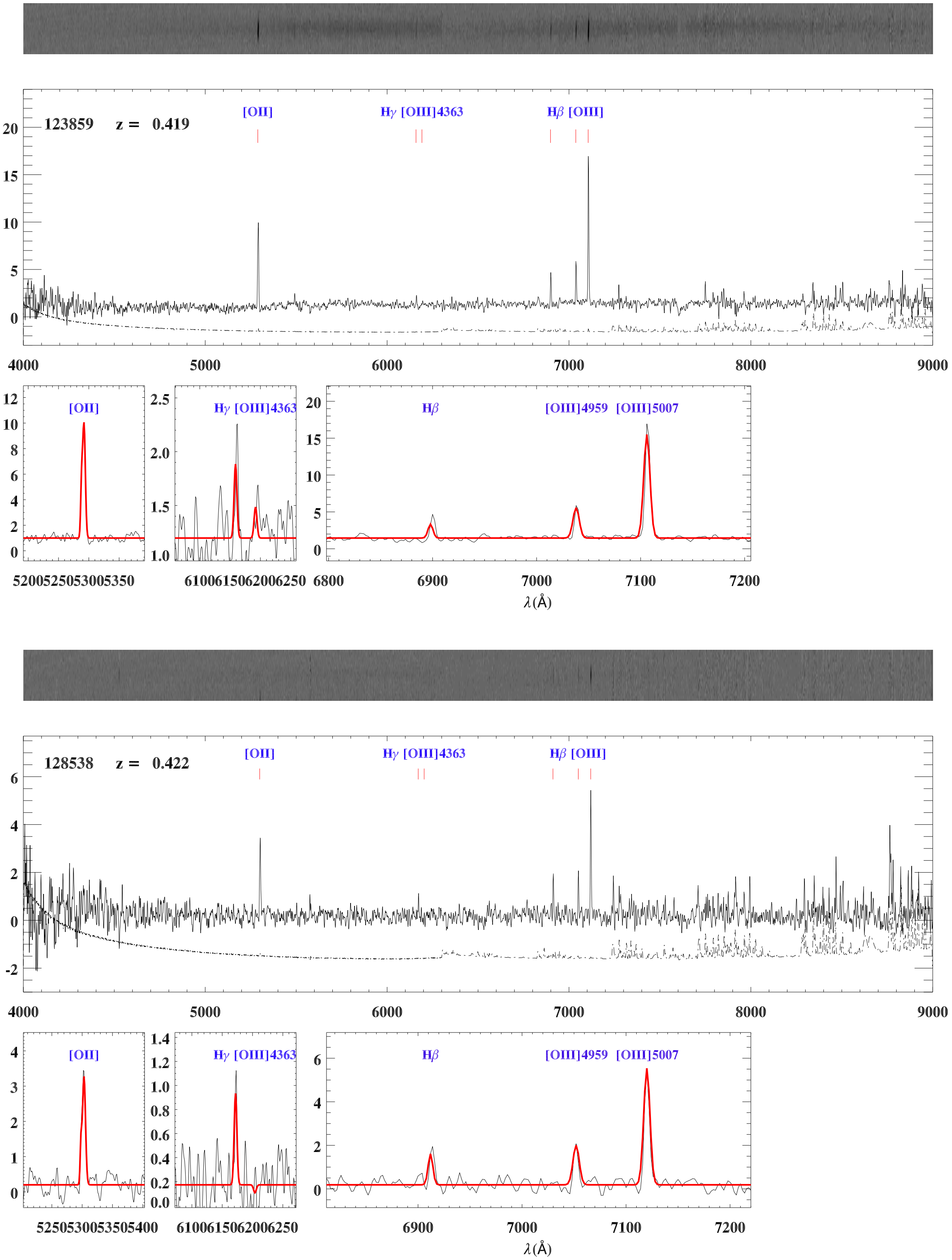

Figure A.2: Continued.

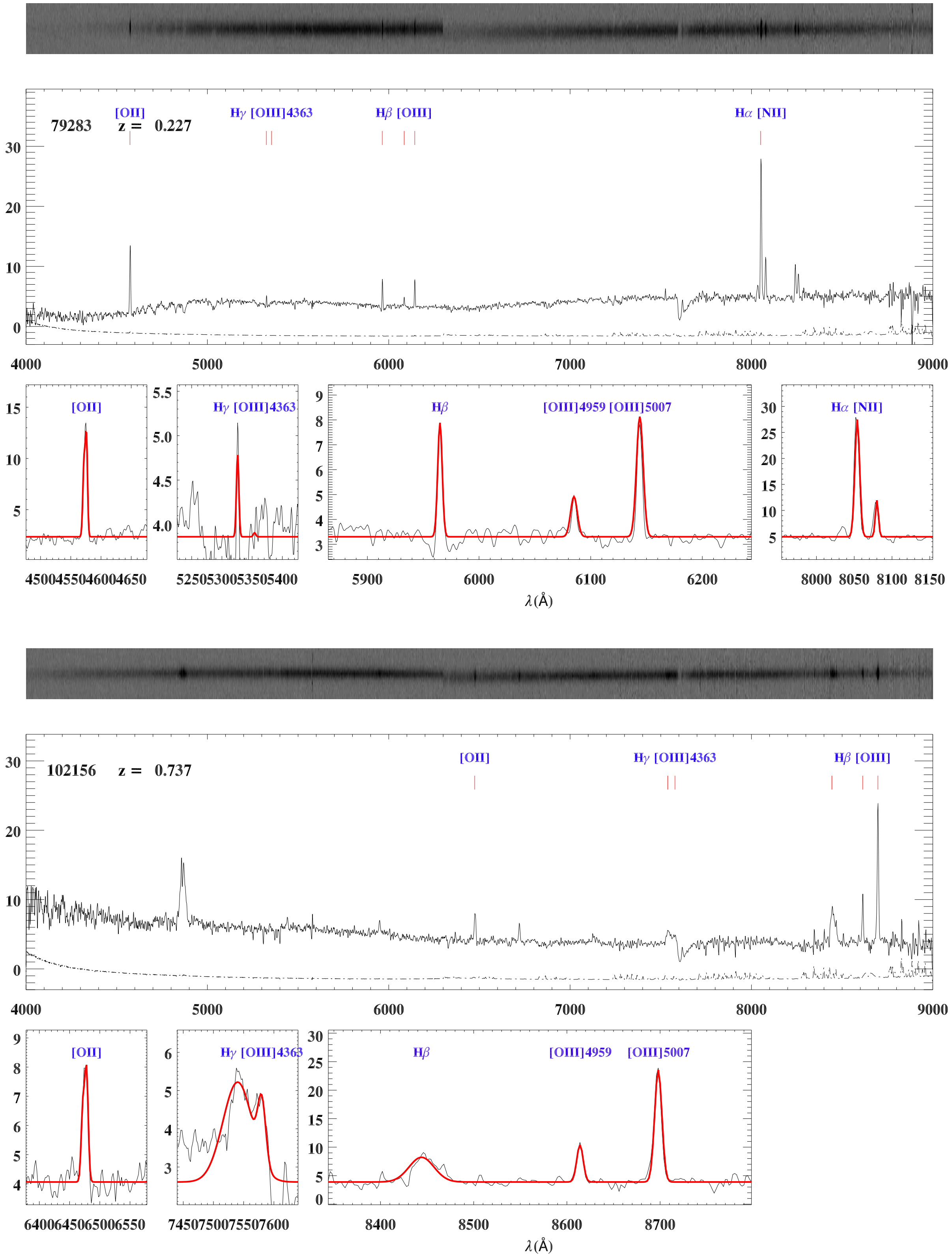

Figure A.3: Continued.

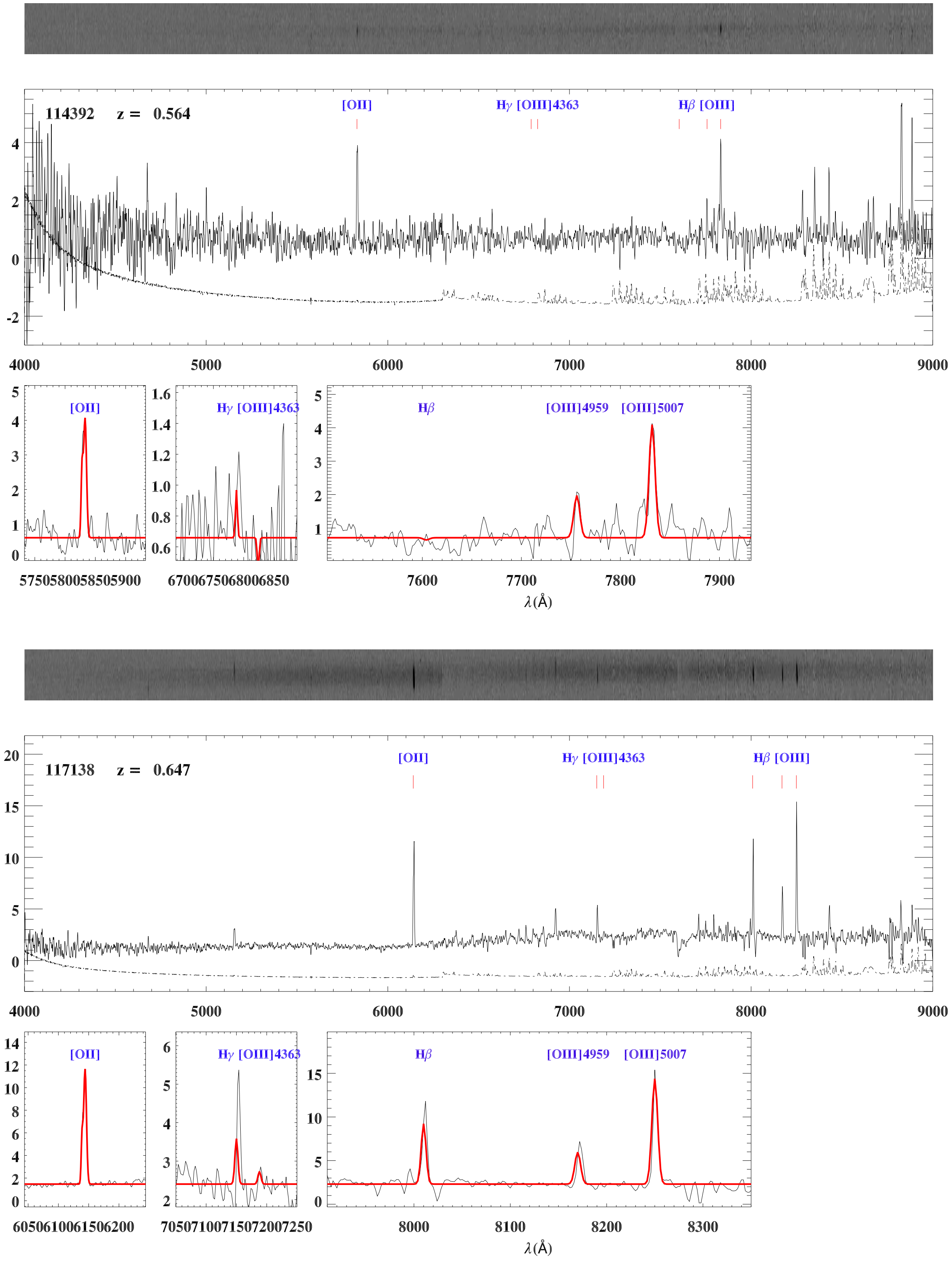

Figure A.4: Continued.

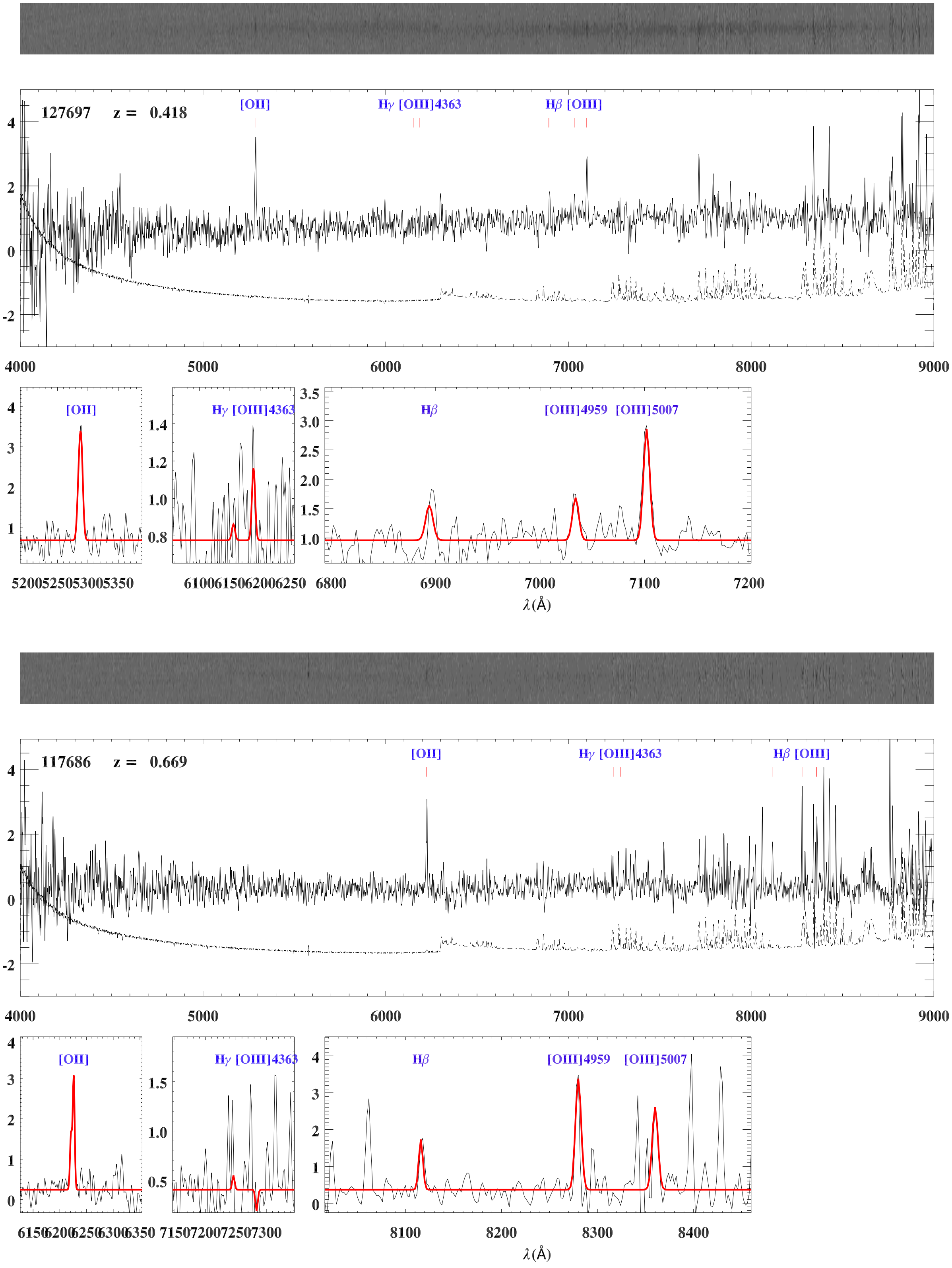

Figure A.5: Continued.

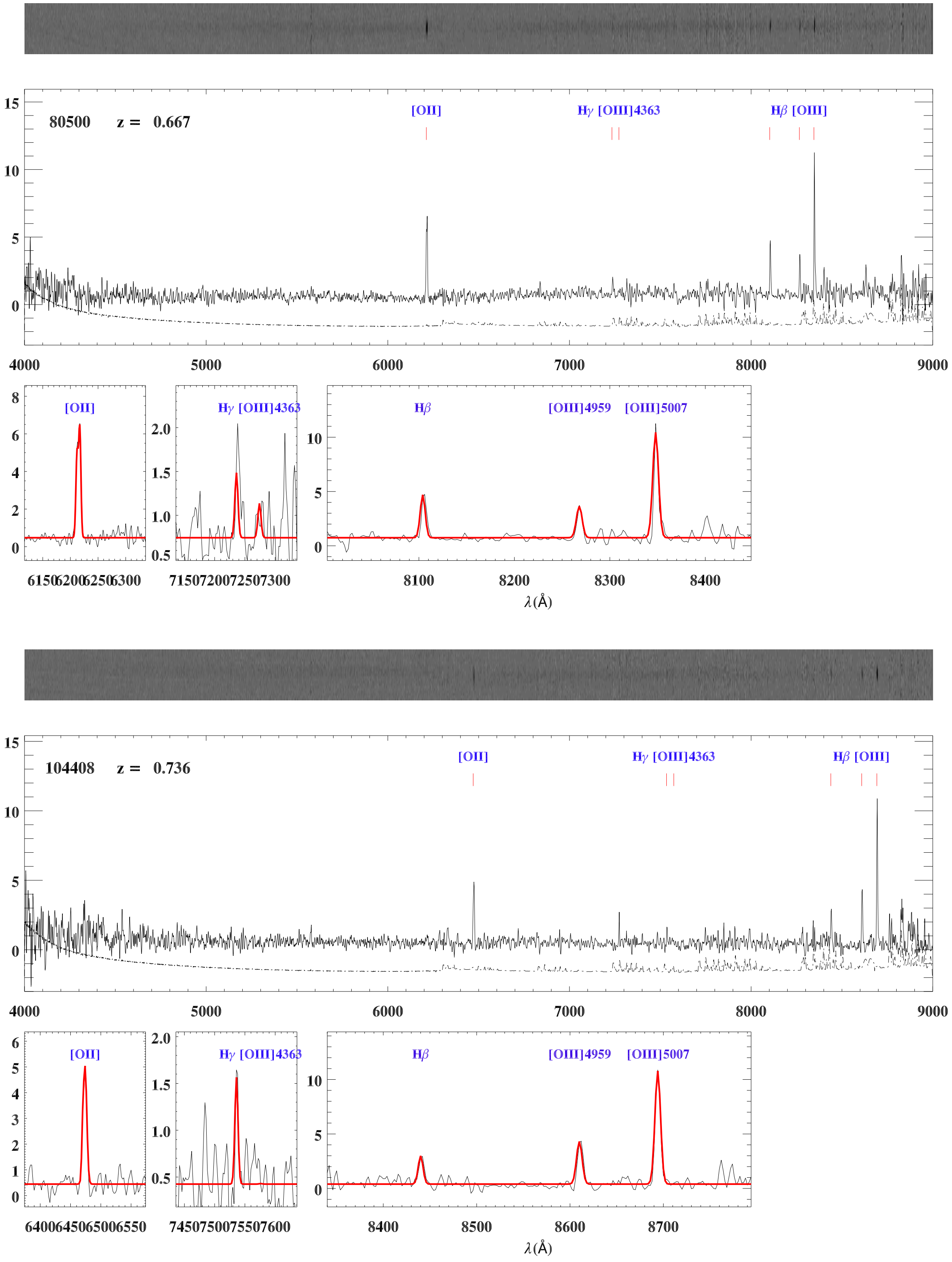

Figure A.6: Continued.

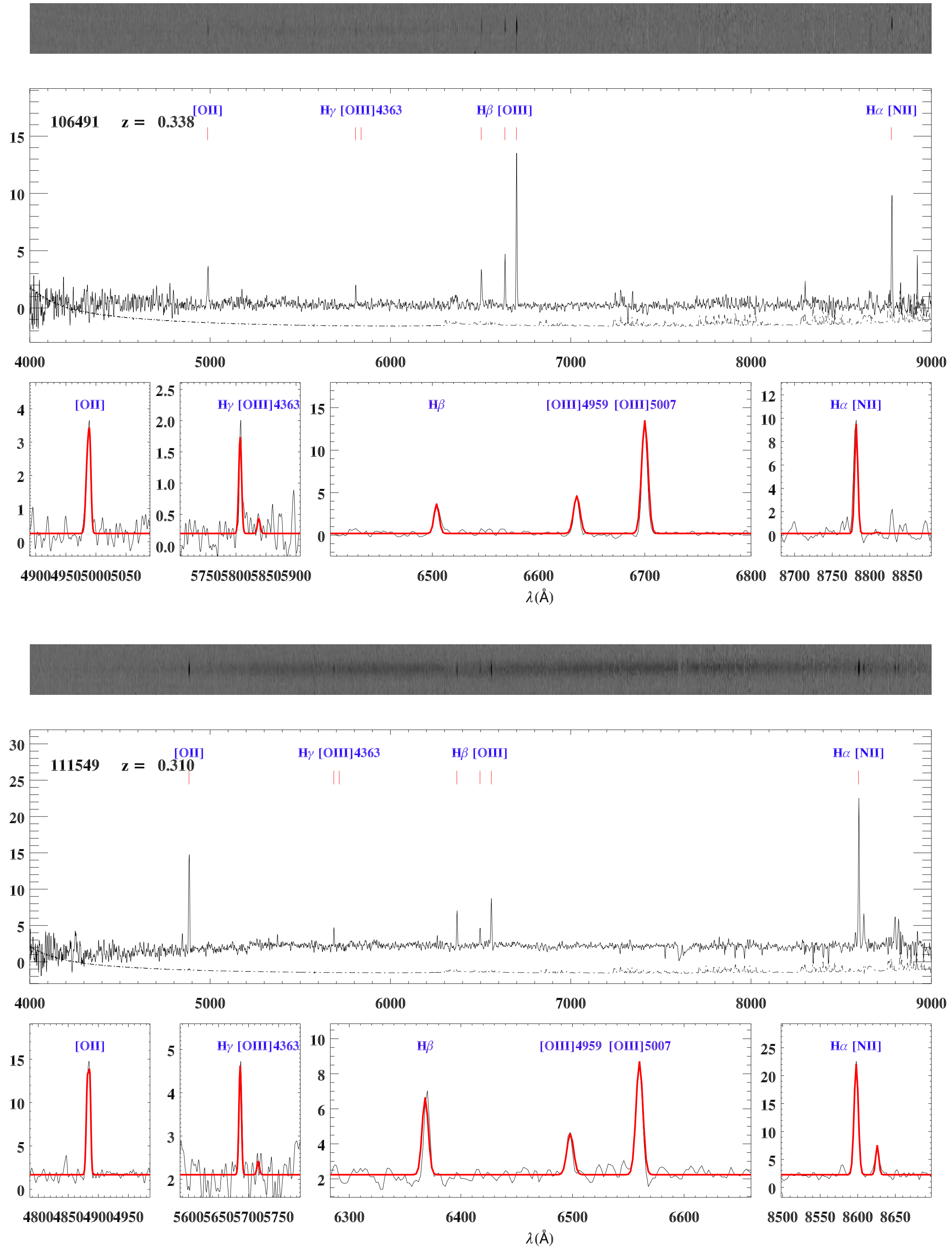

Figure A.7: Continued.

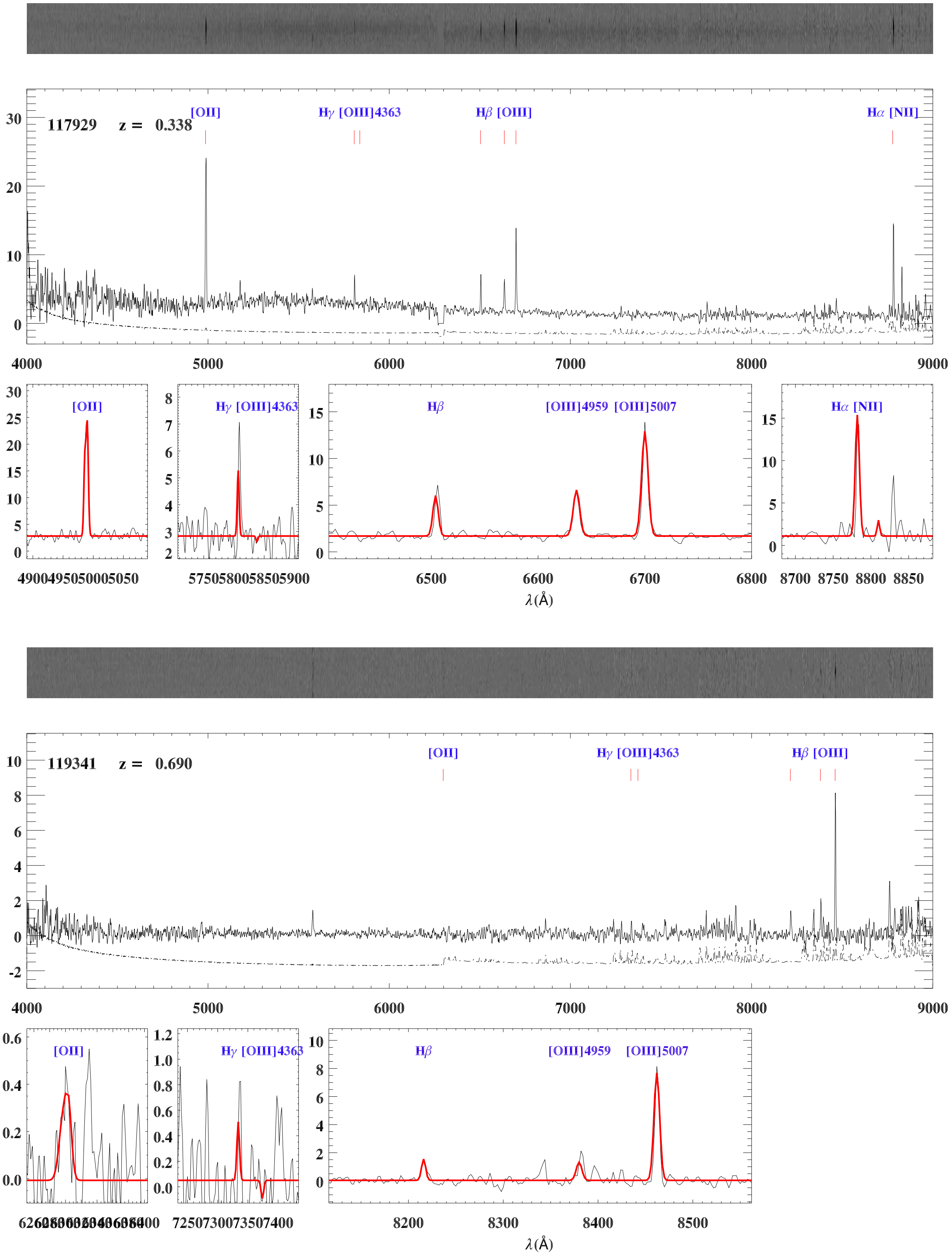

Figure A.8: Continued.

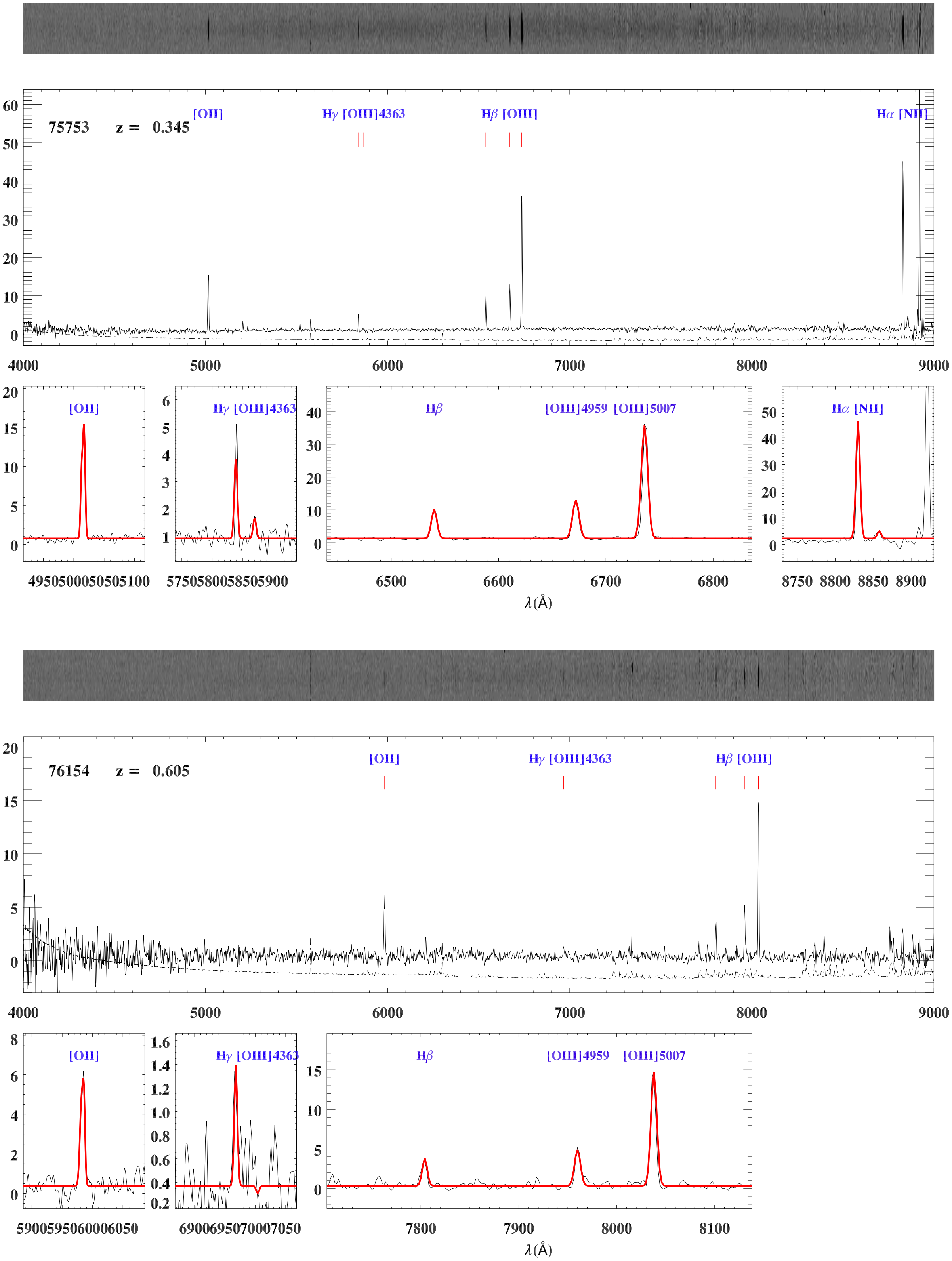

Figure A.9: Continued.

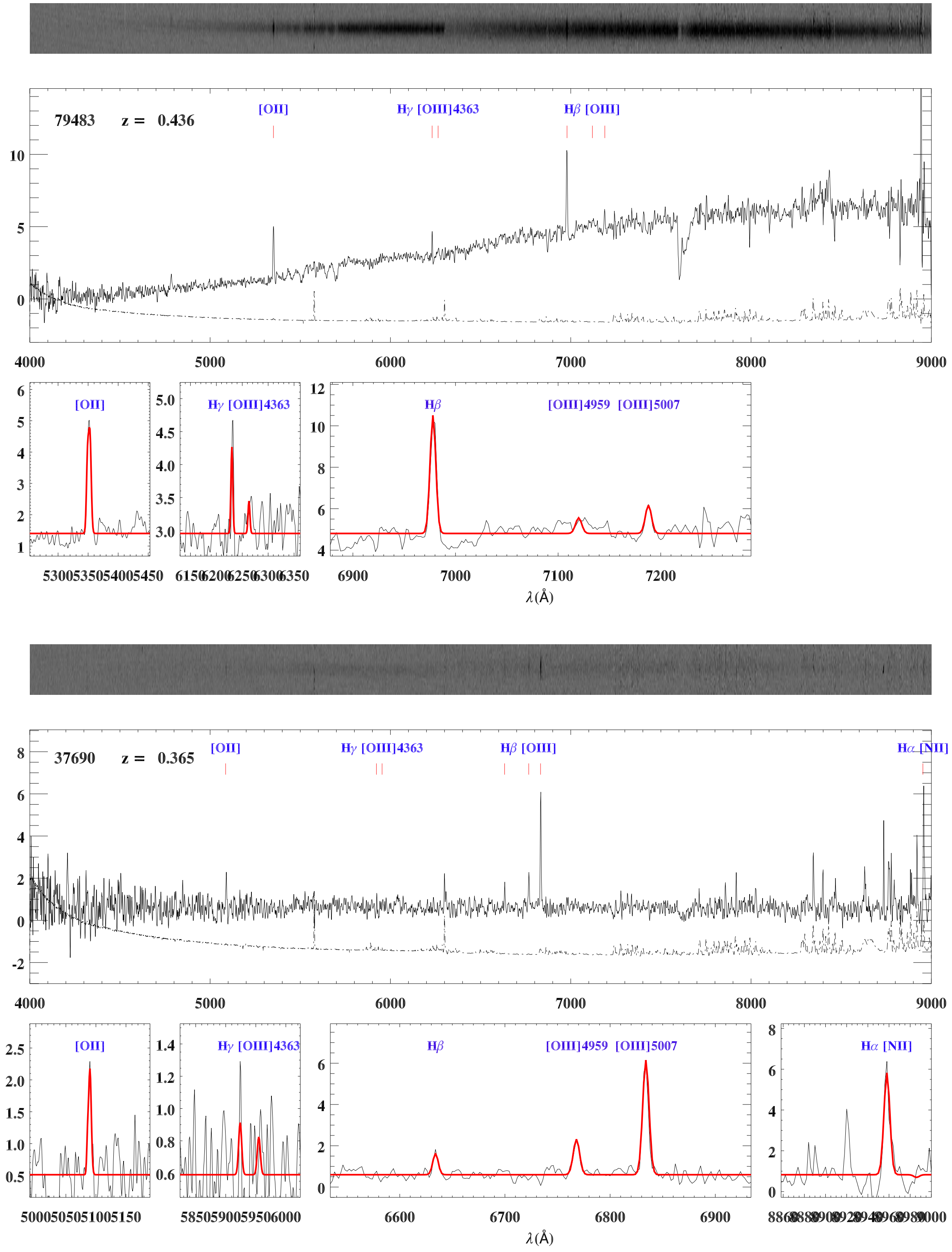

Figure A.10: Continued.

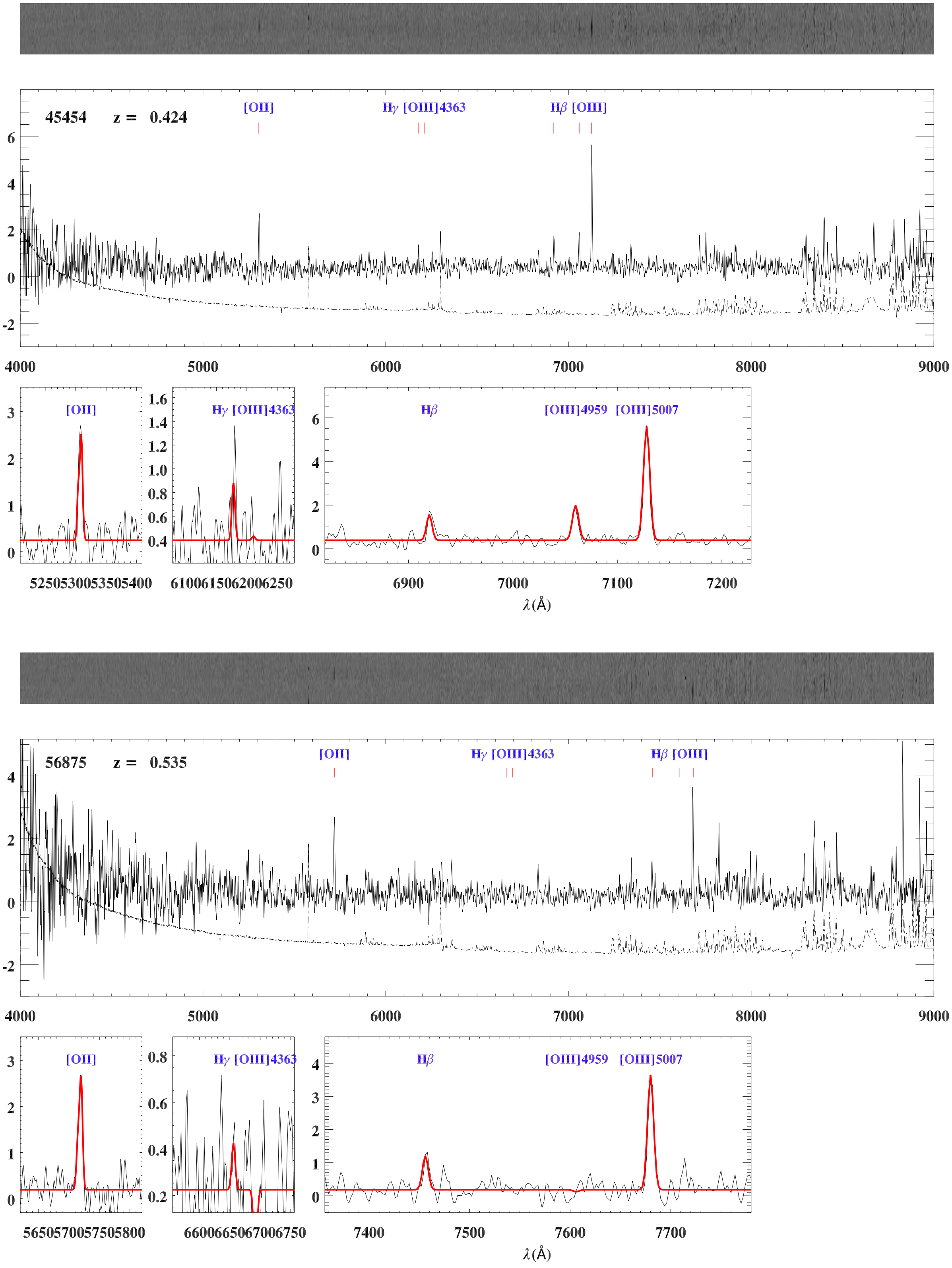

Figure A.11: Continued.

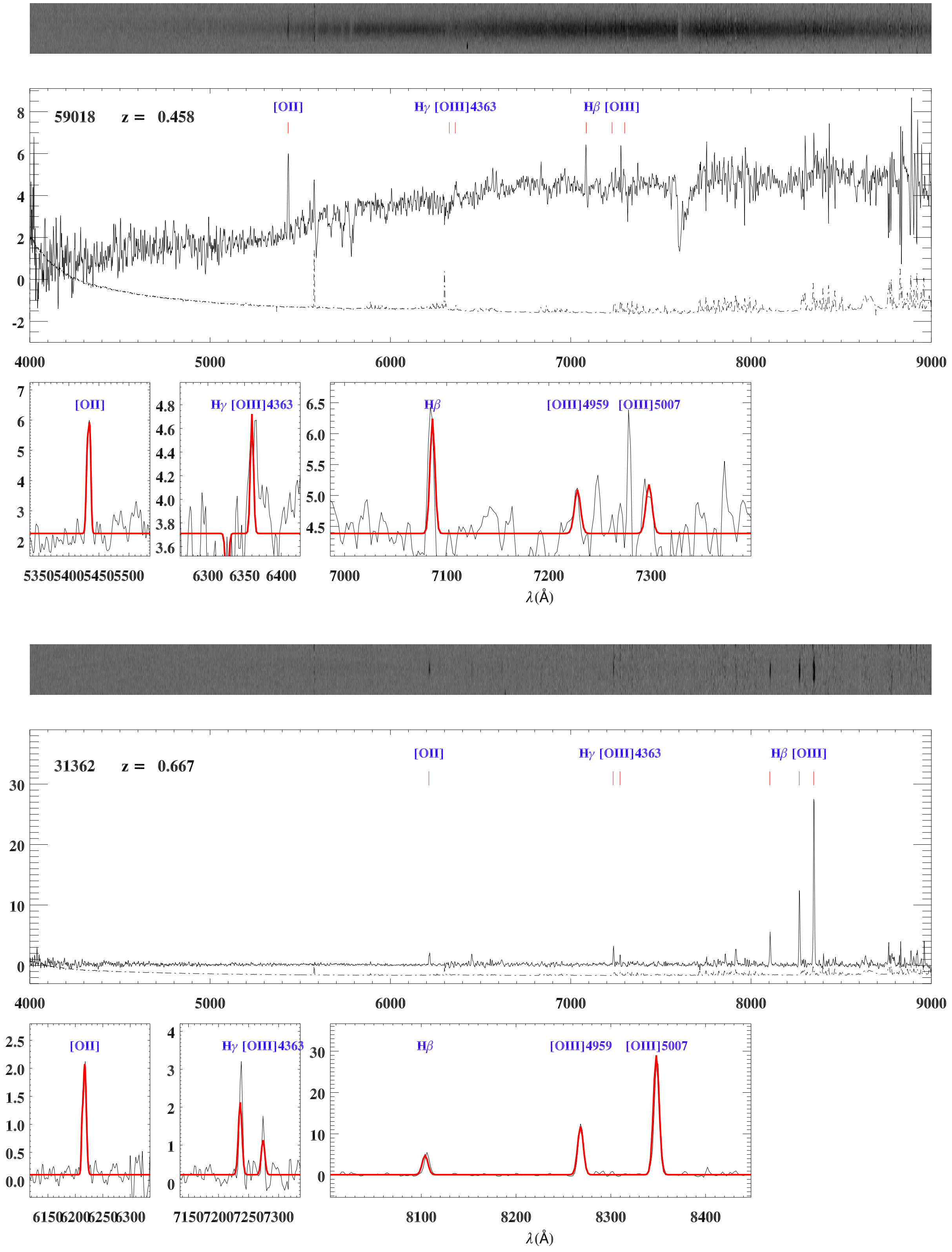

Figure A.12: Continued.

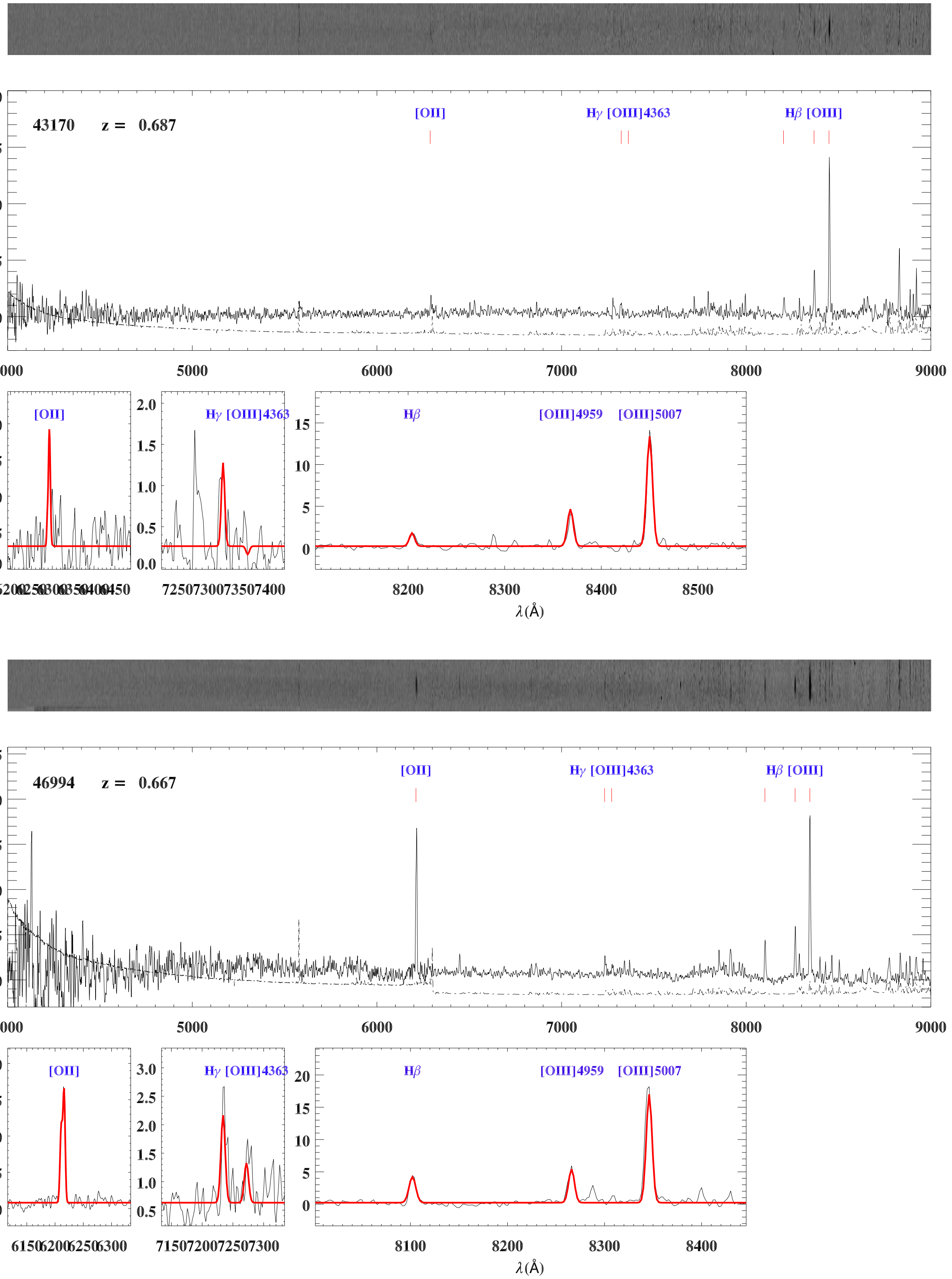

Figure A.13: Continued.

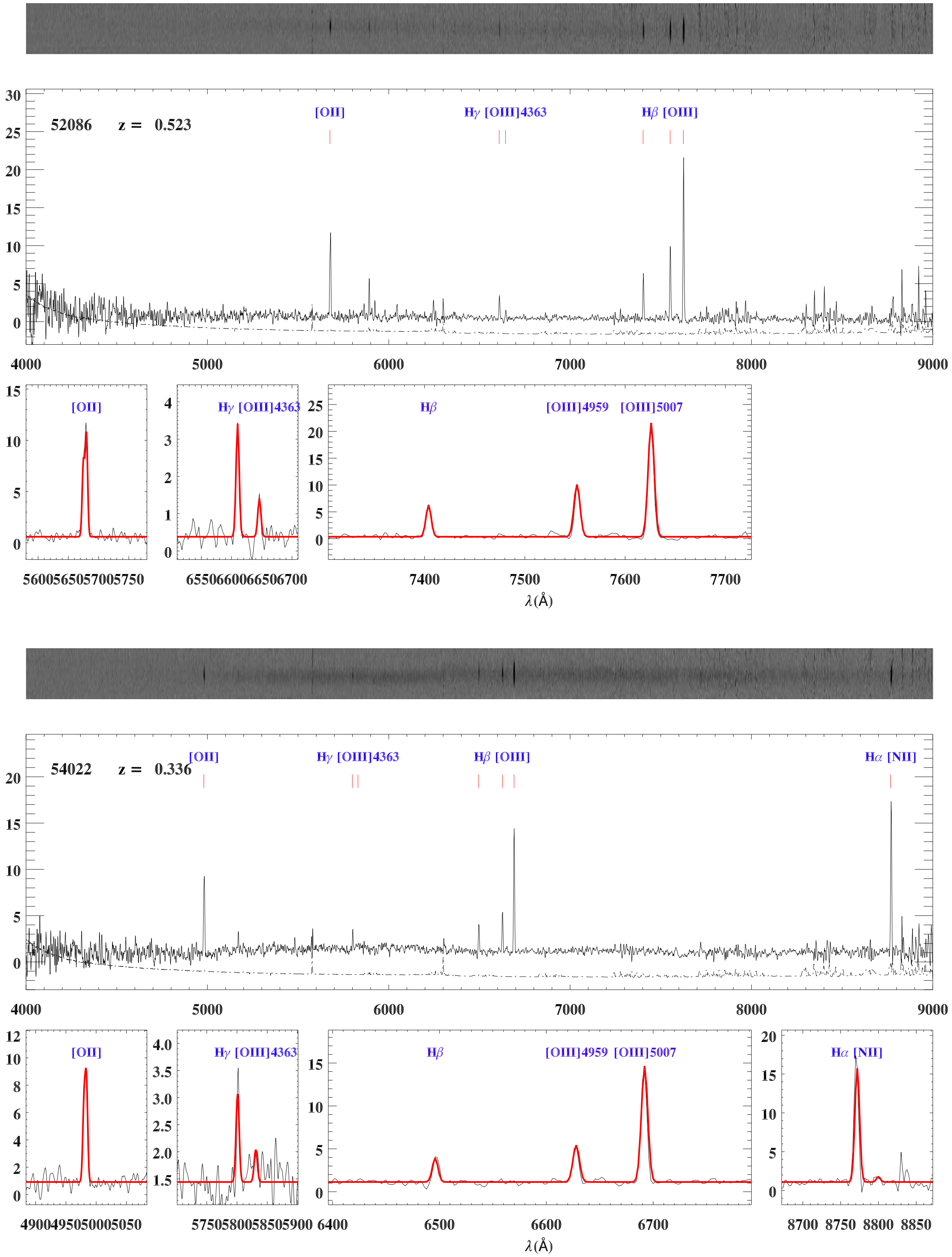

Figure A.14: Continued.

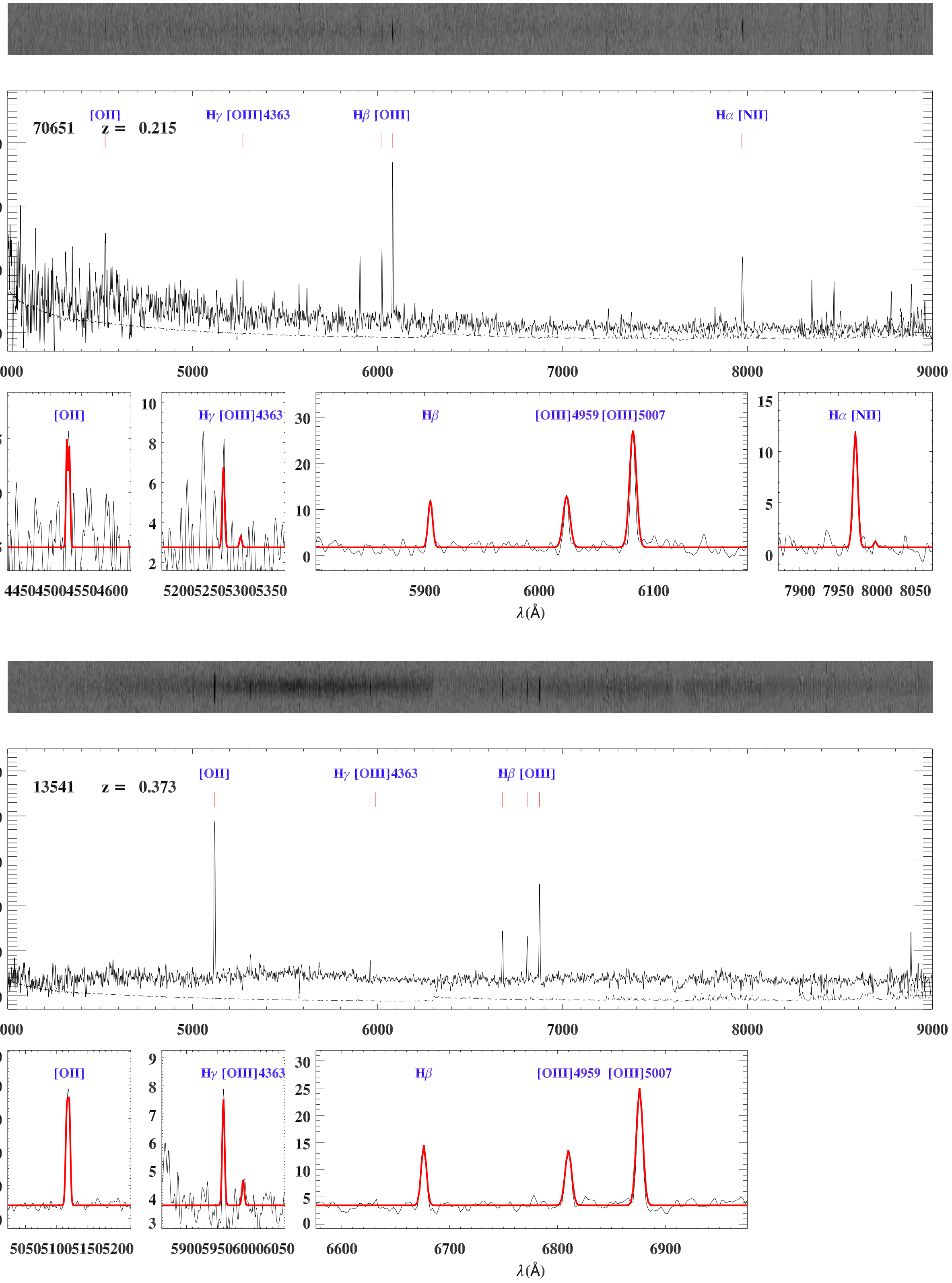

Figure A.15: Continued.

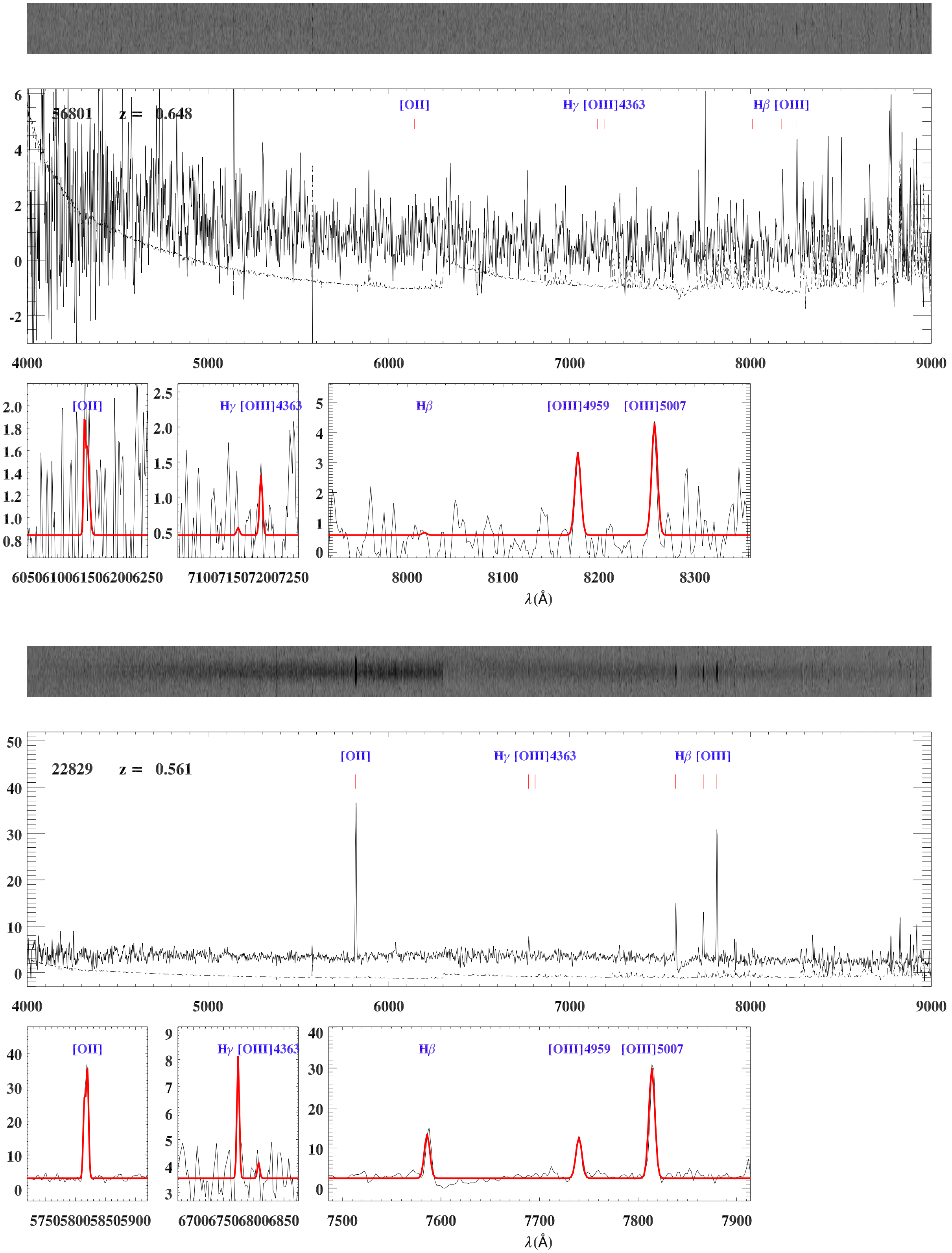

Figure A.16: Continued.

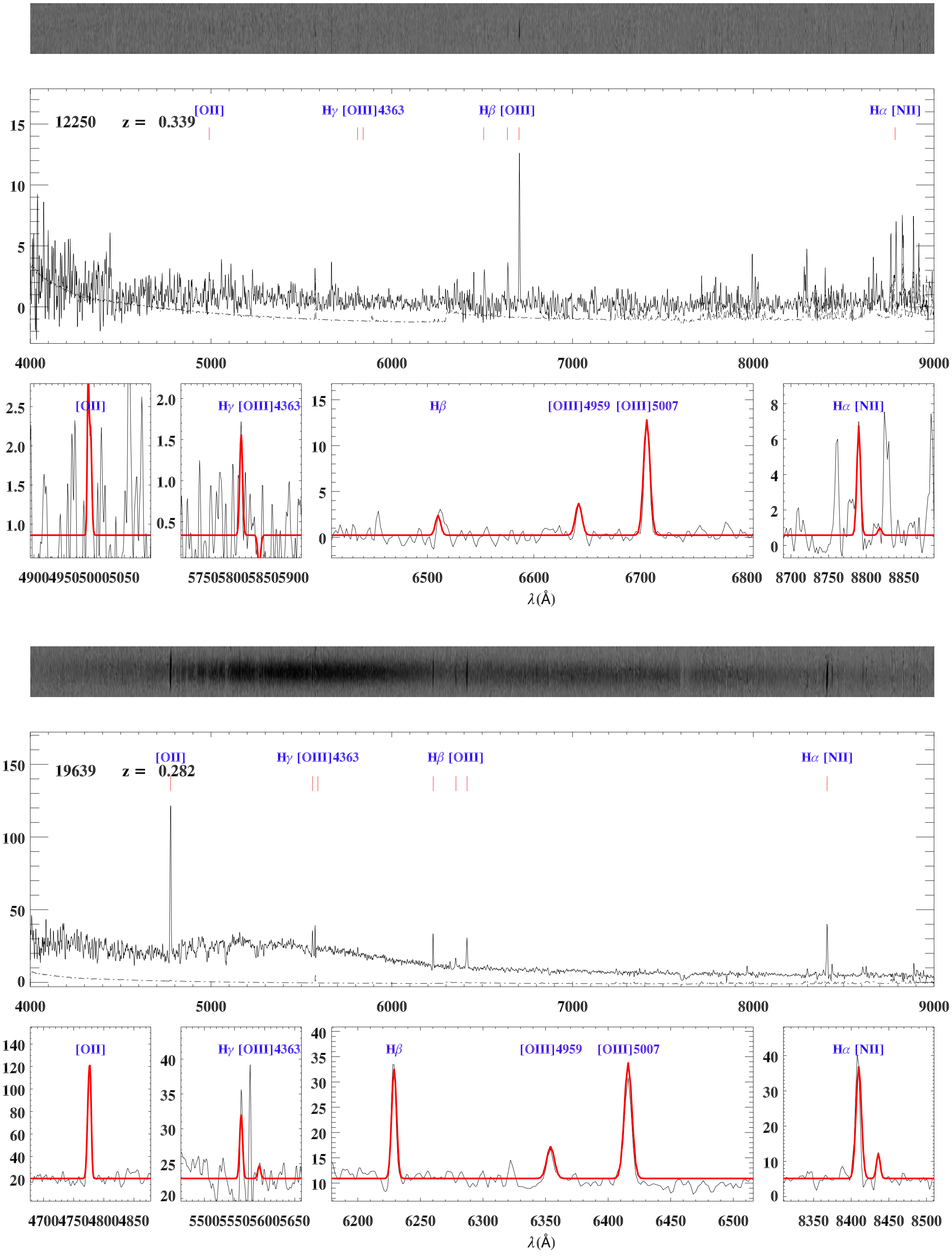

Figure A.17: Continued.

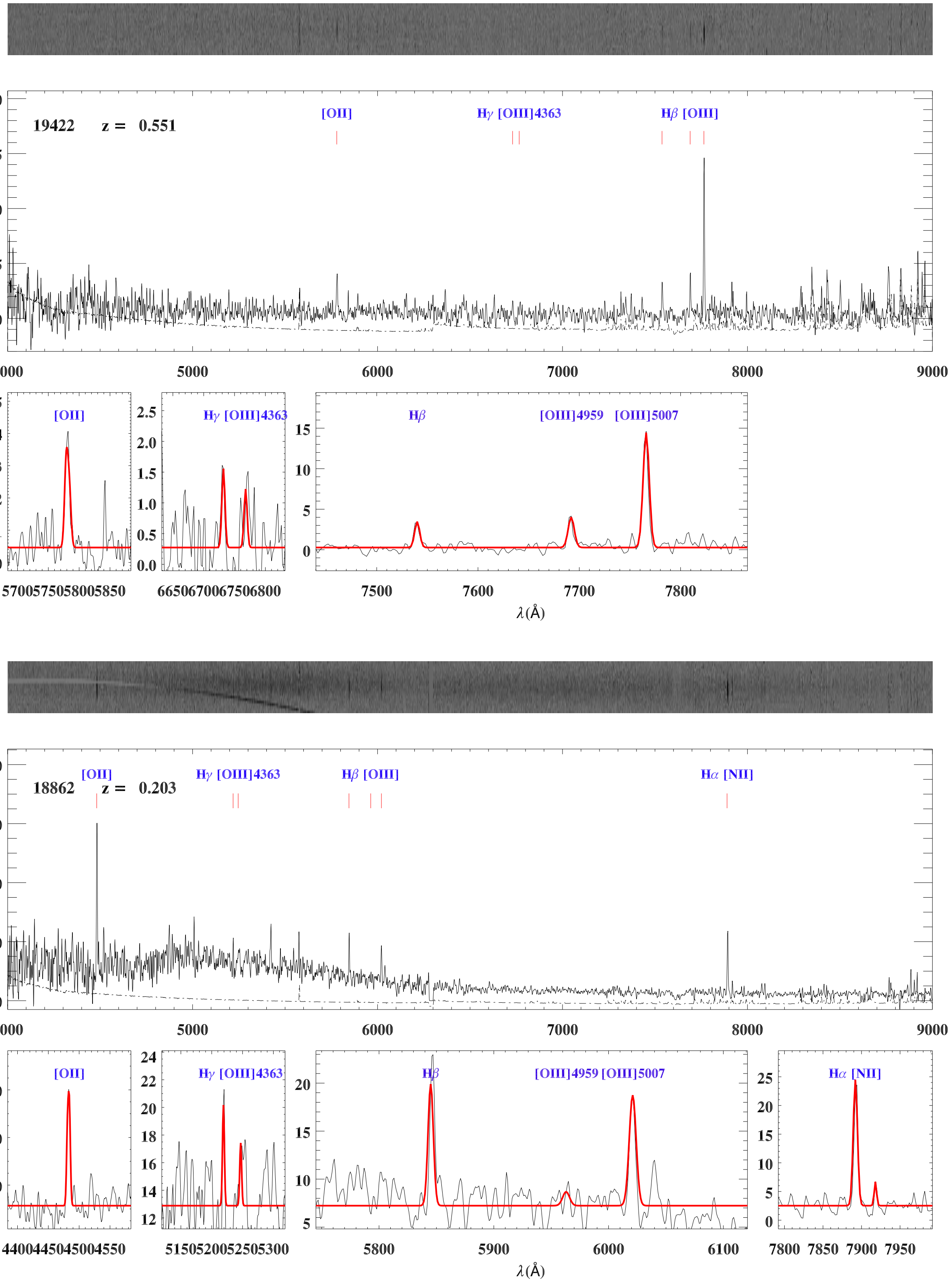

Figure A.18: Continued.

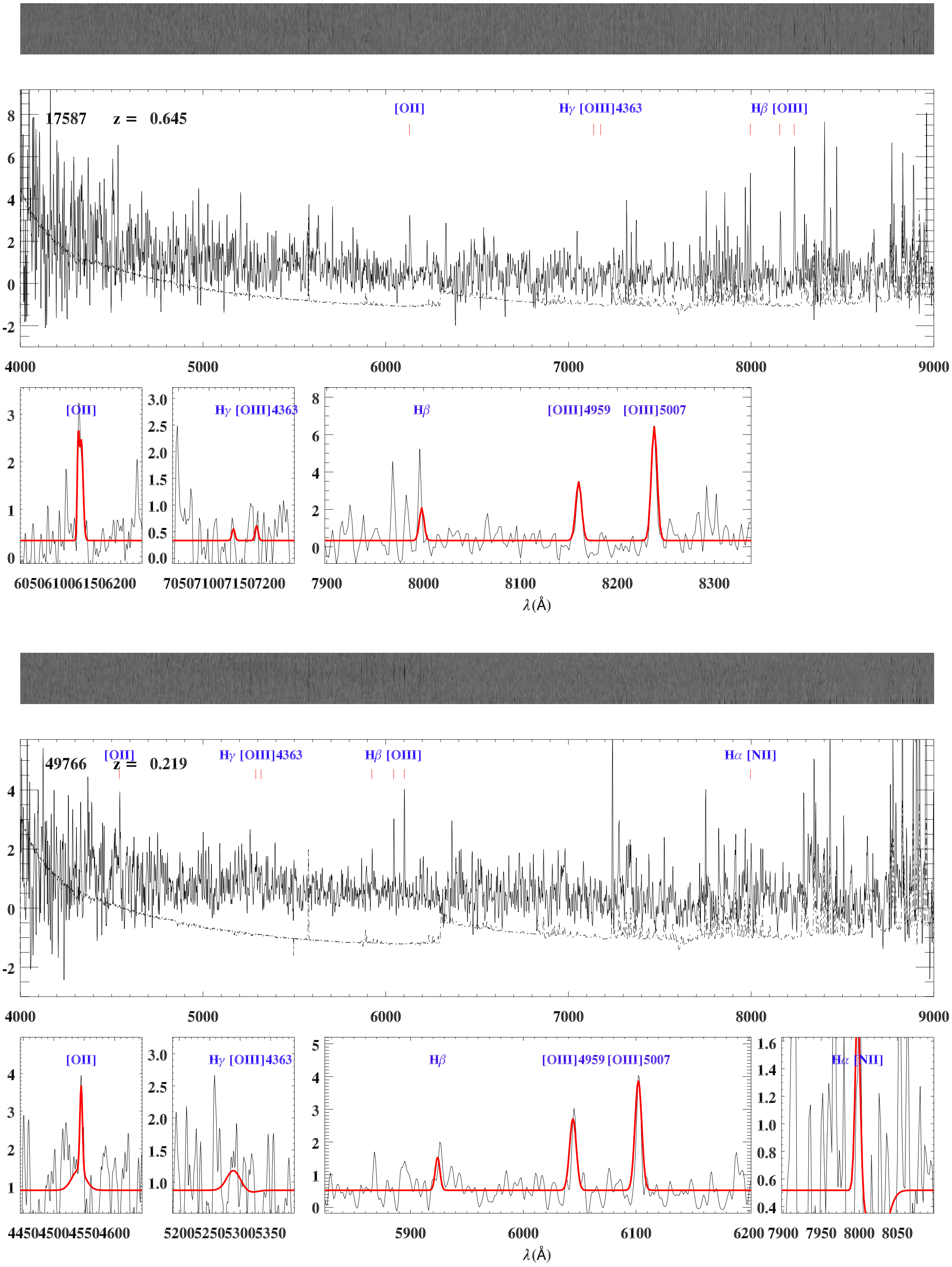

Figure A.19: Continued.

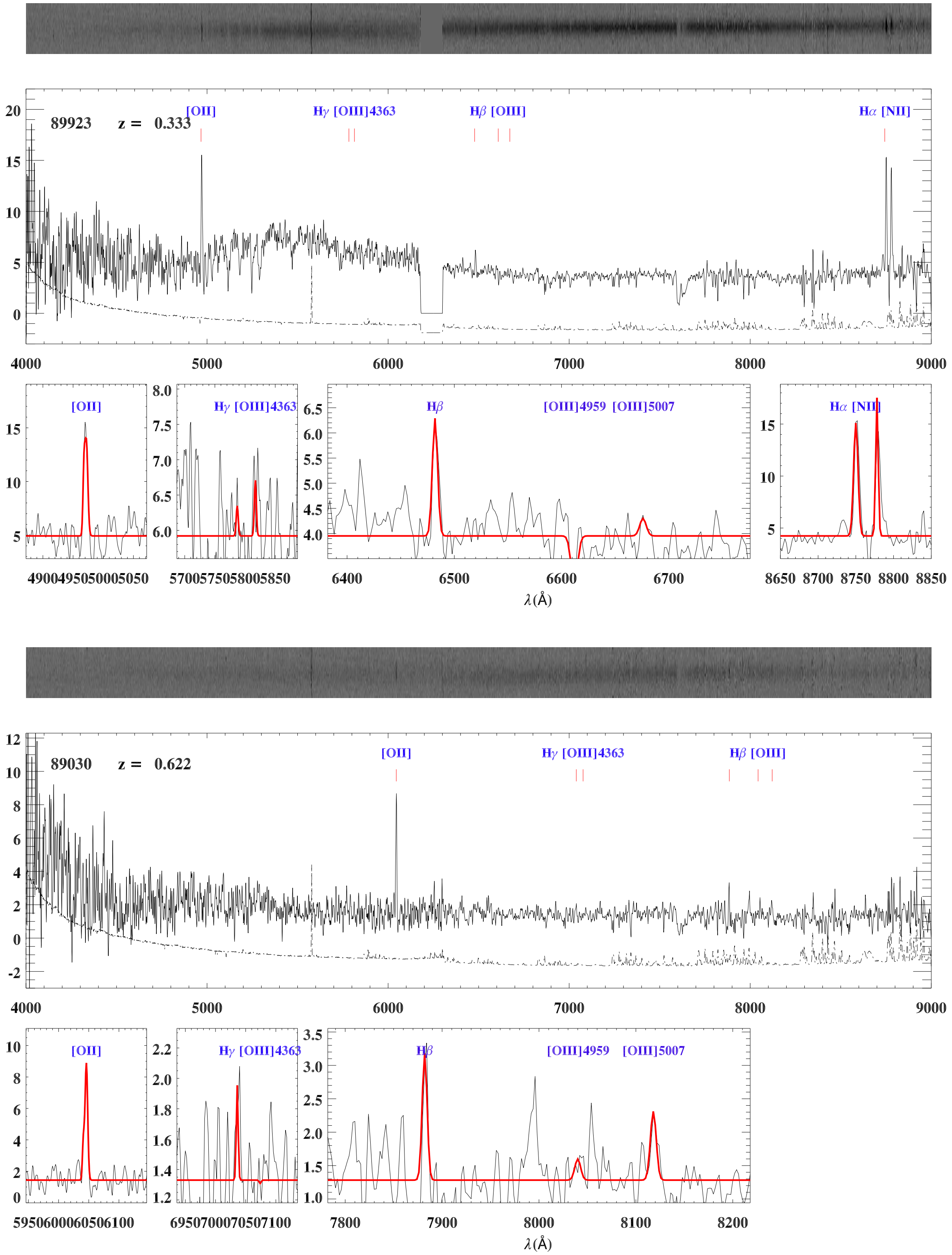

Figure A.20: Continued.

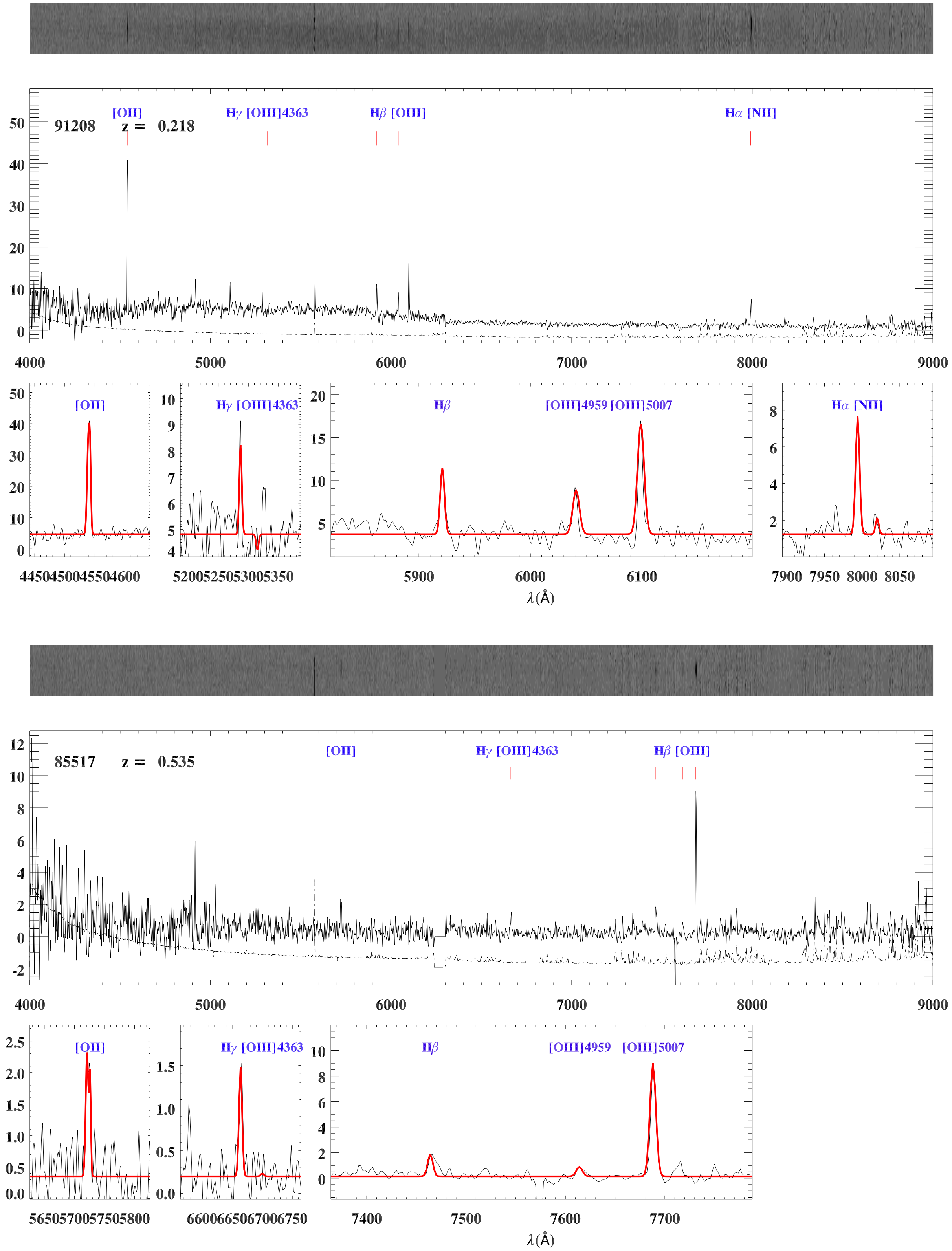

Figure A.21: Continued.

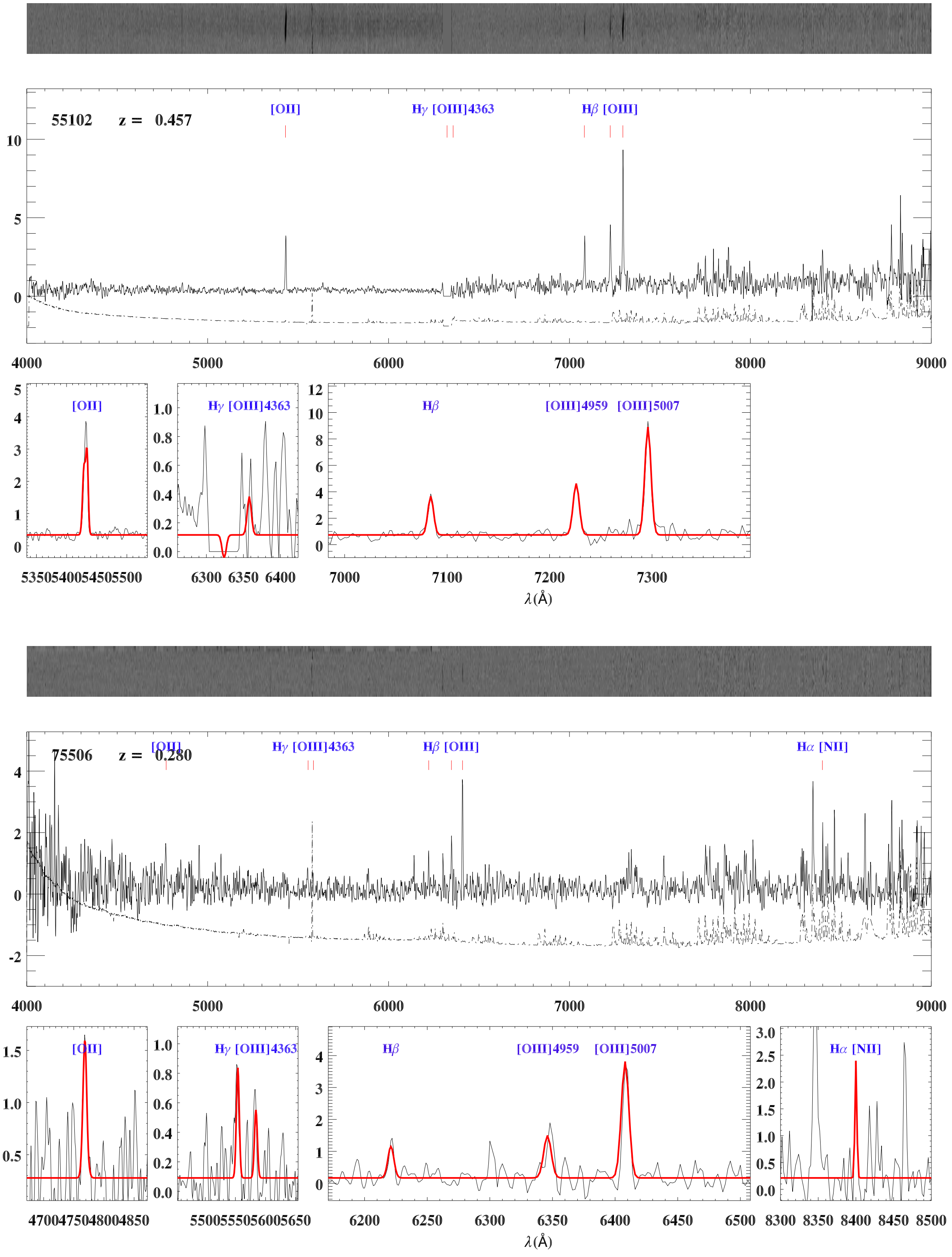

Figure A.22: Continued.

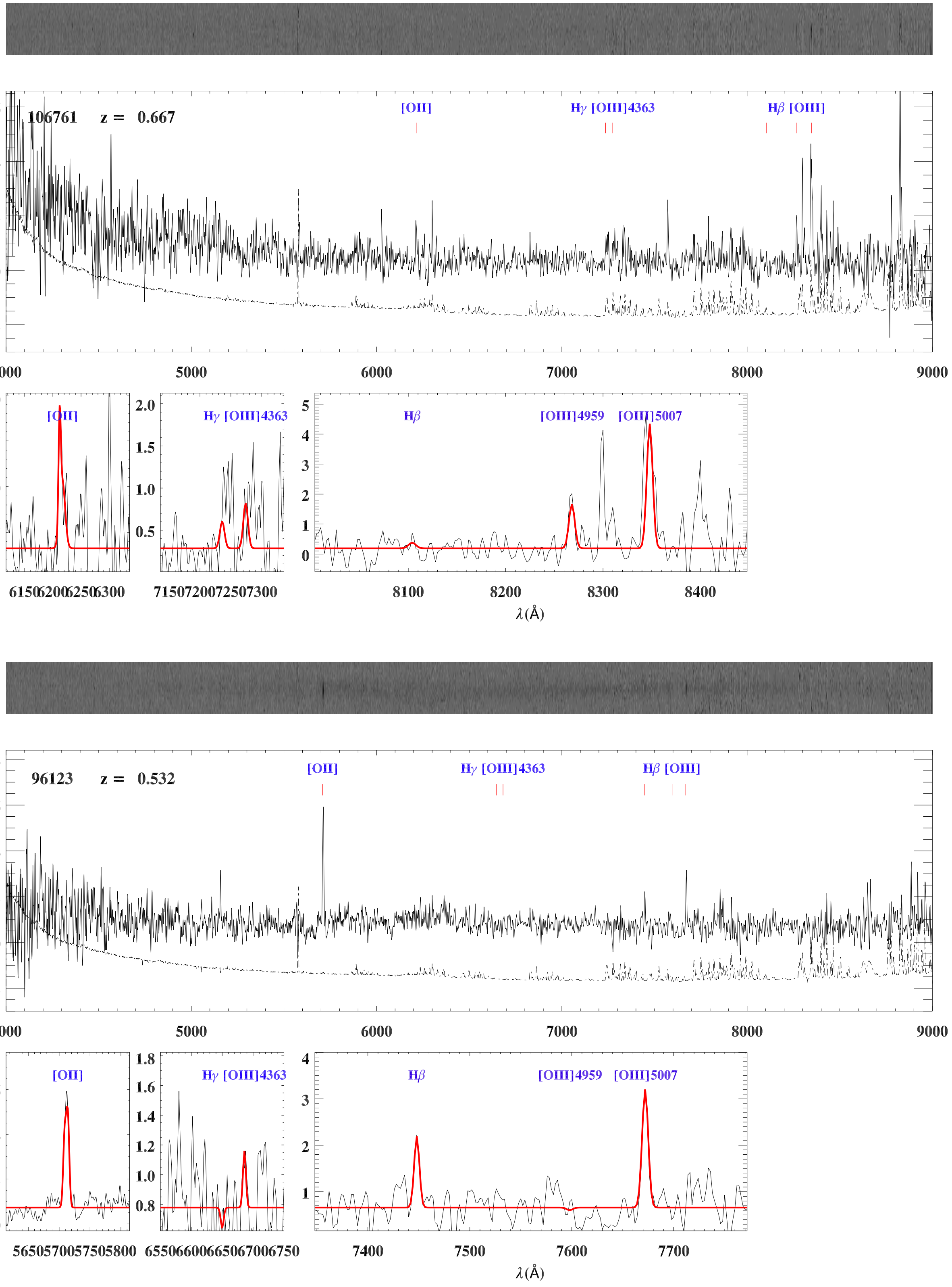

Figure A.23: Continued.

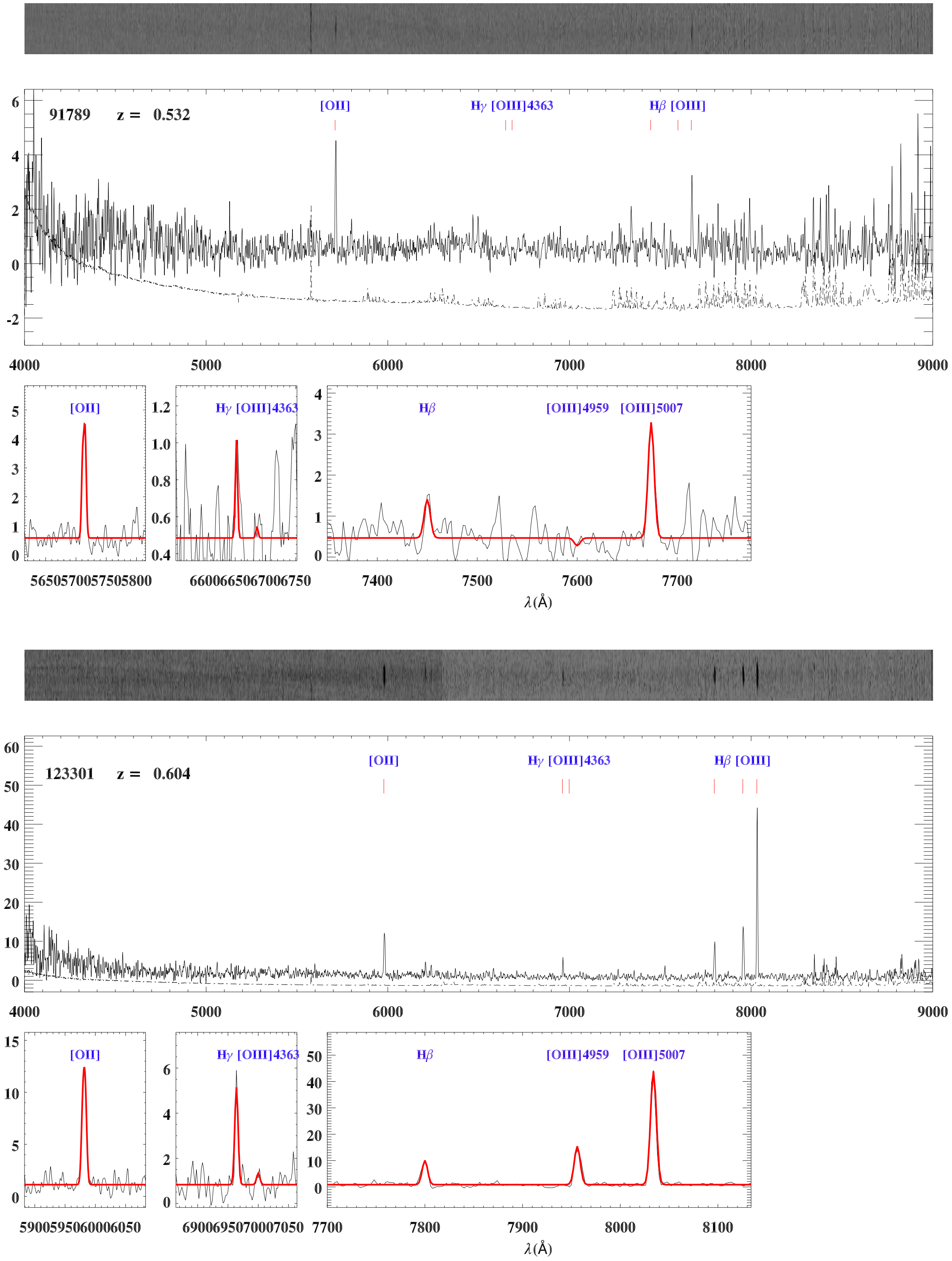

Figure A.24: Continued.

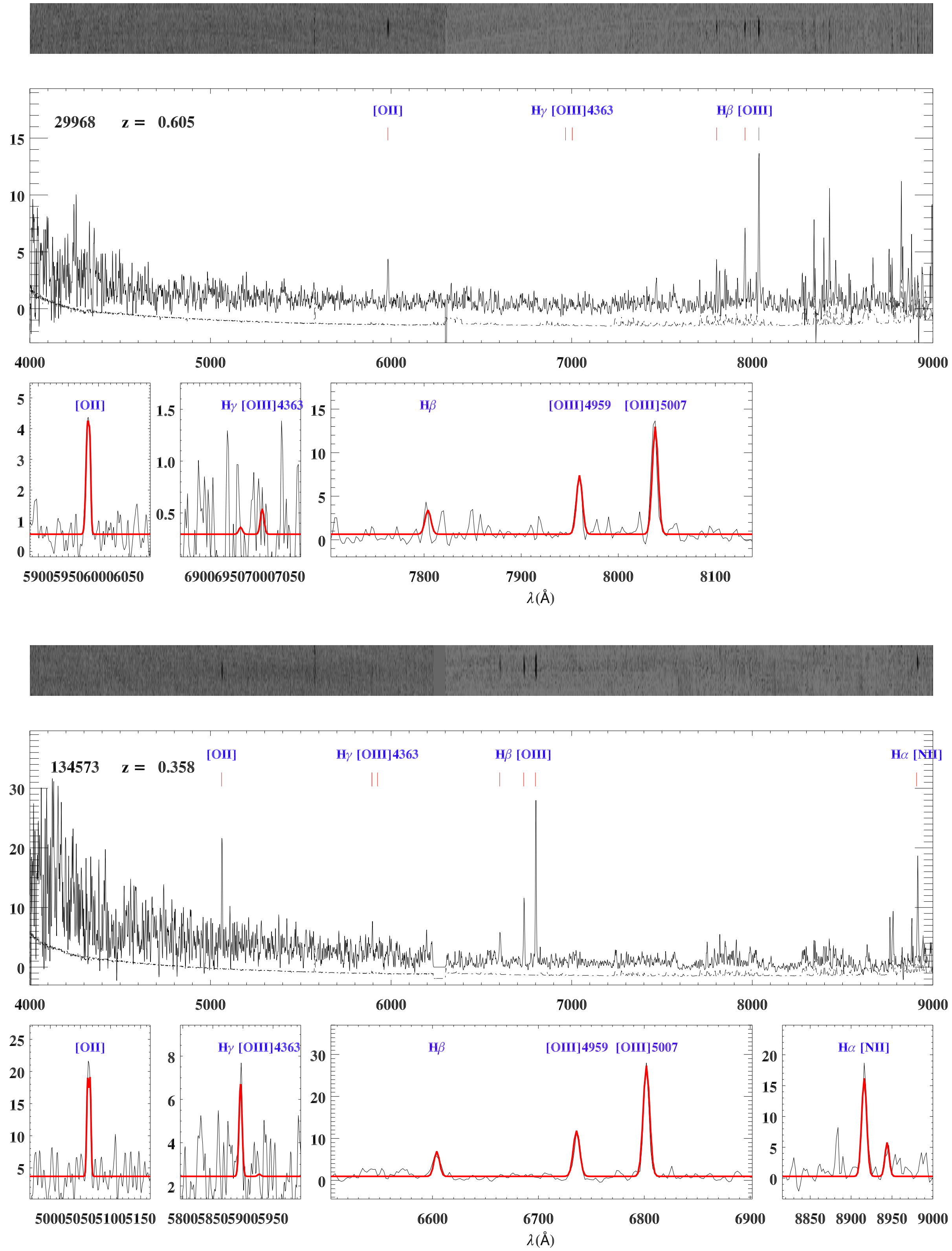

Figure A.25: Continued.

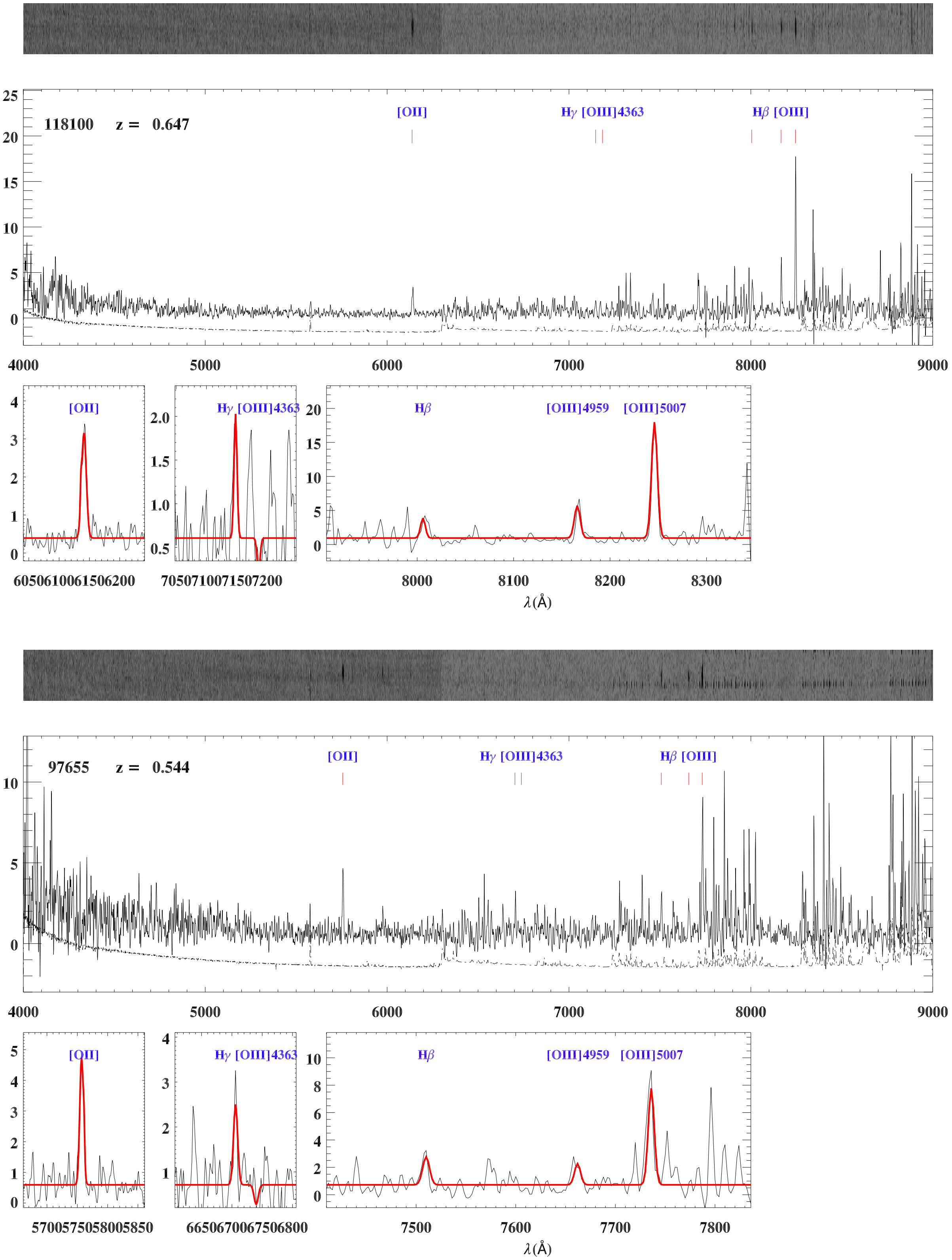

Figure A.26: Continued.

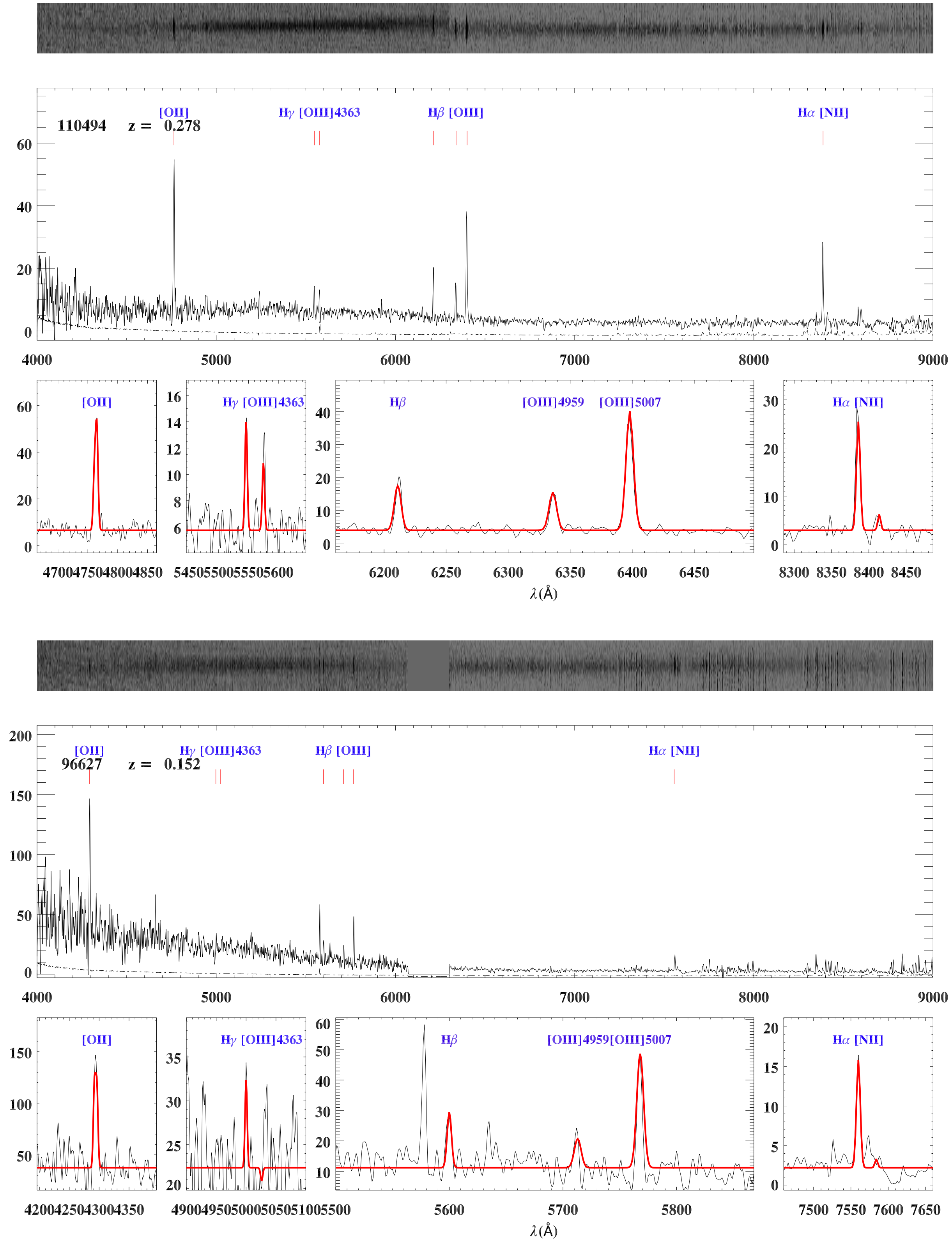

Figure A.27: Continued.

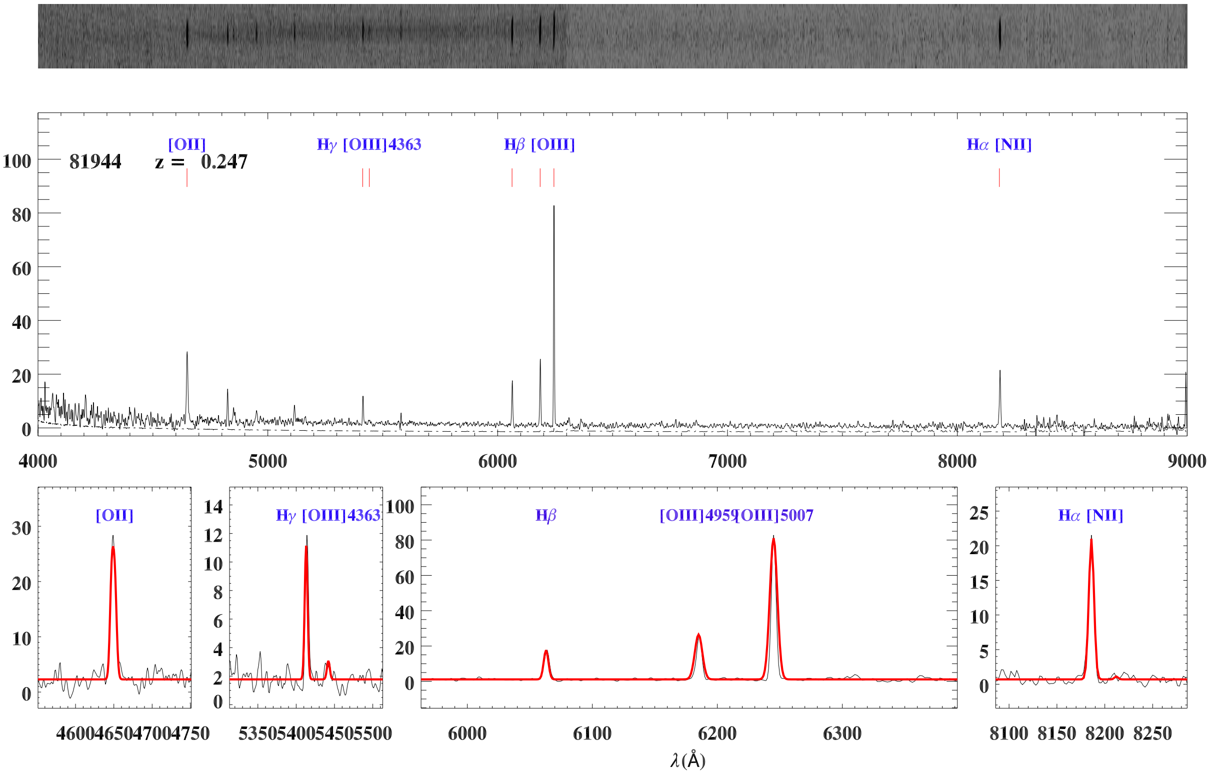

Figure A.28: Continued.

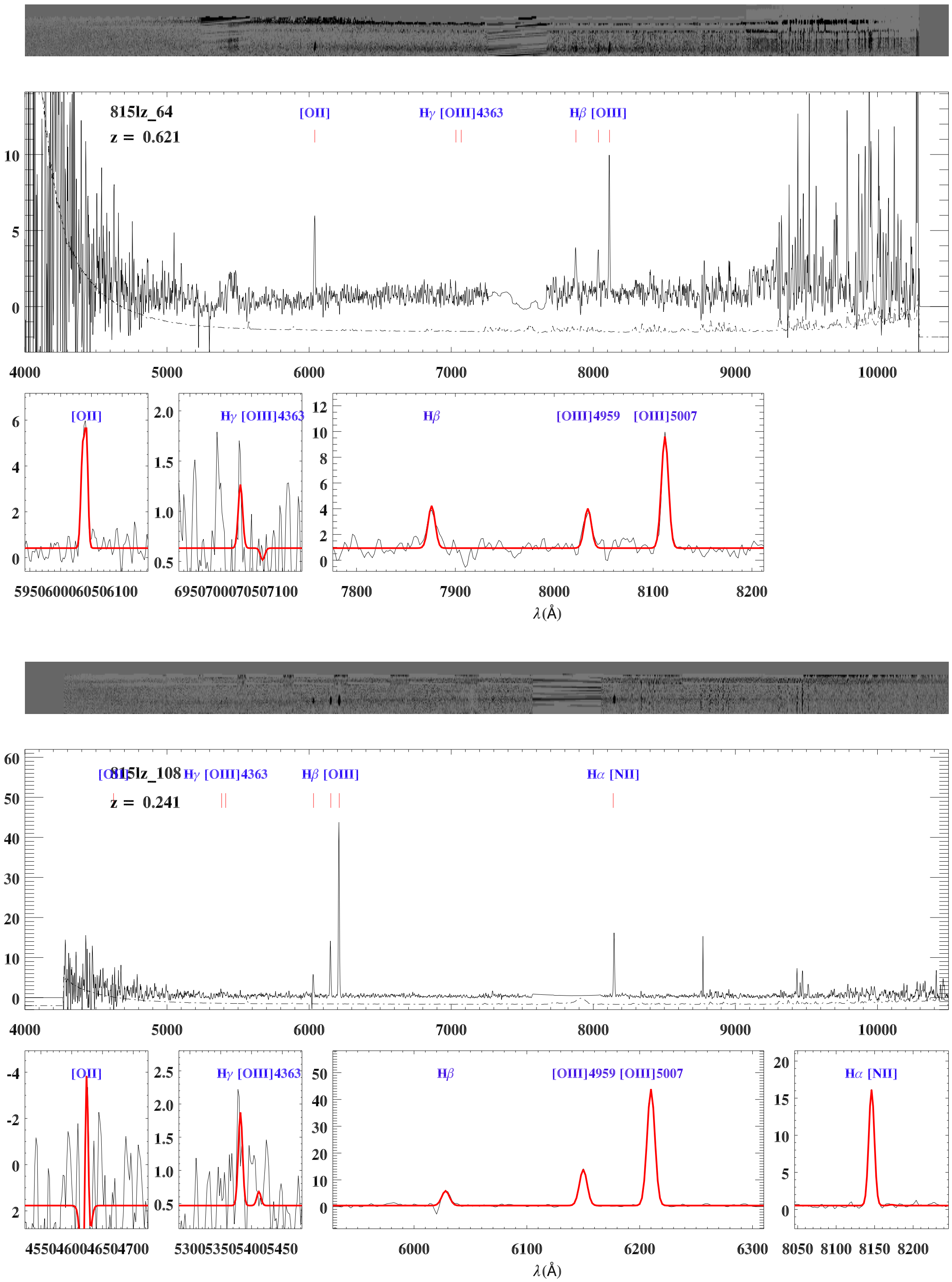

Figure A.29: Spectra of emission line galaxies. The upper panel shows the 2-d spectra, the central panel shows the extracted 1-d spectra, and the lower panels show the gaussian fit of the emission lines.

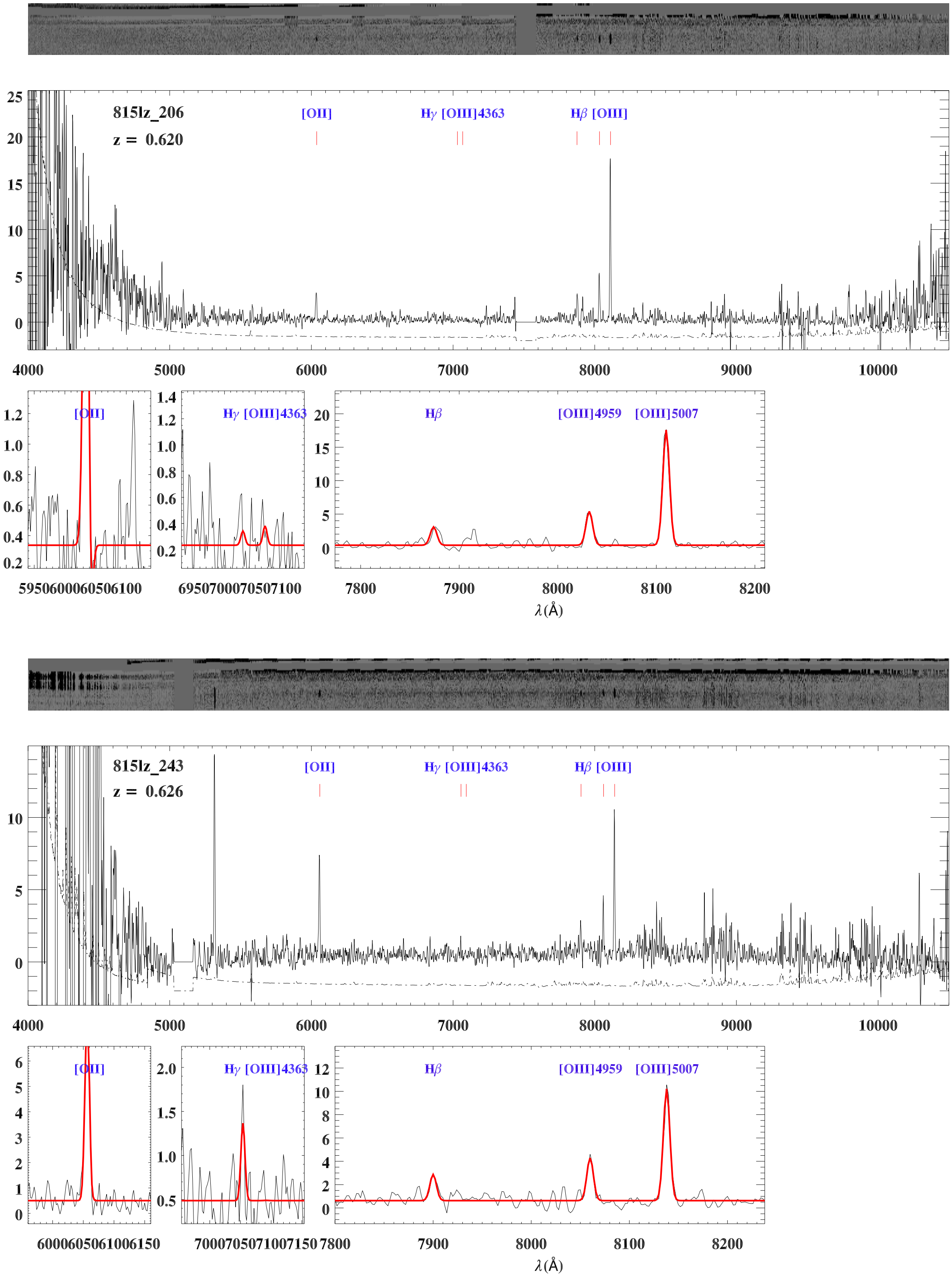

Figure A.30: Continued.

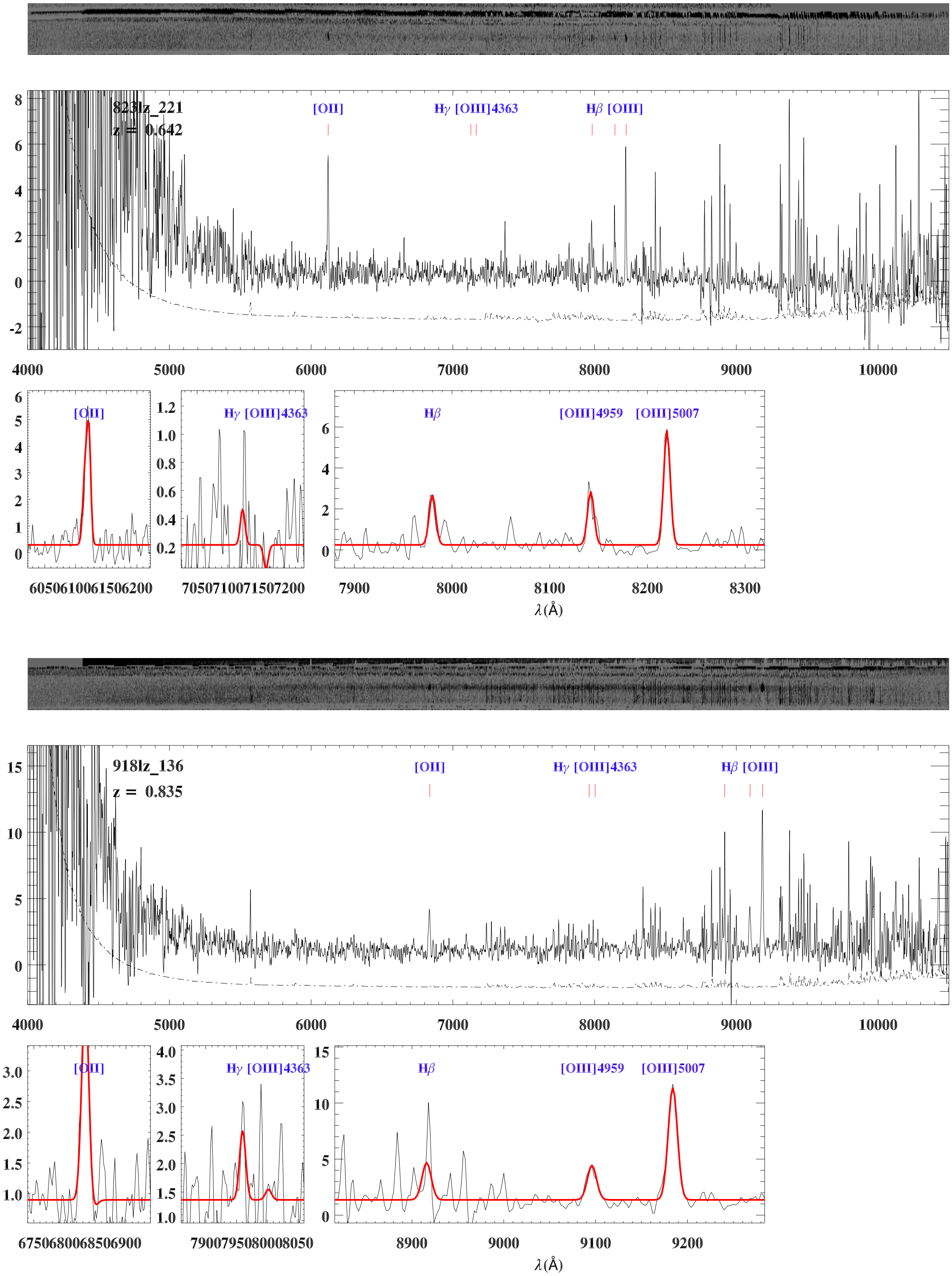

Figure A.31: Continued.

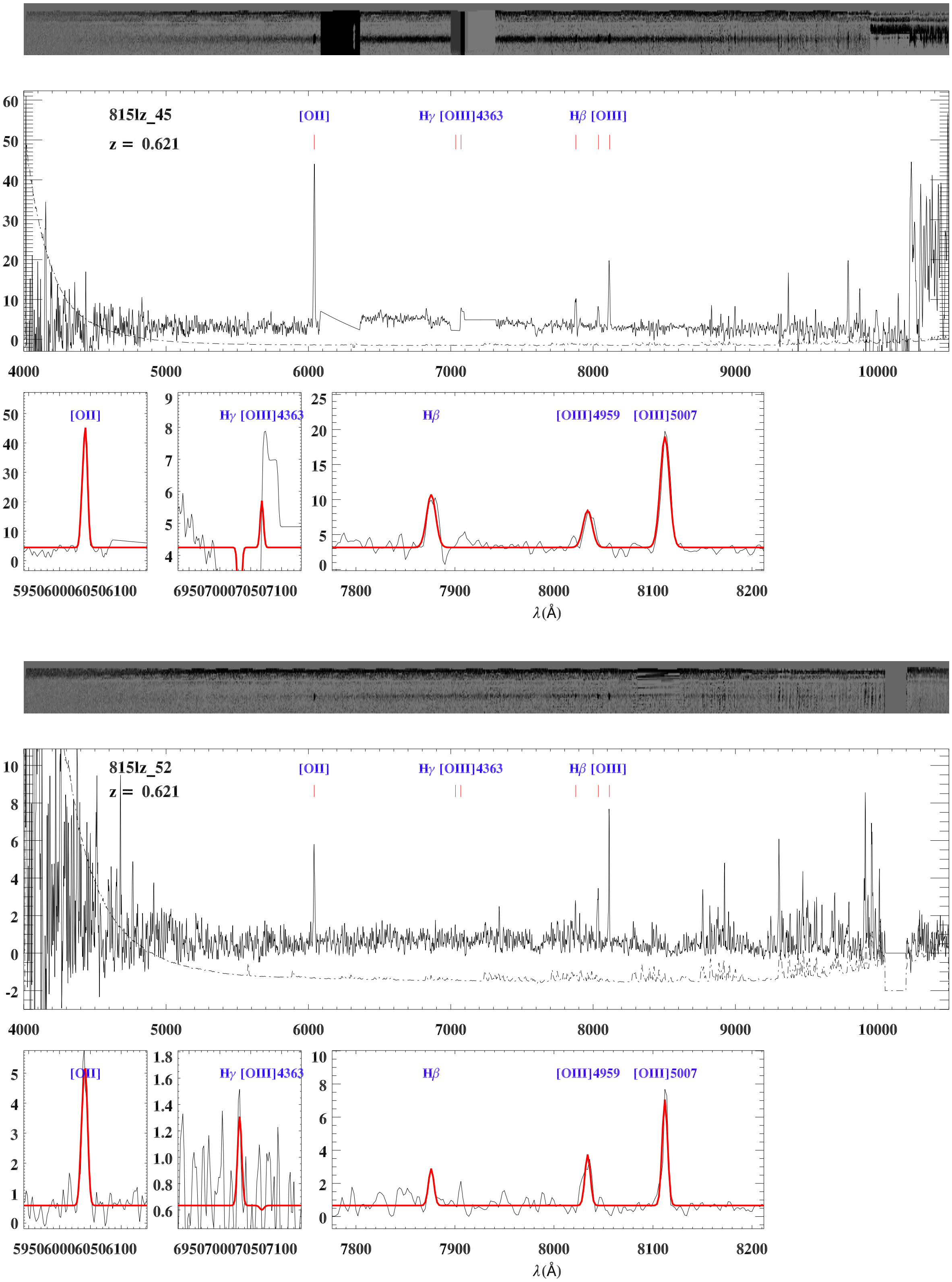

Figure A.32: Continued.

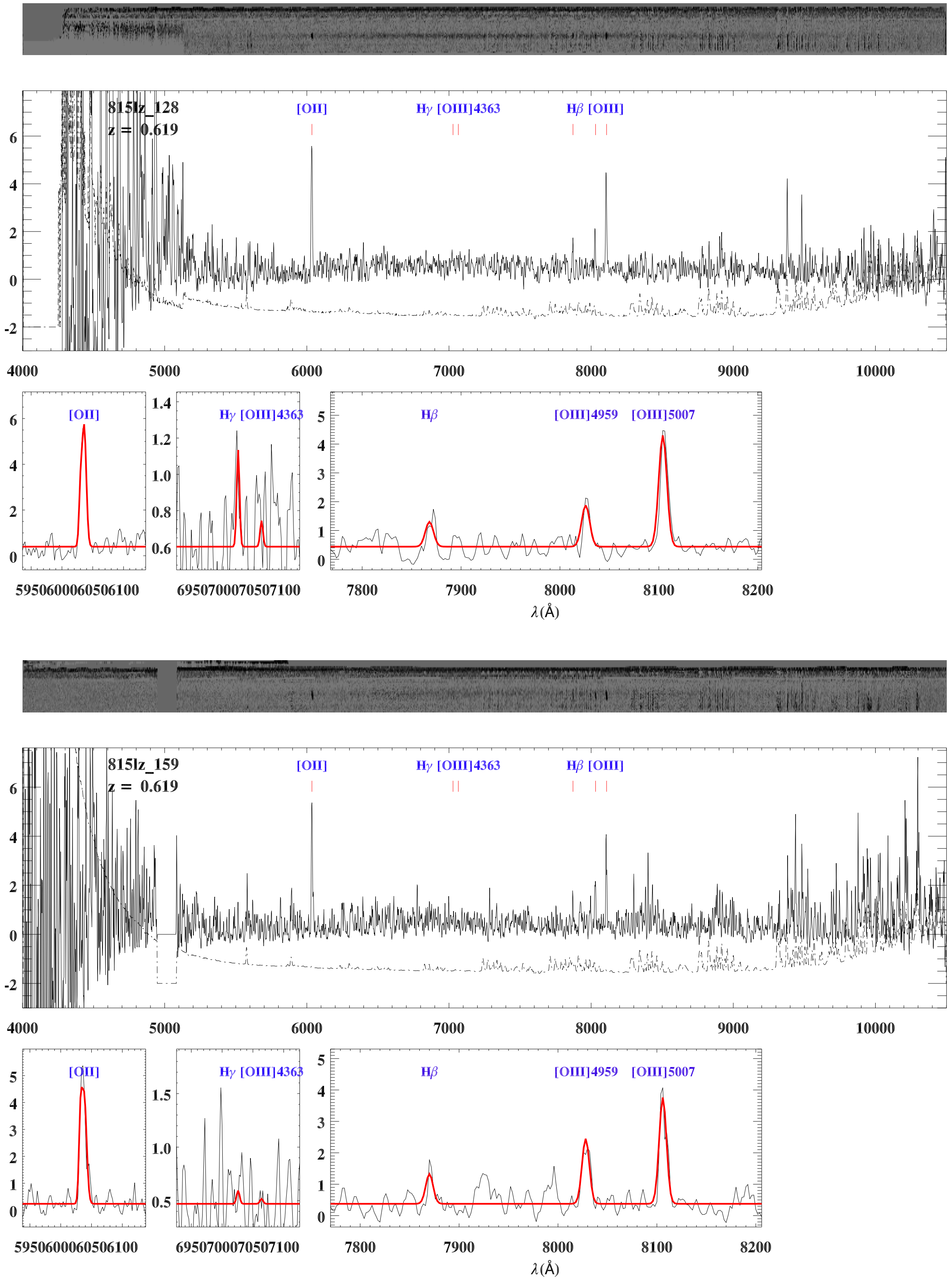

Figure A.33: Continued.

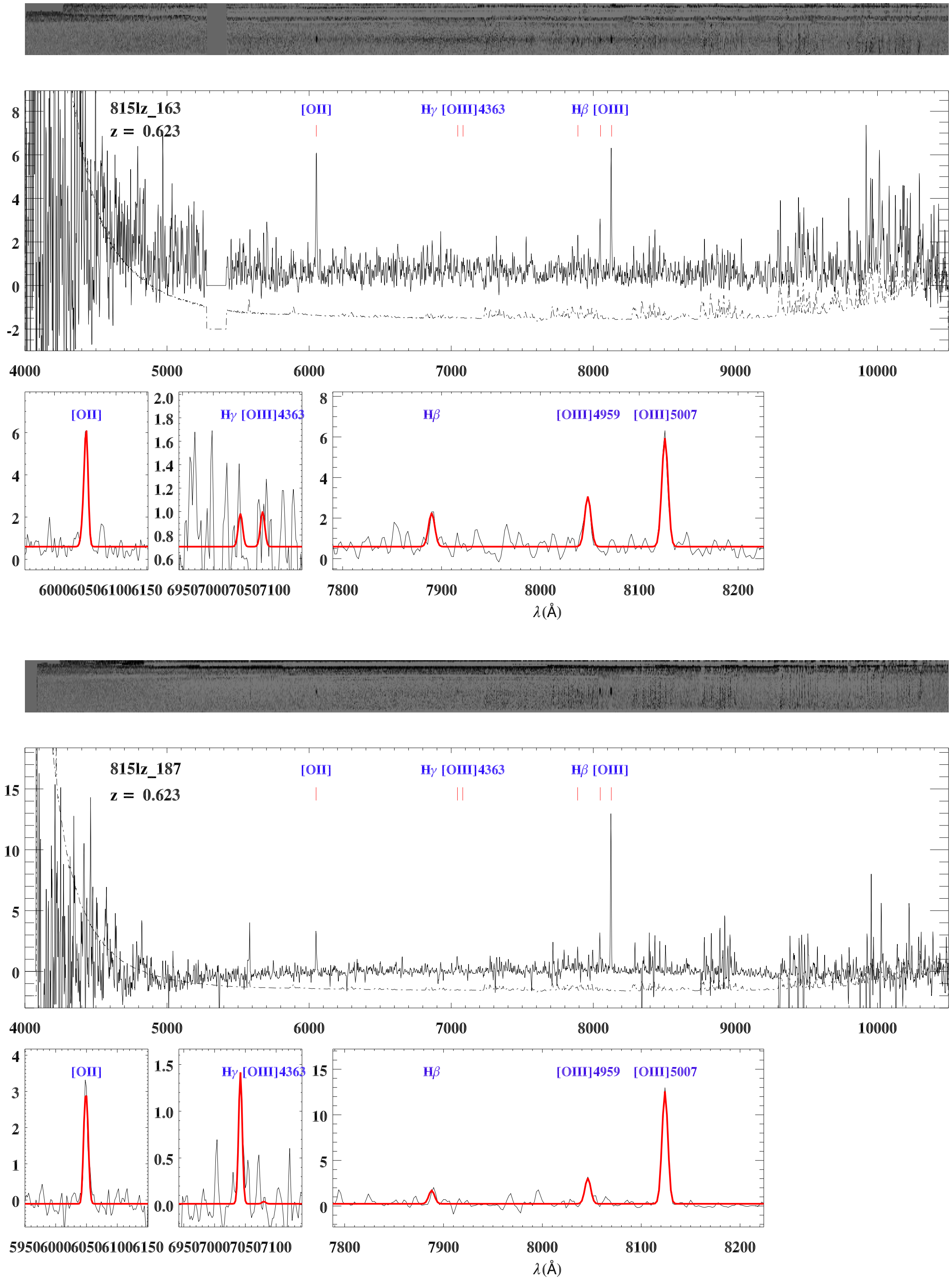

Figure A.34: Continued.

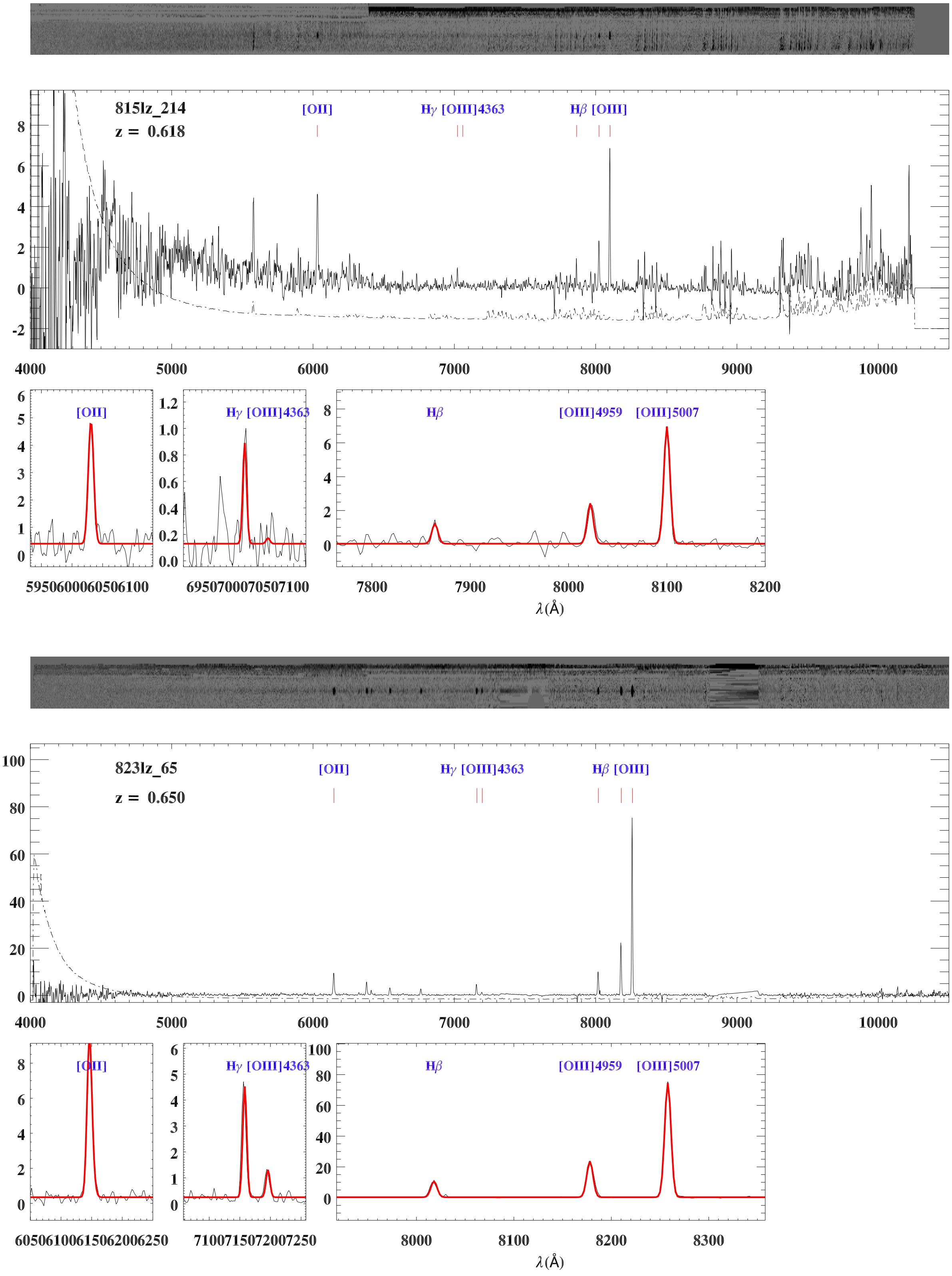

Figure A.35: Continued.

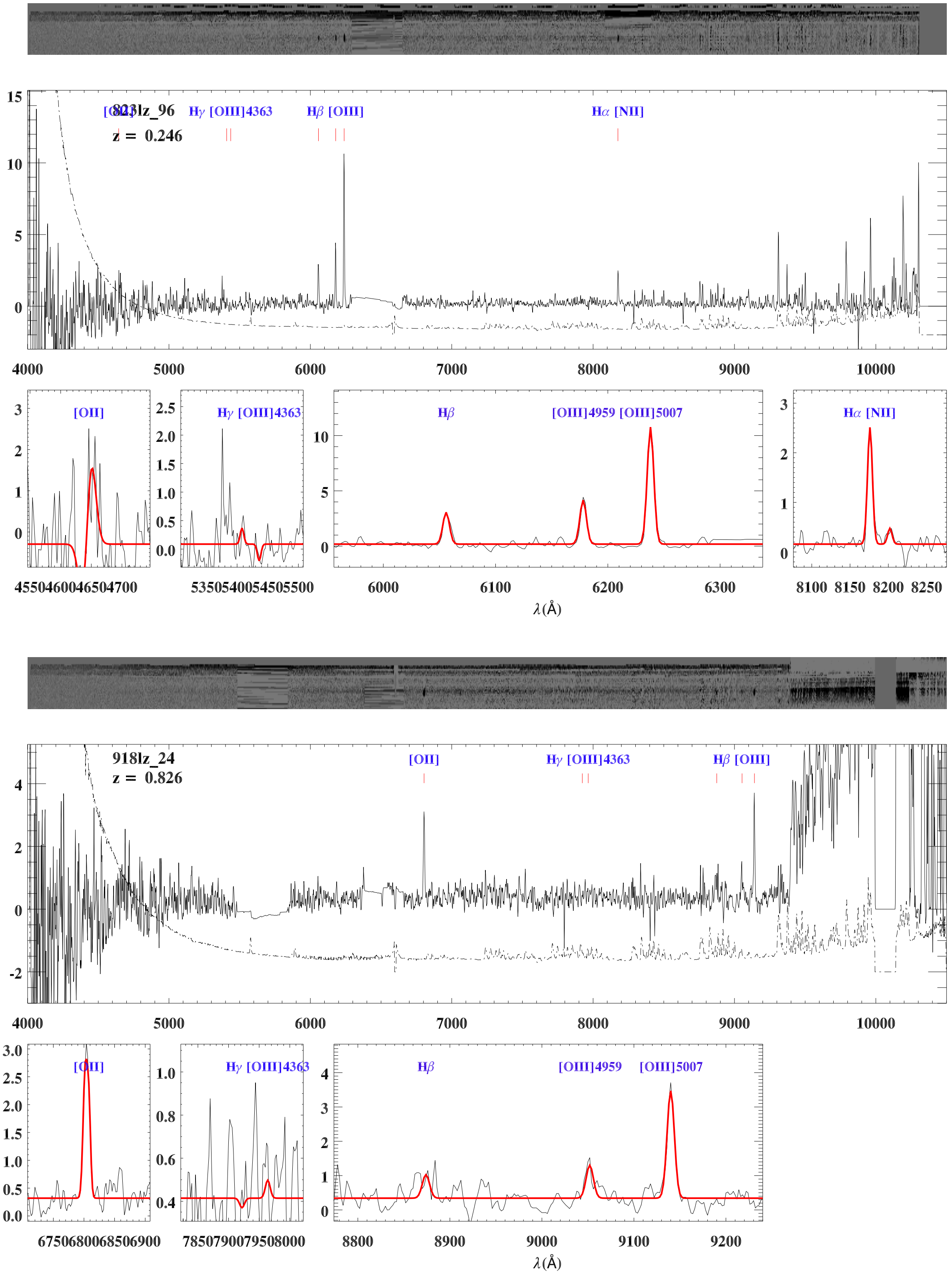

Figure A.36: Continued.

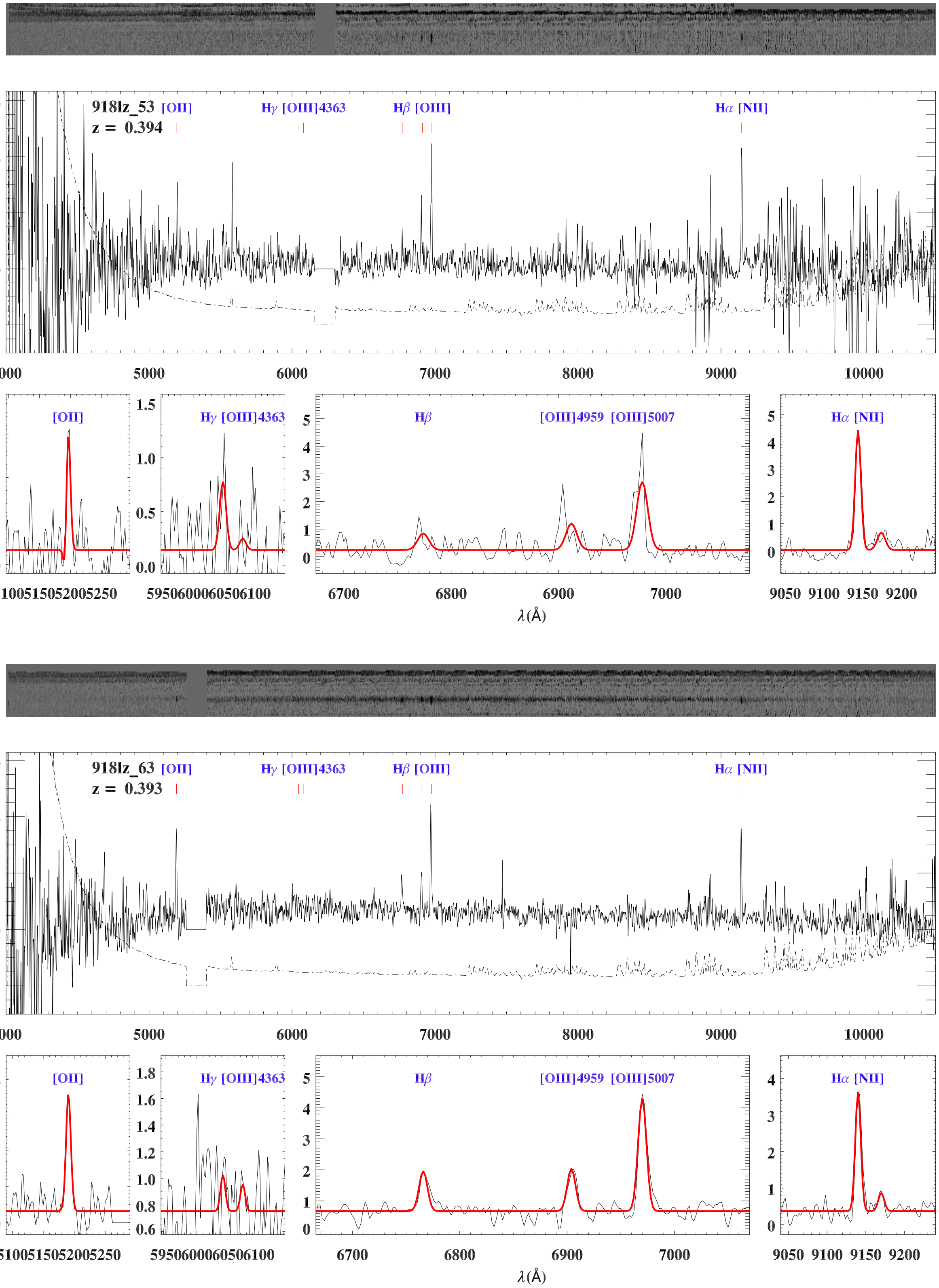

Figure A.37: Continued.

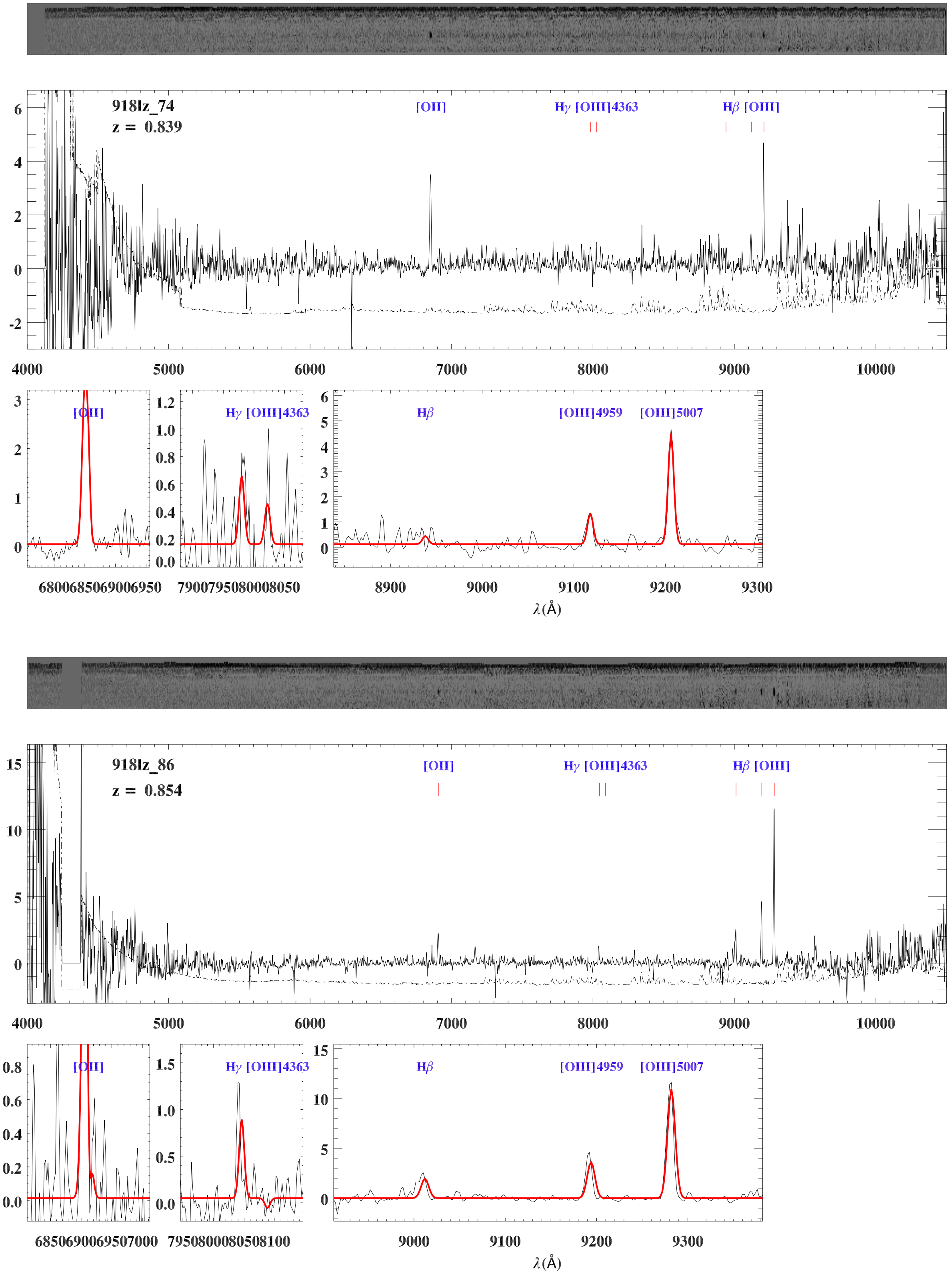

Figure A.38: Continued.

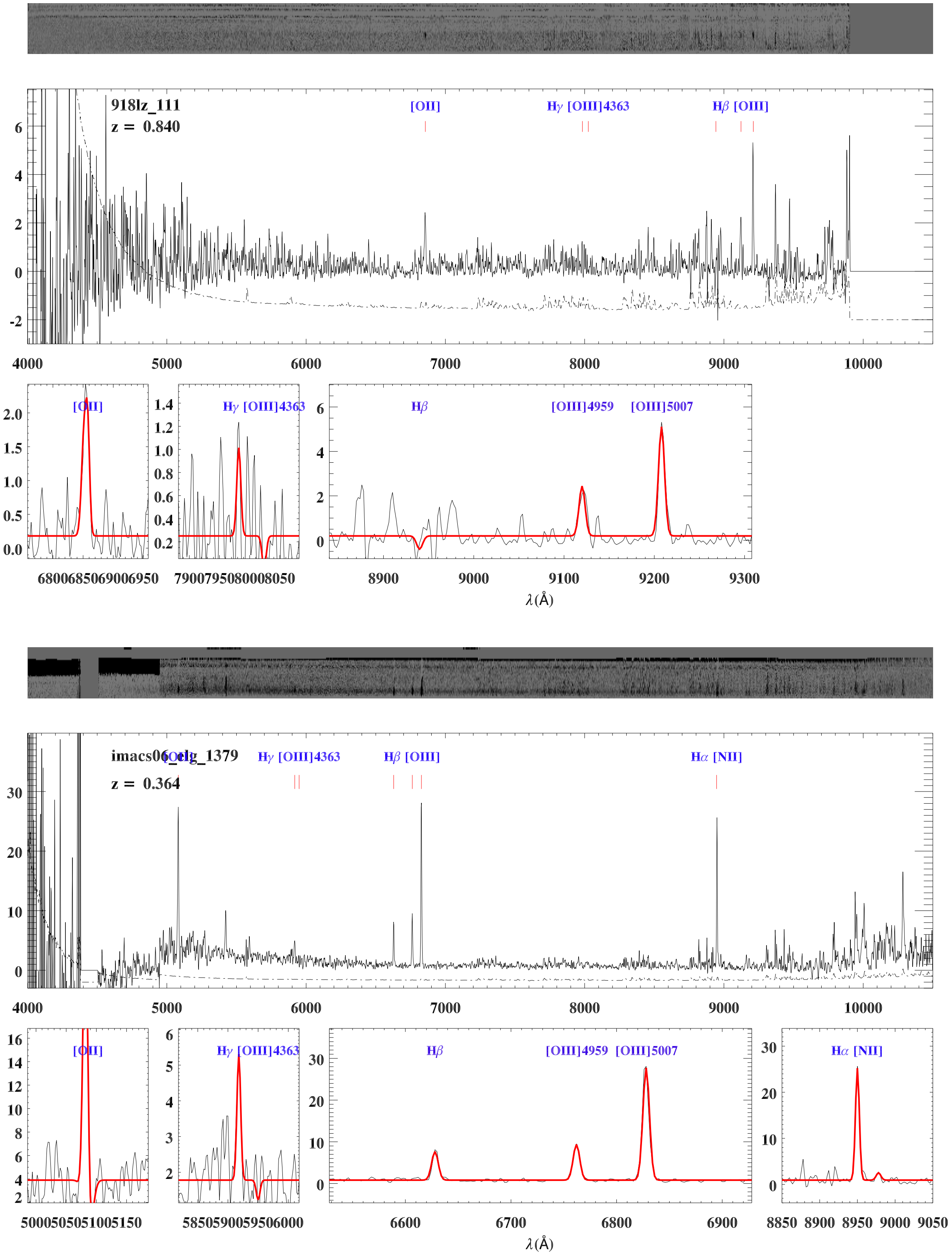

Figure A.39: Continued.

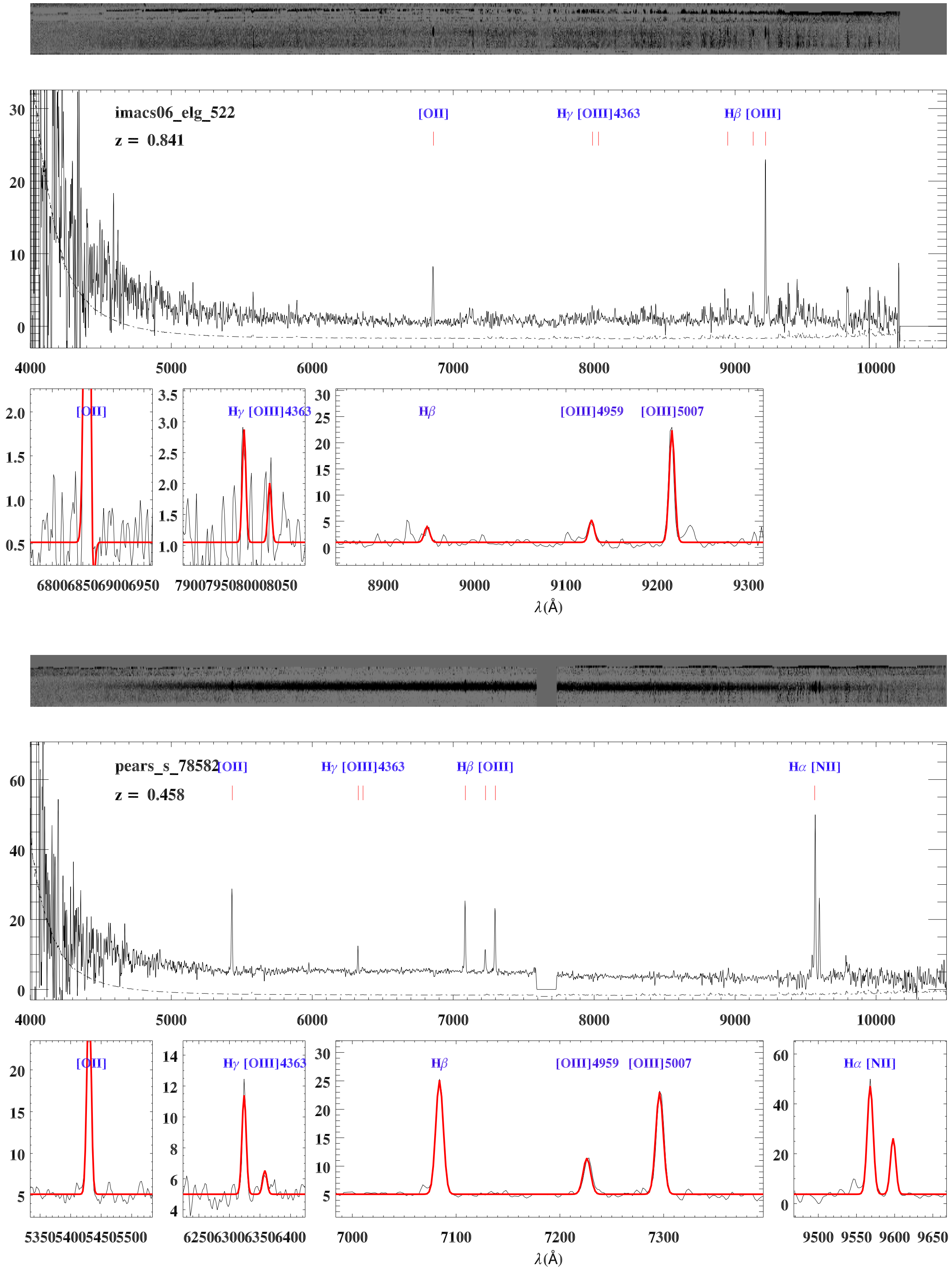

Figure A.40: Continued.

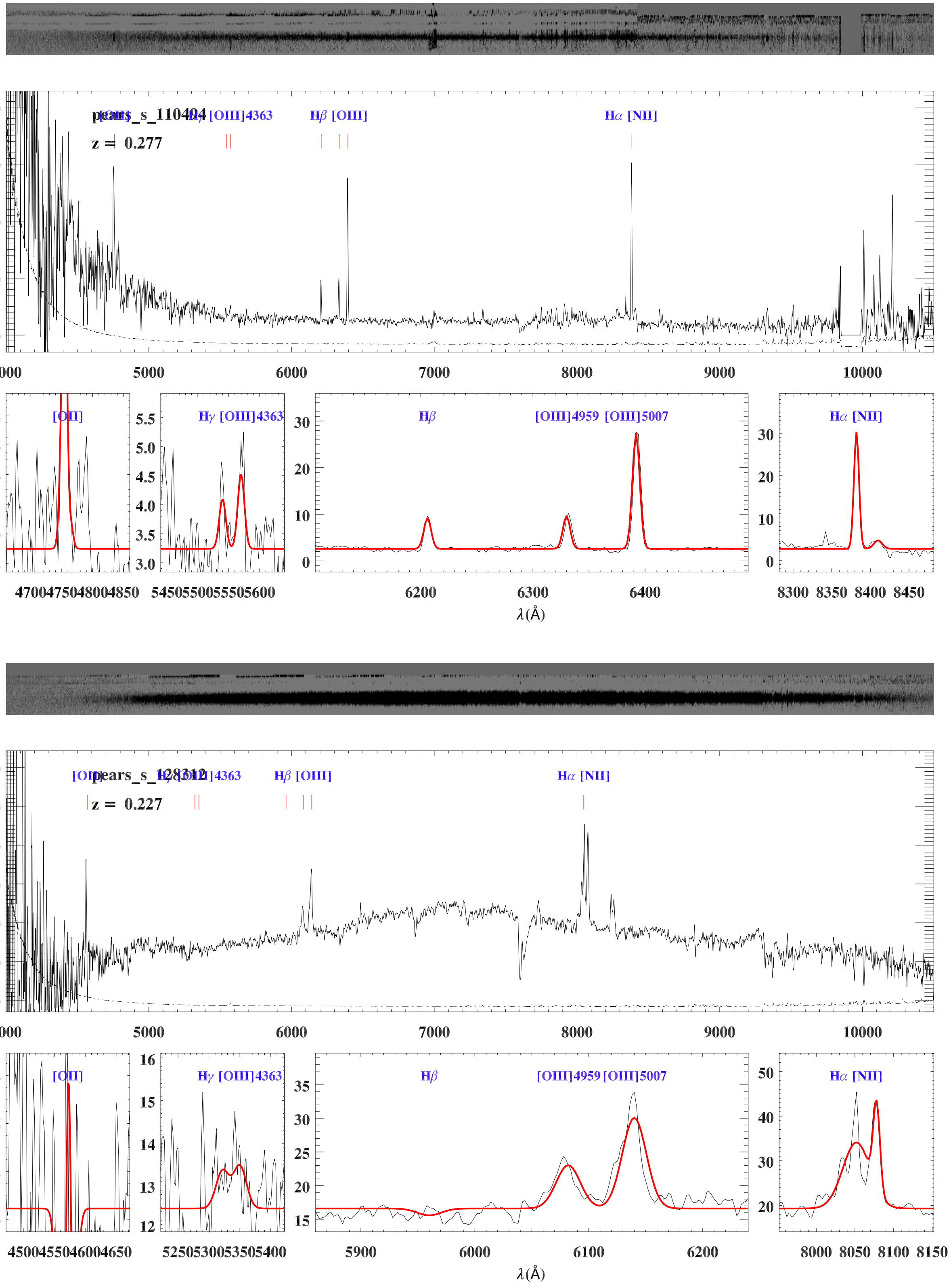

Figure A.41: Continued.

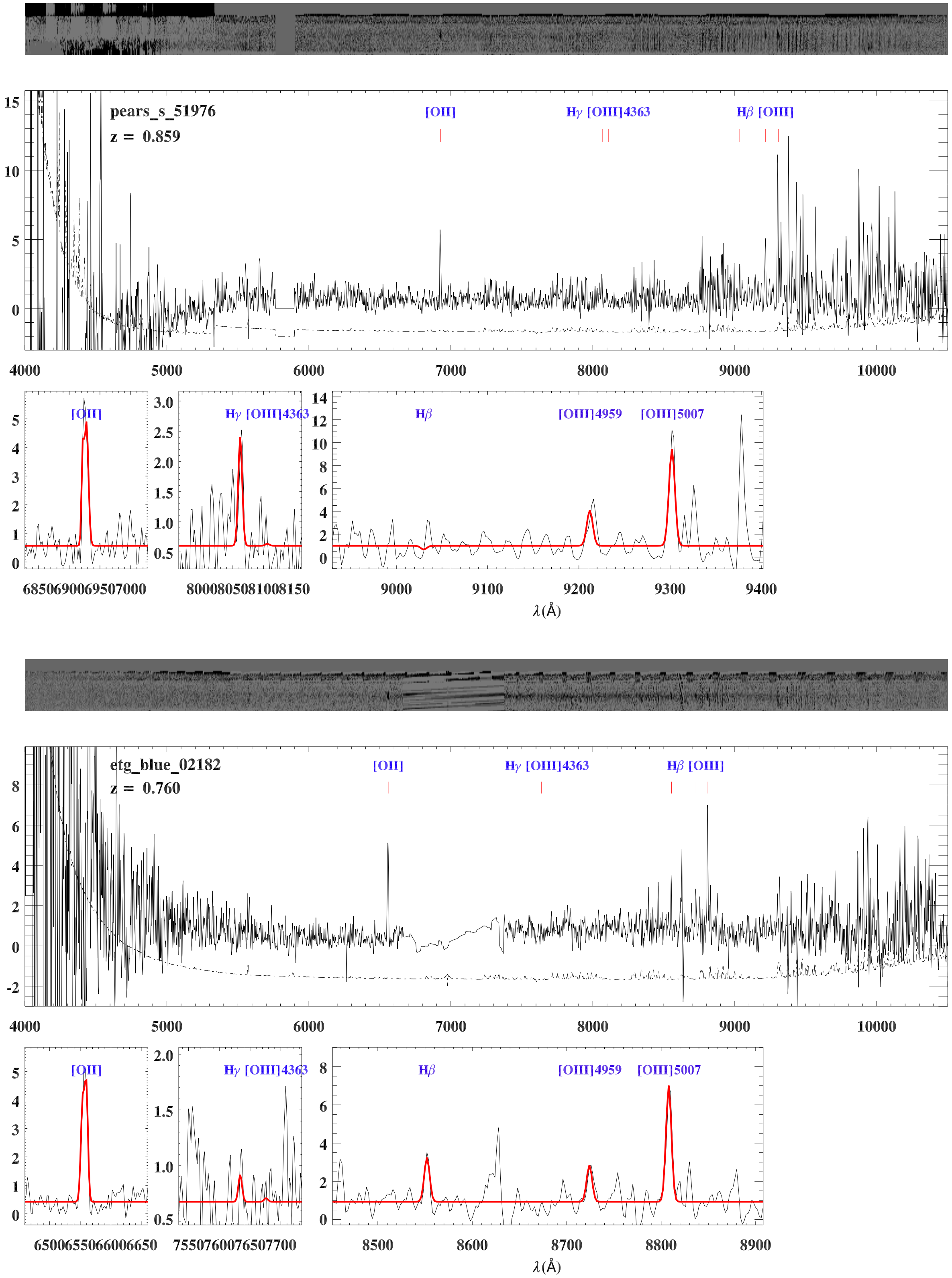

Figure A.42: Continued.

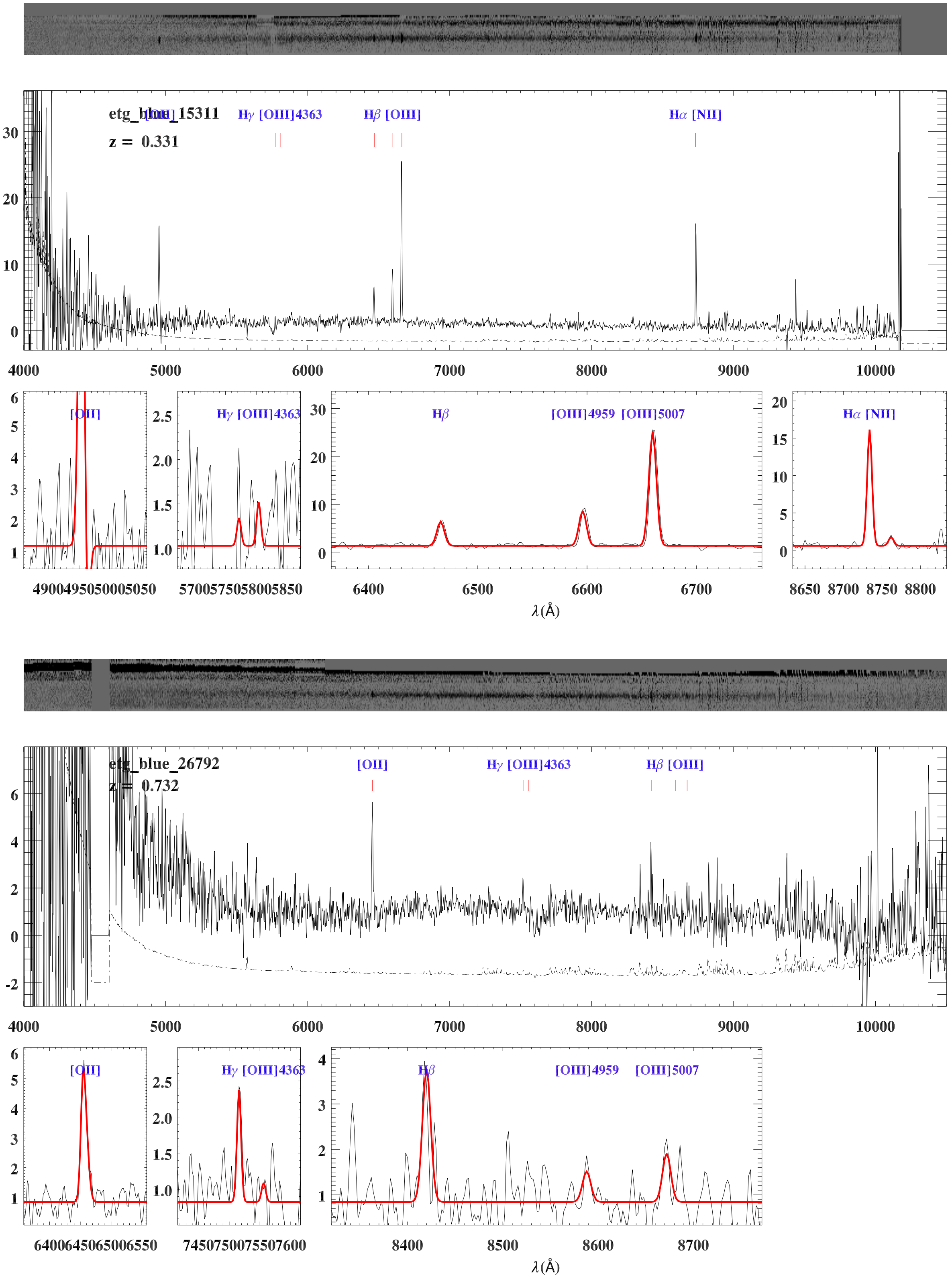

Figure A.43: Continued.

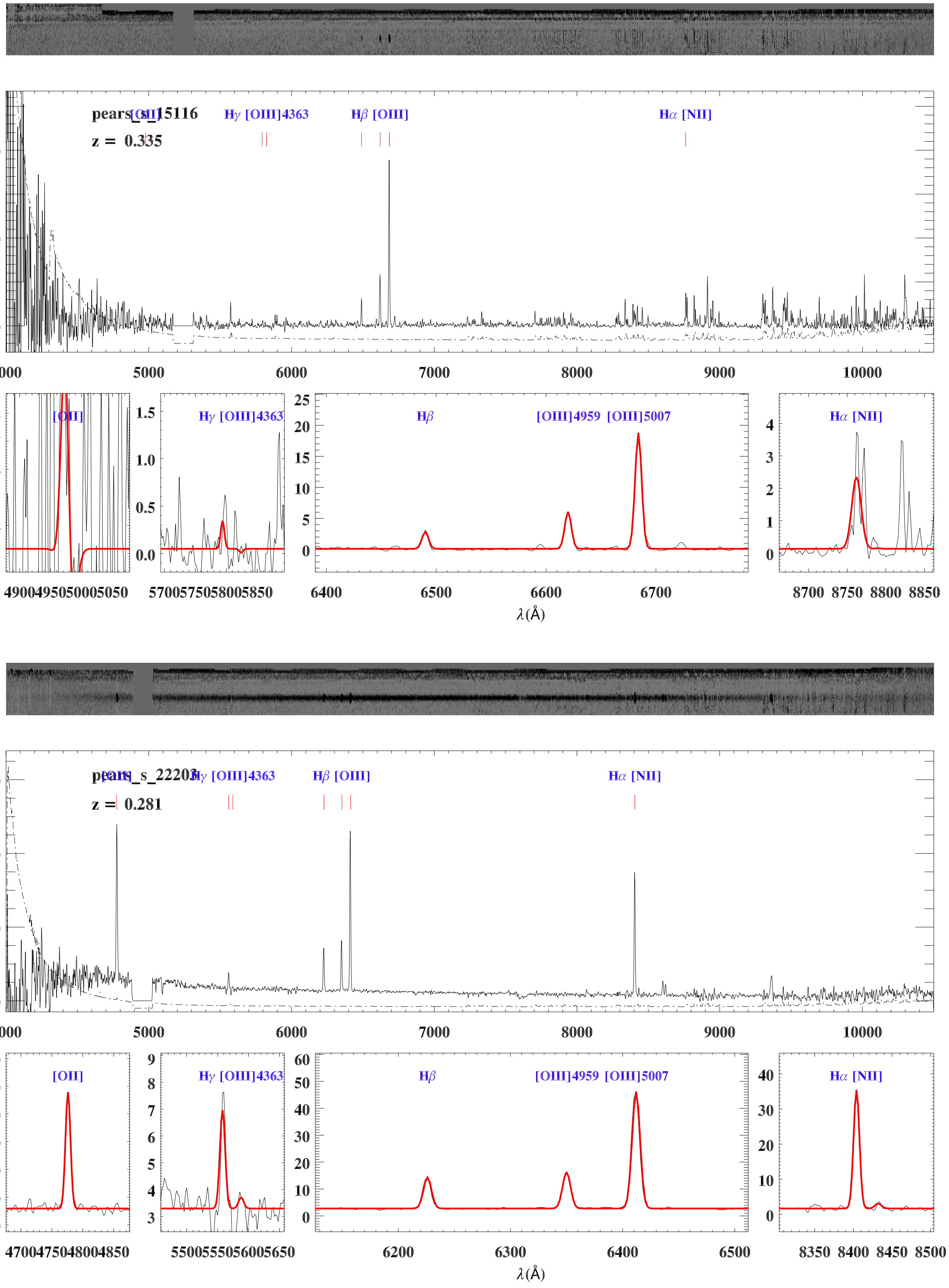

Figure A.44: Continued.

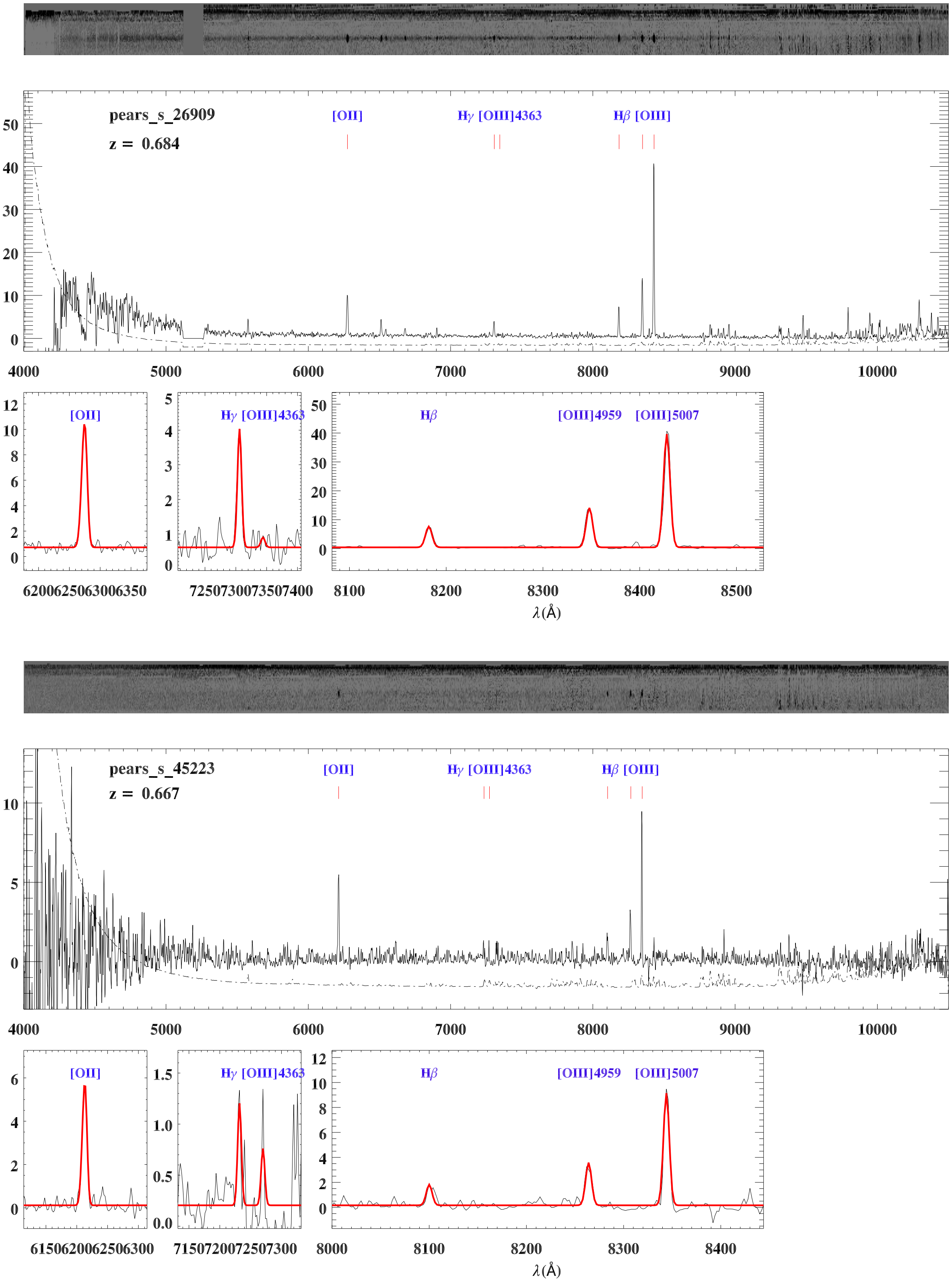

Figure A.45: Continued.

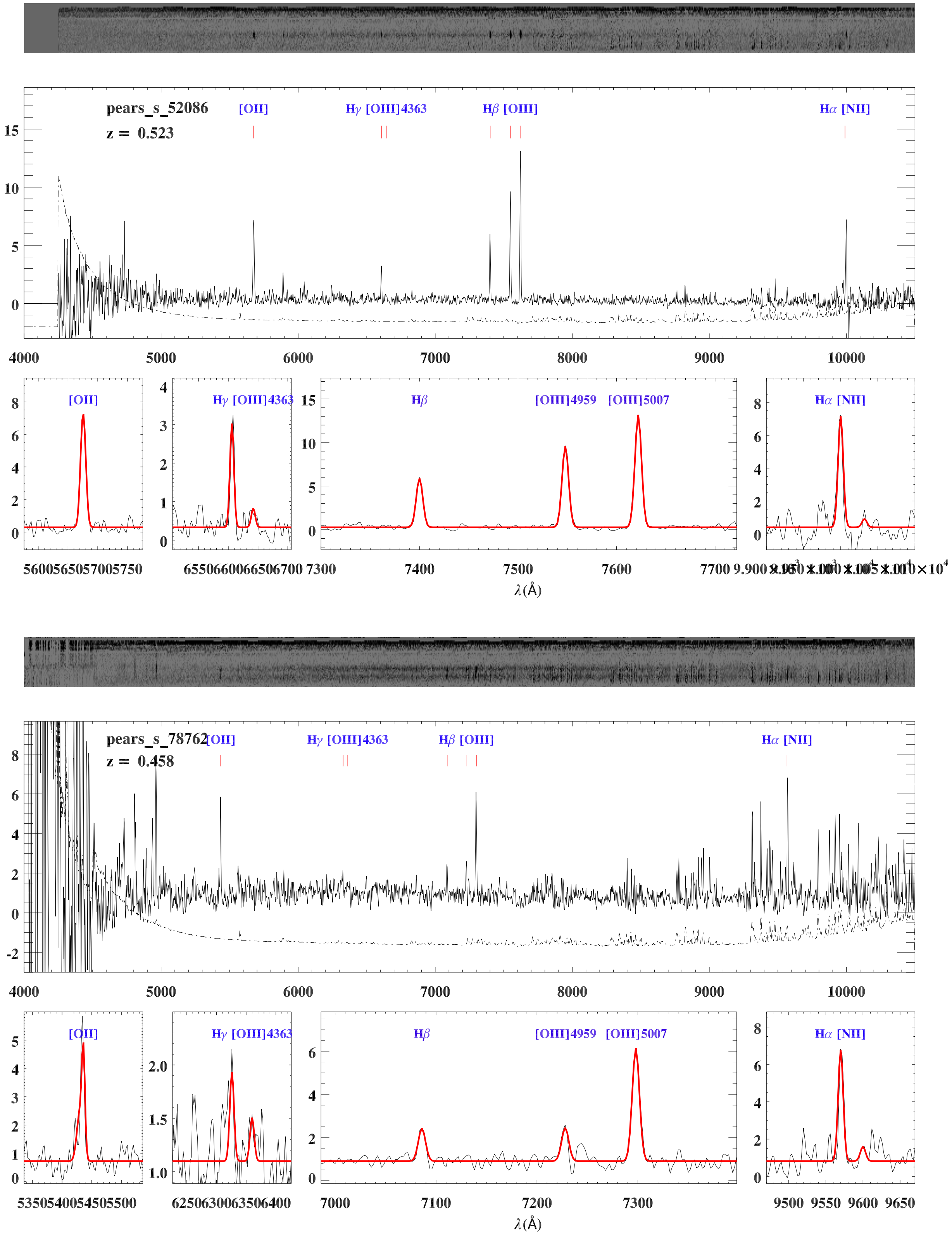

Figure A.46: Continued.

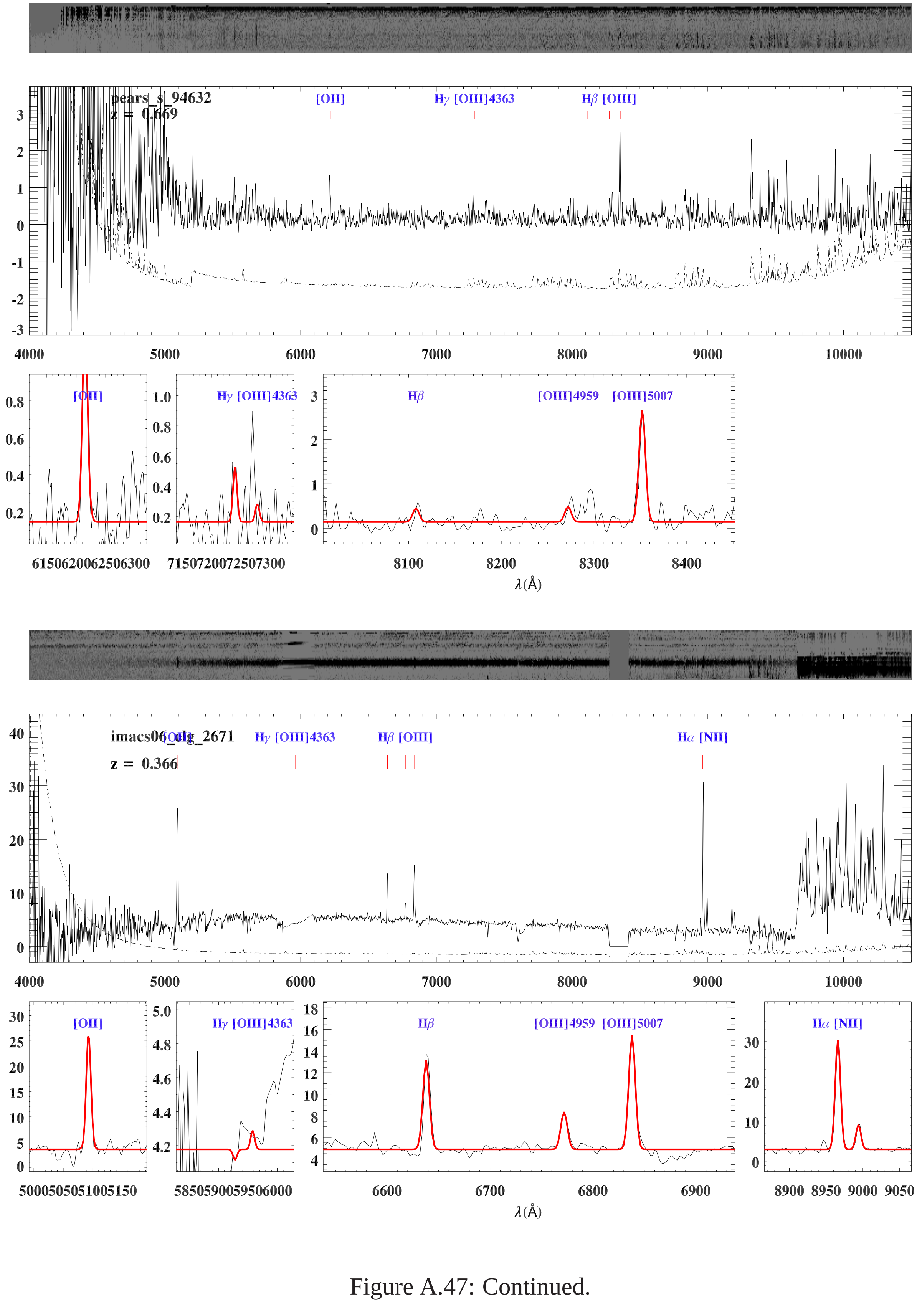

Figure A.47: Continued.

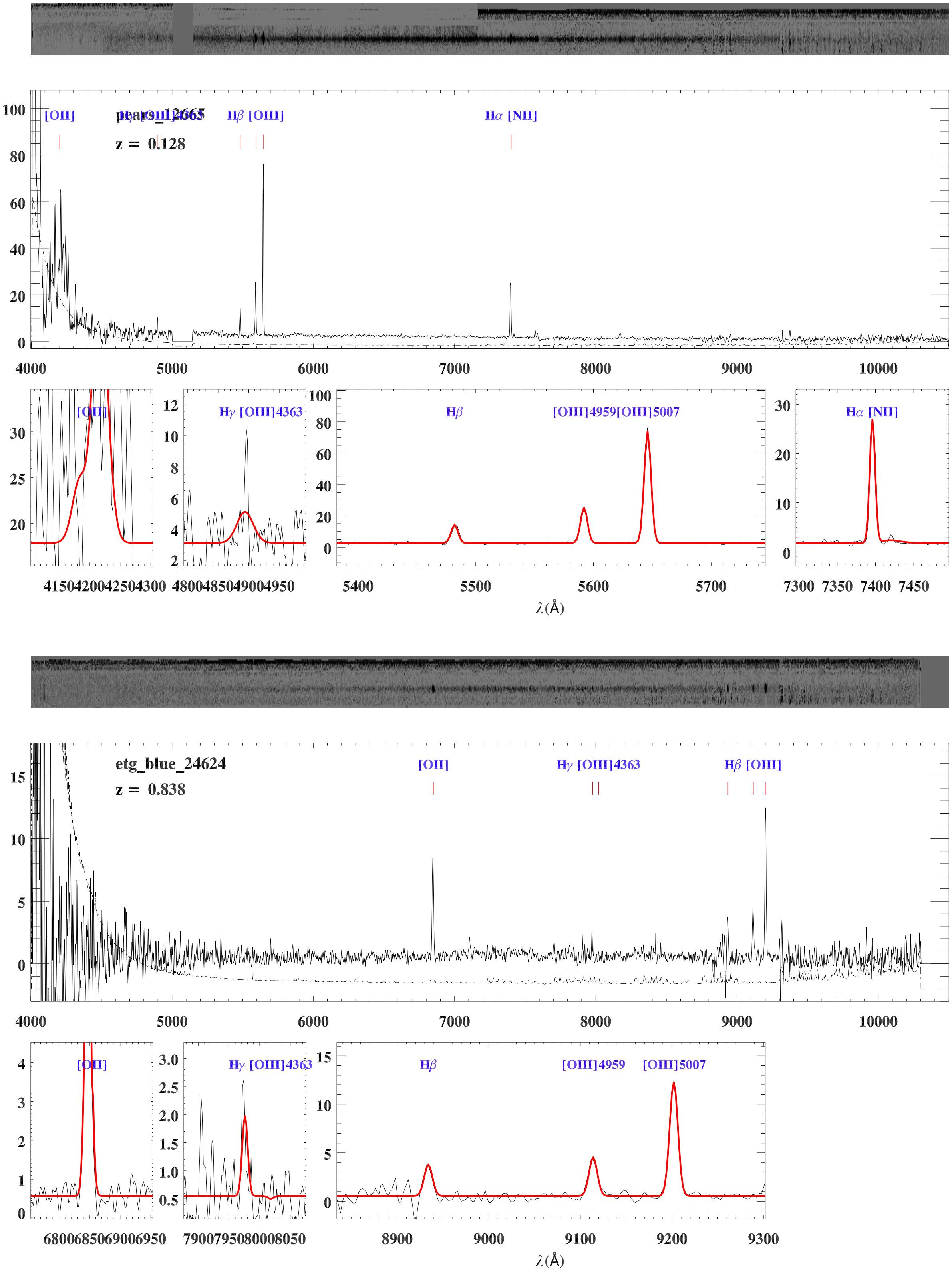

Figure A.48: Continued.

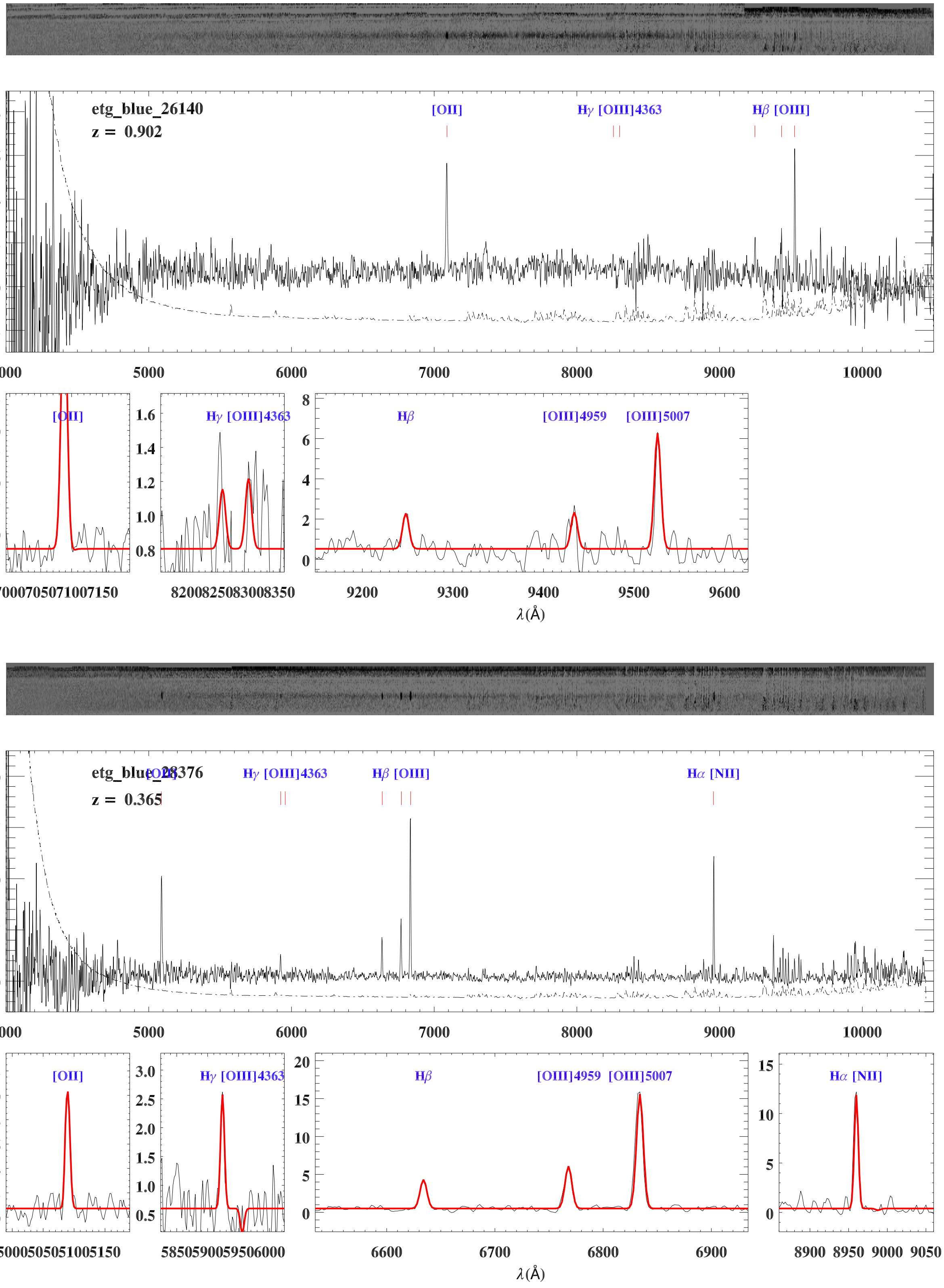

Figure A.49: Continued.

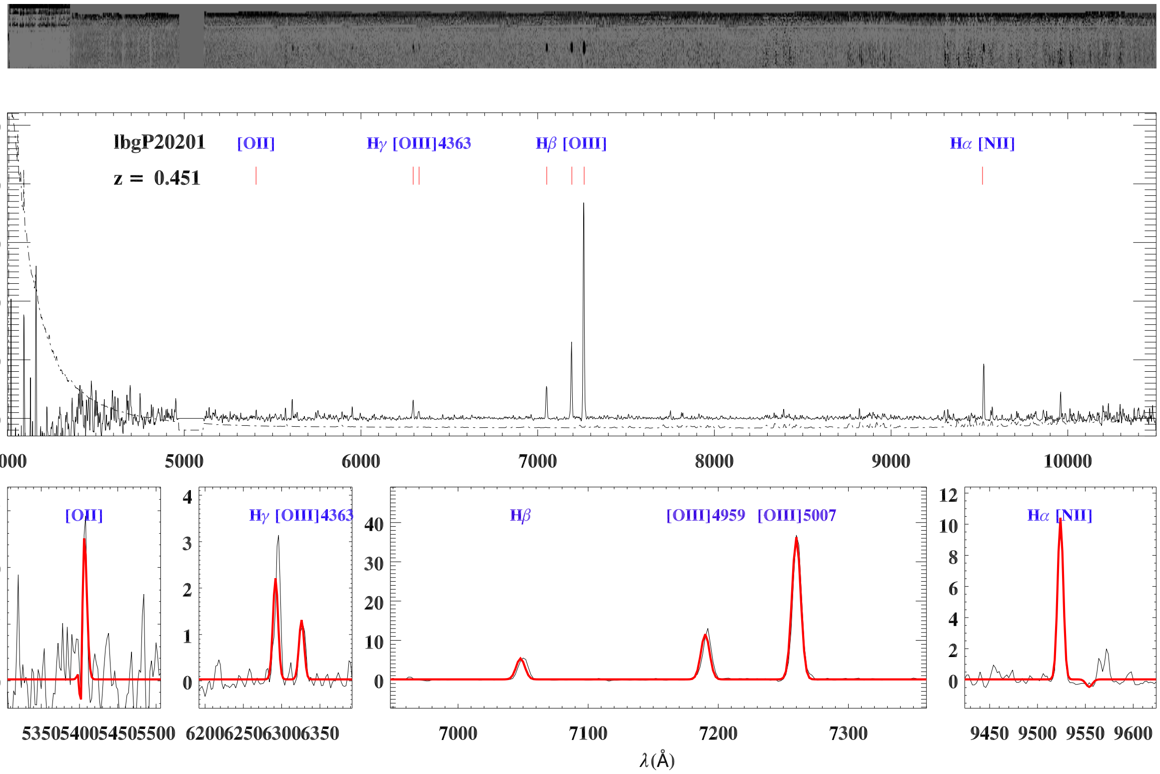

Figure A.50: Continued.